Scalable 1D and 2D Polymer-Based Nanoparticles via Crystallization-Driven Self-Assembly

Charlotte Emily Ellis
Master of Research, Cardiff University, 2017
Master in Science, University of Bristol, 2016

A Dissertation Submitted in Partial Fulfillment of the Requirements for the Degree of

DOCTOR OF PHILOSOPHY

in the Department of Chemistry

We acknowledge with respect the Lekwungen peoples on whose traditional territory the university stands and the Songhees, Esquimalt and WSÁNEĆ peoples whose historical relationships with the land continue to this day.

Supervisory Committee

Scalable 1D and 2D Polymer-Based Nanoparticles via Crystallization-Driven Self-Assembly

Charlotte Emily Ellis
Master of Research, Cardiff University, 2017
Master in Science, University of Bristol, 2016

Supervisory Committee:

Prof. Ian Manners, Department of Chemistry
Supervisor

Prof. David Leitch, Department of Chemistry
Departmental Member

Prof. Rustom Bhiladvala, Department of Mechanical Engineering
Outside Member

Abstract

Self-assembly is ubiquitous in nature. A diverse range of materials with exceptional properties are accessed from a limited number of sub-units, through controlling structural order on all length-scales. Achieving the same level of control to access functional materials akin to those in nature is a key challenge in chemistry. Self-assembly of block copolymers (BCPs) offers a valuable bottom-up route, governed by non-covalent interactions, to access ordered assemblies on the nanoscale. Anisotropic nanostructures, such as one- and two-dimensional (1D and 2D) micelle morphologies, are of particular interest for various applications including those in biomedicine, catalysis, optoelectronics, and materials engineering.

Crystallization-driven self-assembly (CDSA) of BCPs containing a crystallizable core-forming segment presents a robust route to preparing 1D and 2D micelles. Significantly, the use of pre-existing seed micelles in a process termed living CDSA allows access to 1D and 2D nanostructures of controlled size and low size-dispersity. Although CDSA protocols represent powerful tools for the formation controlled 1D and 2D nanostructures, key challenges associated with scale-up of these processes remain. In most cases, increasing the concentration at which living CDSA is performed results in competitive self-nucleation, compromising micelle size-control and -dispersity. Living polymerization-induced crystallization-driven self-assembly (PI-CDSA) has been presented as a promising alternative route to accessing scalable 1D micelles. In this case, the polymerization, self-assembly, and seeded growth of a BCP containing a crystallizable core-forming segment occur *in situ*. However, the scope of living PI-CDSA is currently limited to the use of polyferrocenylsilane (PFS)-based BCPs.

Owing to the diverse range of crystalline core chemistries compatible with CDSA protocols, and therefore various promising applications of 1D and 2D micelles, scale-up is essential to facilitate their further investigation and application. The work presented in this thesis focusses on upscaling

the preparation and processing of controlled 1D and 2D micelles with a crystalline core. The scalable preparation of low dispersity 2D platelet micelles by living CDSA of a charge-terminated PFS homopolymer with surfactant counteranions is presented in Chapter 2. Here, fundamental insight into the effects of living CDSA concentration on platelet dimensions, structure fidelity, and aggregation behaviour is provided. In Chapter 3, the scope of living PI-CDSA is extended to access scalable length-controlled low dispersity 1D nanofibers containing a biodegradable poly(fluorenetrimethylenecarbonate) (PFTMC) crystalline core. PFTMC-based 1D fibers are of interest for biomedical applications, hence, in this work, it is demonstrated that living PI-CDSA can be used to prepare fibers exhibiting biologically-relevant lengths at scalable concentrations. In Chapter 4, the scalable formation of low dispersity 1D micelles by living CDSA of a PFS-based BCP in a continuous flow setup is explored. Processing of 1D micelles into microfibers using simple, low cost, and high throughput electrospinning techniques is demonstrated in Chapter 5. Finally, Chapter 6 summarises the contribution of this thesis to improving the scalability of CDSA protocols and provides future directions for this work.

Table of Contents

List of Figures

List of Schemes

List of Tables

Abbreviations

0D	Zero-dimensional
1D	One-dimensional
2D	Two-dimensional
3D	Three-dimensional
Å	Angstrom
a_0	Solvophilic head group area
AFM	Atomic force microscopy
A_n	Number-average area
AOT	Bis(2-ethylhexyl)sulfosuccinate
A_w	Weight-average area
A_w/A_n	Area-dispersity
-*b*-	Block
BCP	Block copolymer
br	Broad
°C	Degrees Celsius
ca.	Circa
CDSA	Crystallization-driven self-assembly
CMC	Critical micelle concentration
d	doublet
d	Deuterium
Da	Dalton
DBU	1,8-diazacyclo[5.4.0]undec-7-ene
DCM	Dichloromethane

DLS	Dynamic light scattering
DMF	Dimethylformamide
DMSO	Dimethyl sulfoxide
D_n	Number-average diameter
DNA	Deoxyribonucleic acid
DOSY	Diffusion ordered spectroscopy
DP_n	Degree of polymerization
DSC	Differential scanning calorimetry
D_w	Weight-average diameter
D_w/D_n	Dispersity in diameter
f_A	Volume fraction of block A
g	Gram
GPC	Gel permeation chromatography
h	Hour
*i*PrOH	Isopropanol
J	J-coupling constant
l	Solvophobic tail length
L_n	Number-average contour length
L_w	Weight-average contour length
L_w/L_n	Length-dispersity
-*m*-	Micelle block
m	Metre
m	Multiplet
MALDI-TOF MS	Matrix-assisted laser desorption/ionization time-of-flight mass spectrometry

MeCN	Acetonitrile
MeOH	Methanol
mg	Milligram
MHz	Megahertz
min	Minute
mL	Millilitre
mmol	Millimole
M_n	Number-average molecular weight
mol	Mole
m_{unimer}/m_{seed}	Unimer-to-seed mass ratio
M_w	Weight-average molecular weight
M_w/M_n	Molecular weight dispersity
nm	Nanometre
NMP	Nitroxide-mediated polymerization
NMR	Nuclear magnetic resonance
m/z	Mass-to-charge ratio
P	Packing parameter
P2VP	Poly(2-vinylpyridine)
P3HT	Poly(3-hexylthiophene)
PCL	Poly(ε-caprolactone)
PDHF	Poly(di-*n*-hexylfluorene)
PDMA	Poly(*N*,*N*-dimethylacrylamide)
PDMAEMA	Poly(2-(dimethylamino)ethyl methacrylate))
PDMS	Poly(dimethylsiloxane)
PDI	Polydispersity index

PE	Polyethylene
PEG	Poly(ethylene glycol)
PEO	Poly(ethylene oxide)
PFDMS	Poly(ferrocenyldimethylsilane)
PFEMS	Poly(ferrocenylethylmethylsilane)
PFG	Poly(ferrocenyldimethylgermane)
PFS	Polyferrocenylsilane, poly(ferrocenyldimethylsilane)
PFTMC	Poly(fluorenetrimethylenecarbonate)
PGMA	Poly(glycerol monomethacrylate)
PHPMA	Poly(2-hydroxylpropyl methacrylate)
PI	Polyisoprene
PI-CDSA	Polymerization-induced crystallization-driven self-assembly
PIHSA	Polymerization-induced hierarchical self-assembly
PISA	Polymerization-induced self-assembly
PLLA	Poly(*L*-lactide)
PMMA	Poly(methyl methacrylate)
PMVS	Poly(methylvinylsiloxane)
PNIPAM	Poly(*N*-isopropylacrylamide)
ppm	Parts per million
PS	Polystyrene
PtBS	Poly(*tert*-butylstyrene)
RAFT	Reversible addition-fragmentation chain transfer
ran-	Random
$R_{H,app}$	Apparent hydrodynamic radius
RI	Refractive index

R_n	Number-average aspect ratio
RNA	Ribonucleic acid
ROP	Ring-opening polymerization
ROPI-CDSA	Ring-opening polymerization-induced crystallization-driven self-assembly
ROMP	Ring-opening metathesis polymerization
ROMPI-CDSA	Ring-opening metathesis polymerization-induced crystallization-driven self-assembly
rpm	Revolutions per minute
RT	Room temperature
R_w	Weight-average aspect ratio
R_w/R_n	Dispersity in aspect ratio
s	Second
s	Singlet
SAED	Selected area electron diffraction
SAXS	Small-angle X-ray scattering
SDS	Dodecyl sulfate
SEM	Scanning electron microscopy
t	Triplet
TBP	4-*tert*-butylphenol
T_b	Boiling point
T_c	Crystallization temperature
TEM	Transmission electron microscopy
THF	Tetrahydrofuran
T_m	Melting temperature

v	Solvophobic tail volume
vol%	Volume fraction
WAXS	Wide-angle X-ray scattering
W_n	Number-average width
wt%	Weight percent
W_w	Weight-average width
W_w/W_n	Width-dispersity
δ	Chemical shift
λ	Wavelength
μ	Micrometre
σ	Standard deviation
χ	Flory-Huggins parameter
χN	Segregation product

Acknowledgements

This journey would not have been possible without the support of my family, friends, colleagues, and supervisors.

I would like to thank Professor Ian Manners for the opportunity to carry out my PhD in his research group, first in Bristol (Year 0–1.5) and then in Victoria (Year 1.5–4.5). I am sincerely grateful for Ian's supervision and guidance. His high scientific standards and inquisitive nature have played a pivotal role in bringing out the best scientist in me. I am particularly grateful for the opportunity to relocate to Canada with the research group, which has been an amazing life-changing experience. I would also like to thank Deborah O'Hanlon-Manners for her assistance throughout my PhD and the move to Canada. Ian and Deborah's dedicated kindness and support over the past four and a half years have been invaluable.

I have had the pleasure of working alongside some very intelligent, gracious, and inspiring people during my PhD. With there being too many people to name, I would like to highlight some of those that had the greatest impact. From the Manners group, I would like to thank Ali, Ayesha, Casper, Connor, Diego 1, Diego 2, Etienne, Hannah, Harrison, Harvey, Hayley, Horatio, John, Lei, Liam, Marcus, Matt, Nikki, Sam, Steve, Theresa, Tomoya, and Vince. I also extend my thanks to Leah, Natalie, and Zoey, who have been great friends throughout my time at UVic.

I would like to express my gratitude to all my family and friends. Especially to my partner, Logan, for never failing to make me laugh, even on a grey day. His love, support, and charisma are like no other, and have been amazing over the past few years. I would also like to thank my closest friend, Abby, for her unwavering support in times of need, even from across the world. Finally, I would like to give special thanks my parents, Andrea and Andre, and my siblings, Issy and Ollie, for always being my biggest cheerleaders in everything I do.

Chapter 1 Introduction

1.1 Bottom-Up Self-Assembly and Hierarchy in Nature

Nature's ability to precisely control structural order on all length-scales allows for materials with exceptional properties to be prepared.[1,2] This unprecedented control is achieved through self-assembly. Definitions of the term "self-assembly" are boundless in the literature, resulting in ambiguity.[3] Herein, we limit the definition to the autonomous organization of components into high-order structures, whereby the final structure is encoded into the precursors of the material itself.[3–5] Examples of self-assembled systems are ubiquitous in nature and include those on the molecular level, such as lipid bilayers; those on the planetary scale, such as weather systems; and those that form hierarchical materials such as wood, muscle, and bone.[1,3,6]

Bone is a fascinating example of a natural hierarchical structure that is composed of cells in an extracellular matrix consisting of both inorganic and organic phases.[7,8] The structure of bone ranges over several length-scales from the nanoscale to the macroscopic physiological scale, as shown in **Figure 1.1**.[7,8] Bone exhibits excellent mechanical properties whilst being lightweight, self-healing, and adaptive,[8] all of which is owed to the precise organization of its components on the nanoscale.[7] The organic phase of bone is composed of collagen, the most abundant protein in the human body, stabilized by water and a series of lipids and non-collagenous proteins.[7] At the lowest hierarchical level, tropocollagen is formed from three separate collagen molecules folded in a triple helix configuration with a length of ca. 300 nm and a diameter of ca. 1.5 nm.[7–9] At the next level of hierarchy, five tropocollagen triple helices self-organize into collagen microfibrils, driven by hydrophobic and electrostatic interactions.[7] On aggregation of collagen microfibrils, the inorganic phase of bone, hydroxyapatite ($Ca_{10}(PO_4)_6(OH)_2$) nanocrystals, is integrated to produce mineralized collagen fibrils with diameters of approximately 100 nm.[7–9] At the mesoscale, collagen fibrils further assemble to form lamellae (ca. 5 μm) and osteons (ca. 100 μm), which are the basic building

blocks of bone.[2,7] Other collagen-rich tissues such as skin, cartilage, and tendons, consist of the same nanoscale sub-units as bone, yet exhibit vastly different mechanical properties owed to differences in their hierarchical self-assembly.[9] For example, skin is an elastic material whereas cartilage is firm yet exhibits more flexibility than bone.

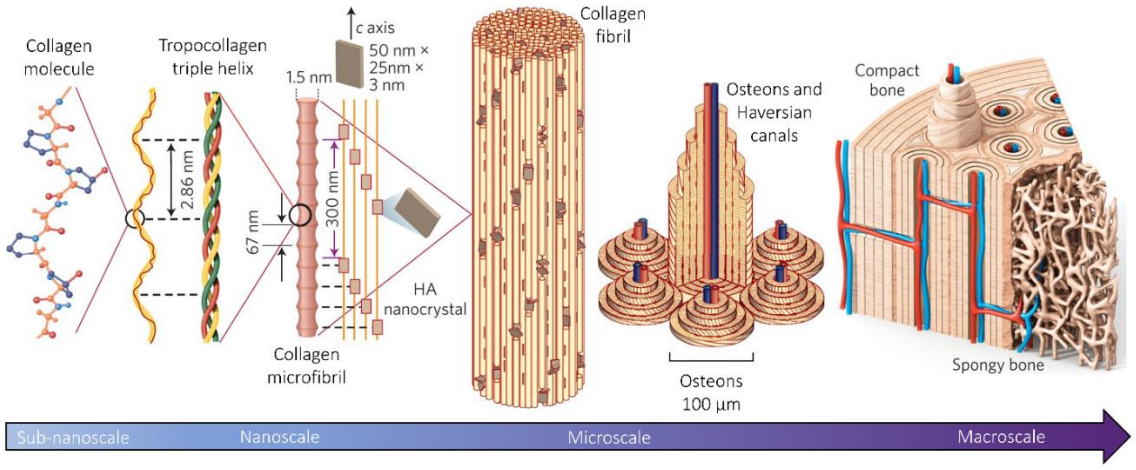

Figure 1.1 Hierarchical structure of bone. Adapted and reproduced with permission from reference 8.

Remarkably, biological materials and systems are mainly assembled from the same limited selection of building blocks – three monosaccharides, five nucleotides, 20 amino acids, and various inorganic components.[10] These, in turn, form di- and polysaccharides (such as cellulose and glycogen), nucleic acids (including DNA and RNA), and over 1000 different proteins.[2,8] The self-assembly of these systems occurs at ambient temperature and the formation of each level of structural hierarchy is driven by various non-covalent interactions.[8] Although weak in comparison to thermal energies, non-covalent interactions form stable hierarchical assemblies when sufficient in number.[3] These non-covalent interactions include van der Waals, Coulombic, hydrophobic, and electrostatic interactions, as well as hydrogen and coordination bonds.[3,5] The relative strengths of non-covalent interactions generally involved in self-assembly are summarised in **Table 1.1**.[11] It should be noted that, although covalent bonds can exhibit comparable bond strengths to those of

metal–ligand interactions, the former are usually irreversibly formed whereas the latter are generally more dynamic and reversible.[5]

Table 1.1 Strength of the main interactions involved in self-assembly.[11]

Interaction	Strength (kJ/mol)
Van der Waals	< 5
π–π interaction	0–50
Hydrogen bond	4–120
Metal–Ligand	0–400

In chemistry, achieving the same exceptional level of structural control to access complex functional materials akin to those in nature is a key challenge. Although chemical synthesis allows for molecules to be made; organized matter cannot be synthesized bond-by-bond.[3] Self-assembly offers a valuable alternative bottom-up route to form hierarchical assemblies through non-covalent interactions.[3] In molecular and macromolecular sciences, self-assembly provides access to ordered materials such as crystalline and supramolecular systems, respectively.[12] On the nanoscale, fields such as photonics, electronics, optics, and theranostics are reliant on self-assembly processes to achieve advances in structural organization and function of materials.[3–5] Increasing our understanding of self-assembly, and how it is employed in nature to control a limited number of sub-units to access a diverse range of functional materials, is therefore of paramount importance.

1.2 Self-Assembly of Small Molecules

The self-assembly of small molecular amphiphiles, such as surfactants or lipids, is largely well-understood. Generally, amphiphilic molecules consist of at least two moieties with chemically differing characteristics. For example, polar and non-polar groups or hydrophilic and hydrophobic components. Molecules which exhibit amphiphilicity readily self-assemble into structures of

varying complexity. The strong tendency of the hydrophobic moiety to avoid contact with water typically drives the aggregation of surfactants to form micelles, in a process termed "micellization". The aqueous solution self-assembly of small molecules is entropy-driven since micellization minimizes the disruption of hydrogen bonding between water molecules caused by hydrophobic chains. Micellization also minimizes enthalpically unfavourable hydrophobe–water interactions while exposing the hydrophilic head groups to water, leading to a further reduction in the total free energy of the system. Conversely, in organic solvents, micellization is enthalpically-driven. This results from the non-polar hydrophobic tail groups preferentially interacting with each other to minimize undesirable hydrophobe–solvent interactions, as well as the polar head group being well-solvated.[11,13–15]

Micelle formation occurs above a certain equilibrium concentration termed the critical micelle concentration (CMC). Above their CMC, molecular amphiphiles assemble into a variety of structures including spherical micelles, bilayer vesicles, and lamellar phases (**Figure 1.2**). The morphology obtained depends on the curvature of the hydrophilic–hydrophobic interface, which in turn is affected by the relative volume fractions of the hydrophilic and hydrophobic components. In general, the packing preferences of small molecules can be described by the packing parameter, *P*, (**Equation 1.1**) in terms of the volume of the hydrophobic chain, *v*; the contact area of the hydrophilic headgroup at the aggregate interface, a_0; and the length of the hydrophobic tail normal to the interface, l_c. The packing parameter, *P*, predicts the equilibrium morphology (**Figure 1.2**b, c) which is typically accessible with small molecular amphiphiles due to their kinetic lability. The packing parameter is defined as:

$$P = \frac{v}{a_0 l_c} \qquad \textbf{Equation 1.1}$$

As the value of the packing parameter increases ($P \leq 1$), the hydrophilic–hydrophobic interfacial curvature decreases, resulting in a change of micelle morphology from spherical, to cylindrical,

and finally to lamellar structures. When the packing parameter is increased further ($P > 1$), reverse micelles form whereby the curvature of the micelle is negative.[11,13]

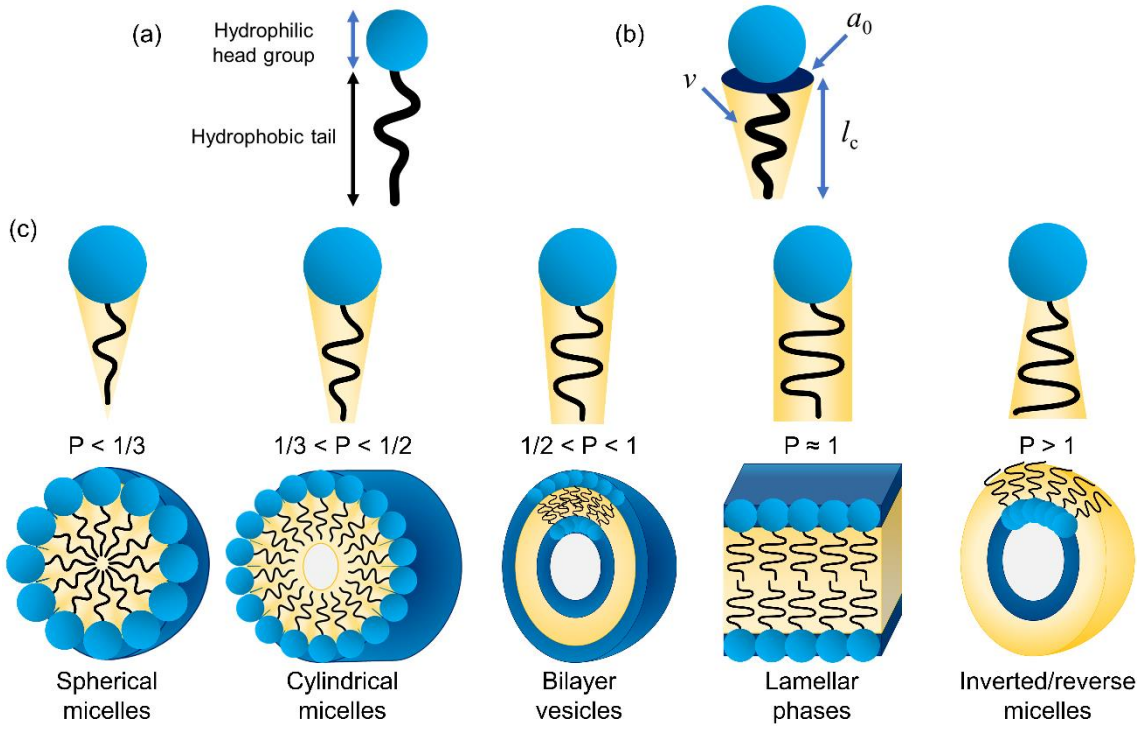

Figure 1.2 Cartoon representation of (a) the structure of a surfactant molecule; (b) the factors which affect the packing parameter, *P*, where v = the volume of the hydrophobic chain, a_0 = the contact area of the hydrophilic headgroup at the aggregate interface, and l_c = the length of the hydrophobic tail normal to the interface; (c) the micelle morphologies of small molecular amphiphiles demonstrated with respect to the packing parameter, *P*.

1.3 Self-Assembly of Block Copolymers

Block copolymers (BCPs) are synthetic amphiphilic macromolecules composed of two or more chemically different polymer segments which are connected by a covalent (or sometimes non-covalent) bond. BCPs of controlled molecular weight and narrow molecular weight distribution can be prepared by a variety of methods including living anionic polymerization;[16] controlled radical polymerization;[17] as well as orthogonal post-polymerization functionalization reactions, such as those exploiting Click chemistry.[18] The ability to access well-defined BCPs makes them

attractive for self-assembly.[15] A variety of interesting and useful nanoscale structures can be obtained through microphase separation in the solid state or through selective block solvation in solution.[15]

1.3.1 Bulk Self-Assembly of Block Copolymers

The self-assembly of BCPs in bulk is driven by an unfavourable mixing enthalpy, resulting from block incompatibility, coupled with a very small mixing entropy. This leads to microphase separation on the nanoscale since the covalent link between the segments prevents macrophase separation. Spontaneous aggregation of the chemically distinct blocks towards an equilibrium condition yields nanostructures based on non-covalent interactions between the segments. This leads to the formation of morphologies such as lamellae (L), hexagonally packed cylinders (H), body-centred spheres (Q^{299}), and double-gyroid phase (Q^{230}), as shown in **Figure 1.3**.

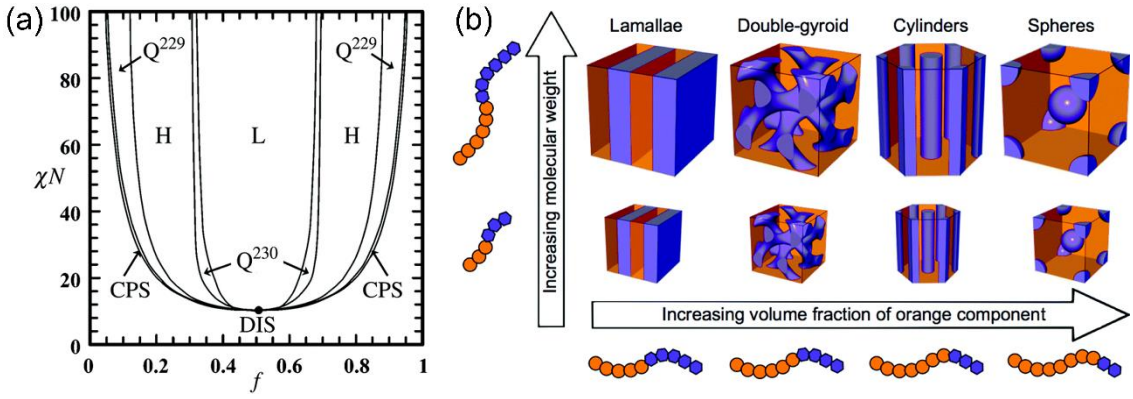

Figure 1.3 (a) Theoretical phase diagram for a linear BCP showing the degree of segregation (χN) against the volume fraction of a block (f). Morphologies: lamellae (L), hexagonally packed cylinders (H), body-centred spheres (Q^{229}), double-gyroid phase (Q^{230}), close-packed spheres (CPS), or disordered (DIS). (b) Schematic depicting the morphologies accessed through BCP self-assembly in bulk depending on BCP structure. Adapted and reproduced with permission from reference 19.

The three key parameters that contribute to the bulk self-assembly of a BCP with A and B blocks are: the volume fractions of the blocks (f, where $f_A + f_B = 1$); the total degree of polymerization ($N = N_A + N_B$); and the Flory-Huggins parameter, χ_{AB}. The degree of incompatibility between the blocks, which drives self-assembly, is described by χ_{AB} and varies inversely with temperature. The degree of microphase separation is determined by the segregation product, χN. With increasing temperature or a decreasing χN, entropy increases while block incompatibility decreases, leading to an order-to-disorder transition (**Figure 1.3**a).[15,19,20]

1.3.2 Solution Self-Assembly of Block Copolymers with an Amorphous Core-Forming Block

On addition of a block-selective solvent, BCPs self-assemble in solution to form core-corona nanoparticles (referred to as micelles). The solution self-assembly of amphiphilic BCPs has been recognised as a valuable bottom-up approach to yield a vast range of micelle morphologies such as spheres, worms, lamellae, and vesicles (or polymersomes).[15] However, the solution self-assembly of BCPs is much more complex than that in bulk, or that of small molecule self-assembly.

In the case of BCPs with an amorphous core-forming block, the micelle morphology is dictated by three contributions to the free energy: the degree of stretching of the core-forming blocks, the core–solvent interfacial tension, and the repulsive interactions between coronal chains. The packing parameter (**Equation 1.1**), which is useful for predicting the self-assembly of small molecules, can also be used to identify the likely thermodynamically preferred micelle morphology (**Figure 1.4**). However, although the packing parameter (**Equation 1.1**) is a useful tool to predict small molecule self-assembly, it provides a purely thermodynamic prediction of morphology which limits its use for BCP self-assembly. Moreover, BCPs are not well-represented by the packing parameter model since the a_0 term does not adequately describe the solvent-swollen corona (**Figure 1.4**b).[15] In practise, the BCP morphology is affected by a myriad of factors including BCP concentration, the solvent system employed, the volume fraction of the solvent-swollen corona, the processing

methods, and the presence of additives such as ions or homopolymer.[15,21,22] The final BCP morphology is therefore often difficult to predict, owing to the complex balance of interactions between the polymer blocks and the solvent.

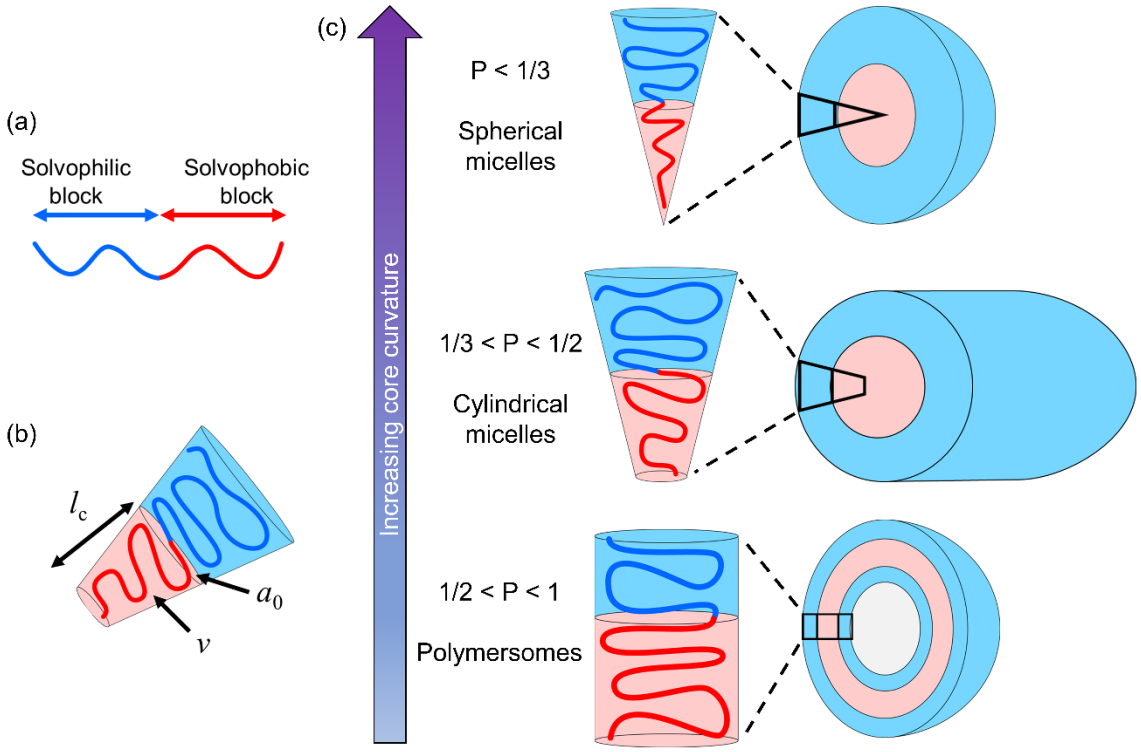

Figure 1.4 Cartoon representation of (a) the structure of an amphiphilic BCP with an amorphous core-forming block; (b) the factors which affect the packing parameter, *P*, where v = the volume of the solvophobic chain, a_0 = the contact area of the solvophilic–solvophobic interface, and l_c = the length of the solvophobic tail normal to the interface; (c) the micelle morphologies of amphiphilic BCPs with an amorphous core-forming block demonstrated with respect to the packing parameter, *P*.

BCP micelles generally possess additional thermodynamic stability in comparison with small molecule aggregates; a consequence of the core-forming block possessing hundreds of solvophobic repeat units in each chain. The CMC, which characterizes the equilibrium between unimer and micelles, is therefore significantly lower for BCPs than for molecular surfactants.[21] Another key

difference between small molecule and BCP self-assembly is that the energy penalty to remove a polymer chain from the core of a micelle into its unimeric state in solution is significantly higher than that of a small molecule, leading to additional kinetic stability of BCP micelles. This is another consequence of the polymeric nature of the core-forming segment. This often leads to the formation of kinetically-trapped nanostructures, resulting in a myriad of possible morphologies. Small molecule assemblies, on the other hand, are highly dynamic, exhibit rapid exchange, and therefore typically lead to the formation of equilibrium structures which correspond to a limited number of potential morphologies.[15,21,23,24]

Non-spherical nanostructures, such as one- or two-dimensional (1D or 2D) cylinders or platelets, are often challenging to access via the self-assembly of BCPs with an amorphous core-forming block, since these morphologies with low interfacial curvature typically exist in restricted regions of the phase space. Although there are many examples where anisotropic nanoparticles have been successfully accessed, the samples are often morphologically impure. Furthermore, there is no control over the size of the resulting 1D or 2D micelles, and they are polydisperse.[15]

1.4 Crystallization-Driven Self-Assembly

Studies of the formation, growth, and structure of polymer single crystals in solution first began in the 1960s.[25–27] Seminal work on BCPs with a crystallizable core-forming block was performed in 1966 by Keller *et al*., who demonstrated that poly(ethylene oxide)-*block*-polystyrene (PEO-*b*-PS) BCPs form square platelets with a crystalline PEO core consisting of the same unit cell as that of PEO homopolymer. It was determined that the platelet crystalline core was surrounded by an amorphous layer of chain-folded PEO, as well as pendant amorphous PS coronal chains. Additionally, it was demonstrated that a colloidally stable form of polymer crystal in solution, such as a BCP in which one block has crystallized and the other remains solubilized, could act as a seed for further growth of the polymer crystal.[26] This early work forms the basis of a process termed

crystallization-driven self-assembly (CDSA), developed from 2000 onwards,[28] which is now well-developed and generally well-understood.

1.4.1 Influence of Core Crystallization on Self-Assembly

When BCPs containing a crystallizable core-forming block are self-assembled in a non-solvent for the core-forming segment, crystallization is induced, typically leading to the formation of micelles with a crystalline core via CDSA.[29] The additional enthalpic contribution of crystallization to the free energy of micellization significantly changes the self-assembly behaviour compared with that of BCPs with an amorphous core-forming block. Core crystallization generally results in the formation of non-spherical nanostructures with zero or low curvature of the core–corona interface being favoured. The equilibrium micelle structure obtained decreases the core–non-solvent interfacial energy, reduce the number of chain folds of the crystalline core-forming segment, and minimize the entropy penalty of coronal chain stretching.[30–32] Moreover, the packing parameter (**Equation 1.1**) is inadequate for predicting the morphology of micelles with a crystalline core since it does not account for a solvent-swollen corona. Instead, factors which thermodynamically impact core crystallization play an important role with respect to the morphology obtained. These include the corona-to-core block ratio,[32,33] BCP molar mass,[34] temperature at which CDSA is performed,[35,36] CDSA cooling rate,[37] amount of common solvent present,[34] and solution concentration.[38] In most cases, the corona-to-core block ratio can be used to predict the morphology formed via CDSA. However, conditions which aid plasticization of the crystalline core, such as increased temperature or a larger fraction of common solvent present, decrease the overall rate of core elongation since unimer solubility is favoured.[39] In theory, these conditions which increase unimer solubility lead to a more thermodynamically favoured morphology being formed, since this results in the core-forming block being allowed to crystallize to a greater extent.[33]

1.4.2 Crystallization-Driven Self-Assembly of PFS-Containing Block Copolymers

The first examples of polyferrocenylsilanes (PFSs), a sub-group of metallopolymer with skeletal iron and silicon atoms, were synthesized, studied, and characterized in the early 1990s.[40–42] The living anionic ring-opening polymerization (ROP) of silicon-bridged [1]ferrocenophanes was reported shortly thereafter, allowing access to PFSs with molecular weight and end-group control. Sequential living anionic polymerization was also demonstrated to allow access to novel PFS-containing BCPs with targeted degree of polymerizations (DP_n) and narrow molecular weight dispersities.[43,44] This allowed for the self-assembly of PFS-containing BCPs to be investigated, as well as examining the effect of changing the BCP chemical composition and respective block lengths.[32]

The solution self-assembly of PFS-containing BCPs was first investigated in the mid-to-late 1990s. It was demonstrated that symmetrically substituted PFS-based materials such as poly(ferrocenyldimethylsilane) (PFDMS; R = R' = Me) are generally able to crystallize, whereas those that are unsymmetrically substituted such as poly(ferrocenylethylmethylsilane) (PFEMS; R = Et, R' = Me) tend to be amorphous.[45] Interestingly, when incorporating a crystallizable PFS segment as the core-forming block in a BCP, self-assembly in non-solvents for PFS was found to access non-spherical morphologies with low interfacial curvature via CDSA.[28,32,45,46] Conversely, amorphous PFS analogues were found to form spherical micelles.[28,47,48] Performing the self-assembly of a crystallizable PFDMS-containing BCP above its melting temperature (T_m), followed by rapid cooling, also yielded spherical micelles due to the absence of core crystallization.[28] These results demonstrated that crystallization of the PFS core-forming block drives the formation of structures with low curvature of the core–corona interface. In this thesis, PFDMS will be the sole focus of this sub-group of metallopolymer, since it is the most extensively studied of the

crystallizable PFSs. PFDMS will therefore be referred to as "PFS" for conciseness and convenience herein.

Micelles with a PFS core-forming block have been extensively studied in the literature and can exist in various morphologies including cylinders,[28,32,46] platelets,[32] toroids,[49] and branched fibers.[37] Although, as noted in the previous section, the factors affecting morphology are complex, the corona-to-core block ratio can generally be used to predict the final micelle morphology. For example, PI_{320}-*b*-PFS_{53} (PI = polyisoprene) has a corona-to-core block ratio of 6:1 and assembles into cylinders in hexanes, a selective solvent for PI (**Figure 1.5**b). The cylindrical morphology arises due to competition between the free energy penalty of PI coronal chain repulsions (which results in an entropic penalty of coronal chain stretching) balanced with the PFS crystalline core lattice energy.[30] CDSA of a similar BCP, PI_{70}-*b*-PFS_{70}, with a block ratio of 1:1, however, assembles into tape-like platelets (**Figure 1.5**c). At this lower block ratio, the energy penalty associated with steric repulsions of the PI corona is not as large, and therefore yields nanostructures with lower curvature of the core–corona interface.[32]

PFS-based nanostructures can be easily visualized by transmission electron microscopy (TEM) since the PFS core is sufficiently electron dense to provide good contrast with the carbon film background. The crystalline core of PFS-based micelles has been thoroughly probed using a variety of techniques including wide-angle X-ray scattering (WAXS),[28,48,50,51] small-angle X-ray scattering (SAXS),[50,51] differential scanning calorimetry (DSC),[50] TEM,[52] atomic force microscopy (AFM),[53] and selected area electron diffraction (SAED).[54] The PFS chains pack perpendicular to the long axis of the micelle and exhibit a lattice with 2D pseudo-hexagonal symmetry.[51]

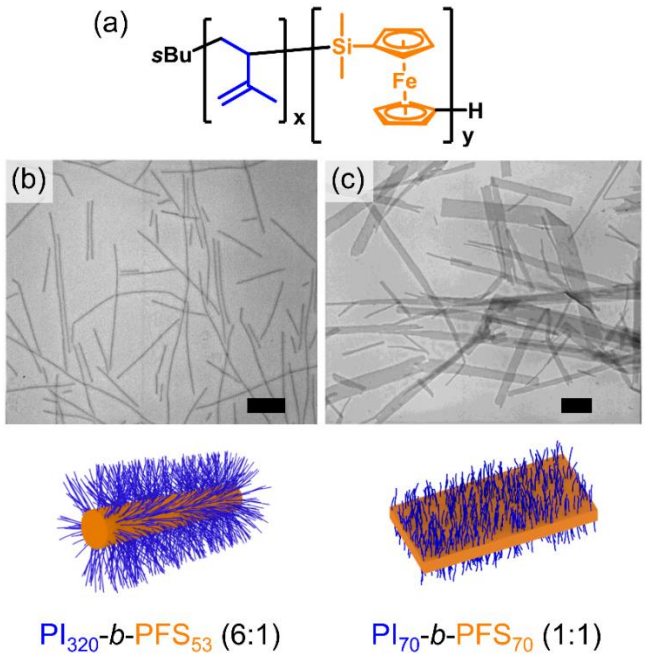

Figure 1.5 (a) General structure of PI-*b*-PFS with block DP_n values of x and y, respectively. TEM images (top) and cartoon representations (bottom) of (a) cylindrical and (b) platelet micelles prepared by CDSA of PI-*b*-PFS. BCP structure and block ratio are also noted below. Adapted and reproduced with permission from reference 32. Scale bars: (b) 250 nm, (c) 500 nm.

1.4.3 Crystallization-Driven Self-Assembly of non-PFS-Containing Block Copolymers

A diverse range of BCPs containing other crystallizable core-forming blocks have been shown to undergo CDSA. These include polyethylene (PE),[55–58] poly(ferrocenyldimethylgermane) (PFG),[59] poly(3-hexylthiophene) (P3HT),[60,61] poly(*p*-phenylenevinylene),[62] poly(di-*n*-hexylfluorene) (PDHF),[63,64] poly(ε-caprolactone) (PCL),[65–69] poly(*L*-lactide) (PLLA),[70,71] PCL/PLLA copolymers,[72] polycarbonates,[73] polyacrylonitrile,[74] poly(isopropyloxazoline),[75,76] polypeptoids,[77–81] as well as BCPs containing a liquid crystalline core-forming block, such as poly(perfluoroalkyl methacrylate),[82–84] and those based on azobenzene,[85] stilbene,[86,87] or cholesterol.[88]

Although morphologically pure 1D fibers or 2D platelets can ultimately be accessed through CDSA, each particular BCP system can behave differently. For example, the CDSA of PLLA-containing BCPs is reported by the groups of Dove and O'Reilly to yield 1D cylinders or 2D platelets depending on the corona-to-core block ratio. However, the CDSA of PLLA-based BCPs with a high block ratio accesses 2D platelets (**Scheme 1.1**a) and those with low block ratios form 1D cylinders (**Scheme 1.1**c). Interestingly, this dependency of the morphology on the block ratio is the inverse relationship to that exhibited by PFS-based BCPs. Dove, O'Reilly, *et al*. indicate this to be an effect of the corona-forming segment solubility, whereby the increased solubility of a relatively longer PLLA block allows for the core to crystallize to a greater extent to form defect-free plates. Furthermore, when employing a blend of cylinder- and platelet-forming BCP, complex nanostructures can be obtained whereby assembly to produce platelets occurs initially, which in turn act as seeds for the epitaxial growth of cylinder-forming BCP (**Scheme 1.1**b).[33]

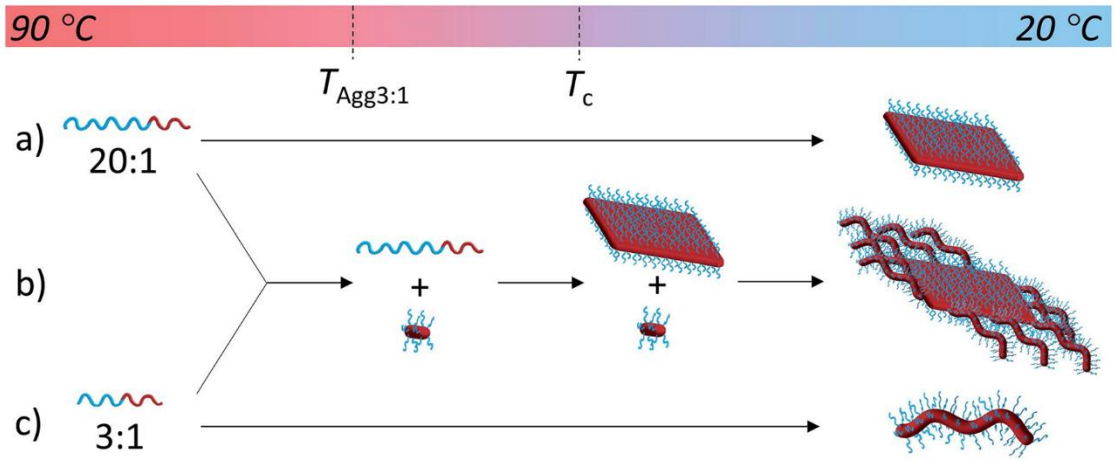

Scheme 1.1 CDSA of PLLA-containing BCPs with block ratios (a) 20:1 (platelet-forming), (b) a mixture of 20:1 and 3:1, and (c) 3:1 (cylinder-forming). An arbitrary scale represents the CDSA process cooling from 90 °C to 20 °C where $T_{Agg3:1}$ = temperature at which aggregation of the cylinder-forming BCP occurs and T_c = PLLA crystallization temperature. Reproduced with permission from reference 33.

1.5 Living Crystallization-Driven Self-Assembly

Thus far, we have discussed CDSA in which nucleation of the crystalline core-forming block occurs randomly and spontaneously. Although CDSA crucially allows for morphological control to target non-spherical structures, the micelles obtained are typically polydisperse in size and lack size-control. This is a result of the rate of self-nucleation being significantly slower than that of elongation of the crystalline core via epitaxial growth. However, dimensional control of BCP-based nanostructures can be achieved by circumventing random self-nucleation events through a process termed "living" CDSA, which consists of adding molecularly dissolved BCP, termed unimer, to pre-existing seed micelles. Living CDSA therefore allows for the formation of nanostructures of controlled size with low size-dispersity (**Figure 1.6**). With respect to 1D micelles, size-dispersity is described by L_w/L_n, where L_w and L_n correspond to the weight- and number-average micelle lengths, respectively. Living CDSA allows access to micelles with low length-dispersities of typically $L_w/L_n \leq 1.10$, where a L_w/L_n value of 1.00 represents a perfectly monodisperse sample.

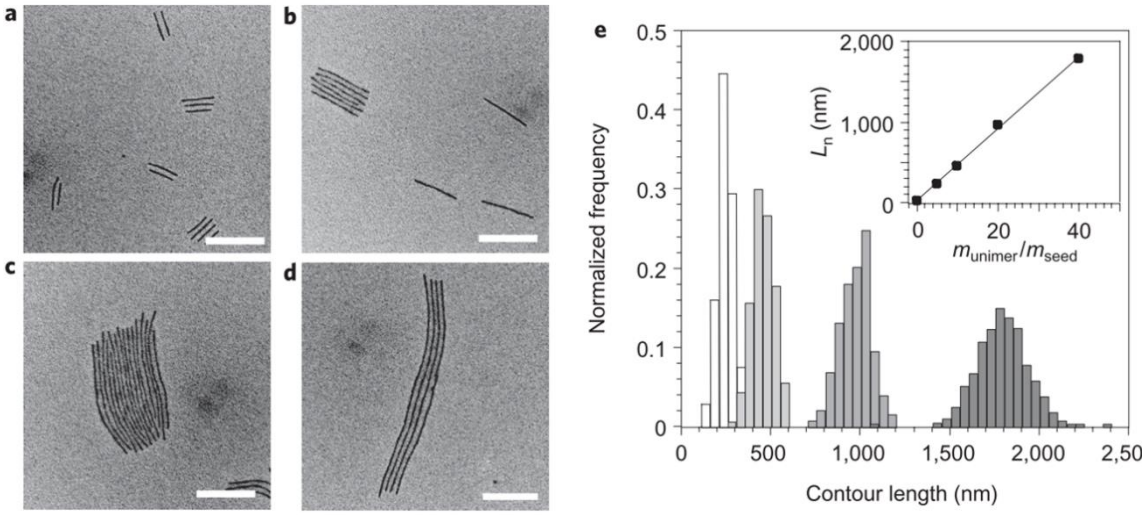

Figure 1.6 TEM images of monodisperse 1D micelles prepared by living CDSA at various m_{unimer}/m_{seed} values of (a) 5, (b) 10, (c) 20, and (d) 40. (e) Histograms of the micelle length

distributions of samples (a)–(d). Inset of (e) shows the linear dependence of micelle length on m_{unimer}/m_{seed}. Reproduced with permission from reference 89. Scale bars: 500 nm.

Polydisperse micelles prepared by CDSA can be fragmented by sonication to access the low aspect ratio seed micelles used in living CDSA. Crucially, the exposed crystalline core termini of the seeds remain active to epitaxial growth. Therefore, the seeds act as nucleation sites and elongate on addition of unimer. Since the rate of elongation is significantly faster than that of self-nucleation, additional nucleation events are negligible, and near-monodisperse micelles can be obtained (**Scheme 1.2**). Under these conditions, the final micelle length can be predicted since it is linearly dependent on the mass ratio of unimer with respect to the seeds (unimer-to-seed ratio, m_{unimer}/m_{seed}) (**Figure 1.6**). Here lies the analogy with living covalent polymerizations, in which the polymer DP_n is linearly dependent on the monomer-to-initiator ratio.

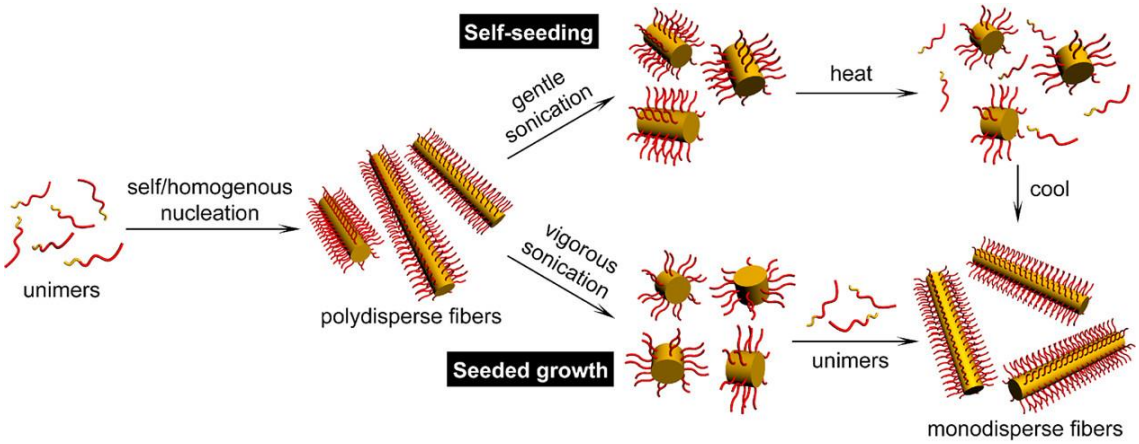

Scheme 1.2 Schematic representation of self-seeding (top) and seeded growth (bottom) as the two routes to preparing 1D micelles of controlled size by living CDSA. Reproduced with permission from reference 90.

Self-seeding (**Scheme 1.2**, top) represents an alternative route to prepare micelles of controlled dimensions and was first developed in the mid 1960s.[91,92] In this case, unimer is not externally added to the system, but instead is freed from the micelles themselves via partial dissolution. Lower

crystallinity regions of the core effectively exhibit lower melting temperatures, leading to dissolution during thermal annealing. On subsequent cooling, the higher crystallinity regions which avoided dissolution then act as seeds for the epitaxial growth of the released unimer (**Scheme 1.2**).[90] The resulting unimer-to-seed ratio generally depends on the self-seeding temperature. However, since the thermal history of the sample can affect the degree of crystallinity and therefore the melting temperature, the fiber lengths of the resulting micelles are less predictable than those formed via living CDSA. Living CDSA (**Scheme 1.2**, bottom) therefore represents a more reproducible and scalable route to low dispersity nanostructures, since seed generation is performed independently, heating at elevated temperatures is not required, and the micelle dimensions are not impacted by concentration or thermal history.[93,94]

1.5.1 Living Crystallization-Driven Self-Assembly of PFS-Containing Block Copolymers

Extensive studies of living CDSA by the groups of Manners and Winnik have focused on accessing 1D cylindrical micelles from BCPs containing a PFS core-forming segment. For example, on probing the living CDSA of PI_{320}-*b*-PFS_{53} it was determined that addition of unimer to pre-existing seeds resulted in growth whilst preserving the internal PFS core structure.[95] The controlled-length structures were found to exhibit long-term stability under dilute conditions, with no evidence for unimer dissociation, new micelle formation, or micelle fusion events. Interestingly, addition of a BCP with a different corona-forming block, PFS_{48}-*b*-$PMVS_{300}$ (PMVS = poly(methylvinylsiloxane)), to the PI_{320}-*b*-PFS_{53} seed micelles resulted in the formation of block comicelles with segmented PI/PMVS coronal chemistries.[95] More recent studies have demonstrated the precise control possible by using living CDSA of fluorescent dye-functionalized $PDMS_{660}$-*b*-PFS_{60} (PDMS = poly(dimethylsiloxane)) to access colour-tunable "barcode" multiblock comicelles (**Figure 1.7**a).[96,97] Other fascinating and precisely controlled structures can be formed by the hierarchical assembly of 1D PFS-based nanostructures which are specifically designed to exhibit

amphiphilicity. For example, incorporating hydrophobic (PFS_{49}-*b*-$PDMS_{504}$) and polar (PFS_{48}-*b*-$P2VP_{414}$, P2VP = poly(2-vinylpyridine)) segments into triblock comicelles results in assembly on multiple levels of structural hierarchy.[98] Supermicelles and hierarchical structures can also be achieved through spatially-confined hydrogen bonding, by controlling the location of hydrogen bond donor and acceptor segments along a 1D micelle.[99,100]

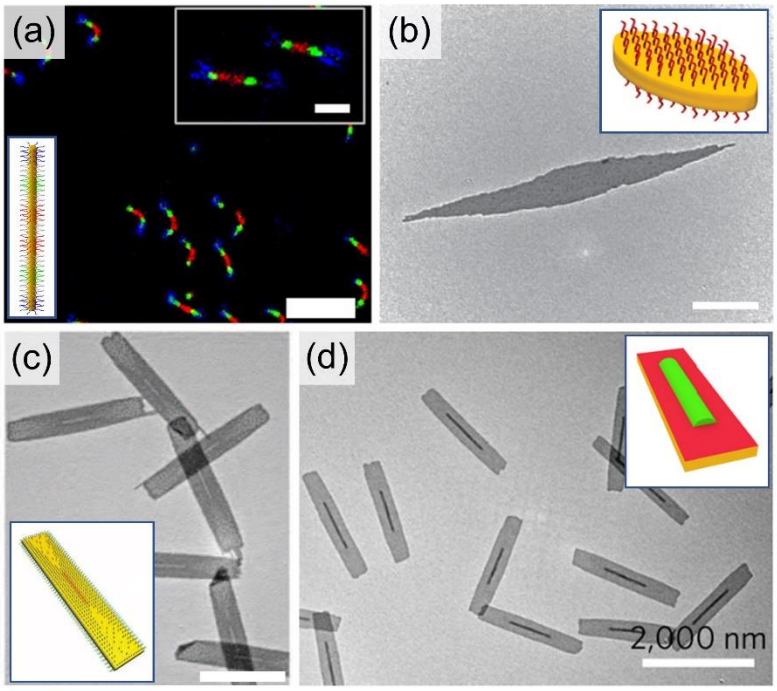

Figure 1.7 1D and 2D PFS-based micelles prepared by living CDSA. (a) Laser scanning confocal microscopy image and cartoon representation of fluorescent 1D multiblock comicelles prepared by seeded growth of different dye-functionalized $PDMS_{660}$-*b*-PFS_{60} unimers from $PDMS_{660}$-*b*-PFS_{60} seeds. Adapted from reference 97. (b) TEM image and cartoon representation of 2D lenticular platelet micelles prepared by seeded growth of PFS_{113}-*b*-$PDMS_{560}$ unimer from 1D PFS_{28}-*b*-$PDMS_{560}$ seed micelles. Adapted from reference 101. (c) TEM image and cartoon representation of 2D rectangular, patchy platelet micelles prepared by seeded growth of a PFS_{36}-*b*-$P2VP_{502}$/PFS_{20} unimer blend from 1D PFS_{28}-*b*-$PDMS_{560}$ seed micelles. Adapted from reference 102. (d) TEM image and cartoon representation of a 2D rectangular platelet micelles

prepared by seeded growth of $PFS_{20}[PPh_2Me]I$ unimer from 1D PFS_{25}-*b*-$P2VP_{250}$ seed micelles. Adapted from reference 54. Scale bars: (a) 5 μm (inset: 1 μm), (b) 500 nm, (c, d) 2 μm.

Living CDSA can also be used to access 2D platelet micelles of various shapes. The first examples of living CDSA in 2D yielded uniform lenticular platelets by adding PFS-containing BCPs with low corona-to-core block ratios (< 5:1) to 1D cylindrical seed micelles (**Figure 1.7**b).[101,103] This morphology was attributed to "poisoning" effects by the corona of the unimer[53] as well as a difference in the crystal facet growth rates of the PFS core.[103] Alternatively, adding a blend of PFS_{20} homopolymer and cylinder-forming PFS_{36}-*b*-$P2VP_{502}$ BCP to 1D seeds was found to prepare 2D rectangular platelet micelles with a patchy structure (**Figure 1.7**c).[102,104] This is thought to be a consequence of the relative solubilities of the blend components, as well as the presence of coronal steric bulk on the seed affecting relative rates and locations of their crystallization.[102,104] Similarly, uniform 2D rectangular platelets can be formed by the living CDSA of charge-terminated PFS homopolymer seeded from 1D cylindrical seeds (**Figure 1.7**d).[54,105] In this case, there are no coronal chains but instead a charged solubilizing phosphonium or ammonium end-group.[54,105] The aforementioned examples all employ 1D seeds to access 2D nanostructures. However, 2D seed micelles can be prepared from PFS homopolymers with charged termini, $PFS_{20}[PPh_2Me]I$, and can be used to access either 2D quasi-hexagonal or rectangular structures, depending on seed micelle preparation.[54] In all the cases discussed here, the platelet area, A_n, is linearly dependent on the unimer-to-seed ratio (m_{unimer}/m_{seed}). The formation of segmented 2D rectangular platelets which exhibit differing coronal and/or core chemistries have also been demonstrated using PFS-based polymers.[54,102,104]

1.5.2 Living Crystallization-Driven Self-Assembly of non-PFS-Containing Block Copolymers

Although a large portion of the literature focuses on PFS-containing BCPs, living CDSA has now been well-established for a diverse range of crystallizable core-forming blocks.[106] Schmalz *et al.*

have demonstrated the living CDSA of PE-containing BCPs to access micelles of up to 500 nm in length which exhibit very low length-dispersity (L_w/L_n = 1.10). Triblock comicelles with a patchy segmented PS/PMMA (PMMA = poly(methyl methacrylate)) corona could also be accessed if a PS-*b*-PE-*b*-PMMA triBCP is employed as the unimer.[107]

The groups of Dove and O'Reilly have demonstrated the living CDSA of PCL-based BCPs, which have potential biomedical applications due to their biocompatibility. First, the living CDSA of PCL_{50}-*b*-$PMMA_{20}$-*b*-$PDMA_{200}$ (PDMA = poly(*N*,*N*-dimethylacrylamide)) was used to access fiber-like micelles of lengths up to 800 nm (L_w/L_n = 1.09). Interestingly, addition of PCL_{50}-*b*-$PDMAEMA_{170}$ (PDMAEMA = poly(2-(dimethylamino)ethyl methacrylate)) unimer to 1D PCL_{50}-*b*-$PDMA_{180}$ seed micelles resulted in the formation of 2D platelets,[68] a phenomenon that is attributed to increased unimer solubility.[33,68] Leveraging this knowledge, further reports demonstrated that length-controlled fiber-like $PDMA_{302}$-*b*-PCL_{60}-*b*-$PDMA_{302}$ micelles up to 1200 nm in length could be accessed through a self-seeding technique (Section 1.5).[108] The solubility of the BCP utilized was found to affect the size and morphology obtained. Dove, O'Reilly, *et al.* were able to tune the BCP solubility by altering the corona-to-core block ratio, solvent quality, and temperature at which living CDSA was performed.[108]

Uniform platelets based on a crystalline core of PLLA, another biocompatible polymer, were first reported by Dove, O'Reilly, *et al.*. Size control was achieved by altering the solubility of the $PLLA_{36}$-*b*-$PDMAEMA_{216}$ unimer through adjusting the solvent system. It was demonstrated that increasing the fraction of tetrahydrofuran (THF, common solvent) relative to ethanol (selective solvent) led to the formation of larger diamond platelets.[109] The living CDSA of PLLA-containing BCPs was reported in collaborative work by the groups of Dove, O'Reilly, and Manners, allowing for the preparation of 1000 nm fiber-like micelles with very low dispersity (L_w/L_n = 1.04). The presence of trifluoroethanol was found to be essential to disrupt hydrogen bond formation between unimer and therefore favour epitaxial crystallization over self-nucleation.[110] Living CDSA has

since been extended to and optimized using a biocompatible crystallizable polycarbonate segment, poly(fluorenetrimethylenecarbonate) (PFTMC). When using poly(ethylene glycol) (PEG) as the coronal segment, low dispersity PEG_{490}-*b*-$PFTMC_{20}$ fibers of lengths up to 1600 nm (L_w/L_n = 1.05) could be formed.[73]

Living CDSA techniques have also been explored using BCPs which contain a crystallizable π-conjugated core-forming block. Self-seeding has been used to access low dispersity fiber-like micelles containing a P3HT core with lengths up to 950 nm (L_w/L_n = 1.10).[111,112] Recently, these results were vastly improved on when a charge-terminated P3HT homopolymer was used rather than a BCP with a corona-forming segment. In this case, an unprecedented level of control was achieved up to 2.8 μm in length (L_w/L_n = 1.08).[113] The living CDSA of PDHF-containing BCPs has also been reported to access controlled fiber-like micelles of 1800 nm in length (L_w/L_n = 1.07) with a π-conjugated crystalline core.[114–116]

1.6 Polymerization-Induced Self-Assembly

Although living CDSA represents a promising route to preparing 1D and 2D nanoparticles of targeted size and shape, this process is generally performed under high dilution (0.002–0.01 weight percent (wt%)). Over the last decade, substantial progress has been made in the upscaling of BCP micelle formation. The methods discussed so far involve using a BCP which is synthesized and purified prior to self-assembly and typically result in small amounts of polymeric nanoparticles. An alternative route termed polymerization-induced self-assembly (PISA) combines the BCP synthesis and self-assembly by performing the steps *in situ*, allowing access to micelles at scalable concentrations (10–50 wt%).[70,117–120]

1.6.1 Polymerization-Induced Self-Assembly of Block Copolymers with an Amorphous Core-Forming Block

The first step of PISA involves preparing a solvophilic macroinitiator that will act as the corona in the resulting micelles. On addition of a second monomer that will form a solvophobic block, macroinitiation occurs and the second polymer block begins to form. As the length or DP_n of the solvophobic block increases, it becomes progressively more insoluble in the solvent system. On reaching a certain critical DP_n, self-assembly is induced to form BCP micelles (**Scheme 1.3**). The morphology obtained can generally be controlled by varying the final corona-to-core block ratio. The literature focuses on the use of controlled radical polymerization techniques such as reversible addition-fragmentation chain-transfer (RAFT) polymerization[70,117–119,121–124] and nitroxide-mediated polymerization (NMP),[120,125,126] but in theory PISA can be conducted using any living polymerization method.[127] Controlled radical polymerizations and other living polymerization techniques allow for the preparation of BCPs with controlled molecular weight and low dispersity.[127,128]

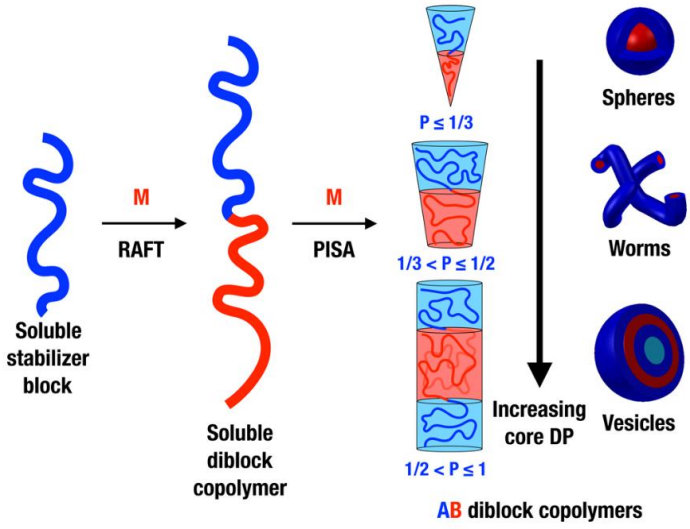

Scheme 1.3 Schematic representation of RAFT-mediated PISA to prepare BCP micelles at scalable concentrations. Reproduced with permission from reference 117.

Throughout the PISA process, the core block DP_n increases leading to changes in the corona-to-core block ratio and therefore the micelle morphology throughout (**Figures 1.8** and **1.9**).[124,129] Typically, spherical micelles are formed first, which in turn evolve into worm-like micelles, then into vesicles (**Scheme 1.3** and **Figures 1.8** and **1.9**).[124,130] Often, mixed micelle morphologies are observed. These morphologies and morphological transitions have been evidenced by various techniques such as TEM (**Figure 1.8**),[129,131–133] SAXS (**Figure 1.9**),[124] and fluorescence spectroscopy.[130] Since PISA typically involves preparing micelles with an amorphous core, the micelle size and morphology will depend on various factors including the composition, molecular weight, and concentration of the BCP,[129,131] as well as temperature[123,131,134,135] and pH.[121,136]

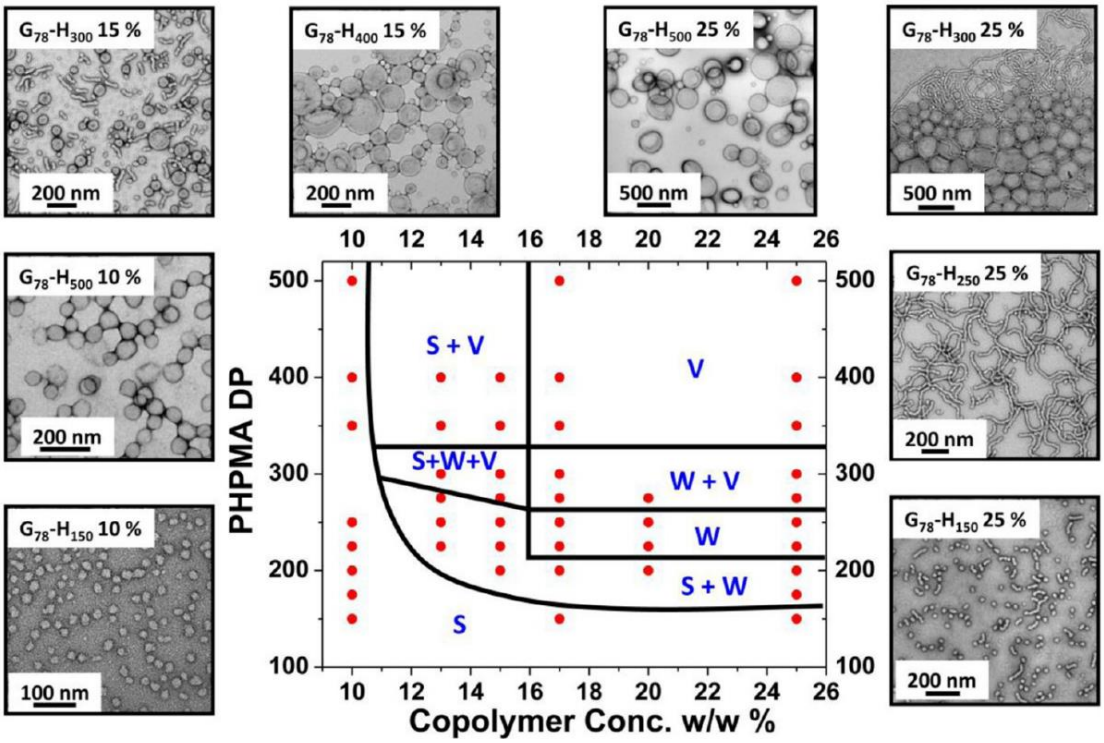

Figure 1.8 Representative TEM images and the corresponding morphology map of a series of poly(glycerol monomethacrylate)-*b*-poly(2-hydroxylpropyl methacrylate) (PGMA-*b*-PHPMA) BCPs prepared by RAFT-mediated PISA at concentrations of 10–25 wt%. S = spheres, W = worms (cylinders), V = vesicles. Reproduced with permission from reference 129.

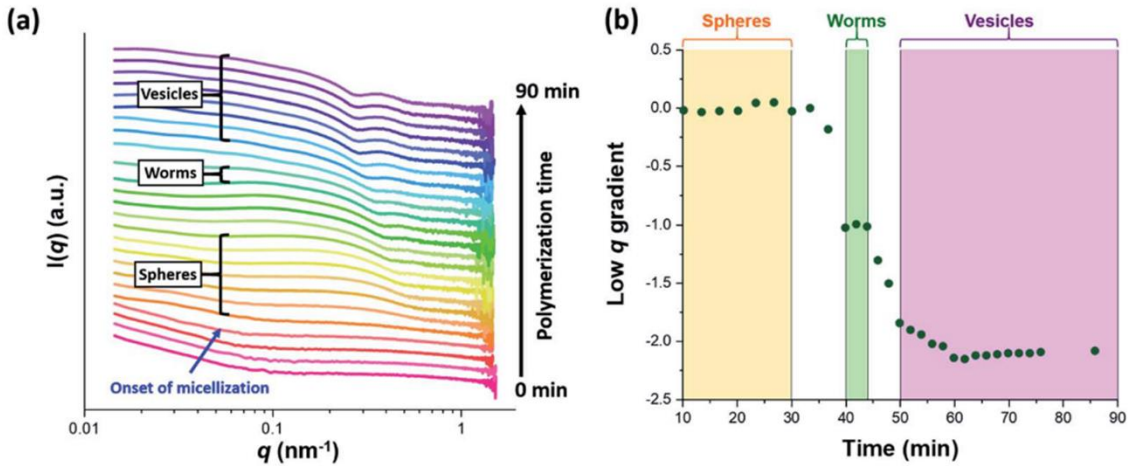

Figure 1.9 (a) SAXS patterns recorded *in situ* during the RAFT-mediated PISA preparation of $PGMA_{45}$-*b*-$PHMPA_{200}$ vesicles at 10 wt%. Labelled are the onset of micellar nucleation, as well as the main morphologies (spheres, worms, vesicles). (b) Change in low *q* gradient (where *q* = scattering vector) during PISA. The morphologies corresponding to each gradient are labelled. Reproduced with permission from reference 124.

Compatible with both aqueous and non-aqueous solvent media,[118,137] and with a wide range of functional monomers,[117] PISA is truly a versatile process. Since PISA is most often mediated by controlled radical polymerization methods,[120,127] the process can often be optimized to achieve 99% monomer conversion within 2 hours with the final BCP exhibiting low molecular weight dispersities (M_w/M_n < 1.20).[17,124,127,128] Although there are many advantages to PISA for the preparation of BCP-based micelles at scalable concentrations, there are some key unresolved challenges. Arguably the biggest drawback results from the micelles exhibiting an amorphous core, since PISA often yields mixed micelle morphologies (as demonstrated in **Figure 1.8**) and lacks the ability to target specific morphologies or nanoparticle sizes. Spherical micelles and vesicles often dominate the phase space (**Figure 1.8**), meaning that morphologically pure 1D or 2D nanoparticles are challenging to obtain by PISA.

1.6.2 Polymerization-Induced Crystallization-Driven Self-Assembly

Polymerization-induced crystallization-driven self-assembly (PI-CDSA) is a process which combines the excellent morphological control characteristic of CDSA with the scalability of PISA. PI-CDSA is a one-pot method which allows for the preparation of morphologically pure but polydisperse 1D cylindrical and 2D platelet micelles at scalable concentrations (10–25 wt%) (**Figure 1.10**). Similar to that in PISA, the polymerization and self-assembly occur *in situ*. The solvophilic corona-forming block is first prepared and acts as a macroinitiator for the polymerization of the second monomer, which polymerizes to form the solvophobic core-forming segment. On reaching the critical core DP_n, where the core-forming block becomes sufficiently solvophobic, self-assembly is induced. The key difference compared with PISA, however, is that the use of a crystallizable core-forming block allows for morphologically pure 1D or 2D nanostructures to be obtained.[138,139]

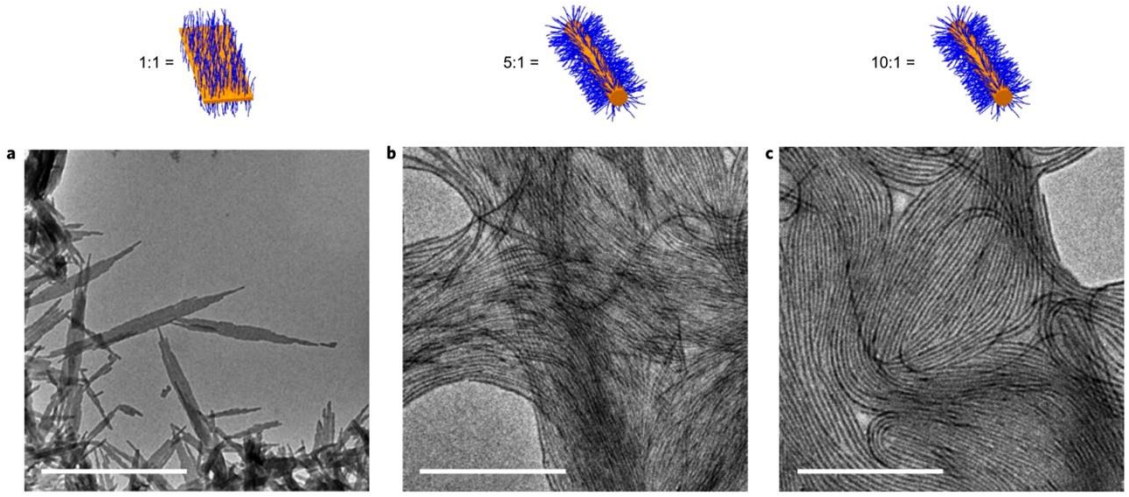

Figure 1.10 TEM images and cartoon representations of polydisperse PI-*b*-PFS micelles prepared by PI-CDSA at 10 wt% in 10 vol% THF/hexanes at corona-to-core block ratios of (a) 1:1, to access 2D lenticular platelet micelles, or (b) 5:1 and (c) 10:1, to access 1D cylindrical

micelles. Solutions were diluted to 1 mg/mL for TEM imaging. Scale bars: 1 μm. Reproduced with permission from reference 138.

Initial studies of PI-CDSA consisted of preparing PFS-based micelles by performing the living anionic polymerization in a selective solvent system of 10 vol% (volume fraction) THF/hexanes to induce self-assembly (**Scheme 1.4**c). PI-CDSA allows for PFS-based micelles to be prepared within 3 h, which is significantly faster than the typical polymerization, purification, and subsequent CDSA route (3 days) (**Scheme 1.4**a, b). Since the PI-CDSA process employs the living anionic polymerization technique, the resulting BCP typically exhibits low dispersities (M_w/M_n < 1.20).[138,139]

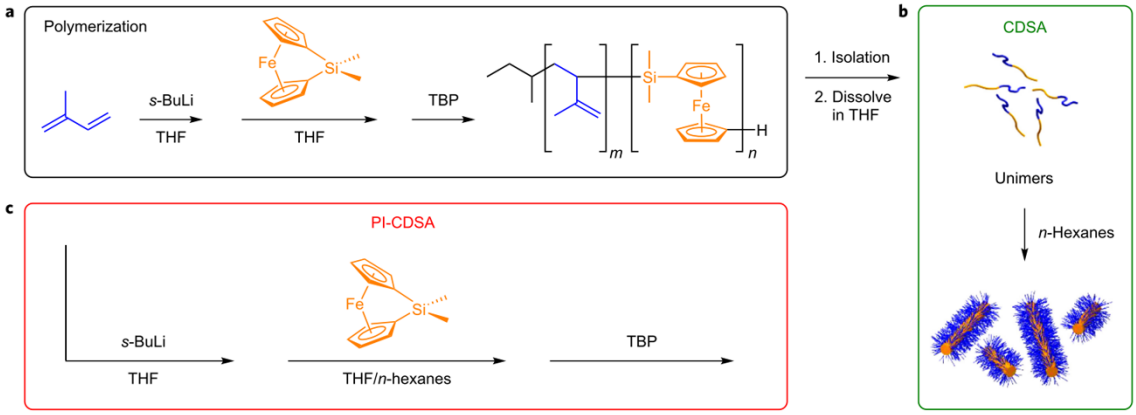

Scheme 1.4 Schematic representations of the preparation of polydisperse PI-*b*-PFS 1D cylindrical micelles. (a) Preparation of PI-*b*-PFS BCP by sequential living anionic polymerization followed by (b) multi-step post-polymerization solution processing of PI-*b*-PFS BCP using CDSA (typically 0.01 wt%). (c) One-pot preparation of PI-*b*-PFS cylindrical micelles using PI-CDSA at 25 wt%. TBP = 4-*tert*-butylphenol, used as the quenching agent. Reproduced with permission from reference 138.

There are now several other non-PFS-based examples of PI-CDSA in the literature. Anisotropic nanoparticles comprising of single-chain ultra high-molecular-weight PE can be prepared by PI-CDSA using an aqueous living catalytic polymerization technique. This method allows access to

uniform nanoparticles due to the controlled catalytic polymerization which minimizes chain transfer processes.[140] PI-CDSA via ring-opening metathesis polymerization (ROMP), termed ROMPI-CDSA, has also been recently reported for the preparation of poly(ruthenocene)-containing 2D lenticular platelets at 10 wt%.[141] The ring-opening polymerization-induced crystallization-driven self-assembly (ROPI-CDSA) of *L*-lactide has also been demonstrated using a PEG-based macroinitiator. In this case, 1D, 2D, and 3D (stacked lamellae) PLLA-based structures were achieved at concentrations of 5–20 wt%.[142] Interestingly, the groups of Chen and Yang have reported a similar technique termed polymerization-induced hierarchical self-assembly (PIHSA) which exploits the liquid crystal ordering of a stilbene-containing monomer through π–π stacking at 5–20 wt%.[86,87] Although the field of PI-CDSA has grown significantly in recent years to include various different polymerization techniques and functional monomers, the key challenge of obtaining scalable low dispersity nanoparticles of targeted size still remains.

1.6.3 Living Polymerization-Induced Crystallization-Driven Self-Assembly

To prepare BCP-based nanoparticles of controlled size and morphology, the seeded growth method living PI-CDSA can be used. Essentially, living PI-CDSA consists of performing PI-CDSA in the presence of pre-prepared seed micelles (**Figure 1.11**) at concentrations up to 10 wt%. This leads to synchronous polymerization, self-assembly, and seeded growth. The preparation of low dispersity micelles of lengths up to 2800 nm (L_w/L_n = 1.01) is achieved through the living PI-CDSA of PI_{154}-*b*-PFS_{29}.[138] This exceptional control over size and morphology has also been extended to prepare block comicelles with segmented core and coronal chemistries. In this case, cylindrical micelles comprising of a segmented PFS/PFG core and PI/PDMS corona, (PI-*b*-PFG)-*m*-(PFS-*b*-PDMS)-*m*-(PI-*b*-PFG) where *m* denotes a micelle block, can be prepared. This technique exploits heteroepitaxial growth of a PFG-containing BCP from PFS-based seeds.[139] Although living PI-

CDSA holds much promise towards upscaling the preparation of 1D BCP-based nanoparticles of controlled size, currently the only examples of the seeded growth method utilize PFS-based BCPs.

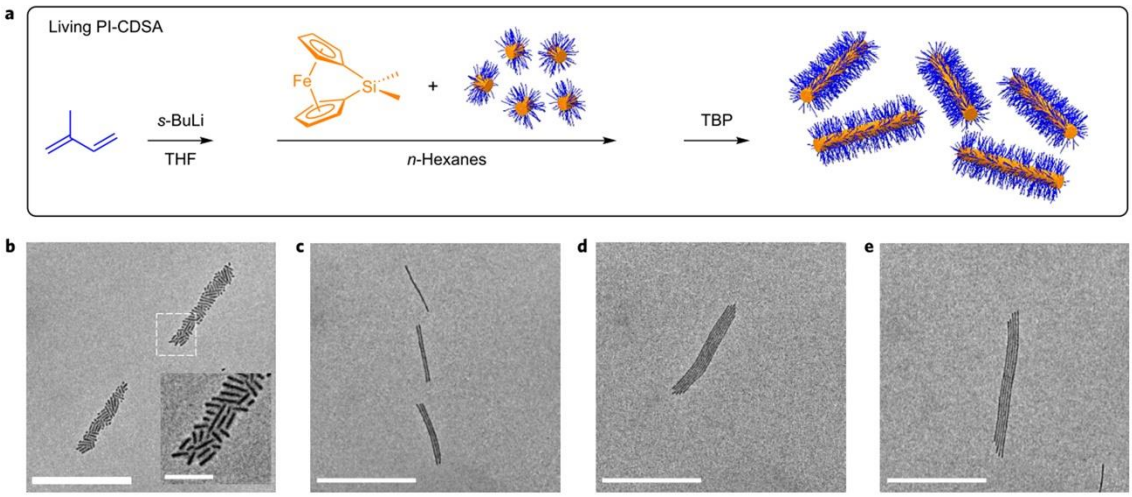

Figure 1.11 Living PI-CDSA of PI-*b*-PFS at 10 wt% in 10 vol% THF/hexanes with a corona-to-core block ratio of 5:1. (a) Schematic representation of the preparation of low dispersity PI-*b*-PFS cylindrical micelles by living PI-CDSA. TBP = 4-*tert*-butylphenol, used as the quenching agent. TEM images of (b) small seed micelles and low dispersity cylindrical micelles prepared by using unimer-to-seed ratios (m_{unimer}/m_{seed}) of (c) 3:1, (d) 6:1, (e) 12:1. Scale bars: 1 μm, (b) inset: 200 nm. Reproduced with permission from reference 138.

1.7 Applications of Block Copolymer Micelles Prepared via Crystallization-Driven Self-Assembly

Owing to the diverse range of coronal and crystalline core chemistries compatible with CDSA protocols, 1D and 2D micelles prepared using these methods are of interest for a wide range of applications,[14,23,94,117,143–152] and will be discussed herein.

1.7.1 Applications of 1D Micelles

Non-spherical nanoparticles are of great interest for biomedical applications.[153–155] 1D micelles have been found to exhibit many advantages over spherical nanoparticles including enhanced

circulation times,[149,156,157] retention,[155,158] cellular uptake and binding,[159–163] and tumor penetration,[153,164,165] as well as exhibiting low immune cell association.[76] Specifically, polymer-based nanoparticles prepared by CDSA protocols show promise in the field of nanomedicine. For example, low dispersity folate-functionalized PDHF-based 1D nanofibers prepared by living CDSA have been shown to exhibit uptake into more than 97% of folate receptor positive HeLa cells.[161] Recently, cellular uptake and penetration of PFS-based cylindrical micelles with lengths of 80–2000 nm was also investigated, finding that nanofibers with lower aspect ratio resulted in tumor penetration to a greater depth.[165]

Over the past decade, significant advances towards the use of π-conjugated BCP-based nanoparticles for optoelectronic properties have been made.[143] Most significantly, organic semiconducting PDHF-based nanofibers prepared by living CDSA exhibit long-range exciton diffusion lengths of 200 nm. This unprecedented characteristic is much higher than that exhibited for conjugated polymer films (5–10 nm),[166,167] and is attributed to the high degree of structural order within the π-conjugated crystalline PDHF core.[114] Use of controlled nanofibers prepared by living CDSA for optoelectronic applications holds many advantageous characteristics, including relatively simple design and preparation compared with that of current bulk heterojunction materials. In another study, charge-carrier mobilities exhibited by uniform P3HT-based nanofibers were found to increase in a super-linear manner with fiber length.[112] Recently, efficient energy transport in films of charge-terminated P3HT-based nanofibers prepared by living CDSA was reported, demonstrating exciton diffusion lengths of 300 nm.[168]

Catalysis is another field which holds potential applications for 1D micelles prepared by CDSA protocols. Greiner, Schmalz, *et al.* reported the use of patchy PE-based 1D micelles loaded with gold nanoparticles and supported on PS fibers through coaxial electrospinning as efficient heterogeneous catalysts (**Scheme 1.5**). In this work, 1D cylindrical micelles were prepared from a PS-*b*-PE-*b*-PMMA triBCP by CDSA, resulting in a corona consisting of alternating PS and PMMA

patches. The PS patches provided optimal adhesion to the PS microfiber during coaxial electrospinning (**Scheme 1.5**a), whereas the PMMA patches allowed for post-polymerization functionalization and loading of catalytic gold nanoparticles (**Scheme 1.5**b).[57]

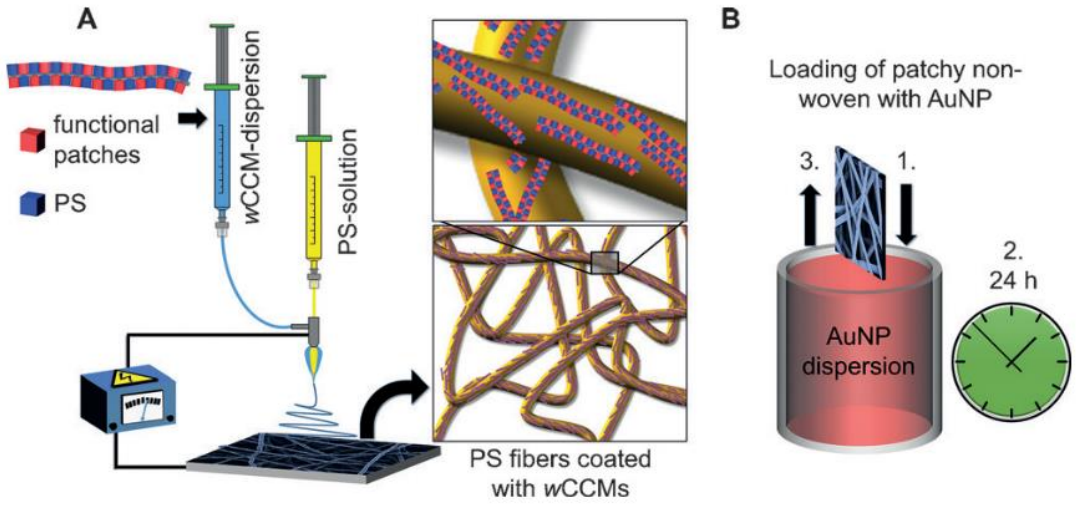

Scheme 1.5 (a) Cartoon representation of the preparation of catalytically active patchy PE-based cylindrical micelles supported on PS fibers by coaxial electrospinning followed by (b) loading with gold nanoparticles in a simple dipping process. Reproduced with permission from reference 57.

1.7.2 Applications of 2D Micelles

The ability to fabricate 2D platelet micelles of controlled size and morphology by CDSA protocols using various core chemistries has presented many opportunities for potential applications. The groups of Dove and O'Reilly have demonstrated the use of PLLA-based 2D diamond-shaped platelets as water-in-water emulsion additives, which exhibit a superior stabilizing effect over that of spherical micelles. Larger platelets were found to form more stable emulsions than smaller platelets and were easily size-tunable by altering the self-assembly solvent composition. 2D platelets formed from biocompatible, biodegradable polymers such as PLLA have potential utilization in the pharmaceutical, agrochemical, cosmetics, or food industries.[109] Further work by these groups also demonstrated that PLLA-containing 2D platelets could be used to adhere to

calcium-alginate hydrogel faces, increasing hydrogel adhesion and mechanical strength compared with spherical or cylindrical micelles.[169]

1.8 Thesis Research Objectives

The introduction to this thesis has highlighted the progress made towards accessing controlled 1D and 2D nanoparticles through BCP self-assembly. Living CDSA is a powerful tool to allow for low dispersity size-tunable nanoparticles to be prepared. However, key challenges associated with the scale-up of these processes remain. Therefore, the work presented in this thesis aims to upscale the preparation and processing of size-tunable, low dispersity 1D and 2D micelles with a crystalline core. These aims are addressed as four key objectives and are outlined below.

1. **Investigate the upscaled preparation of 2D nanoparticles by living CDSA**

Although the preparation of low dispersity size-tunable 2D nanoparticles is relatively well-established using living CDSA, limitations arise regarding scale-up. In most cases, increasing the concentration at which living CDSA is performed results in competitive self-nucleation, compromising micelle size-dispersity, as well as increased platelet aggregation, which presents challenges in post-processing. One of the aims of this thesis is to study how solution concentration affects the 2D self-assembly process to gain insight on the scale-up of 2D platelet preparation.

2. **Investigate PI-CDSA protocols using a biocompatible crystalline core-forming block**

Living PI-CDSA has been demonstrated as a fundamental tool for 1D micelle scale-up by performing the polymerization, self-assembly, and seeded growth *in situ*. However, this process is currently limited to PFS-based BCPs. Various other crystalline core chemistries are compatible with CDSA processes and exhibit interesting applications. For example, 1D polymer-based nanoparticles are of interest for a range of biomedical applications yet are limited with respect to scale-up. This thesis therefore aims to extend the scope of PI-CDSA protocols to use a

polycarbonate-based crystalline core-forming block to access low dispersity size-tunable nanofibers, which have potential applications in nanomedicine, at scalable concentrations.

3. **Investigate the upscaled preparation of 1D micelles in continuous flow**

An alternative approach to tackle scale-up of BCP micelle preparation involves continuous flow chemistry. Continuous flow processes are high throughput techniques which involve the use of channels in a continuous stream rather than in batch. Living CDSA is analogous to living anionic polymerization in that the seed micelles act as initiators and the unimer acts as monomer. Since the synthesis of polymers with narrow molecular weight distributions by living anionic polymerization in continuous flow is well-established, a key objective of this thesis will be to extend this technique to allow for the preparation of low dispersity 1D micelles by the analogous living CDSA in continuous flow.

4. **Investigate the processing of 1D micelles using electrospinning techniques**

Electrospinning techniques are a cost-effective and high throughput method of processing and preparing fibers for use in various applications, from electronic devices to bone tissue scaffolds. This thesis therefore aims to investigate the viability of using electrospinning methods to process 1D micelles into microfibers.

1.9 Thesis Summary and Collaborator Acknowledgements

1.9.1 Thesis Summary

This thesis is comprised of a compilation of research projects focusing on the upscaled preparation and processing of BCP micelles with a crystalline core. Four results chapters are presented, as well as a final conclusions and outlook chapter which highlights the impact of this work and possible future directions.

Chapter 2 explores the upscaled preparation of 2D platelet micelles using living CDSA of a charge-terminated PFS homopolymer with surfactant counteranions. The effects of various factors, including temperature and concentration, on platelet dimensions, structure fidelity, and aggregation behaviour have been investigated.

Chapter 3 describes living PI-CDSA to access scalable low dispersity 1D nanofibers containing a biodegradable poly(fluorenetrimethylenecarbonate) crystalline core. This is the first example which extends the scope of living PI-CDSA beyond PFS-based BCPs.

Chapter 4 investigates the scalable preparation of low dispersity 1D cylindrical micelles by living CDSA in continuous flow. The preparation of polydisperse 1D micelles and 1D seed micelles in continuous flow are also described.

Chapter 5 discusses the processing of 1D cylindrical micelles into microfibers through simple, low cost, and high throughput electrospinning techniques. This chapter describes the preparation of electrospun microfibers consisting solely of 1D micelles with a crystalline core, the first examples where a template material is not required.

Chapter 6 describes an outline for how the work in this thesis could be continued.

1.9.2 Collaborator Acknowledgements

In accordance with the expectations of Professor Ian Manners, each chapter of this thesis has been written in a self-contained fashion such that it may be published in a peer-reviewed scientific journal. The work in this thesis was often performed in collaboration with colleagues both within the Manners research group at the University of Victoria, as well as academics and students at other research institutions as outlined below.

Chapter 2 has been reproduced from *Polymer Chemistry*, **2021**, *12* (25), 3650-3660. Dr Tomoya Fukui (University of Victoria) synthesized PFS_{24}-*b*-$P2VP_{384}$ and added scientific insight. SAED experiments and analysis were conducted by Dr Christina Cordoba and Dr Arthur Blackburn

(University of Victoria). Charlotte E. Ellis (University of Victoria) conducted the synthesis of all other materials, and performed the self-assembly, characterization, and data analysis.

Chapter 3 contains yet unpublished results. J. Diego Garcia-Hernandez (University of Victoria) synthesized the fluorenetrimethylenecarbonate monomer and added scientific insight. Charlotte E. Ellis (University of Victoria) conducted the synthesis of all other materials, and performed the self-assembly, characterization, and data analysis.

Chapter 4 contains yet unpublished results. PFS_{32}-*b*-PFS_{448} was synthesized by Dr Yunxiang He (University of Bristol). Self-assembly, characterization, and data analysis was conducted jointly by Ayesha Nadeem and Charlotte E. Ellis (University of Victoria). Dr Steven T. G. Street (University of Victoria) added scientific insight. Research was conducted at the University of Victoria.

Chapter 5 contains yet unpublished results. Synthesis and self-assembly of PI_{192}-*b*-PFS_{27}, *ran*-PI_{124}/$PtBS_{125}$-*b*-PFS_{37}, and $PtBS_{257}$-*b*-PFS_{38} was performed by Dr Alex M. Oliver (University of Bristol). Synthesis and self-assembly of $PDHF_{17}$-*b*-$P2VP_{250}$ was completed by Dr Huda Shaikh (University of Victoria). Electrospinning experiments were conducted jointly by Dr Alex M. Oliver (University of Bristol), Charlotte E. Ellis (University of Bristol, University of Victoria), and Dr Christian Hils (University of Bayreuth) from the groups of Dr Holger Schmalz and Prof. Andreas Greiner. Raman spectroscopy was conducted by Dr Holger Schmalz (University of Bayreuth). Andreas Frank (University of Bayreuth) performed SEM analysis. Werner Reichstein (University of Bayreuth) conducted fluorescence imaging. The research was led and organized by Charlotte E. Ellis. Research was conducted at the University of Bristol, University of Bayreuth, and University of Victoria.

1.10 References

(1) Fratzl, P.; Weinkamer, R. Nature's Hierarchical Materials. *Prog. Mater. Sci.* **2007**, *52* (8), 1263–1334.

(2) Meyers, M. A.; Chen, P. Y.; Lin, A. Y. M.; Seki, Y. Biological Materials: Structure and Mechanical Properties. *Prog. Mater. Sci.* **2008**, *53* (1), 1–206.

(3) Whitesides, G. M. Self-Assembly at All Scales. *Science* **2002**, *295* (5564), 2418–2421.

(4) Isaacoff, B. P.; Brown, K. A. Progress in Top-Down Control of Bottom-Up Assembly. *Nano Lett.* **2017**, *17* (11), 6508–6510.

(5) Whitesides, G. M.; Boncheva, M. Beyond Molecules: Self-Assembly of Mesoscopic and Macroscopic Components. *Proc. Natl. Acad. Sci. U. S. A.* **2002**, *99* (8), 4769–4774.

(6) Scacchi, A.; Nikkhah, S. J.; Sammalkorpi, M.; Ala-Nissila, T. Self-Assembly in Soft Matter with Multiple Length Scales. *Phys. Rev. Res.* **2021**, *3* (2), L02208.

(7) Liu, Y.; Luo, D.; Wang, T. Hierarchical Structures of Bone and Bioinspired Bone Tissue Engineering. *Small* **2016**, *34*, 4611–4632.

(8) Wegst, U. G. K.; Bai, H.; Saiz, E.; Tomsia, A. P.; Ritchie, R. O. Bioinspired Structural Materials. *Nat. Mater.* **2015**, *14*, 23–36.

(9) Vesentini, S.; Gautieri, A. Nanomechanics of Collagen Microfibrils. *Muscles. Ligaments Tendons J.* **2013**, *3* (1), 23–34.

(10) Marth, J. D. A Unified Vision of the Building Blocks of Life. *Nat. Cell Biol.* **2008**, *10* (9), 1015–1016.

(11) Lombardo, D.; Calandra, P.; Pasqua, L.; Magazù, S. Self-Assembly of Organic Nanomaterials and Biomaterials: The Bottom-up Approach for Functional Nanostructures Formation and Advanced Applications. *Materials (Basel).* **2020**, *13* (5).

(12) Grzybowski, B. A.; Wilmer, C. E.; Kim, J.; Browne, K. P.; Bishop, K. J. M. Self-Assembly: From Crystals to Cells. *Soft Matter* **2009**, *5* (6), 1110–1128.

(13) Hill, J. P.; Shrestha, L. K.; Ishihara, S.; Ji, Q.; Ariga, K. Self-Assembly: From Amphiphiles to Chromophores and Beyond. *Molecules* **2014**, *19* (6), 8589–8609.

(14) Tritschler, U.; Pearce, S.; Gwyther, J.; Whittell, G. R.; Manners, I. 50th Anniversary Perspective: Functional Nanoparticles from the Solution Self-Assembly of Block Copolymers. *Macromolecules* **2017**, *50* (9), 3439–3463.

(15) Mai, Y.; Eisenberg, A. Self-Assembly of Block Copolymers. *Chem. Soc. Rev.* **2012**, *41* (18), 5969–5985.

(16) Quirk, R. P.; Zhuo, Q.; Jang, S. H.; Lee, Y.; Lizarraga, G. Principles of Anionic Polymerization: An Introduction. In *Applications of Anionic Polymerization Research*; 1998; pp 2–27.

(17) Perrier, S. 50th Anniversary Perspective: RAFT Polymerization - A User Guide. *Macromolecules* **2017**, *50* (19), 7433–7447.

(18) Iha, R. K.; Wooley, K. L.; Nyström, A. M.; Burke, D. J.; Kade, M. J.; Hawker, C. J. Applications of Orthogonal Click Chemistries in the Synthesis of Functional Soft Materials. *Chem. Rev.* **2009**, *109* (11), 5620–5686.

(19) Dumanli, A. G.; Savin, T. Recent Advances in the Biomimicry of Structural Colours. *Chem. Soc. Rev.* **2016**, *45* (24), 6698–6724.

(20) Cochran, E. W.; Garcia-Cervera, C. J.; Fredrickson, G. H. Stability of the Gyroid Phase in Diblock Copolymers at Strong Segregation. *Macromolecules* **2006**, *39* (7), 2449–2451.

(21) Hayward, R. C.; Pochan, D. J. Tailored Assemblies of Block Copolymers in Solution: It Is All about the Process. *Macromolecules* **2010**, *43* (8), 3577–3584.

(22) Jain, S.; Bates, F. S. Consequences of Nonergodicity in Aqueous Binary PEO-PB Micellar Dispersions. *Macromolecules* **2004**, *37* (4), 1511–1523.

(23) Schacher, F. H.; Rupar, P. A.; Manners, I. Functional Block Copolymers: Nanostructured Materials with Emerging Applications. *Angew. Chem. Int. Ed.* **2012**, *51* (32), 7898–7921.

(24) Wong, C. K.; Qiang, X.; Müller, A. H. E.; Gröschel, A. H. Self-Assembly of Block Copolymers into Internally Ordered Microparticles. *Prog. Polym. Sci.* **2020**, *102*.

(25) Keller, A. Polymer Single Crystals. *Polymer* **1962**, *3*, 393–421.

(26) Lotz, B.; Kovacs, A. J.; Bassett, G. A.; Keller, A. Properties of Copolymers Composed of One Poly-Ethylene-Oxide and One Polystyrene Block - II. Morphology of Single Crystals. *Kolloid-Zeitschrift Zeitschrift für Polym.* **1966**, *209* (2), 115–128.

(27) Keller, A.; Pedemonte, E. A Study of Growth Rates of Polyethylene Single Crystal. *J. Cryst. Growth* **1973**, *18*, 111–123.

(28) Massey, J. A.; Temple, K.; Cao, L.; Rharbi, Y.; Raez, J.; Winnik, M. A.; Manners, I. Self-Assembly of Organometallic Block Copolymers: The Role of Crystallinity of the Core-Forming Polyferrocene Block in the Micellar Morphologies Formed by

Poly(Ferrocenylsilane-b-Dimethylsiloxane) in n-Alkane Solvents. *J. Am. Chem. Soc.* **2000**, *122* (47), 11577–11584.

(29) Ungar, G.; Zeng, X.-B. Learning Polymer Crystallization with the Aid of Linear, Branched and Cyclic Model Compounds. *Chem. Rev.* **2001**, *101* (12), 4157–4188.

(30) Vilgis, T.; Halperin, A. Aggregation of Coil-Crystalline Block Copolymers: Equilibrium Crystallization. *Macromolecules* **1991**, *24* (8), 2090–2095.

(31) Tang, X.; Chen, W.; Li, L. The Tough Journey of Polymer Crystallization: Battling with Chain Flexibility and Connectivity. *Macromolecules* **2019**, *52* (10), 3575–3591.

(32) Cao, L.; Manners, I.; Winnik, M. A. Influence of the Interplay of Crystallization and Chain Stretching on Micellar Morphologies: Solution Self-Assembly of Coil-Crystalline Poly(Isoprene-Block-Ferrocenylsilane). *Macromolecules* **2002**, *35* (22), 8258–8260.

(33) Inam, M.; Cambridge, G.; Pitto-Barry, A.; Laker, Z. P. L.; Wilson, N. R.; Mathers, R. T.; Dove, A. P.; O'Reilly, R. K. 1D vs. 2D Shape Selectivity in the Crystallization-Driven Self-Assembly of Polylactide Block Copolymers. *Chem. Sci.* **2017**, *8* (6), 4223–4230.

(34) Hsiao, M.-S.; Yusoff, S. F. M.; Winnik, M. A.; Manners, I. Crystallization-Driven Self-Assembly of Block Copolymers with a Short Crystallizable Core-Forming Segment: Controlling Micelle Morphology through the Influence of Molar Mass and Solvent Selectivity. *Macromolecules* **2014**, *47* (7), 2361–2372.

(35) Guerin, G.; Rupar, P. A.; Molev, G.; Manners, I.; Jinnai, H.; Winnik, M. A. Lateral Growth of 1D Core-Crystalline Micelles upon Annealing in Solution. *Macromolecules* **2016**, *49* (18), 7004–7014.

(36) Fan, B.; Liu, L.; Li, J. H.; Ke, X. X.; Xu, J. T.; Du, B. Y.; Fan, Z. Q. Crystallization-Driven One-Dimensional Self-Assembly of Polyethylene-b-Poly(Tert-Butylacrylate) Diblock Copolymers in DMF: Effects of Crystallization Temperature and the Corona-Forming Block. *Soft Matter* **2015**, *12* (1), 67–76.

(37) Song, S.; Jiang, J.; Nikbin, E.; Howe, J. Y.; Manners, I.; Winnik, M. A. The Role of Cooling Rate in Crystallization-Driven Block Copolymer Self-Assembly. *Chem. Sci.* **2022**, *13* (2), 396–409.

(38) Ellis, C. E.; Fukui, T.; Cordoba, C.; Blackburn, A.; Manners, I. Towards Scalable, Low Dispersity, and Dimensionally Tunable 2D Platelets Using Living Crystallization-Driven

Self-Assembly. *Polym. Chem.* **2021**, *12* (25), 3650–3660.

(39) Boott, C. E.; Leitao, E. M.; Hayward, D. W.; Laine, R. F.; Mahou, P.; Guerin, G.; Winnik, M. A.; Richardson, R. M.; Kaminski, C. F.; Whittell, G. R.; Manners, I. Probing the Growth Kinetics for the Formation of Uniform 1D Block Copolymer Nanoparticles by Living Crystallization-Driven Self-Assembly. *ACS Nano* **2018**, *12* (9), 8920–8933.

(40) Foucher, D. A.; Tang, B.-Z.; Manners, I. Ring-Opening Polymerization of Strained, Ring-Tilted Ferrocenophanes: A Route to High Molecular Weight Poly (Ferrocenylsilanes). *J. Am. Chem. Soc.* **1992**, *114* (15), 6246–6248.

(41) Manners, I. Poly(Ferrocenylsilanes): Novel Organometallic Plastics. *Chem. Commun.* **1999**, No. 10, 857–865.

(42) Hailes, R. L. N.; Oliver, A. M.; Gwyther, J.; Whittell, G. R.; Manners, I. Polyferrocenylsilanes: Synthesis, Properties, and Applications. *Chem. Soc. Rev.* **2016**, *45* (19), 5358–5407.

(43) Rulkens, R.; Ni, Y.; Manners, I. Living Anionic Ring-Opening Polymerization of Silicon-Bridged [1]Ferrocenophanes: Synthesis and Characterization of Poly(Ferrocenylsilane)-Polysiloxane Block Copolymers. *J. Am. Chem. Soc.* **1994**, *116* (26), 12121–12122.

(44) Ni, Y.; Rulkens, R.; Manners, I. Transition Metal-Based Polymers with Controlled Architectures: Well-Defined Poly(Ferrocenylsilane) Homopolymers and Multiblock Copolymers via the Living Anionic Ring-Opening Polymerization of Silicon-Bridged [1]Ferrocenophanes. *J. Am. Chem. Soc.* **1996**, *118* (17), 4102–4114.

(45) Du, V. A.; Manners, I. Poly(Ferrocenylmethylsilane): An Unsymmetrically Substituted, Atactic, but Semicrystalline Polymetallocene. *Macromolecules* **2013**, *46* (12), 4742–4753.

(46) Massey, J. A.; Power-Billard, K. N.; Manners, I.; Winnik, M. A. Self-Assembly of a Novel Organometallic-Inorganic Block Copolymer in Solution and the Solid State: Nonintrusive Observation of Novel Wormlike Poly(Ferrocenyldimethylsilane)-b-Poly(Dimethylsiloxane) Micelles. *J. Am. Chem. Soc.* **1998**, *120* (37), 9533–9540.

(47) Korczagin, I.; Hempenius, M. A.; Fokkink, R. G.; Cohen Stuart, M. A.; Al-Hussein, M.; Bomans, P. H. H.; Frederik, P. M.; Vancso, G. J. Self-Assembly of Poly(Ferrocenyldimethylsilane-b-Methyl Methacrylate) Block Copolymers in a Selective Solvent. *Macromolecules* **2006**, *39* (6), 2306–2315.

(48) Wang, H.; Winnik, M. A.; Manners, I. Synthesis and Self-Assembly of Poly(Ferrocenyldimethylsilane-b-2-Vinylpyridine) Diblock Copolymers. *Macromolecules* **2007**, *40* (10), 3784–3789.

(49) Cai, J.; Mineart, K. P.; Li, X.; Spontak, R. J.; Manners, I.; Qiu, H. Hierarchical Self-Assembly of Toroidal Micelles into Multidimensional Nanoporous Superstructures. *ACS Macro Lett.* **2018**, *7* (8), 1040–1045.

(50) Lammertink, R. G. H.; Hempenius, M. A.; Manners, I.; Vancso, G. J. Crystallization and Melting Behavior of Poly(Ferrocenyldimethylsilanes) Obtained by Anionic Polymerization. *Macromolecules* **1998**, *31* (3), 795–800.

(51) Gilroy, J. B.; Rupar, P. A.; Whittell, G. R.; Chabanne, L.; Terrill, N. J.; Winnik, M. A.; Manners, I.; Richardson, R. M. Probing the Structure of the Crystalline Core of Field-Aligned, Monodisperse, Cylindrical Polyisoprene-Block-Polyferrocenylsilane Micelles in Solution Using Synchrotron Small- and Wide-Angle X-Ray Scattering. *J. Am. Chem. Soc.* **2011**, *133* (42), 17056–17062.

(52) Wang, X.; Liu, K.; Arsenault, A. C.; Rider, D. A.; Ozin, G. A.; Winnik, M. A.; Manners, I. Shell-Cross-Linked Cylindrical Polyisoprene-b-Polyferrocenylsilane (PI-b-PFS) Block Copolymer Micelles: One-Dimensional (1D) Organometallic Nanocylinders. *J. Am. Chem. Soc.* **2007**, *129* (17), 5630–5639.

(53) Yusoff, S. F. M.; Hsiao, M.-S.; Schacher, F. H.; Winnik, M. A.; Manners, I. Formation of Lenticular Platelet Micelles via the Interplay of Crystallization and Chain Stretching: Solution Self-Assembly of Poly(Ferrocenyldimethylsilane)- Block -Poly(2-Vinylpyridine) with a Crystallizable Core-Forming Metalloblock. *Macromolecules* **2012**, *45* (9), 3883–3891.

(54) He, X.; Hsiao, M.-S.; Boott, C. E.; Harniman, R. L.; Nazemi, A.; Li, X.; Winnik, M. A.; Manners, I. Two-Dimensional Assemblies from Crystallizable Homopolymers with Charged Termini. *Nat. Mater.* **2017**, *16*, 481–488.

(55) Schmalz, H.; Schmelz, J.; Drechsler, M.; Yuan, J.; Walther, A.; Schweimer, K.; Mihut, A. M. Thermo-Reversible Formation of Wormlike Micelles with a Microphase-Separated Corona from a Semicrystalline Triblock Terpolymer. *Macromolecules* **2008**, *41* (9), 3235–3242.

(56) Schmelz, J.; Karg, M.; Hellweg, T.; Schmalz, H. General Pathway toward Crystalline-Core

Micelles with Tunable Morphology and Corona Segregation. *ACS Nano* **2011**, *5* (12), 9523–9534.

(57) Schöbel, J.; Burgard, M.; Hils, C.; Dersch, R.; Dulle, M.; Volk, K.; Karg, M.; Greiner, A.; Schmalz, H. Bottom-Up Meets Top-Down: Patchy Hybrid Nonwovens as an Efficient Catalysis Platform. *Angew. Chem. Int. Ed.* **2017**, *56* (1), 405–408.

(58) Hils, C.; Schmelz, J.; Drechsler, M.; Schmalz, H. Janus Micelles by Crystallization-Driven Self-Assembly of an Amphiphilic, Double-Crystalline Triblock Terpolymer. *J. Am. Chem. Soc*. **2021**, *143* (38), 15582–15586.

(59) Gädt, T.; Ieong, N. S.; Cambridge, G.; Winnik, M. A.; Manners, I. Complex and Hierarchical Micelle Architectures from Diblock Copolymers Using Living, Crystallization-Driven Polymerizations. *Nat. Mater.* **2009**, *8*, 144–150.

(60) Kamps, A. C.; Fryd, M.; Park, S. J. Hierarchical Self-Assembly of Amphiphilic Semiconducting Polymers into Isolated, Bundled, and Branched Nanofibers. *ACS Nano* **2012**, *6* (3), 2844–2852.

(61) Hayward, D. W.; Lunn, D. J.; Seddon, A.; Finnegan, J. R.; Gould, O. E. C.; Magdysyuk, O.; Manners, I.; Whittell, G. R.; Richardson, R. M. Structure of the Crystalline Core of Fiber-like Polythiophene Block Copolymer Micelles. *Macromolecules* **2018**, *51* (8), 3097–3106.

(62) Mori, T.; Watanabe, T.; Minagawa, K.; Tanaka, M. Self-Assembly of Oligo(p-Phenylenevinylene)-Block-Poly(Ethylene Oxide) in Polar Media and Solubilization of an Oligo(p-Phenylenevinylene) Homooligomer inside the Assembly. *J. Polym. Sci. Part A Polym. Chem.* **2005**, *43* (8), 1569–1578.

(63) Tian, Y.; Chen, C. Y.; Yip, H. L.; Wu, W. C.; Chen, W. C.; Jen, A. K. Y. Synthesis, Nanostructure, Functionality and Application of Polyfluorene-Block-Poly(N-Isopropylacrylamide)S. *Macromolecules* **2010**, *43* (1), 282–291.

(64) Yu, Y. Y.; Hsu, C. Y.; Li, G. Y. Synthesis and Morphological Transformation of Conjugated Amphiphilic Diblock Copolymers in Mixed Solvents. *J. Nanomater.* **2013**, *2013*.

(65) Du, Z. X.; Xu, J. T.; Fan, Z. Q. Micellar Morphologies of Poly(ε-Caprolactone)-b-Poly(Ethylene Oxide) Block Copolymers in Water with a Crystalline Core. *Macromolecules* **2007**, *40* (21), 7633–7637.

(66) Du, Z. X.; Xu, J. T.; Fan, Z. Q. Regulation of Micellar Morphology of PCL-b-PEO Block Copolymers by Crystallization Temperature. *Macromol. Rapid Commun.* **2008**, *29* (6), 467–471.

(67) He, W.-N.; Zhou, B.; Xu, J.-T.; Du, B.-Y.; Fan, Z.-Q. Two Growth Modes of Semicrystalline Cylindrical Poly(ε-Caprolactone)-b -Poly(Ethylene Oxide) Micelles. *Macromolecules* **2012**, *45* (24), 9768–9778.

(68) Arno, M. C.; Inam, M.; Coe, Z.; Cambridge, G.; Macdougall, L. J.; Keogh, R.; Dove, A. P.; O'Reilly, R. K. Precision Epitaxy for Aqueous 1D and 2D Poly(ϵ-Caprolactone) Assemblies. *J. Am. Chem. Soc.* **2017**, *139* (46), 16980–16985.

(69) Ganda, S.; Dulle, M.; Drechsler, M.; Förster, B.; Förster, S.; Stenzel, M. H. Two-Dimensional Self-Assembled Structures of Highly Ordered Bioactive Crystalline-Based Block Copolymers. *Macromolecules* **2017**, *50* (21), 8544–8553.

(70) Sun, J.-T.; Hong, C.-Y.; Pan, C.-Y. Recent Advances in RAFT Dispersion Polymerization for Preparation of Block Copolymer Aggregates. *Polym. Chem.* **2013**, *4* (4), 873–881.

(71) Yu, W.; Inam, M.; Jones, J. R.; Dove, A. P.; O'Reilly, R. K. Understanding the CDSA of Poly(Lactide) Containing Triblock Copolymers. *Polym. Chem.* **2017**, *8* (36), 5504–5512.

(72) Zhang, J.; Wang, L. Q.; Wang, H.; Tu, K. Micellization Phenomena of Amphiphilic Block Copolymers Based on Methoxy Poly(Ethylene Glycol) and Either Crystalline or Amorphous Poly(Caprolactone-b-Lactide). *Biomacromolecules* **2006**, *7* (9), 2492–2500.

(73) Finnegan, J. R.; He, X.; Street, S. T. G.; Garcia-Hernandez, J. D.; Hayward, D. W.; Harniman, R. L.; Richardson, R. M.; Whittell, G. R.; Manners, I. Extending the Scope of "Living" Crystallization-Driven Self Assembly: Well-Defined 1D Micelles and Block Comicelles from Crystallizable Polycarbonate Block Copolymers. *J. Am. Chem. Soc.* **2018**, *140* (49), 17127–17140.

(74) Lazzari, M.; Scalarone, D.; Vazquez-Vazquez, C.; López-Quintela, M. A. Cylindrical Micelles from the Self-Assembly of Polyacrylonitrile-Based Diblock Copolymers in Nonpolar Selective Solvents. *Macromol. Rapid Commun.* **2008**, *29* (4), 352–357.

(75) Nishimura, T.; Sumi, N.; Mukai, S. A.; Sasaki, Y.; Akiyoshi, K. Supramacromolecular Injectable Hydrogels by Crystallization-Driven Self-Assembly of Carbohydrate-Conjugated Poly(2-Isopropyloxazoline)s for Biomedical Applications. *J. Mater. Chem. B*

2019, *7* (41), 6362–6369.

(76) Finnegan, J. R.; Pilkington, E.; Alt, K.; Rahim, M. A.; Kent, S. J.; Davis, T. P.; Kempe, K. Stealth Nanorods via the Aqueous Living Crystallisation-Driven Self-Assembly of Poly(2-Oxazoline)S. *Chem. Sci.* **2021**, *12*, 7350–7360.

(77) Lee, C. U.; Smart, T. P.; Guo, L.; Epps, T. H.; Zhang, D. Synthesis and Characterization of Amphiphilic Cyclic Diblock Copolypeptoids from N-Heterocyclic Carbene-Mediated Zwitterionic Polymerization of N-Substituted N-Carboxyanhydride. *Macromolecules* **2011**, *44* (24), 9574–9585.

(78) Wei, Y.; Tian, J.; Zhang, Z.; Zhu, C.; Sun, J.; Li, Z. Supramolecular Nanosheets Assembled from Poly(Ethylene Glycol)- b-Poly(N-(2-Phenylethyl)Glycine) Diblock Copolymer Containing Crystallizable Hydrophobic Polypeptoid: Crystallization Driven Assembly Transition from Filaments to Nanosheets. *Macromolecules* **2019**, *52* (4), 1546–1556.

(79) Sun, J.; Jiang, X.; Lund, R.; Downing, K. H.; Balsara, N. P.; Zuckermann, R. N. Self-Assembly of Crystalline Nanotubes from Monodisperse Amphiphilic Diblock Copolypeptoid Tiles. *Proc. Natl. Acad. Sci. U. S. A.* **2016**, *113* (15), 3954–3959.

(80) Jiang, N.; Yu, T.; Darvish, O. A.; Qian, S.; Mkam Tsengam, I. K.; John, V.; Zhang, D. Crystallization-Driven Self-Assembly of Coil-Comb-Shaped Polypeptoid Block Copolymers: Solution Morphology and Self-Assembly Pathways. *Macromolecules* **2019**, *52* (22), 8867–8877.

(81) Shi, Z.; Wei, Y.; Zhu, C.; Sun, J.; Li, Z. Crystallization-Driven Two-Dimensional Nanosheet from Hierarchical Self-Assembly of Polypeptoid-Based Diblock Copolymers. *Macromolecules* **2018**, *51* (16), 6344–6351.

(82) Gao, Y.; Li, X.; Hong, L.; Liu, G. Mesogen-Driven Formation of Triblock Copolymer Cylindrical Micelles. *Macromolecules* **2012**, *45* (3), 1321–1330.

(83) Li, X.; Gao, Y.; Xing, X.; Liu, G. Polygonal Micellar Aggregates of a Triblock Terpolymer Containing a Liquid Crystalline Block. *Macromolecules* **2013**, *46* (18), 7436–7442.

(84) Shen, L.; Guo, H.; Zheng, J.; Wang, X.; Yang, Y.; An, Z. RAFT Polymerization-Induced Self-Assembly as a Strategy for Versatile Synthesis of Semifluorinated Liquid-Crystalline Block Copolymer Nanoobjects. *ACS Macro Lett.* **2018**, *7* (3), 287–292.

(85) Guan, S.; Zhang, C.; Wen, W.; Qu, T.; Zheng, X.; Zhao, Y.; Chen, A. Formation of

Anisotropic Liquid Crystalline Nanoparticles via Polymerization-Induced Hierarchical Self-Assembly. *ACS Macro Lett.* **2018**, *7* (3), 358–363.

(86) Guan, S.; Wen, W.; Yang, Z.; Chen, A. Liquid Crystalline Nanowires by Polymerization Induced Hierarchical Self-Assembly. *Macromolecules* **2020**, *53* (1), 465–472.

(87) Guan, S.; Chen, A. One-Pot Synthesis of Cross-Linked Block Copolymer Nanowires via Polymerization-Induced Hierarchical Self-Assembly and Photodimerization. *ACS Macro Lett.* **2020**, *9* (1), 14–19.

(88) Jia, L.; Lévy, D.; Durand, D.; Impéror-Clerc, M.; Cao, A.; Li, M. H. Smectic Polymer Micellar Aggregates with Temperature-Controlled Morphologies. *Soft Matter* **2011**, *7* (16), 7395–7403.

(89) Gilroy, J. B.; Gädt, T.; Whittell, G. R.; Chabanne, L.; Mitchels, J. M.; Richardson, R. M.; Winnik, M. A.; Manners, I. Monodisperse Cylindrical Micelles by Crystallization-Driven Living Self-Assembly. *Nat. Chem.* **2010**, *2*, 566–570.

(90) Qiu, H.; Gao, Y.; Du, V. A.; Harniman, R. L.; Winnik, M. A.; Manners, I. Branched Micelles by Living Crystallization-Driven Block Copolymer Self-Assembly under Kinetic Control. *J. Am. Chem. Soc.* **2015**, *137* (6), 2375–2385.

(91) Blundell, D. J.; Keller, A.; Kovacs, A. J. A New Self-Nucleation Phenomenon and Its Applications to the Growing of Polymer Crystals from Solution. *J. Polym. Sci. Part B Polym. Lett.* **1966**, *4*, 481–486.

(92) Blundell, D. J.; Keller, A. Nature of Self-Seeding Polyethylene Crystal Nuclei. *J. Macromol. Sci. Part B* **1968**, *2* (2), 301–336.

(93) Macfarlane, L. R.; Li, X.; Faul, C. F. J.; Manners, I. Efficient and Controlled Seeded Growth of Poly(3-Hexylthiophene) Block Copolymer Nanofibers through Suppression of Homogeneous Nucleation. *Macromolecules* **2021**, *54* (24), 11269–11280.

(94) MacFarlane, L. R.; Zhao, C.; Cai, J.; Qiu, H.; Manners, I. Emerging Applications for Living Crystallization-Driven Self-Assembly. *Chem. Sci.* **2021**, *12* (13), 4661–4682.

(95) Wang, X.; Manners, I.; Winnik, M. A. Cylindrical Block Copolymer Micelles and Co-Micelles of Controlled Length and Architecture. *Science* **2007**, *317* (5838), 644–648.

(96) He, F.; Gädt, T.; Manners, I.; Winnik, M. A. Fluorescent "Barcode" Multiblock Co-Micelles

via the Living Self-Assembly of Di- and Triblock Copolymers with a Crystalline Core-Forming Metalloblock. *J. Am. Chem. Soc.* **2011**, *133* (23), 9095–9103.

(97) Hudson, Z. M.; Lunn, D. J.; Winnik, M. A.; Manners, I. Colour-Tunable Fluorescent Multiblock Micelles. *Nat. Commun.* **2014**, *5*, 3372.

(98) Qiu, H.; Hudson, Z. M.; Winnik, M. A.; Manners, I. Multidimensional Hierarchical Self-Assembly of Amphiphilic Cylindrical Block Comicelles. *Science* **2015**, *347* (6228), 1329–1332.

(99) Li, X.; Gao, Y.; Boott, C. E.; Winnik, M. A.; Manners, I. Non-Covalent Synthesis of Supermicelles with Complex Architectures Using Spatially Confined Hydrogen-Bonding Interactions. *Nat. Commun.* **2015**, *6*, 8127.

(100) Li, X.; Gao, Y.; Harniman, R. L.; Winnik, M. A.; Manners, I. Hierarchical Assembly of Cylindrical Block Comicelles Mediated by Spatially Confined Hydrogen-Bonding Interactions. *J. Am. Chem. Soc.* **2016**, *138* (39), 12902–12912.

(101) Hudson, Z. M.; Boott, C. E.; Robinson, M. E.; Rupar, P. A.; Winnik, M. A.; Manners, I. Tailored Hierarchical Micelle Architectures Using Living Crystallization-Driven Self-Assembly in Two Dimensions. *Nat. Chem.* **2014**, *6*, 893–898.

(102) Qiu, H.; Gao, Y.; Boott, C. E.; Gould, O. E. C.; Harniman, R. L.; Miles, M. J.; Webb, S. E. D.; Winnik, M. A.; Manners, I. Uniform Patchy and Hollow Rectangular Platelet Micelles from Crystallizable Polymer Blends. *Science* **2016**, *352* (6286), 697–702.

(103) Presa Soto, A.; Gilroy, J. B.; Winnik, M. A.; Manners, I. Pointed-Oval-Shaped Micelles from Crystalline-Coil Block Copolymers by Crystallization-Driven Living Self-Assembly. *Angew. Chem. Int. Ed.* **2010**, *49* (44), 8220–8223.

(104) Nazemi, A.; He, X.; Macfarlane, L. R.; Harniman, R. L.; Hsiao, M.-S.; Winnik, M. A.; Faul, C. F. J.; Manners, I. Uniform "Patchy" Platelets by Seeded Heteroepitaxial Growth of Crystallizable Polymer Blends in Two Dimensions. *J. Am. Chem. Soc.* **2017**, *139* (12), 4409–4417.

(105) Pearce, S.; He, X.; Hsiao, M.-S.; Harniman, R. L.; MacFarlane, L. R.; Manners, I. Uniform, High-Aspect-Ratio, and Patchy 2D Platelets by Living Crystallization-Driven Self-Assembly of Crystallizable Poly(Ferrocenyldimethylsilane)-Based Homopolymers with Hydrophilic Charged Termini. *Macromolecules* **2019**, *52* (16), 6068–6079.

(106) Ganda, S.; Stenzel, M. H. Concepts, Fabrication Methods and Applications of Living Crystallization-Driven Self-Assembly of Block Copolymers. *Prog. Polym. Sci.* **2020**, *101*, 101195.

(107) Schmelz, J.; Schedl, A. E.; Steinlein, C.; Manners, I.; Schmalz, H. Length Control and Block-Type Architectures in Worm-like Micelles with Polyethylene Cores. *J. Am. Chem. Soc.* **2012**, *134* (34), 14217–14225.

(108) Yu, W.; Foster, J. C.; Dove, A. P.; O'Reilly, R. K. Length Control of Biodegradable Fiber-Like Micelles via Tuning Solubility: A Self-Seeding Crystallization-Driven Self-Assembly of Poly(ε-Caprolactone)-Containing Triblock Copolymers. *Macromolecules* **2020**, *53* (4), 1514–1521.

(109) Inam, M.; Jones, J. R.; Pérez-Madrigal, M. M.; Arno, M. C.; Dove, A. P.; O'Reilly, R. K. Controlling the Size of Two-Dimensional Polymer Platelets for Water-in-Water Emulsifiers. *ACS Cent. Sci.* **2018**, *4* (1), 63–70.

(110) He, Y.; Eloi, J.-C.; Harniman, R. L.; Richardson, R. M.; Whittell, G. R.; Mathers, R. T.; Dove, A. P.; O'Reilly, R. K.; Manners, I. Uniform Biodegradable Fiber-Like Micelles and Block Comicelles via "Living" Crystallization-Driven Self-Assembly of Poly(L-Lactide) Block Copolymers: The Importance of Reducing Unimer Self-Nucleation via Hydrogen Bond Disruption. *J. Am. Chem. Soc.* **2019**, *141* (48), 19088–19098.

(111) Qian, J.; Li, X.; Lunn, D. J.; Gwyther, J.; Hudson, Z. M.; Kynaston, E. L.; Rupar, P. A.; Winnik, M. A.; Manners, I. Uniform, High Aspect Ratio Fiber-like Micelles and Block Co-Micelles with a Crystalline π-Conjugated Polythiophene Core by Self-Seeding. *J. Am. Chem. Soc.* **2014**, *136* (11), 4121–4124.

(112) Li, X.; Wolanin, P. J.; MacFarlane, L. R.; Harniman, R. L.; Qian, J.; Gould, O. E. C.; Dane, T. G.; Rudin, J.; Cryan, M. J.; Schmaltz, T.; Frauenrath, H.; Winnik, M. A.; Faul, C. F. J.; Manners, I. Uniform Electroactive Fibre-like Micelle Nanowires for Organic Electronics. *Nat. Commun.* **2017**, *8*, 15909.

(113) Fukui, T.; Garcia-Hernandez, J. D.; MacFarlane, L. R.; Lei, S.; Whittell, G. R.; Manners, I. Seeded Self-Assembly of Charge-Terminated Poly(3-Hexylthiophene) Amphiphiles Based on the Energy Landscape. *J. Am. Chem. Soc.* **2020**, *142* (35), 15038–15048.

(114) Jin, X.; Price, M. B.; Finnegan, J. R.; Boott, C. E.; Richter, J. M.; Rao, A.; Menke, S. M.; Friend, R. H.; Whittell, G. R.; Manners, I. Long-Range Exciton Transport in Conjugated

Polymer Nanofibers Prepared by Seeded Growth. *Science* **2018**, *900* (6391), 897–900.

(115) Zhang, Y.; Shaikh, H.; Sneyd, A. J.; Tian, J.; Xiao, J.; Blackburn, A.; Rao, A.; Friend, R. H.; Manners, I. Efficient Energy Funneling in Spatially Tailored Segmented Conjugated Block Copolymer Nanofiber−Quantum Dot or Rod Conjugates. *J. Am. Chem. Soc.* **2021**, *143* (18), 7032–7041.

(116) Shaikh, H.; Jin, X.-H.; Harniman, R. L.; Richardson, R. M.; Whittell, G. R.; Manners, I. Solid-State Donor-Acceptor Coaxial Heterojunction Nanowires via Living Crystallization-Driven Self-Assembly. *J. Am. Chem. Soc.* **2020**, *142* (31), 13469–13480.

(117) Canning, S. L.; Smith, G. N.; Armes, S. P. A Critical Appraisal of RAFT-Mediated Polymerization-Induced Self-Assembly. *Macromolecules* **2016**, *49* (6), 1985–2001.

(118) Warren, N. J.; Armes, S. P. Polymerization-Induced Self-Assembly of Block Copolymer Nano-Objects via RAFT Aqueous Dispersion Polymerization. *J. Am. Chem. Soc.* **2014**, *136* (29), 10174–10185.

(119) Hunter, S. J.; Armes, S. P. Pickering Emulsifiers Based on Block Copolymer Nanoparticles Prepared by Polymerization-Induced Self-Assembly. *Langmuir* **2020**, *36* (51), 15463–15484.

(120) Charleux, B.; Delaittre, G.; Rieger, J.; D'Agosto, F. Polymerization-Induced Self-Assembly: From Soluble Macromolecules to Block Copolymer Nano-Objects in One Step. *Macromolecules* **2012**, *45* (17), 6753–6765.

(121) Masuko, K.; Kumano, C.; Sugawara, R.; Nakabayashi, K.; Mori, H. Polymerization-induced Self-assembly of Amino-acid-based Nano-objects by Reversible Addition–Fragmentation Chain-transfer Dispersion Polymerization. *J. Polym. Sci.* **2021**, *59*, 1664–1677.

(122) Guimarães, T. R.; Bong, Y. L.; Thompson, S. W.; Moad, G.; Perrier, S.; Zetterlund, P. B. Polymerization-Induced Self-Assembly via RAFT in Emulsion: Effect of Z-Group on the Nucleation Step. *Polym. Chem.* **2021**, *12* (1), 122–133.

(123) Dao, T. P. T.; Vezenkov, L.; Subra, G.; Amblard, M.; In, M.; Le Meins, J.-F.; Aubrit, F.; Moradi, M.-A.; Ladmiral, V.; Semsarilar, M. Self-Assembling Peptide-Polymer Nano-Objects via Polymerization-Induced Self-Assembly. *Macromolecules* **2020**, *53* (16), 7034–7043.

(124) Czajka, A.; Armes, S. P. In Situ SAXS Studies of a Prototypical RAFT Aqueous Dispersion Polymerization Formulation: Monitoring the Evolution in Copolymer Morphology during Polymerization-Induced Self-Assembly. *Chem. Sci.* **2020**, *11* (42), 11443–11454.

(125) Qiao, X. G.; Dugas, P.-Y.; Charleux, B.; Lansalot, M.; Bourgeat-Lami, E. Nitroxide-Mediated Polymerization-Induced Self-Assembly of Amphiphilic Block Copolymers with a pH/Temperature Dual Sensitive Stabilizer Block. *Polym. Chem.* **2017**, *8* (27), 4014–4029.

(126) Qiao, X. G.; Lansalot, M.; Bourgeat-Lami, E.; Charleux, B. Nitroxide-Mediated Polymerization-Induced Self-Assembly of Poly(Poly(Ethylene Oxide) Methyl Ether Methacrylate-Co-Styrene)-b-Poly(n-Butyl Methacrylate-Co-Styrene) Amphiphilic Block Copolymers. *Macromolecules* **2013**, *46* (11), 4285–4295.

(127) Liu, C.; Hong, C.-Y.; Pan, C.-Y. Polymerization Techniques in Polymerization-Induced Self-Assembly (PISA). *Polym. Chem.* **2020**, *11* (22), 3673–3689.

(128) Pearce, S.; Perez-Mercader, J. PISA: Construction of Self-Organized and Self-Assembled Functional Vesicular Structures. *Polym. Chem.* **2021**, *12* (1), 29–49.

(129) Blanazs, A.; Ryan, A. J.; Armes, S. P. Predictive Phase Diagrams for RAFT Aqueous Dispersion Polymerization: Effect of Block Copolymer Composition, Molecular Weight, and Copolymer Concentration. *Macromolecules* **2012**, *45* (12), 5099–5107.

(130) Rho, J. Y.; Scheutz, G. M.; Häkkinen, S.; Garrison, J. B.; Song, Q.; Yang, J.; Richardson, R.; Perrier, S.; Sumerlin, B. S. In Situ Monitoring of PISA Morphologies. *Polym. Chem.* **2021**, No. 27, 3947–3952.

(131) Sobotta, F. H.; Kuchenbrod, M.; Hoeppener, S.; Brendel, J. C. One Polymer Composition, Various Morphologies: The Decisive Influence of Conditions on the Polymerization-Induced Self-Assembly (PISA) of: N-Acryloyl Thiomorpholine. *Nanoscale* **2020**, *12* (39), 20171–20176.

(132) Wan, W. M.; Sun, X. L.; Pan, C. Y. Morphology Transition in RAFT Polymerization for Formation of Vesicular Morphologies in One Pot. *Macromolecules* **2009**, *42* (14), 4950–4952.

(133) Wan, W. M.; Hong, C. Y.; Pan, C. Y. One-Pot Synthesis of Nanomaterials via RAFT Polymerization Induced Self-Assembly and Morphology Transition. *Chem. Commun.* **2009**, No. 39, 5883–5885.

(134) Ikkene, D.; Arteni, A. A.; Ouldali, M.; Six, J.-L.; Ferji, K. Self-Assembly of Amphiphilic Copolymers Containing Polysaccharide: PISA: Versus Nanoprecipitation, and the Temperature Effect. *Polym. Chem.* **2020**, *11* (29), 4729–4740.

(135) Xu, S.; Corrigan, N.; Boyer, C. Forced Gradient Copolymerisation: A Simplified Approach for Polymerisation-Induced Self-Assembly. *Polym. Chem.* **2021**, *12* (1), 57–68.

(136) Canning, S. L.; Neal, T. J.; Armes, S. P. PH-Responsive Schizophrenic Diblock Copolymers Prepared by Polymerization-Induced Self-Assembly. *Macromolecules* **2017**, *50* (16), 6108–6116.

(137) Derry, M. J.; Fielding, L. A.; Armes, S. P. Polymerization-Induced Self-Assembly of Block Copolymer Nanoparticles via RAFT Non-Aqueous Dispersion Polymerization. *Prog. Polym. Sci.* **2016**, *52*, 1–18.

(138) Boott, C. E.; Gwyther, J.; Harniman, R. L.; Hayward, D. W.; Manners, I. Scalable and Uniform 1D Nanoparticles by Synchronous Polymerization, Crystallization and Self-Assembly. *Nat. Chem.* **2017**, *9*, 785–792.

(139) Oliver, A. M.; Gwyther, J.; Boott, C. E.; Davis, S. A.; Pearce, S.; Manners, I. Scalable Fiber-like Micelles and Block Co-Micelles by Polymerization-Induced Crystallization-Driven Self-Assembly. *J. Am. Chem. Soc.* **2018**, *140* (51), 18104–18114.

(140) Schnitte, M.; Staiger, A.; Casper, L. A.; Mecking, S. Uniform Shape Monodisperse Single Chain Nanocrystals by Living Aqueous Catalytic Polymerization. *Nat. Commun.* **2019**, *10*, 2592.

(141) Sha, Y.; Rahman, M. A.; Zhu, T.; Cha, Y.; McAlister, C. W.; Tang, C. ROMPI-CDSA: Ring-Opening Metathesis Polymerization-Induced Crystallization-Driven Self-Assembly of Metallo-Block Copolymers. *Chem. Sci.* **2019**, *10* (42), 9782–9787.

(142) Hurst, P. J.; Rakowski, A. M.; Patterson, J. P. Ring-Opening Polymerization-Induced Crystallization-Driven Self-Assembly of Poly-L-Lactide-Block-Polyethylene Glycol Block Copolymers (ROPI-CDSA). *Nat. Commun.* **2020**, *11*, 4690.

(143) MacFarlane, L. R.; Shaikh, H.; Garcia-Hernandez, J. D.; Vespa, M.; Fukui, T.; Manners, I. Functional Nanoparticles through π-Conjugated Polymer Self-Assembly. *Nat. Rev. Mater.* **2021**, *6*, 7–26.

(144) Pearce, A. K.; Wilks, T. R.; Arno, M. C.; O'Reilly, R. K. Synthesis and Applications of

Anisotropic Nanoparticles with Precisely Defined Dimensions. *Nat. Rev. Chem.* **2021**, *5*, 21–45.

(145) Ma, J.; Lu, G.; Huang, X.; Feng, C. π-Conjugated-Polymer-Based Nanofibers through Living Crystallization-Driven Self-Assembly: Preparation, Properties and Applications. *Chem. Commun.* **2021**, *57*, 13259–13274.

(146) Karayianni, M.; Pispas, S. Block Copolymer Solution Self-Assembly: Recent Advances, Emerging Trends, and Applications. *J. Polym. Sci.* **2021**, *59*, 1874–1898.

(147) Brendel, J. C.; Schacher, F. H. Block Copolymer Self-Assembly in Solution-Quo Vadis? *Chem. - An Asian J.* **2018**, *13* (3), 230–239.

(148) Truong, N. P.; Quinn, J. F.; Whittaker, M. R.; Davis, T. P. Polymeric Filomicelles and Nanoworms: Two Decades of Synthesis and Application. *Polym. Chem.* **2016**, *7* (26), 4295–4312.

(149) Elsabahy, M.; Wooley, K. L. Design of Polymeric Nanoparticles for Biomedical Delivery Applications. *Chem. Soc. Rev.* **2012**, *41*, 2545–2561.

(150) Blanazs, A.; Armes, S. P.; Ryan, A. J. Self-Assembled Block Copolymer Aggregates: From Micelles to Vesicles and Their Biological Applications. *Macromol. Rapid Commun.* **2009**, *30* (4–5), 267–277.

(151) Gröschel, A. H.; Walther, A.; Löbling, T. I.; Schacher, F. H.; Schmalz, H.; Müller, A. H. E. Guided Hierarchical Co-Assembly of Soft Patchy Nanoparticles. *Nature* **2013**, *503*, 247–251.

(152) Boott, C. E.; Nazemi, A.; Manners, I. Synthetic Covalent and Non-Covalent 2D Materials. *Angew. Chem. Int. Ed.* **2015**, *54* (47), 13876–13894.

(153) Kinnear, C.; Moore, T. L.; Rodriguez-Lorenzo, L.; Rothen-Rutishauser, B.; Petri-Fink, A. Form Follows Function: Nanoparticle Shape and Its Implications for Nanomedicine. *Chem. Rev.* **2017**, *117* (17), 11476–11521.

(154) Meyer, R. A.; Green, J. J. Shaping the Future of Nanomedicine: Anisotropy in Polymeric Nanoparticle Design. *Wiley Interdiscip. Rev. Nanomedicine Nanobiotechnology* **2016**, *8* (2), 191–207.

(155) Zhao, Y.; Wang, Y.; Ran, F.; Cui, Y.; Liu, C.; Zhao, Q.; Gao, Y.; Wang, D. A Comparison

between Sphere and Rod Nanoparticles Regarding Their in Vivo Biological Behavior and Pharmacokinetics. *Sci. Rep.* **2017**, *7*, 4131.

(156) Geng, Y. A. N.; Dalhaimer, P.; Cai, S.; Tsai, R.; Minko, T.; Discher, D. E. Shape Effects of Filaments versus Spherical Particles in Flow and Drug Delivery. *Nat. Nanotechnol.* **2007**, *2* (4), 249–255.

(157) Mandal, S.; Eksteen-Akeroyd, Z. H.; Jacobs, M. J.; Hammink, R.; Koepf, M.; Lambeck, A. J. A.; van Hest, J. C. M.; Wilson, C. J.; Blank, K.; Figdor, C. G.; Rowan, A. E. Therapeutic Nanoworms: Towards Novel Synthetic Dendritic Cells for Immunotherapy. *Chem. Sci.* **2013**, *4* (11), 4168–4174.

(158) Bruckman, M. A.; Randolph, L. N.; Vanmeter, A.; Hern, S.; Shoffstall, A. J.; Taurog, R. E.; Steinmetz, N. F. Biodistribution, Pharmacokinetics, and Blood Compatibility of Native and PEGylated Tobacco Mosaic Virus Nano-Rods and -Spheres in Mice. *Virology* **2014**, *449*, 163–173.

(159) Dasgupta, S.; Auth, T.; Gompper, G. Shape and Orientation Matter for the Cellular Uptake of Nonspherical Particles. *Nano Lett.* **2014**, *14* (2), 687–693.

(160) Song, Y.; Elsabahy, M.; Collins, C. A.; Khan, S.; Li, R.; Hreha, T. N.; Shen, Y.; Lin, Y.-N.; Letteri, R. A.; Su, L.; Dong, M.; Zhang, F.; Hunstad, D. A.; Wooley, K. L. Morphologic Design of Silver-Bearing Sugar-Based Polymer Nanoparticles for Uroepithelial Cell Binding and Antimicrobial Delivery. *Nano Lett.* **2021**, *21* (12), 4990–4998.

(161) Street, S. T. G.; He, Y.; Jin, X.-H.; Hodgson, L.; Verkade, P.; Manners, I. Cellular Uptake and Targeting of Low Dispersity, Dual Emissive, Segmented Block Copolymer Nanofibers. *Chem. Sci.* **2020**, *11* (32), 8394–8408.

(162) Huang, X.; Teng, X.; Chen, D.; Tang, F.; He, J. The Effect of the Shape of Mesoporous Silica Nanoparticles on Cellular Uptake and Cell Function. *Biomaterials* **2010**, *31* (3), 438–448.

(163) Barua, S.; Yoo, J.; Kolhar, P.; Wakankar, A.; Gokarn, Y. R.; Mitragotri, S. Particle Shape Enhances Specificity of Antibody-Displaying Nanoparticles. *Proc. Natl. Acad. Sci.* **2013**, *110* (9), 3270–3275.

(164) Cutler, C. S.; Wang, L. V.; Liu, Y.; Xia, Y. Radioactive 198Au-Doped Nanostructures with Different Shapes for In Vivo Analyses of Their Biodistribution, Tumor Uptake, and

Intratumoral Distribution. *ACS Nano* **2014**, *8* (5), 4385–4394.

(165) Yu, Q.; Roberts, M. G.; Houdaihed, L.; Liu, Y.; Ho, K.; Walker, G. C.; Allen, C.; Reilly, R. M.; Manners, I.; Winnik, M. A. Investigating the Influence of Block Copolymer Micelle Length on Cellular Uptake and Penetration in a Multicellular Tumor Spheroid Model. *Nanoscale* **2021**, *13* (1), 280–291.

(166) Tamai, Y.; Ohkita, H.; Benten, H.; Ito, S. Exciton Diffusion in Conjugated Polymers: From Fundamental Understanding to Improvement in Photovoltaic Conversion Efficiency. *J. Phys. Chem. Lett.* **2015**, *6* (17), 3417–3428.

(167) Mikhnenko, O. V.; Blom, P. W. M.; Nguyen, T. Q. Exciton Diffusion in Organic Semiconductors. *Energy Environ. Sci.* **2015**, *8* (7), 1867–1888.

(168) Sneyd, A. J.; Fukui, T.; Paleček, D.; Prodhan, S.; Wagner, I.; Zhang, Y.; Sung, J.; Collins, S. M.; Slater, T. J. A.; Andaji-Garmaroudi, Z.; Macfarlane, L. R.; Garcia-Hernandez, J. D.; Wang, L.; Whittell, G. R.; Hodgkiss, J. M.; Chen, K.; Beljonne, D.; Manners, I.; Friend, R. H.; Rao, A. Efficient Energy Transport in an Organic Semiconductor Mediated by Transient Exciton Delocalization. *Sci. Adv.* **2021**, *7* (32), eabh4232.

(169) Arno, M. C.; Inam, M.; Weems, A. C.; Li, Z.; Binch, A. L. A.; Platt, C. I.; Richardson, S. M.; Hoyland, J. A.; Dove, A. P.; O'Reilly, R. K. Exploiting the Role of Nanoparticle Shape in Enhancing Hydrogel Adhesive and Mechanical Properties. *Nat. Commun.* **2020**, *11*, 1420.

Chapter 2 Towards Scalable, Low Dispersity, and Dimensionally Tunable 2D Platelets Using Living Crystallization-Driven Self-Assembly

This chapter has been reproduced from:

Charlotte E. Ellis, Tomoya Fukui, Cristina Cordoba, Arthur Blackburn, and Ian Manners, *Polym. Chem.* **2021**, *12* (25), 3650–3660.

2.1 Abstract

Nanoscale two-dimensional (2D) rectangular platelets based on polymeric precursors are of interest as a result of their potentially useful properties and applications. Low dispersity 2D platelets can be prepared from crystallizable polymeric amphiphiles via the seeded growth method known as living crystallization-driven self-assembly (CDSA) but only at very low solution concentrations of ca. 0.002–0.01 wt%. This severely limits the ability to explore their properties in detail and to investigate new applications. In this proof-of-concept work we report significant improvements in the scalability of low dispersity 2D nanoparticles prepared via living CDSA of phosphonium-capped poly(ferrocenyldimethylsilane) (PFS) homopolymers, $PFS_{23}[PPh_2Me]X$, with surfactant counteranions (X^-) at concentrations up to 0.2 wt%, 20 times higher than previously reported. At higher concentrations, platelets are still formed but at the cost of a loss in fidelity. The effects of different counteranions, temperature and concentration on platelet dimensions, structure fidelity, and aggregation behaviour were also explored. Moreover, increasing the temperature at which self-assembly was performed was found to improve the platelet fidelity and yield lower aspect ratio structures at high concentrations.

2.2 Introduction

Nanoscale two-dimensional (2D) structures, such as metallic nanosheets and graphene, are of broad interest due to their unique properties and wide range of potential applications.[1–4] Platelets formed from homopolymer and block copolymer (BCP) self-assembly in solution are examples of 2D nanostructures based on soft matter,[4–6] and are of interest for a range of applications such as emulsion stabilizers, liquid crystals, nanomotors, and composite reinforcement.[3–10] Examples of 2D platelets prepared from the self-assembly of all-amorphous BCPs in selective solvents are relatively rare as spontaneous closure to form vesicles is generally favoured during the micelle growth process.[6] The presence of a crystallizable core-forming block during BCP self-assembly, however, generally favours the formation of morphologies with low curvature of the core-corona interface via crystallization-driven self-assembly (CDSA).[6,11–18] Planar structures are obtained since the lattice energy of the resulting rigid crystalline core overcomes the entropically disfavoured stretching of the corona.[6,11–18] CDSA involves a nucleation and growth process that allows access to morphologically pure 1D or 2D micelles. Generally, at low corona-to-core block ratios (e.g. 1:1) 2D platelet micelles are formed,[19–21] whereas 1D cylinders are favoured for BCPs with relatively long corona segments.[22] However, CDSA does not permit size-control over the resulting nanostructures or allow access to low dispersities, as the rate of self-nucleation is slower than that of the subsequent growth step.

The formation of uniform 1D and 2D micelles with dimensional control can be achieved via the seeded growth process termed "living" CDSA.[23,24] Ultrasonication of polydisperse micelles prepared via CDSA results in fragmentation to yield low dispersity, small "seed" micelles.[23–26] The exposed crystalline core of the seed, either at the fiber termini or platelet edges, remains active to epitaxial growth upon the addition of molecularly dissolved BCP or "unimer".[23,24] Low dispersity micelles are obtained via living CDSA where the spontaneous nucleation step is circumvented by the presence of seeds, which act as efficient initiators for the growth step.[23,24] 1D fiber-like or 2D

platelet micelles can be targeted depending on the corona-to-core block ratio of the added unimer,[23,24,27] or in the latter case, also by the use of a crystallizable charge-terminated homopolymer[28–30] or homopolymer/BCP blend.[31,32] The length or area of the resulting 1D or 2D micelles, respectively, is linearly dependent on the unimer-to-seed mass ratio, allowing for micelle size to be predetermined and controlled.[23,24] Living CDSA has now been achieved for a diverse range of polymeric amphiphiles with crystallizable core-forming segments such as poly(ferrocenyldimethylsilane) (PFS),[6,23,25,26] poly(3-hexylthiophene),[33] poly(di-*n*-hexylfluorene),[34] poly(ε-caprolactone),[15,16] poly(*L*-lactide),[7,17,35] polyethylene,[36] poly(*p*-phenylenevinylene) and related materials,[20,37,38] polycarbonate,[27] and poly(isopropyloxazoline).[39]

Although living CDSA represents a promising route to 2D nanoparticles of targeted size and shape, this process has been performed only under high dilution conditions. The use of higher concentrations is expected to lead to competitive self-nucleation, resulting in 2D platelets with reduced size-control and higher area-dispersity. Aggregation in solution should also be favoured as concentration increases, limiting the long-term colloidal stability. The formation of 2D platelets via living CDSA of BCPs is therefore typically carried out at concentrations of up to only ca. 0.002 wt%.[24,28–32,40–42] The living CDSA of charge-terminated homopolymers, however, allows access to well-defined 2D platelets at concentrations of up to 0.01 wt%, a notable five-fold increase.[28–30]

Over the last decade substantial progress has been made in the upscaling of BCP nanoparticle formation by combining the BCP synthesis and self-assembly steps in a process termed polymerization-induced self-assembly (PISA).[43–49] The PISA approach has also been established for BCPs with crystallizable core-forming blocks to yield polydisperse 1D or 2D nanoparticles.[50–58] We have recently shown that uniform 1D micelles of controlled length can be prepared at scalable concentrations of up to 25 wt% by a seeded growth process termed living polymerization-induced CDSA (PI-CDSA), in which BCP synthesis and seeded growth occur *in situ*.[50,51] However, due to

the generally lower colloidal stability of platelet micelles, the use of living PI-CDSA to upscale uniform 2D nanoparticle formation from BCPs has proved significantly more challenging.

With respect to scale-up, the use of crystallizable homopolymers with charged termini therefore appears to provide advantages over using charge-neutral BCP systems either in 2D living CDSA or PI-CDSA processes, including reliably targeting the 2D platelet morphology and improving colloidal stability.[28–30] Herein, we describe our attempts to access low dispersity 2D platelets at more scalable concentrations through the living CDSA of phosphonium-capped PFS homopolymers with a variety of counteranions.

2.3 Results and Discussion

2.3.1 Synthesis and Characterization of Phosphonium-Capped PFS Homopolymers with Surfactant Counteranions

The chemical structures of PFS_{24}-*b*-$P2VP_{384}$ (P2VP = poly(2-vinylpyridine)), used to prepare 1D seed micelles, and the phosphonium-capped PFS homopolymers utilized in this study are shown in **Figure 2.1**. PFS_{24}-*b*-$P2VP_{384}$ was prepared by living anionic polymerization[59,60] and $PFS_{23}[PPh_2Me]I$ was synthesized according to previously reported procedures.[28] Briefly, $PFS_{23}PPh_2$ was prepared via the living anionic polymerization of 1,1-dimethylsila[1]ferrocenophane in THF followed by quenching with chlorodiphenylphosphine.[28] $PFS_{23}[PPh_2Me]I$ was then prepared by the subsequent quaternization of $PFS_{23}PPh_2$ with excess methyl iodide.[28] Complete quaternization was established using ^{1}H NMR integration of the peaks for the terminal phenyl groups (multiplet at 7.77–7.61 ppm) and the newly introduced terminal methyl substituent (doublet at 3.04 ppm) (**Figure S2.1**a, b). The appearance of a new doublet in the ^{1}H NMR spectrum at 3.04 ppm from P-CH_3 (J = 13.0 Hz) as well as a shift from -17.5 to +24.1 ppm in the ^{31}P NMR spectrum was observed after the quaternization reaction (**Figures 2.1** and **2.2**). Exchange reactions were carried out on $PFS_{23}[PPh_2Me]I$ to prepare $PFS_{23}[PPh_2Me]SDS$ and

PFS_{23}[PPh_2Me]AOT by metathesis, utilizing an excess of sodium dodecyl sulfate (Na[SDS]) or bis(2-ethylhexyl)sulfosuccinate sodium salt (Na[AOT]), respectively. Displaced iodide counteranions after the exchange process were removed as the sodium salt by repeated washing with methanol. Complete counteranion replacement was established through integration of proton resonances corresponding to the relevant surfactant counteranion and the phenyl groups of the homopolymer terminus (**Figure S2.1**c, d). A shift in the doublet corresponding to P-CH_3 of the terminal phosphonium group from 3.04 to 2.97 and 2.96 ppm was also observed in the ^{1}H NMR spectrum on formation of PFS_{23}[PPh_2Me]SDS and PFS_{23}[PPh_2Me]AOT, respectively.

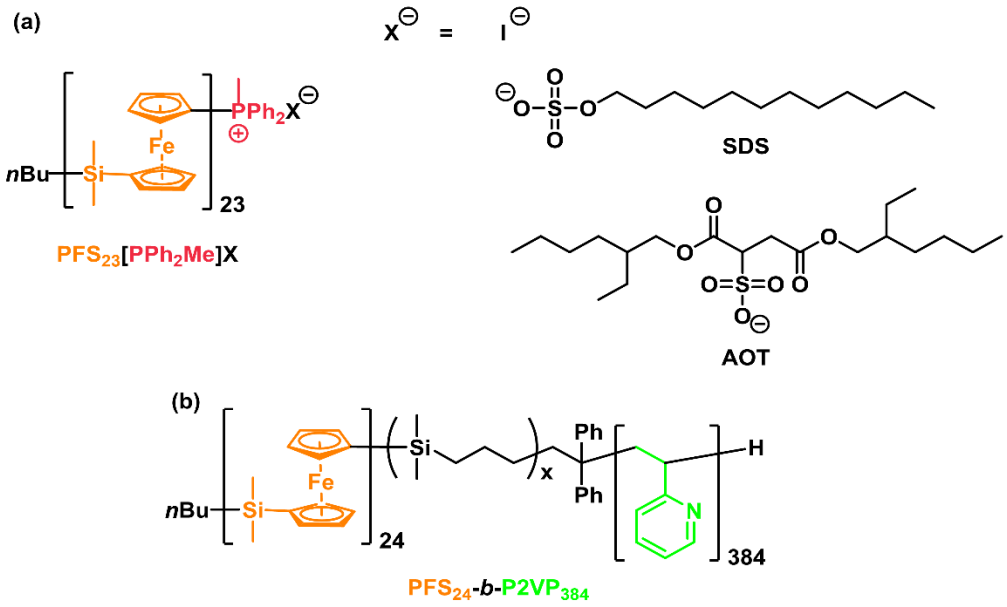

Figure 2.1 Chemical structures of (a) PFS homopolymers and (b) PFS_{24}-*b*-$P2VP_{384}$ BCP utilized in this study.

The number-average molecular mass (M_n) of the PFS_{23}[PPh_2Me]X homopolymers was found to be 5,830 Da by matrix-assisted laser desorption time-of-flight (MALDI-TOF) mass spectrometry (**Figure S2.3**), corresponding to a degree of polymerization (DP_n) of 23 (target DP_n = 20). The molecular weight dispersities were low, M_w/M_n = 1.07, as determined by gel permeation chromatography (GPC). The determined DP_n value of 23 by MALDI-TOF mass spectrometry was

in good agreement with that found by ^{1}H NMR spectroscopy (DP_n = 23), through a comparison of the integration of the terminal methyl group with the cyclopentadienyl proton signals in the PFS main chain. The molecular mass of $PFS_{23}[PPh_2Me]X$ by ^{1}H NMR spectroscopy was therefore calculated to be 5,827 Da, which further corroborates that obtained by MALDI-TOF mass spectrometry.

^{1}H DOSY NMR spectroscopic analysis of $PFS_{23}[PPh_2Me]$SDS and $PFS_{23}[PPh_2Me]$AOT in THF-d_8 showed that the resonances arising from the cation-terminated PFS homopolymer and the respective surfactant counteranion exhibit similar diffusion coefficients (**Figure S2.4**a, c). A shift in diffusion coefficients corresponding to signals from the surfactant is also observed on comparing the surfactant-bound polymer with the respective surfactant sodium salts (**Figure S2.4**b, d and **Table S2.1**). These results indicate that the polymeric cation $PFS_{23}[PPh_2Me]^+$ and the surfactant counteranion, $[SDS]^-$ or $[AOT]^-$, exist as an ion pair in THF,[61] which was used as the common solvent in the following studies. The presence of an ion pair is consistent with the aforementioned sensitivity of the doublet ^{1}H NMR resonance for the terminal methyl substituent of the phosphonium group to the nature of the counteranion.

2.3.2 Scaled Preparation of 1D PFS-*b*-P2VP Cylindrical Seeds

The seeded growth of PFS homopolymers with charged termini from 1D seed micelles represents a promising route to access uniform 2D platelets.[28–30] Using transmission electron microscopy (TEM), PFS-*b*-P2VP and PFS homopolymer can easily be distinguished by the observed contrast due to the presence of the electron-rich P2VP corona, allowing easy identification of the $PFS_{23}[PPh_2Me]X$ platelet area.[31] Thus, PFS-*b*-P2VP 1D seed micelles were selected for the study.

Polydisperse cylindrical micelles were prepared via the CDSA of PFS_{24}-*b*-$P2VP_{384}$ in isopropanol (*i*PrOH) at a concentration of 5 mg/mL (0.6 wt%), ca. 10-fold more concentrated than for typical CDSA experiments. The solution was heated at 80 °C for 24 h, to ensure complete dissolution of

the PFS_{24}-*b*-$P2VP_{384}$ BCP at this high concentration before cooling slowly to room temperature.[62] Characterization by TEM showed the formation of polydisperse cylindrical micelles (**Figure 2.2**a). Sonication of the polydisperse PFS_{24}-*b*-$P2VP_{384}$ micelles at 0 °C for 4 h yielded short but polydisperse fragmented cylindrical micelles (L_n = 22 nm, L_w/L_n = 1.46, where L_w is the weight-average length and L_n is the number-average length) (**Figure S2.5**). The fragmented fibers were then heated at 80 °C for 30 min, which yielded lower dispersity seed micelles of slightly greater length (L_n = 26 nm, L_w/L_n = 1.19) (**Figures 2.2**b and **S2.6**). The small increase in length is believed to be a result of a partial self-seeding process,[63] where the very short duration of the annealing experiment prevents equilibrium being reached where all of the micelle regions of lower crystallinity that are soluble at 80 °C actually dissolve. Therefore, micelles with only a small increase in length, rather than much longer micelles, subsequently form on cooling. The absence of any substantial increase in length after heat treatment may also be a result of the high concentration of the seed solution (0.6 wt%) which would hinder fractional micelle dissolution.[62,64]

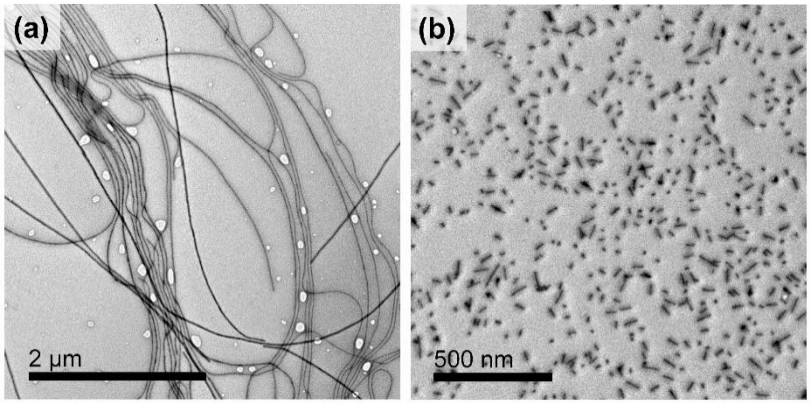

Figure 2.2 TEM images of (a) polydisperse 1D micelles prepared by CDSA of PFS_{24}-*b*-$P2VP_{384}$ in *i*PrOH at 5 mg/mL after solvent evaporation and (b) low dispersity 1D seed micelles prepared by sonication and subsequent annealing of polydisperse PFS_{24}-*b*-$P2VP_{384}$ micelles in *i*PrOH at 5 mg/mL (L_n = 26 nm, L_w/L_n = 1.19). Solution samples of 1 mg/mL were drop-cast and imaged after solvent evaporation. Scale bars: (a) 2 µm, (b) 500 nm.

2.3.3 Growth of 2D Platelet Micelles via Living CDSA of Phosphonium-Capped PFS Homopolymers with a Surfactant Counteranion at Low Concentration (0.01 wt%)

With the aim of improving the colloidal stability and thus scalability of 2D platelets based on phosphonium-capped PFS homopolymers, we selected surfactant counteranions, $[SDS]^-$ and $[AOT]^-$ (**Figure 2.1**a), in addition to iodide for our study. It is well known that gold nanoparticles are stabilized by the adsorption of surfactants, through imparting an effective charge on the nanoparticle as well as by providing steric stabilization.[65–68] To extend this concept to 2D polymer-based nanoparticles, the seeded growth of $PFS_{23}[PPh_2Me]I$, $PFS_{23}[PPh_2Me]SDS$ and $PFS_{23}[PPh_2Me]AOT$ from short cylindrical PFS_{24}-*b*-$P2VP_{384}$ seeds (L_n = 26 nm, L_w/L_n = 1.19) was investigated. Unimer solutions (10 mg/mL) of the respective phosphonium-capped homopolymers were prepared in THF, then injected into solutions of PFS_{24}-*b*-$P2VP_{384}$ seed micelles in *i*PrOH with vigorous mixing by use of a vortex mixer for 3 s (**Figure 2.3**a). Vigorous mixing was found to be essential to access low dispersity structures and did not induce any structural defects (**Figure S2.7**). Each of the self-assembly experiments led to a final solution concentration of 0.1 mg/mL (0.01 wt%), ca. 5 times higher than typically reported for the 2D living CDSA of BCPs. The solutions were aged for 24 h prior to characterization by TEM. By this method, low dispersity 2D platelet micelles could be obtained in which the platelet area (A_n) was found to be linearly dependent on the unimer-to-seed mass ratio (m_{unimer}/m_{seed}) (**Figure 2.3**b). The platelet contour areas and corresponding TEM images and histograms are shown in **Tables S2.2**–**S2.4** and **Figures S2.8–S2.13**, respectively. All dispersities, in both the platelet areas (A_w/A_n) and aspect ratios (R_w/R_n), were found to be below 1.03, demonstrating the size and dimensional control associated with this protocol.

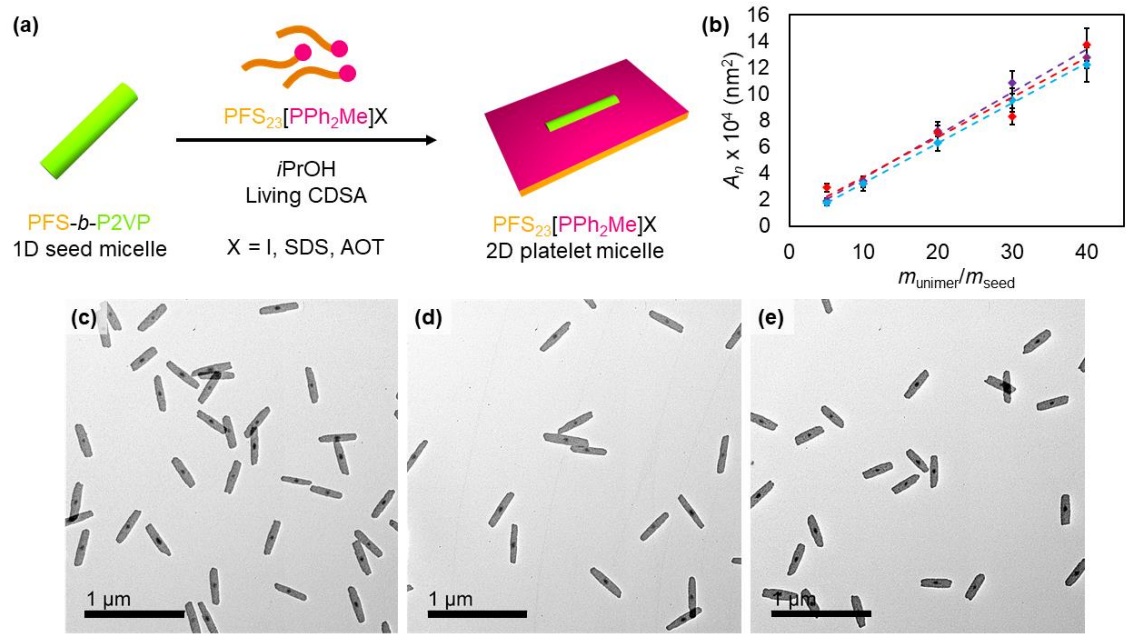

Figure 2.3 (a) Schematic representation for the formation of uniform 2D platelet micelles by the living CDSA of $PFS_{23}[PPh_2Me]X$ (X = I, SDS or AOT) from cylindrical PFS_{24}-*b*-$P2VP_{384}$ seeds. (b) Linear dependence of $PFS_{23}[PPh_2Me]X$ platelet area (A_n) on unimer-to-seed mass ratio (m_{unimer}/m_{seed}) at 0.01 wt% in *i*PrOH for X = I (purple), SDS (blue), AOT (red). Error bars represent the standard deviation of measured areas. Representative TEM images of (c) $PFS_{23}[PPh_2Me]I$, (e) $PFS_{23}[PPh_2Me]SDS$ and (e) $PFS_{23}[PPh_2Me]AOT$ platelet micelles formed by seeded growth from PFS_{24}-*b*-$P2VP_{384}$ 1D seed micelles (L_n = 26 nm, L_w/L_n = 1.19) in *i*PrOH at 0.01 wt% and m_{unimer}/m_{seed} = 10. Scale bars: 1 µm.

Interestingly, at any given m_{unimer}/m_{seed} value, the self-assembly behaviour under the low concentration conditions studied (0.01 wt%) did not appear to be significantly affected by changing the counteranion from iodide to the more bulky, hydrophobic surfactant anions $[SDS]^-$ and $[AOT]^-$. For example, there were no notable changes in platelet area (A_n), length (L_n), width (W_n) and thus aspect ratio (R_n) on switching the counteranion (**Figures 2.3**c–e and **S2.14**). This suggests that, as previously observed,[28] the counteranion plays an insignificant role in the self-assembly

process for phosphonium-terminated PFS homopolymers at a concentration of 0.01 wt% and thus has a negligible effect on the final 2D structure.

As previously observed for 2D nanostructures formed from the living CDSA of PFS-containing amphiphiles initiated using 1D seeds,[28,29,31] the platelet R_n value decreases on increasing the m_{unimer}/m_{seed} value. In the present work, this was found to correspond to a more significant increase in platelet width (ca. 32% increase) with respect to length (ca. 20% increase) for every 10 equivalents of unimer added, independent of the counteranion present (**Figure S2.14**). These observations indicate that PFS crystal growth from the lateral edges of the nanostructure is increasingly favoured over that from the terminal core-solvent interface as the m_{unimer}/m_{seed} value increases. This is likely an effect arising from the distinct self-assembly preferences of the 1D seed and added unimer. Due to the presence of coronal P2VP chains in the 1D seed, initial growth of the phosphonium-capped PFS unimer would be expected to occur exclusively at the two seed termini.[59] On the other hand, as the phosphonium cap does not lead to the same steric inhibition of lateral growth as the P2VP corona present in the seed, CDSA of $PFS_{23}[PPh_2Me]X$ is known to favour the formation of 2D platelets.[28] Thus, an increase in competitive growth in the lateral versus the terminal direction would be anticipated as the amount of added $PFS_{23}[PPh_2Me]X$ unimer (and as the m_{unimer}/m_{seed} value) increases. Our studies indicate that this results in platelet R_n values which are relatively low (ca. 2.7–3.7) at high m_{unimer}/m_{seed} ratios (**Figure S2.14**c).

2.3.4 Growth of 2D Platelet Micelles at Higher Concentrations (0.1–0.4 wt%)

2.3.4.1 Effect of Concentration on the Living CDSA of $PFS_{23}[PPh_2Me]X$

The effect of concentration on the seeded growth of $PFS_{23}[PPh_2Me]I$, $PFS_{23}[PPh_2Me]SDS$ and $PFS_{23}[PPh_2Me]AOT$ from 1D PFS_{24}-*b*-$P2VP_{384}$ seeds (L_n = 26 nm, L_w/L_n = 1.19) was probed. As before, unimer solutions (10 mg/mL) of the phosphonium-capped homopolymers were prepared in

THF and were added to seed micelles in *i*PrOH and aged for 24 h prior to characterization by TEM. The final self-assembly solutions were prepared at concentrations between 1 and 4 mg/mL (0.1–0.4 wt%) and were analysed both in solution by dynamic light scattering (DLS) and after solvent evaporation by TEM. Vigorous mixing was again found to be essential to obtain good structure fidelity and low size-dispersity of the resultant platelets (**Figure S2.7**), suggesting that the unimer addition occurs very rapidly at these higher concentrations.

At concentrations of up to 0.2 wt%, it appears both the counteranion and living CDSA concentration have little effect on the self-assembly process, since the platelet area, length, width, and aspect ratio are comparable to those obtained at 0.01 wt% (**Figures 2.4**, **2.5**, and **S2.14**, and **Tables S2.5**–**S2.7**). For example, PFS_{23}[PPh_2Me]SDS platelets prepared at 0.2 wt% (A_n = 325 x 10^2 nm^2, A_w/A_n = 1.07, R_n = 3.7, R_w/R_n = 1.02) are comparable with the analogous platelets formed at 0.01 wt% (A_n = 320 x 10^2 nm^2, A_w/A_n = 1.03, R_n = 5.1, R_w/R_n = 1.02) (**Tables S2.3** and **S2.6**).

At 2D living CDSA concentrations above 0.3 wt%, however, the choice of counteranion was found to be crucial with respect to platelet colloidal stability and the degree of structure fidelity (**Figures 2.5** and **S2.14**). At these concentrations, optimal control over platelet structure fidelity was obtained when [SDS]$^-$ was used as the counteranion. From the TEM images shown in **Figure 2.4**, it is evident that the platelet structure fidelity generally decreases on increasing the concentration. It should be noted, however, that although there is an increase in area-dispersity with increasing concentration (**Tables S2.5**–**S2.7**), platelet size analysis was carried out by approximating the micelles as "perfect" rectangles. Values of A_n are therefore overestimated at higher concentrations as the platelet morphology diverges from a rectangle towards a more rounded, lenticular-like morphology. This compromise in accuracy of the size measurements contributes to the increase in area-dispersity of PFS_{23}[PPh_2Me]SDS platelets from A_w/A_n = 1.01 (at 0.01 wt%) to A_w/A_n = 1.24 (at 0.4 wt%), for example. Again, vigorous mixing was found to be essential in accessing the lowest dispersity nanostructures due to rapid self-assembly at high concentrations.

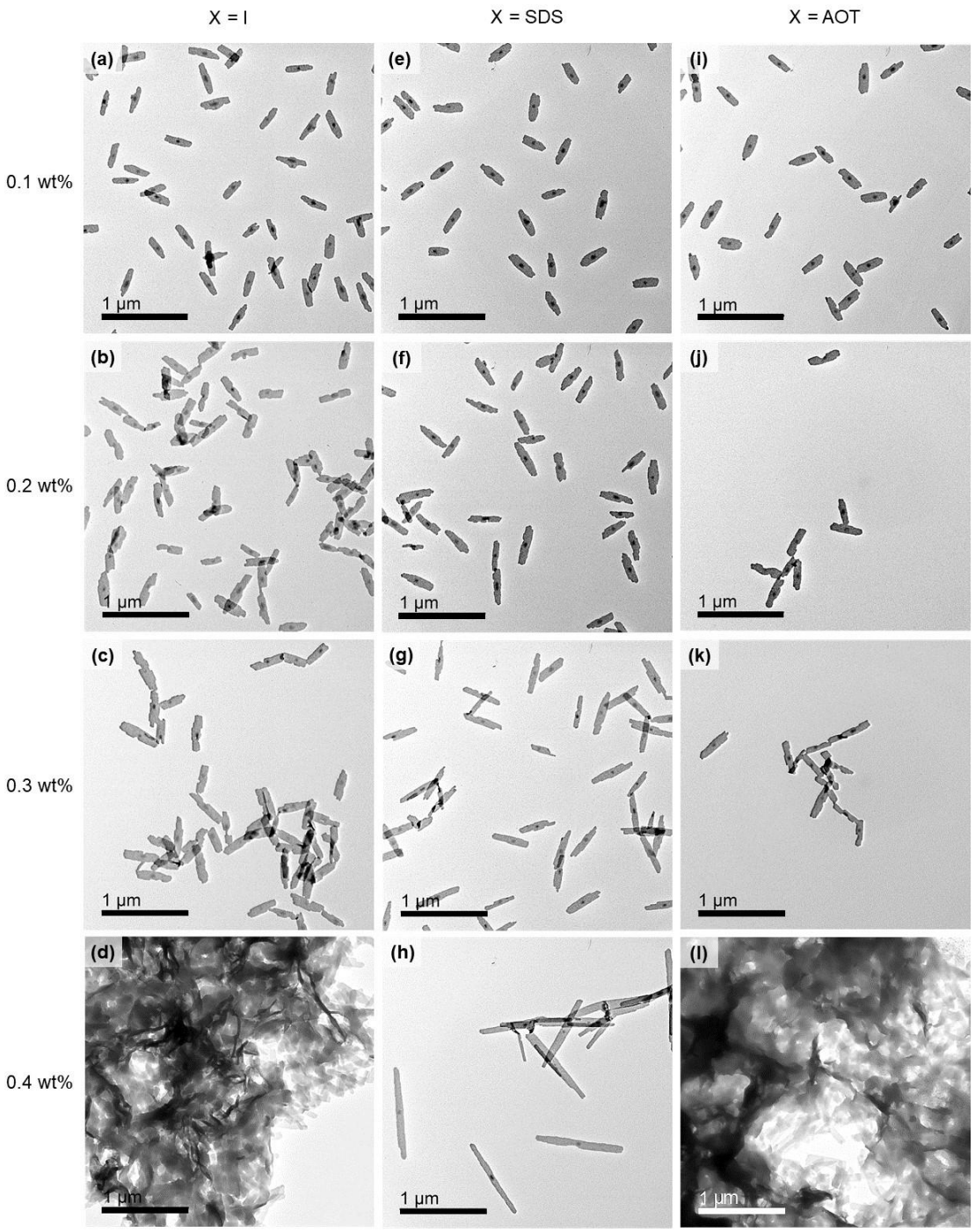

Figure 2.4 Representative TEM images of (a)–(d) $PFS_{23}[PPh_2Me]I$, (e)–(h) $PFS_{23}[PPh_2Me]SDS$ and (i)–(l) $PFS_{23}[PPh_2Me]AOT$ platelet micelles formed through seeded growth from PFS_{24}-*b*-

P2VP$_{384}$ 1D micelles (L_n = 26 nm, L_w/L_n = 1.19) in *i*PrOH at m_{unimer}/m_{seed} = 10 and at various concentrations (0.1–0.4 wt%). Scale bars: 1 μm.

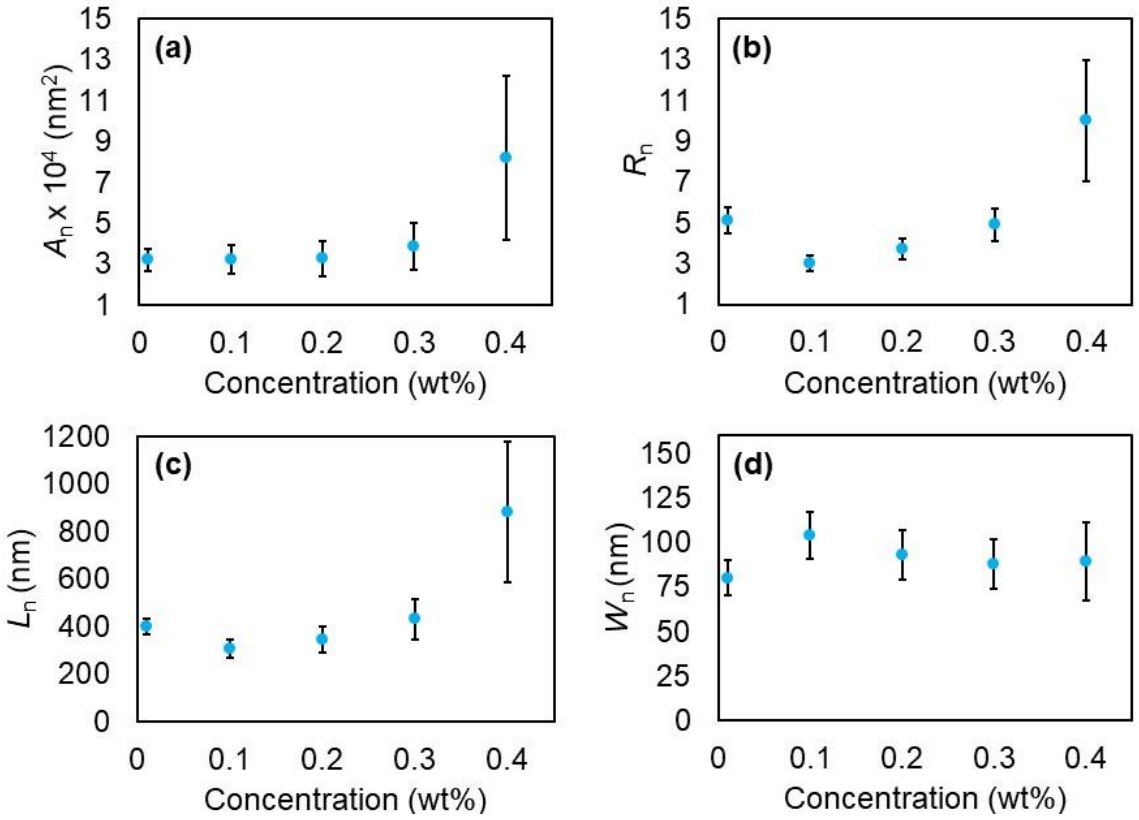

Figure 2.5 Dependence of PFS$_{23}$[PPh$_2$Me]SDS platelet (a) number-average area (A_n), (b) number-average aspect ratio (R_n), (c) number-average length (L_n), and (d) number-average width (W_n) on concentration (0.01–0.4 wt%) of the 2D living CDSA experiments in *i*PrOH. PFS$_{23}$[PPh$_2$Me]SDS platelets were formed through seeded growth from PFS$_{24}$-*b*-P2VP$_{384}$ 1D micelles (L_n = 26 nm, L_w/L_n = 1.19) in *i*PrOH at m_{unimer}/m_{seed} = 10. Error bars represent the standard deviation.

The divergence from rectangular towards a lenticular-like morphology at higher concentrations suggests that polycrystalline platelets are formed, rather than structures with a single crystalline core.[59] This was confirmed by Selected-Area Electron Diffraction (SAED) analysis of PFS$_{23}$[PPh$_2$Me]SDS platelets prepared at 0.4 wt% which showed the presence of four pairs of

diffraction arcs at several locations along the platelet micelle (**Figure 2.6**c, e–g, and i), with the lack of a clear quasi-hexagonal diffraction pattern in all diffraction patterns (**Figure 2.6**b–i). This result indicates that the PFS core exists in a polycrystalline state under these living CDSA conditions.[59] The formation of polycrystalline PFS might be explained by an increased rate of self-assembly and crystallization as the concentration is increased.

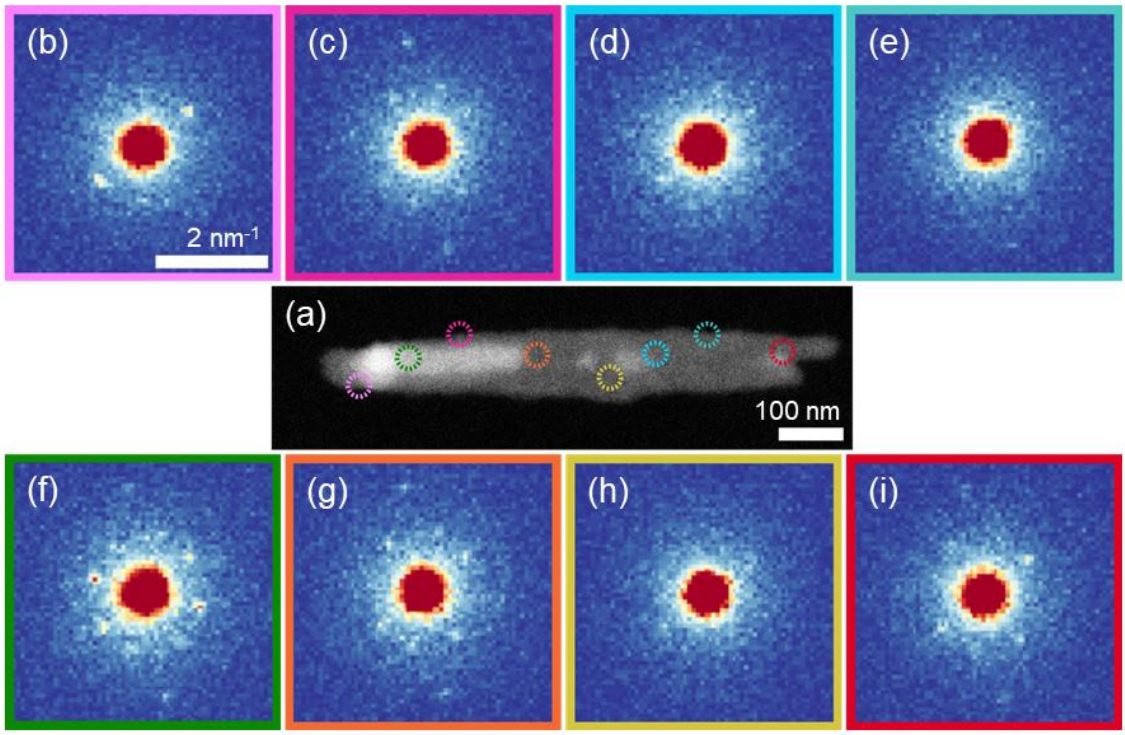

Figure 2.6 (a) Low-angle annular dark field (LAADF) image of PFS_{23}[PPh_2Me]SDS platelet micelle formed through seeded growth from PFS_{24}-*b*-$P2VP_{384}$ 1D micelles (L_n = 26 nm, L_w/L_n = 1.19) in *i*PrOH at 0.4 wt% and m_{unimer}/m_{seed} = 10 and (b)–(i) the corresponding arc-type SAED patterns of different regions along the platelet micelle. Coloured circles indicate the beam location (beam size = 70 nm) at which data was collected for the corresponding SAED experiments. Scale bars: (a) 100 nm, (b)–(i) 2 nm^{-1}.

In the case of R_n, a general increase with concentration was observed (**Figures 2.5**b and **S2.14**). This is a result of a more significant increase in platelet length compared with width on increasing

the concentration of the 2D living CDSA experiments (**Figures 2.5**c, d and **S2.14**). This suggests that as the concentration of the self-assembly solution increases, the growth kinetics shift to favour polycrystalline lenticular micelles whereby unimer deposition at the seed termini parallel to the seed long-axis (longitudinal growth) is favoured in comparison to lateral growth.[59] This is corroborated by our observation of the formation of higher aspect ratio lenticular-like polycrystalline platelets rather than a low aspect ratio rectangular morphology with increasing solution concentration (**Figures 2.4** and **2.6**).

The phenomenon of favoured longitudinal growth from the 1D seed has previously been observed in several similar systems. For example, addition of platelet-forming BCP to 1D seeds initially yields dumbbell-like micelles through preferential growth from the seed termini. Further addition of unimer results in the formation of lenticular platelets through encapsulation of the seed.[24] A preferential longitudinal growth direction has also been observed in 2D living CDSA systems which involve seeded growth of either a charge-terminated homopolymer or a BCP/homopolymer blend from 1D seeds. In these examples, the preferential growth direction can be visualized by the formation of segmented block comicelle platelets, where the platelet L_n is observed to increase more significantly than the corresponding value of W_n with each unimer addition.[28,29,31,32] Furthermore, when a BCP/homopolymer blend is employed in the form of unimers, crystallization of the homopolymer (which is expected to occur faster than that of the BCP) is observed predominantly in the longitudinal direction of the seed.[31] Similarly, the addition of cylinder-forming BCP to 2D micelles prepared via living CDSA results in the formation of hierarchical structures whereby cylinders grow preferentially along the seed long-axis.[35,41,69,70] Previous studies also show that platelets prepared by the CDSA of polyisoprene-*b*-PFS (with a corona-to-core block ratio of 1) in the absence of seeds are observed to form elongated tape-like sheets as opposed to low aspect ratio structures, suggesting that there is a preferred growth direction along one axis of the polymer crystal.[22,70] Considering our results and the aforementioned previous studies, we

believe that the observed preference for crystal growth in the longitudinal direction is a result of the relative kinetics of PFS core crystallization from different facets, and that this is affected by solution concentration.[71]

2.3.4.2 Comparison with Platelets Prepared by the 2D Living CDSA of PFS_{20}-*b*-$P2VP_{19}$ at Higher Concentrations

For comparison, we investigated the seeded growth of a BCP, PFS_{20}-*b*-$P2VP_{19}$, from the same 1D PFS_{24}-*b*-$P2VP_{384}$ seed micelles (L_n = 26 nm, L_w/L_n = 1.19) and under the same self-assembly conditions (m_{unimer}/m_{seed} = 10, 0.01–0.4 wt% in *i*PrOH). PFS_{20}-*b*-$P2VP_{19}$ was selected for this study since it exhibits a very low block ratio and is therefore expected to favour the formation of platelets,[19–22] as well as having a PFS segment of comparable DP_n to that of the initially studied phosphonium-capped homopolymers, $[PFS_{23}PPh_2Me]X$. The living CDSA procedure was carried out in the same way as previously described, notably involving unimer addition to the seeds with vigorous mixing to obtain nanostructures with the lowest accessible size-dispersity. Ill-defined lenticular-like platelets with relatively high aspect ratios (R_n = 4.6–6.8) were obtained under all concentrations studied (**Figure S2.15** and **Table S2.8**). Although these nanostructures exhibited similar dispersities in both the platelet area (A_w/A_n = 1.05–1.20) and aspect ratio (R_w/R_n = 1.04–1.08) compared with those formed from $PFS_{23}[PPh_2Me]X$ (A_w/A_n = 1.01–1.24, R_w/R_n = 1.01–1.09), lower dispersity structures were accessed from the latter (A_w/A_n < 1.04, R_w/R_n < 1.03). This suggests that the presence of a polar phosphonium-counteranion pair at the terminus of the PFS homopolymer promotes more controlled growth compared to that of a coronal block under these high concentration conditions.

2.3.4.3 $PFS_{23}[PPh_2Me]X$ Platelet Defect Formation with Increasing Concentration

As the 2D living CDSA concentration is increased, an increasing number of defects were observed. The most common type of defect appeared to be a result of platelet "fusion" (**Figure S2.16**a). This defect occurs more frequently at higher concentrations, being present in up to 7% of $PFS_{23}[PPh_2Me]X$ nanostructures formed at 0.1 wt%, 2–33% at 0.2 wt%, 13–40% at 0.3 wt%, and in 38% (X = SDS) at 0.4 wt%. At all concentrations, $PFS_{23}[PPh_2Me]SDS$ platelets exhibit the lowest percentage of fusion defects compared with that of $PFS_{23}[PPh_2Me]I$ and $PFS_{23}[PPh_2Me]AOT$ (0 vs. 7% at 0.1 wt%, 2 vs. 14 and 33% at 0.2 wt%, 13 vs. 32 and 40% at 0.3 wt%) (**Figure S2.16**b). A similar fusion phenomenon has previously been observed in the end-to-end coupling of cylindrical micelles with a crystalline PFS core on addition of PFS homopolymer.[72] Since the frequency of this type of defect increases with concentration, we believe that the occurrence of platelet fusion is due to both a decrease in the average distance between the growing platelet micelles as well as an increased rate of self-assembly and unimer growth,[71] making a fusion event more probable.

Platelet fragmentation, which also contributes to producing nanostructure defects, similarly appears to be more common at higher self-assembly concentrations (**Figure S2.16**c). However, this is thought to be a result of the formation of higher aspect ratios at increased concentration. Higher aspect ratio platelets would be more susceptible to fragmentation under the shear forces experienced on vigorous mixing during self-assembly and also upon sample drying before TEM analysis.[25]

Platelet formation by living CDSA (m_{unimer}/m_{seed} = 10) was probed by DLS (**Figures S2.17** and **S2.18**, and **Table S2.9**) to determine whether fragmentation occurs in solution and/or on solvent evaporation during TEM sample preparation. It should be noted that the apparent hydrodynamic

radius ($R_{H,app}$) measured in DLS is the diameter of a sphere that has the same translational diffusion coefficient as the particle in question.[73] Although the absolute $R_{H,app}$ values for anisotropic $PFS_{23}[PPh_2Me]X$ platelets are not insightful, the relative values can provide a useful indication of comparative size of the nanostructures. L_n was determined by TEM size-analysis for $PFS_{23}[PPh_2Me]X$ platelets (**Table S2.10**) to provide insight into the significance of any changes in $R_{H,app}$ on increasing concentration. From TEM size-analysis, $PFS_{23}[PPh_2Me]X$ platelets are comparable in length at all concentrations except 0.4 wt%, where data could only be obtained for X = SDS (L_n = 306–432 nm) (**Table S2.10**). By DLS, the platelets prepared at 0.1 and 0.2 wt% exhibit $R_{H,app}$ values of 2127–3274 nm (**Figures S2.17**a, b, **S2.18**a, b, and **Table S2.9**). Although dissimilar in comparison with L_n values from TEM (**Table S2.10**), this suggests that there is little difference in the platelet size, suggesting fragmentation is negligible at these concentrations. At 0.3 wt%, a significant variation in $R_{H,app}$ is observed. $PFS_{23}[PPh_2Me]I$ platelets exhibit the lowest value ($R_{H,app}$ = 1162 ± 417 nm) compared with $PFS_{23}[PPh_2Me]AOT$ ($R_{H,app}$ = 2618 ± 158 nm) and $PFS_{23}[PPh_2Me]SDS$ ($R_{H,app}$ = 3991 ± 939 nm) (**Figures S2.17**c and **S2.18**c). Similarly, at 0.4 wt%, the $R_{H,app}$ of $PFS_{23}[PPh_2Me]I$ platelets was found to be 270 ± 160 nm, which is considerably smaller than that of $PFS_{23}[PPh_2Me]SDS$ ($R_{H,app}$ = 1081 ± 57 nm) and $PFS_{23}[PPh_2Me]AOT$ ($R_{H,app}$ = 2314 ± 273 nm) (**Figures S2.17**d and **S2.18**d). These results are indicative that $PFS_{23}[PPh_2Me]I$ platelet fragmentation occurs in solution at 0.3 and 0.4 wt% to a higher degree than that in the presence of surfactant counteranions. The $R_{H,app}$ value for $PFS_{23}[PPh_2Me]SDS$ at 0.4 wt% is significantly decreased compared with lower concentrations, suggesting that platelet fragmentation occurs under these conditions. Since $PFS_{23}[PPh_2Me]SDS$ platelets exhibit an increased aspect ratio at 0.4 wt%, it is likely that an increased susceptibility to fragmentation under shear forces results in this defect occurring.[25]

There was little evidence for self-nucleation apparent by TEM at any of the concentrations studied. Depending on the counteranion, over 93–97% of the platelets appear to possess a clear electron

dense PFS_{24}-*b*-$P2VP_{384}$ seed in the center (**Figure S2.16**d). In the few cases in which the seed cannot be observed, self-nucleation may still be absent, as platelet fragmentation during vigorous mixing or TEM sample preparation could explain the presence of the seedless structures.

In order to minimize structural defects and dispersities in size and aspect ratio, the use of surfactant counteranions, $[SDS]^-$ or $[AOT]^-$, appears to be essential. This is thought to be due to both the imparted polarity as well as the increased solubilising effect of the surfactants compared with the iodide counteranion.[28] By TEM and DLS, platelets formed from $PFS_{23}[PPh_2Me]SDS$ appear to be the most colloidally stable at higher concentrations (**Figures 2.4**h, **S2.17**, and **S2.18**), due to the minimal aggregation detected after solvent evaporation, and these also exhibit the least number of structural defects (**Figure S2.16**). This suggests that the solubilising effect of the surfactant $[SDS]^-$ is larger compared with that of $[AOT]^-$.

2.3.4.4 Effect of Temperature on the Living CDSA of $PFS_{23}[PPh_2Me]X$

To further investigate the parameters which impact the living CDSA of phosphonium-capped PFS homopolymers from 1D seeds, the effect of temperature (40 ºC) was investigated. On increasing the temperature at which 2D living CDSA was performed from room temperature (22 ºC) to 40 ºC, an improvement in structure fidelity is observed only in the case of the phosphonium-capped homopolymers with surfactant counteranions (**Figures 2.7**, **S2.19**, and **Table S2.11**). Thus, in the case of $PFS_{23}[PPh_2Me]I$, there appeared to be no significant change in the structure fidelity or presence of aggregation (**Figure S2.19**a, d). Performing the living CDSA of $PFS_{23}[PPh_2Me]SDS$ at room temperature (22 ºC) and 0.4 wt%, we observed the formation of polydisperse, high aspect ratio platelets (A_w/A_n = 1.24, R_n = 10.0) (**Figures 2.4**h and **S2.19**b). However, when the self-assembly temperature was increased to 40 ºC there appeared to be more control over the self-assembly process at this higher concentration. Lower dispersity platelets which exhibit a significantly reduced aspect ratio were formed (A_w/A_n = 1.12, R_n = 4.6) (**Figures 2.7**a and **S2.19**e), despite the living CDSA concentration being 200 times higher than that previously reported for

BCP systems and 40 times higher than that of charge-terminated homopolymers.[24,28] The reduction in aspect ratio at 40 ºC is a result of a 43% decrease in platelet length (from L_n = 880 to 500 nm) and a 22% increase in platelet width (from W_n = 90 to 110 nm) compared with platelets prepared at 22 ºC. Similarly, the living CDSA of PFS_{23}[PPh_2Me]AOT at room temperature (22 ºC) yielded aggregates for which size analysis could not be performed by TEM (**Figures 2.4**i and **S2.19**c). Performing the living CDSA of PFS_{23}[PPh_2Me]AOT at 40 °C, however, improved the structure fidelity significantly and yielded low dispersity platelets (A_w/A_n = 1.10, R_n = 4.5) (**Figures 2.7**b and **S2.19**f). Increasing the temperature at which self-assembly is performed is believed to slow the core crystal growth rate,[71] leading to more efficient crystallization. Plasticization of the PFS core at elevated temperatures may also facilitate core crystallization.[35]

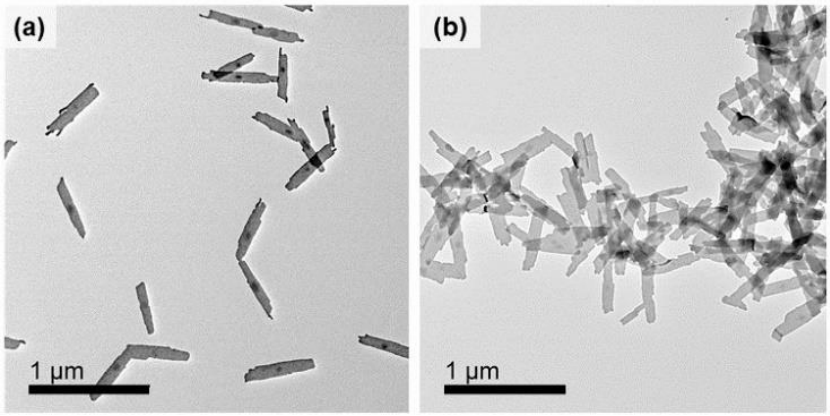

Figure 2.7 Representative TEM images of (a) PFS_{23}[PPh_2Me]SDS and (b) PFS_{23}[PPh_2Me]AOT platelet micelles formed through high concentration (0.4 wt%) seeded growth at 40 ºC from PFS_{24}-*b*-$P2VP_{384}$ 1D micelles (L_n = 26 nm, L_w/L_n = 1.19) in *i*PrOH at m_{unimer}/m_{seed} = 10. Scale bars: 1 μm.

2.4 Summary

We report a significant improvement in the scalability of low dispersity 2D platelets prepared via living CDSA of phosphonium-capped PFS homopolymers with surfactant counteranions, PFS_{23}[PPh_2Me]SDS and PFS_{23}[PPh_2Me]AOT, from 1D seeds. At room temperature (22 ºC),

increasing the 2D self-assembly concentration beyond 0.2 wt% resulted in a decrease in the platelet structure fidelity as well as an increase in the frequency of structural defects, such as fragmentation or fusion. Further to this, higher aspect ratio polydisperse lenticular-like platelets were formed. In these cases, performing the 2D living CDSA at 40 °C, rather than 22 °C, was found to improve the size-control, dispersity, and fidelity of the platelets. This is likely due to higher PFS core chain mobility as well as a decrease in the living CDSA rate at elevated temperatures, which facilitates controlled crystallization of the core.[35,71] At higher concentrations, the use of a surfactant counteranion, particularly $[SDS]^-$, was found to allow improved size-control and colloidal stability. This proof-of-concept work also provides fundamental understanding of the factors that influence the scale-up of 2D living CDSA, including defect formation.

2.5 References

(1) Zu, S.; Bao, Y.; Fang, Z. Planar Plasmonic Chiral Nanostructures. *Nanoscale* **2016**, *8* (7), 3900–3905.

(2) Huang, X.; Tang, S.; Mu, X.; Dai, Y.; Chen, G.; Zhou, Z.; Ruan, F.; Yang, Z.; Zheng, N. Freestanding Palladium Nanosheets with Plasmonic and Catalytic Properties. *Nat. Nanotechnol.* **2011**, *6*, 28–32.

(3) Zhuang, X.; Mai, Y.; Wu, D.; Zhang, F.; Feng, X. Two-Dimensional Soft Nanomaterials: A Fascinating World of Materials. *Adv. Mater.* **2015**, *27* (3), 403–427.

(4) Boott, C. E.; Nazemi, A.; Manners, I. Synthetic Covalent and Non-Covalent 2D Materials. *Angew. Chem. Int. Ed.* **2015**, *54* (47), 13876–13894.

(5) Mai, Y.; Eisenberg, A. Self-Assembly of Block Copolymers. *Chem. Soc. Rev.* **2012**, *41* (18), 5969–5985.

(6) Tritschler, U.; Pearce, S.; Gwyther, J.; Whittell, G. R.; Manners, I. 50th Anniversary Perspective: Functional Nanoparticles from the Solution Self-Assembly of Block Copolymers. *Macromolecules* **2017**, *50* (9), 3439–3463.

(7) Inam, M.; Jones, J. R.; Pérez-Madrigal, M. M.; Arno, M. C.; Dove, A. P.; O'Reilly, R. K. Controlling the Size of Two-Dimensional Polymer Platelets for Water-in-Water

Emulsifiers. *ACS Cent. Sci.* **2018**, *4* (1), 63–70.

(8) Dong, B.; Zhou, T.; Zhang, H.; Li, C. Y. Directed Self-Assembly of Nanoparticles for Nanomotors. *ACS Nano* **2013**, *7* (6), 5192–5198.

(9) Hu, Y.; Wu, K.-Y.; Zhu, T.; Shen, P.; Zhou, Y.; Li, X.; Wang, C.-L.; Tu, Y.; Li, C. Y. Unique Supramolecular Liquid-Crystal Phases with Different Two-Dimensional Crystal Layers. *Angew. Chem. Int. Ed.* **2018**, *57* (41), 13454–13458.

(10) Mei, S.; Li, C. Y. Terraced and Smooth Gradient Polymer Brushes via a Polymer Single-Crystal Assisted Grafting-To Method. *Angew. Chem. Int. Ed.* **2018**, *57* (48), 15758–15761.

(11) Hailes, R. L. N.; Oliver, A. M.; Gwyther, J.; Whittell, G. R.; Manners, I. Polyferrocenylsilanes: Synthesis, Properties, and Applications. *Chem. Soc. Rev.* **2016**, *45* (19), 5358–5407.

(12) Massey, J. A.; Temple, K.; Cao, L.; Rharbi, Y.; Raez, J.; Winnik, M. A.; Manners, I. Self-Assembly of Organometallic Block Copolymers: The Role of Crystallinity of the Core-Forming Polyferrocene Block in the Micellar Morphologies Formed by Poly(Ferrocenylsilane-b-Dimethylsiloxane) in n-Alkane Solvents. *J. Am. Chem. Soc.* **2000**, *122* (47), 11577–11584.

(13) Lotz, B.; Kovacs, A. J.; Bassett, G. A.; Keller, A. Properties of Copolymers Composed of One Poly-Ethylene-Oxide and One Polystyrene Block - II. Morphology of Single Crystals. *Kolloid-Zeitschrift Zeitschrift für Polym.* **1966**, *209* (2), 115–128.

(14) Chen, W. Y.; Li, C. Y.; Zheng, J. X.; Huang, P.; Zhu, L.; Ge, Q.; Quirk, R. P.; Lotz, B.; Deng, L.; Wu, C.; Thomas, E. L.; Cheng, S. Z. D. "Chemically Shielded" Poly(Ethylene Oxide) Single Crystal Growth and Construction of Channel-Wire Arrays with Chemical and Geometric Recognitions on a Submicrometer Scale. *Macromolecules* **2004**, *37* (14), 5292–5299.

(15) Arno, M. C.; Inam, M.; Coe, Z.; Cambridge, G.; Macdougall, L. J.; Keogh, R.; Dove, A. P.; O'Reilly, R. K. Precision Epitaxy for Aqueous 1D and 2D Poly(ϵ-Caprolactone) Assemblies. *J. Am. Chem. Soc.* **2017**, *139* (46), 16980–16985.

(16) Yu, W.; Foster, J. C.; Dove, A. P.; O'Reilly, R. K. Length Control of Biodegradable Fiber-Like Micelles via Tuning Solubility: A Self-Seeding Crystallization-Driven Self-Assembly of Poly(ε-Caprolactone)-Containing Triblock Copolymers. *Macromolecules* **2020**, *53* (4),

1514–1521.

(17) He, Y.; Eloi, J.-C.; Harniman, R. L.; Richardson, R. M.; Whittell, G. R.; Mathers, R. T.; Dove, A. P.; O'Reilly, R. K.; Manners, I. Uniform Biodegradable Fiber-Like Micelles and Block Comicelles via "Living" Crystallization-Driven Self-Assembly of Poly(L-Lactide) Block Copolymers: The Importance of Reducing Unimer Self-Nucleation via Hydrogen Bond Disruption. *J. Am. Chem. Soc.* **2019**, *141* (48), 19088–19098.

(18) Schmelz, J.; Karg, M.; Hellweg, T.; Schmalz, H. General Pathway toward Crystalline-Core Micelles with Tunable Morphology and Corona Segregation. *ACS Nano* **2011**, *5* (12), 9523–9534.

(19) Wang, J.; Zhu, W.; Peng, B.; Chen, Y. A Facile Way to Prepare Crystalline Platelets of Block Copolymers by Crystallization-Driven Self-Assembly. *Polymer* **2013**, *54*, 6760–6767.

(20) Han, L.; Wang, M.; Jia, X.; Chen, W.; Qian, H.; He, F. Uniform Two-Dimensional Square Assemblies from Conjugated Block Copolymers Driven by π-π Interactions with Controllable Sizes. *Nat. Commun.* **2018**, *9*, 865.

(21) Wang, J.; Lu, Y.; Chen, Y. Fabrication of 2D Surface-Functional Polymer Platelets via Crystallization-Driven Self-Assembly of Poly(ε-Caprolactone)-Contained Block Copolymers. *Polymer* **2019**, *160*, 196–203.

(22) Cao, L.; Manners, I.; Winnik, M. A. Influence of the Interplay of Crystallization and Chain Stretching on Micellar Morphologies: Solution Self-Assembly of Coil-Crystalline Poly(Isoprene-Block-Ferrocenylsilane). *Macromolecules* **2002**, *35* (22), 8258–8260.

(23) Gilroy, J. B.; Gädt, T.; Whittell, G. R.; Chabanne, L.; Mitchels, J. M.; Richardson, R. M.; Winnik, M. A.; Manners, I. Monodisperse Cylindrical Micelles by Crystallization-Driven Living Self-Assembly. *Nat. Chem.* **2010**, *2*, 566–570.

(24) Hudson, Z. M.; Boott, C. E.; Robinson, M. E.; Rupar, P. A.; Winnik, M. A.; Manners, I. Tailored Hierarchical Micelle Architectures Using Living Crystallization-Driven Self-Assembly in Two Dimensions. *Nat. Chem.* **2014**, *6*, 893–898.

(25) Guerin, G.; Wang, H.; Manners, I.; Winnik, M. A. Fragmentation of Fiberlike Structures: Sonication Studies of Cylindrical Block Copolymer Micelles and Behavioral Comparisons to Biological Fibrils. *J. Am. Chem. Soc.* **2008**, *130* (44), 14763–14771.

(26) Wang, X.; Manners, I.; Winnik, M. A. Cylindrical Block Copolymer Micelles and Co-Micelles of Controlled Length and Architecture. *Science* **2007**, *317* (5838), 644–648.

(27) Finnegan, J. R.; He, X.; Street, S. T. G.; Garcia-Hernandez, J. D.; Hayward, D. W.; Harniman, R. L.; Richardson, R. M.; Whittell, G. R.; Manners, I. Extending the Scope of "Living" Crystallization-Driven Self Assembly: Well-Defined 1D Micelles and Block Comicelles from Crystallizable Polycarbonate Block Copolymers. *J. Am. Chem. Soc.* **2018**, *140* (49), 17127–17140.

(28) He, X.; Hsiao, M.-S.; Boott, C. E.; Harniman, R. L.; Nazemi, A.; Li, X.; Winnik, M. A.; Manners, I. Two-Dimensional Assemblies from Crystallizable Homopolymers with Charged Termini. *Nat. Mater.* **2017**, *16*, 481–488.

(29) Pearce, S.; He, X.; Hsiao, M.-S.; Harniman, R. L.; MacFarlane, L. R.; Manners, I. Uniform, High-Aspect-Ratio, and Patchy 2D Platelets by Living Crystallization-Driven Self-Assembly of Crystallizable Poly(Ferrocenyldimethylsilane)-Based Homopolymers with Hydrophilic Charged Termini. *Macromolecules* **2019**, *52* (16), 6068–6079.

(30) He, X.; He, Y.; Hsiao, M.-S.; Harniman, R. L.; Pearce, S.; Winnik, M. A.; Manners, I. Complex and Hierarchical 2D Assemblies via Crystallization-Driven Self-Assembly of Poly(L-Lactide) Homopolymers with Charged Termini. *J. Am. Chem. Soc.* **2017**, *139* (27), 9221–9228.

(31) Qiu, H.; Gao, Y.; Boott, C. E.; Gould, O. E. C.; Harniman, R. L.; Miles, M. J.; Webb, S. E. D.; Winnik, M. A.; Manners, I. Uniform Patchy and Hollow Rectangular Platelet Micelles from Crystallizable Polymer Blends. *Science* **2016**, *352* (6286), 697–702.

(32) Nazemi, A.; He, X.; Macfarlane, L. R.; Harniman, R. L.; Hsiao, M.-S.; Winnik, M. A.; Faul, C. F. J.; Manners, I. Uniform "Patchy" Platelets by Seeded Heteroepitaxial Growth of Crystallizable Polymer Blends in Two Dimensions. *J. Am. Chem. Soc.* **2017**, *139* (12), 4409–4417.

(33) Fukui, T.; Garcia-Hernandez, J. D.; MacFarlane, L. R.; Lei, S.; Whittell, G. R.; Manners, I. Seeded Self-Assembly of Charge-Terminated Poly(3-Hexylthiophene) Amphiphiles Based on the Energy Landscape. *J. Am. Chem. Soc.* **2020**, *142* (35), 15038–15048.

(34) Jin, X.; Price, M. B.; Finnegan, J. R.; Boott, C. E.; Richter, J. M.; Rao, A.; Menke, S. M.; Friend, R. H.; Whittell, G. R.; Manners, I. Long-Range Exciton Transport in Conjugated Polymer Nanofibers Prepared by Seeded Growth. *Science* **2018**, *900* (6391), 897–900.

(35) Inam, M.; Cambridge, G.; Pitto-Barry, A.; Laker, Z. P. L.; Wilson, N. R.; Mathers, R. T.; Dove, A. P.; O'Reilly, R. K. 1D vs. 2D Shape Selectivity in the Crystallization-Driven Self-Assembly of Polylactide Block Copolymers. *Chem. Sci.* **2017**, *8* (6), 4223–4230.

(36) Schmelz, J.; Schedl, A. E.; Steinlein, C.; Manners, I.; Schmalz, H. Length Control and Block-Type Architectures in Worm-like Micelles with Polyethylene Cores. *J. Am. Chem. Soc.* **2012**, *134* (34), 14217–14225.

(37) Shin, S.; Menk, F.; Kim, Y.; Lim, J.; Char, K.; Zentel, R.; Choi, T.-L. Living Light-Induced Crystallization-Driven Self-Assembly for Rapid Preparation of Semiconducting Nanofibers. *J. Am. Chem. Soc.* **2018**, *140* (19), 6088–6094.

(38) Tao, D.; Feng, C.; Cui, Y.; Yang, X.; Manners, I.; Winnik, M. A.; Huang, X. Monodisperse Fiber-like Micelles of Controlled Length and Composition with an Oligo(p-Phenylenevinylene) Core via "Living" Crystallization-Driven Self-Assembly. *J. Am. Chem. Soc.* **2017**, *139* (21), 7136–7139.

(39) Finnegan, J. R.; Pilkington, E.; Alt, K.; Rahim, M. A.; Kent, S. J.; Davis, T. P.; Kempe, K. Stealth Nanorods via the Aqueous Living Crystallisation-Driven Self-Assembly of Poly(2-Oxazoline)S. *Chem. Sci.* **2021**, *12*, 7350–7360.

(40) Yusoff, S. F. M.; Hsiao, M.-S.; Schacher, F. H.; Winnik, M. A.; Manners, I. Formation of Lenticular Platelet Micelles via the Interplay of Crystallization and Chain Stretching: Solution Self-Assembly of Poly(Ferrocenyldimethylsilane)- Block -Poly(2-Vinylpyridine) with a Crystallizable Core-Forming Metalloblock. *Macromolecules* **2012**, *45* (9), 3883–3891.

(41) Presa Soto, A.; Gilroy, J. B.; Winnik, M. A.; Manners, I. Pointed-Oval-Shaped Micelles from Crystalline-Coil Block Copolymers by Crystallization-Driven Living Self-Assembly. *Angew. Chem. Int. Ed.* **2010**, *49* (44), 8220–8223.

(42) Rizis, G.; Van De Ven, T. G. M.; Eisenberg, A. Homopolymers as Structure-Driving Agents in Semicrystalline Block Copolymer Micelles. *ACS Nano* **2015**, *9* (4), 3627–3640.

(43) Canning, S. L.; Smith, G. N.; Armes, S. P. A Critical Appraisal of RAFT-Mediated Polymerization-Induced Self-Assembly. *Macromolecules* **2016**, *49* (6), 1985–2001.

(44) Warren, N. J.; Armes, S. P. Polymerization-Induced Self-Assembly of Block Copolymer Nano-Objects via RAFT Aqueous Dispersion Polymerization. *J. Am. Chem. Soc.* **2014**, *136*

(29), 10174–10185.

(45) Jennings, J.; Cornel, E. J.; Derry, M. J.; Beattie, D. L.; Rymaruk, M. J.; Deane, O. J.; Ryan, A. J.; Armes, S. P. Synthesis of High χ-Low N Diblock Copolymers via Polymerization-Induced Self-Assembly. *Angew. Chem. Int. Ed.* **2020**, *59* (27), 10848–10853.

(46) Qiao, X. G.; Dugas, P.-Y.; Charleux, B.; Lansalot, M.; Bourgeat-Lami, E. Nitroxide-Mediated Polymerization-Induced Self-Assembly of Amphiphilic Block Copolymers with a pH/Temperature Dual Sensitive Stabilizer Block. *Polym. Chem.* **2017**, *8* (27), 4014–4029.

(47) Qiao, X. G.; Lambert, O.; Taveau, J.-C.; Dugas, P.-Y.; Charleux, B.; Lansalot, M.; Bourgeat-Lami, E. Nitroxide-Mediated Polymerization-Induced Self-Assembly of Block Copolymers at the Surface of Silica Particles: Toward New Hybrid Morphologies. *Macromolecules* **2017**, *50* (10), 3796–3806.

(48) Liu, C.; Hong, C.-Y.; Pan, C.-Y. Polymerization Techniques in Polymerization-Induced Self-Assembly (PISA). *Polym. Chem.* **2020**, *11* (22), 3673–3689.

(49) Xu, X.-F.; Pan, C.-Y.; Zhang, W.-J.; Hong, C.-Y. Polymerization-Induced Self-Assembly Generating Vesicles with Adjustable PH-Responsive Release Performance. *Macromolecules* **2019**, *52* (5), 1965–1975.

(50) Boott, C. E.; Gwyther, J.; Harniman, R. L.; Hayward, D. W.; Manners, I. Scalable and Uniform 1D Nanoparticles by Synchronous Polymerization, Crystallization and Self-Assembly. *Nat. Chem.* **2017**, *9*, 785–792.

(51) Oliver, A. M.; Gwyther, J.; Boott, C. E.; Davis, S. A.; Pearce, S.; Manners, I. Scalable Fiber-like Micelles and Block Co-Micelles by Polymerization-Induced Crystallization-Driven Self-Assembly. *J. Am. Chem. Soc.* **2018**, *140* (51), 18104–18114.

(52) Sha, Y.; Rahman, M. A.; Zhu, T.; Cha, Y.; McAlister, C. W.; Tang, C. ROMPI-CDSA: Ring-Opening Metathesis Polymerization-Induced Crystallization-Driven Self-Assembly of Metallo-Block Copolymers. *Chem. Sci.* **2019**, *10* (42), 9782–9787.

(53) Hurst, P. J.; Rakowski, A. M.; Patterson, J. P. Ring-Opening Polymerization-Induced Crystallization-Driven Self-Assembly of Poly-L-Lactide-Block-Polyethylene Glycol Block Copolymers (ROPI-CDSA). *Nat. Commun.* **2020**, *11*, 4690.

(54) Guan, S.; Wen, W.; Yang, Z.; Chen, A. Liquid Crystalline Nanowires by Polymerization Induced Hierarchical Self-Assembly. *Macromolecules* **2020**, *53* (1), 465–472.

(55) Yin, R.; Sahoo, D.; Xu, F.; Huang, W.; Zhou, Y. Scalable Preparation of Crystalline Nanorods through Sequential Polymerization-Induced and Crystallization-Driven Self-Assembly of Alternating Copolymers. *Polym. Chem.* **2020**, *11* (13), 2312–2317.

(56) Guan, S.; Chen, A. One-Pot Synthesis of Cross-Linked Block Copolymer Nanowires via Polymerization-Induced Hierarchical Self-Assembly and Photodimerization. *ACS Macro Lett.* **2020**, *9* (1), 14–19.

(57) Schnitte, M.; Staiger, A.; Casper, L. A.; Mecking, S. Uniform Shape Monodisperse Single Chain Nanocrystals by Living Aqueous Catalytic Polymerization. *Nat. Commun.* **2019**, *10*, 2592.

(58) Guerre, M.; Semsarilar, M.; Godiard, F.; Améduri, B.; Ladmiral, V. Polymerization-Induced Self-Assembly of PVAc-b-PVDF Block Copolymers via RAFT Dispersion Polymerization of Vinylidene Fluoride in Dimethyl Carbonate. *Polym. Chem.* **2017**, *8* (9), 1477–1487.

(59) Hsiao, M.-S.; Yusoff, S. F. M.; Winnik, M. A.; Manners, I. Crystallization-Driven Self-Assembly of Block Copolymers with a Short Crystallizable Core-Forming Segment: Controlling Micelle Morphology through the Influence of Molar Mass and Solvent Selectivity. *Macromolecules* **2014**, *47* (7), 2361–2372.

(60) Wang, H.; Winnik, M. A.; Manners, I. Synthesis and Self-Assembly of Poly(Ferrocenyldimethylsilane-b-2-Vinylpyridine) Diblock Copolymers. *Macromolecules* **2007**, *40* (10), 3784–3789.

(61) Jarrett-Wilkins, C. N.; Musgrave, R. A.; Hailes, R. L. N.; Harniman, R. L.; Faul, C. F. J.; Manners, I. Linear and Branched Fiber-like Micelles from the Crystallization-Driven Self-Assembly of Heterobimetallic Block Copolymer Polyelectrolyte/Surfactant Complexes. *Macromolecules* **2019**, *52* (19), 7289–7300.

(62) Guerin, G.; Molev, G.; Pichugin, D.; Rupar, P. A.; Qi, F.; Cruz, M.; Manners, I.; Winnik, M. A. Effect of Concentration on the Dissolution of One-Dimensional Polymer Crystals: A TEM and NMR Study. *Macromolecules* **2019**, *52* (1), 208–216.

(63) Qian, J.; Lu, Y.; Chia, A.; Zhang, M.; Rupar, P. A.; Gunari, N.; Walker, G. C.; Cambridge, G.; He, F.; Guerin, G.; Manners, I.; Winnik, M. A. Self-Seeding in One Dimension: A Route to Uniform Fiber-like Nanostructures from Block Copolymers with a Crystallizable Core-Forming Block. *ACS Nano* **2013**, *7* (5), 3754–3766.

(64) Guerin, G.; Rupar, P. A.; Molev, G.; Manners, I.; Jinnai, H.; Winnik, M. A. Lateral Growth of 1D Core-Crystalline Micelles upon Annealing in Solution. *Macromolecules* **2016**, *49* (18), 7004–7014.

(65) Longo, A.; Calandra, P.; Casaletto, M. P.; Giordano, C.; Venezia, A. M.; Liveri, V. T. Synthesis and Physico-Chemical Characterization of Gold Nanoparticles Softly Coated by AOT. *Mater. Chem. Phys.* **2006**, *96* (1), 66–72.

(66) Kitchens, C. L.; McLeod, M. C.; Roberts, C. B. Solvent Effects on the Growth and Steric Stabilization of Copper Metallic Nanoparticles in AOT Reverse Micelle Systems. *J. Phys. Chem. B* **2003**, *107* (41), 11331–11338.

(67) Zhang, W.; Qiao, X.; Chen, J. Synthesis and Characterization of Silver Nanoparticles in AOT Microemulsion System. *Chem. Phys.* **2006**, *330* (3), 495–500.

(68) Rogowski, J. L.; Verma, M. S.; Gu, F. X. Discrimination of Proteins Using an Array of Surfactant-Stabilized Gold Nanoparticles. *Langmuir* **2016**, *32* (30), 7621–7629.

(69) Rupar, P. A.; Cambridge, G.; Winnik, M. A.; Manners, I. Reversible Cross-Linking of Polyisoprene Coronas in Micelles, Block Comicelles, and Hierarchical Micelle Architectures Using Pt(0)-Olefin Coordination. *J. Am. Chem. Soc.* **2011**, *133* (42), 16947–16957.

(70) Gädt, T.; Ieong, N. S.; Cambridge, G.; Winnik, M. A.; Manners, I. Complex and Hierarchical Micelle Architectures from Diblock Copolymers Using Living, Crystallization-Driven Polymerizations. *Nat. Mater.* **2009**, *8*, 144–150.

(71) Boott, C. E.; Leitao, E. M.; Hayward, D. W.; Laine, R. F.; Mahou, P.; Guerin, G.; Winnik, M. A.; Richardson, R. M.; Kaminski, C. F.; Whittell, G. R.; Manners, I. Probing the Growth Kinetics for the Formation of Uniform 1D Block Copolymer Nanoparticles by Living Crystallization-Driven Self-Assembly. *ACS Nano* **2018**, *12* (9), 8920–8933.

(72) Mohd Yusoff, S. F.; Gilroy, J. B.; Cambridge, G.; Winnik, M. A.; Manners, I. End-to-End Coupling and Network Formation Behavior of Cylindrical Block Copolymer Micelles with a Crystalline Polyferrocenylsilane Core. *J. Am. Chem. Soc.* **2011**, *133* (29), 11220–11230.

(73) Stetefeld, J.; McKenna, S. A.; Patel, T. R. Dynamic Light Scattering: A Practical Guide and Applications in Biomedical Sciences. *Biophys. Rev.* **2016**, *8* (4), 409–427.

2.6 Supplementary Material

2.6.1 Materials and Methods

Solvents were dried and de-oxygenated using a Solvent Purification System (SPS). THF used for anionic polymerization was distilled from Na/benzophenone. All materials were purchased from Sigma-Aldrich and used as received unless otherwise stated. Self-assembly experiments were performed in HPLC grade solvents, filtered through a 0.2 μm membrane. Dimethylsila[1]ferrocenophane was prepared by literature procedure.[1] Polymers PFS_{24}-*b*-$P2VP_{384}$ (M_n = 46,420 Da, M_w/M_n = 1.19), $PFS_{23}[PPh_2Me]I$ (M_n = 5,830 Da, M_w/M_n = 1.07), and PFS_{20}-*b*-$P2VP_{19}$ (M_n = 6,450 Da, M_w/M_n = 1.10), were prepared by literature procedures.[2,3]

2.6.2 Instrumentation

Nuclear magnetic resonance (NMR) spectroscopy. ^1H and ^{31}P NMR were obtained using a Varian 500 MHz spectrometer. ^{13}P NMR analyses used an internal reference of triphenylphosphine in THF (100 mg/mL). ^1H DOSY NMR was conducted using a Varian 500 MHz spectrometer, with a 900 ms diffusion delay (Δ) and a diffusion gradient length (δ) of 2500 μs. Polymer and surfactant samples were analysed at a concentration of 5 mg/mL or 10 mg/mL, respectively. NMR data was processed using MestReNova.

Gel permeation chromatography (GPC). GPC was conducted using a Malvern Omnisec Resolve/Reveal equipped with a triple detector array, automatic sampler, pump, injector, inline degasser column oven (set at 35 °C), elution columns consisting of styrene/divinylbenzene gels (of pore size 500–5,000 Å), refractometer, four-capillary differential viscometer, UV/Vis detector (λ = 440 nm) and dual angle laser light scattering detector (7° and 90°). GPC grade THF with 1 wt% triethylamine was used as the eluent, with a set flow rate of 1 mL/min. Samples were dissolved in THF at 2 mg/mL and filtered through a 0.2 μm polytetrafluoroethylene membrane prior to analysis.

Matrix-assisted laser desorption/ionization time-of-flight (MALDI-TOF) mass spectrometry. MALDI-TOF was performed on a Bruker Ultraflex III TOF/TOF instrument. Samples were prepared by mixing 10 µL of polymer sample in THF (2 mg/mL) with 100 µL of trans-2-[3-(4-*tert*-butylphenyl)-2-methyl-2-propenylidene] malonitrile in THF (20 mg/mL). Approximately 2 µL of this mixture was deposited onto a polished steel plate and allowed to dry.

Transmission electron microscopy (TEM). Copper grids (500 mesh) were purchased from Ted Pella, Inc. and carbon films were prepared by using a Leica EM ACE600 instrument. Carbon films were deposited onto the copper grids by floatation on water and allowed to dry over 24 hours. Samples for electron microscopy were prepared by drop-casting 8 µL of micelle colloidal solution onto a carbon-coated copper grid followed by solvent evaporation. TEM images were obtained using a JEOL JEM 1011 operating at 80 kV, equipped with a Gatan Orius SC1000 CCD camera.

Measurements were undertaken by hand using ImageJ software, developed by the US National Institute for Health. The platelet area (A), length (L) and width (W) were measured by using the rotated rectangle tool. The aspect ratio (R) was calculated for each platelet by the following equation:

$$R = \frac{L}{W}$$

The number-average area (A_n) and weight-average area (A_w) were calculated according to the following equations:

$$A_n = \frac{\sum_i^n N_i A_i}{\sum_i^n N_i} \qquad A_w = \frac{\sum_i^n N_i A_i^2}{\sum_i^n N_i A_i}$$

The number-average length (L_n) and weight-average length (L_w) were calculated according to the following equations:

$$L_n = \frac{\sum_i^n N_i L_i}{\sum_i^n N_i} \qquad L_w = \frac{\sum_i^n N_i L_i^2}{\sum_i^n N_i L_i}$$

The number-average width (W_n) and weight-average width (W_w) were calculated according to the following equations:

$$W_n = \frac{\sum_i^n N_i W_i}{\sum_i^n N_i} \qquad W_w = \frac{\sum_i^n N_i W_i^2}{\sum_i^n N_i W_i}$$

The number-average aspect ratio (R_n) and weight-average aspect ratio (R_w) were calculated according to the following equations:

$$R_n = \frac{\sum_i^n N_i R_i}{\sum_i^n N_i} \qquad R_w = \frac{\sum_i^n N_i R_i^2}{\sum_i^n N_i R_i}$$

A minimum of 100 micelles were measured for each data point. Errors displayed are standard deviations of each data set.

Selected-area electron diffraction (SAED) analysis. Four-dimensional scanning transmission electron microscopy (4D-STEM) data for 2D nanostructures was collected using a STEM Hitachi HF-3300v with a hybrid pixel array detector MerlinEM (Quantum Detectors) operating in low-magnification mode at 200 kV. Hitachi High-Technologies Canada's Azorus software was used to control and acquire diffraction data. Diffraction data was collected from a 2.5 x 3.5 μm sample area on a 30 x 40 grid. In the surveyed area, 1,200 diffraction patterns were collected. The sample was exposed to the beam (beam size = 70 nm) for 2 ms during collection each diffraction pattern, giving an average dose of approximately 3 $e^-/Å^2$, including the preacquisition sample positioning exposure. Resulting data from such acquisitions was first inspected using Azorus software. Post-collection processing was performed using pixStem and HyperSpy open-source Python libraries from multidimensional data analysis. It should be noted that obtaining further evidence for the core crystallinity was challenging due to issues with the beam-sensitivity of the PFS-based platelets, as well as beam overlap with the central 1D PFS_{24}-*b*-$P2VP_{384}$ seed.

Dynamic light scattering (DLS). DLS was performed using a Malvern Panalytical Zetasizer Ultra/Pro instrument equipped with a laser with a wavelength of 633 nm and a detector oriented at 173º to the incident radiation.

Ultrasonication. Micelle sonication was carried out using a Fisherbrand FB11203 sonication bath (37 W sonication power).

2.6.3 Synthetic Procedures

2.6.3.1 Synthesis of phosphine-terminated PFS homopolymer, $PFS_{23}PPh_2$

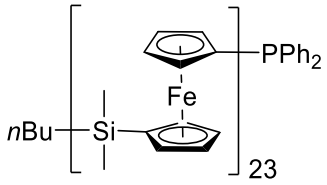

Dimethylsila[1]ferrocenophane (484 mg, 2.00 mmol) in dry, degassed tetrahydrofuran (THF) (5 mL) was initiated with *n*-butyl lithium (1.6 M in hexanes, 63 µL, 0.10 mmol) at room temperature to target a degree of polymerization (DP_n) of 20. After 45 min, the colour of the solution had changed from red to amber, indicating complete conversion of the monomer. The reaction was terminated by the addition of chlorodiphenylphosphine (373 µL, 2.02 mmol) and stirred for 90 min. The resulting polymer was precipitated into degassed methanol, followed by washing with the same non-solvent 3 times. The polymer was dried under vacuum for 1 h to afford an orange solid. ^{1}H NMR analysis was used to determine the homopolymer structure of $PFS_{23}PPh_2$.

Yield: 387 mg (80%). ^{1}H NMR (500 MHz, $CDCl_3$): δ (ppm) = 7.39–7.29 (m, 10H, P*Ph*$_2$), 4.21 (m, 92H, Cp*H*), 4.01 (m, 92H, Cp*H*), 0.46 (s, 138H, Si(C*H*$_3$)$_2$), 0.40 (s, 2H, Me(CH$_2$)$_2$C*H*$_2$SiMe$_2$), 0.19 (s, 6H, *n*-BuSi(C*H*$_3$)$_2$); ^{31}P NMR (500 MHz, $CDCl_3$): δ (ppm) = -17.5; M_w/M_n (GPC) = 1.08.

2.6.3.2 Quaternization of phosphine-terminated PFS homopolymer to prepare the phosphonium derivative $PFS_{23}[PPh_2Me]I$

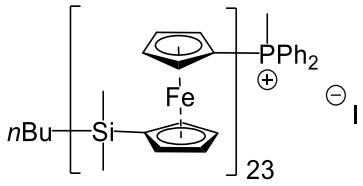

To a solution of $PFS_{23}PPh_2$ (300 mg, 0.06 mmol) in THF (3 mL) was added an excess of MeI (300 µL, 4.80 mmol). After 3 h, the polymer was precipitated in degassed hexanes, followed by washing with hexanes 3 times. The polymer was dried under vacuum for 1 h to afford an orange solid. Complete quaternization was determined using integration of the P*Ph*$_2$ (7.77–7.61 ppm) and P-C*H*$_3$ (3.04 ppm) proton resonances within the ^{1}H NMR spectrum (Figure S1a,b). The polymer was stored in the absence of light. Using the degree of polymerization (DP_n) determined via ^{1}H NMR analysis (DP_n = 23), the M_n could be calculated through summation of the molar masses of the *n*-butyl and phosphonium end groups with that of the main chain: (242.17 Da x 23) + 57.12 Da + 200.19 Da = 5827.22 Da. This value was in good agreement with the M_n obtained via MALDI-TOF mass spectrometry.

Yield: 278 mg (90%). ^{1}H NMR (500 MHz, $CDCl_3$): δ (ppm) = 7.77–7.61 (m, 10H, P*Ph*$_2$), 4.56 (t, 2H, Cp(α-*H*)-[$PPh_2Me]^+$) 4.36 (t, 2H, Cp(β-*H*)-[$PPh_2Me]^+$) 4.21 (m, 92H, Cp*H*), 4.01 (m, 92H, Cp*H*), 3.04 (d, J = 13.0 Hz, 3H, P-C*H*$_3$), 0.46 (s, 138H, Si(C*H*$_3$)$_2$), 0.34 (m, 6H, Si(C*H*$_3$)$_2$(Cp)Fe(Cp)-[$PPh_2Me]^+$), 0.19 (s, 6H, *n*-BuSi(C*H*$_3$)$_2$); ^{31}P NMR (500 MHz, THF): δ (ppm) = +24.1; M_n (MALDI-TOF) = 5,830 Da; M_n (^{1}H NMR) = 5,827 Da; M_w/M_n (GPC) = 1.07.

2.6.3.3 Anion exchange of $PFS_{23}[PPh_2Me]I$ homopolymer to prepare $PFS_{23}[PPh_2Me]SDS$

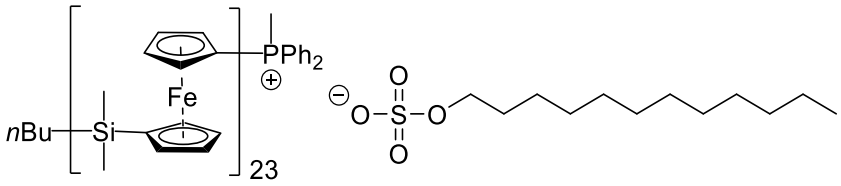

To a solution of $PFS_{23}[PPh_2Me]I$ (100 mg, 0.02 mmol) in THF (3 mL) was added an excess of sodium dodecyl sulfate, [SDS]Na, (952 mg, 3.30 mmol). A precipitate formed immediately. The reaction was stirred for 1 h before precipitation into methanol. The polymer was washed with methanol 3 times to remove NaI. Drying under vacuum for 1 h afforded an orange solid. The polymer was stored in the absence of light. Complete anion exchange was confirmed by ^{1}H NMR through integration analysis of the ratio of the P*Ph*$_2$ and -C*H*$_2$- signals. Using the degree of polymerization (DP_n) determined via ^{1}H NMR analysis (DP_n = 23), the M_n could be calculated through summation of the molar masses of the *n*-butyl and phosphonium end groups with that of the main chain: (242.17 Da x 23) + 57.12 Da + 200.19 Da = 5827.22 Da. This value was in good agreement with the M_n obtained via MALDI-TOF mass spectrometry.

Yield: 97 mg (92%). ^{1}H NMR (500 MHz, $CDCl_3$): δ (ppm) = 7.72–7.60 (m, 10H, P*Ph*$_2$), 4.55 (t, 2H, Cp(α-*H*)-[$PPh_2Me]^+$), 4.42 (t, 2H, Cp(β-*H*)-[$PPh_2Me]^+$), 4.21 (m, 92H, Cp*H*), 4.02 (m, 92H, Cp*H*), 2.97 (d, J = 13.0 Hz, 3H, P-C*H*$_3$), 2.22 (t, J = 7.0 Hz, 1H, (SO_4)C*H*$_2$-), 2.01 (d, 7.0 Hz, 1H, (SO_4)C*H*$_2$-), 1.68 (p, J = 7.0 Hz, 2H, (SO_4)CH_2C*H*$_2$-), 1.36–1.23 (m, 18H, -C*H*$_2$-), 0.46 (s, 138H, Si(C*H*$_3$)$_2$), 0.34 (m, 6H, Si(C*H*$_3$)$_2$(Cp)Fe(Cp)-[$PPh_2Me]^+$), 0.21 (s, 6H, *n*-BuSi(C*H*$_3$)$_2$); ^{31}P NMR (500 MHz, THF): δ (ppm) = +23.8; M_n (MALDI-TOF) = 5,830 Da; M_n (^{1}H NMR) = 5,827 Da; M_w/M_n (GPC) = 1.07.

2.6.3.4 Anion exchange of $PFS_{23}[PPh_2Me]I$ homopolymer to prepare $PFS_{23}[PPh_2Me]AOT$

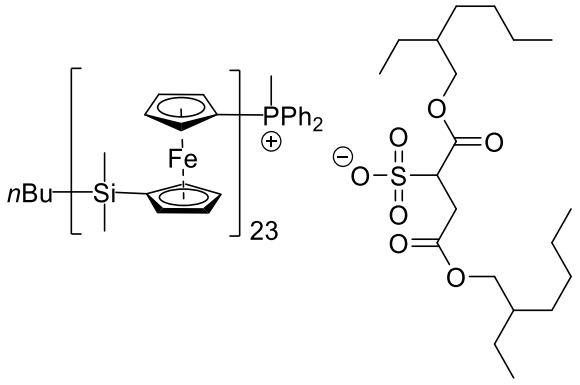

To a solution of $PFS_{23}[PPh_2Me]I$ (100 mg, 0.02 mmol) in THF (3 mL) was added an excess of dioctyl sulfosuccinate sodium salt, [AOT]Na, (1.47 g, 3.30 mmol). A precipitate formed immediately. The reaction was stirred for 1 h before precipitation into methanol. The polymer was washed with methanol 3 times to remove NaI. After drying under vacuum for 1 h, an orange solid was afforded. The polymer was stored in the absence of light. Complete anion exchange was confirmed by ^{1}H NMR through integration analysis of the ratio of the P*Ph*$_2$ and C*H*$_2$ signals. Using the degree of polymerization (DP_n) determined via ^{1}H NMR analysis (DP_n = 23), the M_n could be calculated through summation of the molar masses of the *n*-butyl and phosphonium end groups with that of the main chain: (242.17 Da x 23) + 57.12 Da + 200.19 Da = 5827.22 Da. This value was in good agreement with the M_n obtained via MALDI-TOF mass spectrometry.

Yield: 102 mg (94%). ^{1}H NMR (500 MHz, $CDCl_3$): δ (ppm) = 7.74–7.59 (m, 10H, P*Ph*$_2$), 4.52 (t, 2H, Cp(α-*H*)-[$PPh_2Me]^+$), 4.42 (t, 2H, Cp(β-*H*)-[$PPh_2Me]^+$), 4.21 (t, J = 2.0 Hz, 92H, Cp*H*), 4.01 (t, J = 2.0 Hz, 92H, Cp*H*), 3.97–3.90 (m, 4H, -C*H*$_2$COO-), 3.36 (dd, J = 17.5, 12.0 Hz, 1H, -CH(SO_3)C*H*$_2$-), 3.18 (dd, J = 17.5, 3.0 Hz, 1H, -CH(SO_3)C*H*$_2$-), 2.96 (d, J = 13.5 Hz, 3H, P-C*H*$_3$), 1.48–1.39 (m, 2H, -C*H*-), 1.37–1.27 (m, 16H, -C*H*$_2$-), 0.88–0.81 (m, 12H, -CH_2C*H*$_3$), 0.46 (s, 138H, Si(C*H*$_3$)$_2$), 0.31 (m, 6H, Si(C*H*$_3$)$_2$(Cp)Fe(Cp)-[$PPh_2Me]^+$), 0.19 (s, 6H, *n*-BuSi(C*H*$_3$)$_2$); ^{31}P NMR

(500 MHz, THF): δ (ppm) = +23.6; M_n (MALDI-TOF) = 5,830 Da; M_n (^{1}H NMR) = 5,827 Da; M_w/M_n (GPC) = 1.07.

2.6.3.5 Synthesis of PFS_{24}-*b*-$P2VP_{384}$

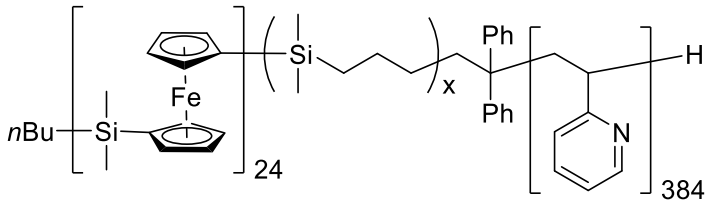

Dimethylsila[1]ferrocenophane (210 mg, 0.87 mmol) in THF (2 mL) was initiated with *n*-butyl lithium (1.6 M in hexanes, 22 µL, 0.04 mmol) at room temperature. After 30 min, the colour of the solution changed from red to amber, indicating complete conversion of the monomer. Sequential addition of 1,1-dimethylsilacyclobutane (DMSB) (14 µL, 0.11 mmol) followed by 1,1-diphenylethylene (DPE) (37.0 µL, 0.21 mmol) into the living PFS polymer solution caused a change in colour from amber to dark red within a minute, indicating the formation of a diphenylmethyl-type carbanion. After a total of 40 min, an aliquot (415 µL) for molecular weight analysis was removed and quenched with 4-*t*-butylphenol. Dry LiCl (ca. 10 mg) and 2-vinylpyridine (1.2 mL, 11.1 mmol) were dissolved in THF (5.6 mL). The living PFS and 2-vinylpyridine/LiCl solutions were both cooled to -78 °C for 15 min before they were combined. The reaction proceeded for 60 min at -78 °C before termination with 4-*t*-butylphenol. The polymer was precipitated into hexanes from THF 3 times and was then dried under vacuum overnight to afford a light orange solid. GPC and ^{1}H NMR analysis were used to determine the final block copolymer composition of PFS_{24}-*b*-$P2VP_{384}$.

Yield: 1.06 g (77%). ^{1}H NMR (500 MHz, $CDCl_3$): δ (ppm) = 8.23 (m, 16H, NC*H*C), 7.26–6.16 (m, 48H, aromatic *H*), 4.21 (m, 4H, Cp*H*), 4.00 (m, 4H, Cp*H*), 2.40–1.42 (br, alkyl *H*), 0.45 (s, 6H, $Si(CH_3)_2$); M_n (GPC) = 46,420 Da; M_w/M_n (GPC) = 1.19.

2.6.3.6 Synthesis of PFS_{20}-*b*-$P2VP_{19}$

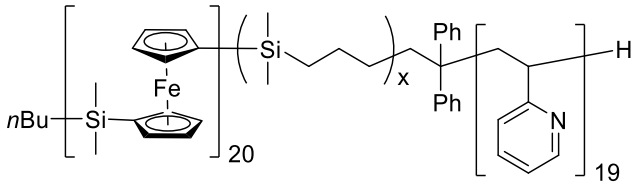

Dimethylsila[1]ferrocenophane (100 mg, 0.4 mmol) in THF (2 mL) was initiated with *n*-butyl lithium (1.6 M in hexanes, 10 µL, 0.016 mmol) at room temperature. After 30 min, the colour of the solution changed from red to amber, indicating complete conversion of the monomer. Sequential addition of 1,1-dimethylsilacyclobutane (DMSB) (6.2 µL, 0.048 mmol) followed by 1,1-diphenylethylene (DPE) (17 µL, 0.096 mmol) into the living PFS polymer solution caused a change in colour from amber to dark red within a minute, indicating the formation of a diphenylmethyl-type carbanion. After a total of 40 min, an aliquot (250 µL) for molecular weight analysis was removed and quenched with 4-*t*-butylphenol. Dry LiCl (ca. 1 mg) and 2-vinylpyridine (32 µL, 0.3 mmol) were dissolved in THF (500 µL). The living PFS and 2-vinylpyridine/LiCl solutions were both cooled to -78 °C for 15 min before they were combined. The reaction proceeded for 40 min at -78 °C before termination with 4-*t*-butylphenol. The polymer was precipitated into hexanes from THF 3 times and was then dried under vacuum overnight to afford a light orange solid. MALDI-TOF and ^{1}H NMR analysis were used to determine the final block copolymer composition of PFS_{20}-*b*-$P2VP_{19}$.

Yield: 89 mg (68%). ^{1}H NMR (500 MHz, $CDCl_3$): δ (ppm) = 8.22 (m, 1H, NC*H*C), 7.22–6.22 (m, 3H, aromatic *H*), 4.22 (s, 4H, Cp*H*), 4.02 (s, 4H, Cp*H*), 2.40–1.46 (br, alkyl *H*), 0.44 (s, 6H, Si(CH_3)$_2$); M_n (GPC) = 6,450 Da; M_w/M_n (GPC) = 1.10.

2.6.4 Self-Assembly Procedures

2.6.4.1 Formation of uniform 1D PFS_{24}-*b*-$P2VP_{384}$ cylindrical seed micelles (L_n = 26 nm, L_w/L_n = 1.19) at 0.6 wt%

A 5 mg/mL (0.6 wt%) solution of PFS_{24}-*b*-$P2VP_{384}$ in *i*PrOH was prepared and heated at 80 °C with stirring for 24 h, to ensure complete dissolution of the polymer. The solution was left to cool slowly to room temperature (22 ºC) without stirring after turning off the heating source. TEM analysis after a further 24 h confirmed the presence of polydisperse cylindrical micelles. The fibres were sonicated at 0 °C for 4 h, to yield low aspect ratio by polydisperse micelles (L_n = 22 ± 15 nm, L_w/L_n = 1.46). These fibres were then annealed at 80 °C for 30 min to improve the micelle length-dispersity. Uniform 1D seed micelles resulted and were carefully measured by hand using ImageJ software (as previously described on page S3). L_n = 26 ± 10 nm, L_w/L_n = 1.19.

2.6.4.2 Formation of uniform 2D platelet micelles at 0.01 wt%

To *i*PrOH (1 mL) was added 25 μL of PFS_{24}-*b*-$P2VP_{384}$ seeds (L_n = 26 nm, L_w/L_n = 1.19) in *i*PrOH (0.5 mg/mL). To this colloidal solution was added a specific amount of unimer solution in THF (10 mg/mL) whilst vigorously shaking by vortex mixer for 3 s. The solution was left for 24 h before TEM analysis. Uniform low aspect ratio platelets were observed and were carefully measured by hand using ImageJ software (as described on page S3).

2.6.4.3 Formation of 2D platelet micelles at scalable concentrations (0.1–0.4 wt%)

To various amounts of iPrOH (to prepare 1, 2, 3, 4 and 5 mg/mL solutions) was added 10 μL of PFS_{24}-*b*-$P2VP_{384}$ seeds (L_n = 26 nm, L_w/L_n = 1.19) in *i*PrOH (5 mg/mL). The solution was manually shaken for 3 s before 50 μL of unimer solution in THF (10 mg/mL) was added whilst vigorously shaking by vortex mixer for 3 s. The solutions were left for 12 h before TEM analysis. Samples

diluted to 0.1 mg/mL for analysis. The resultant nanostructures were carefully measured by hand using ImageJ software (as described in Section 0).

2.6.5 Supplementary Figures

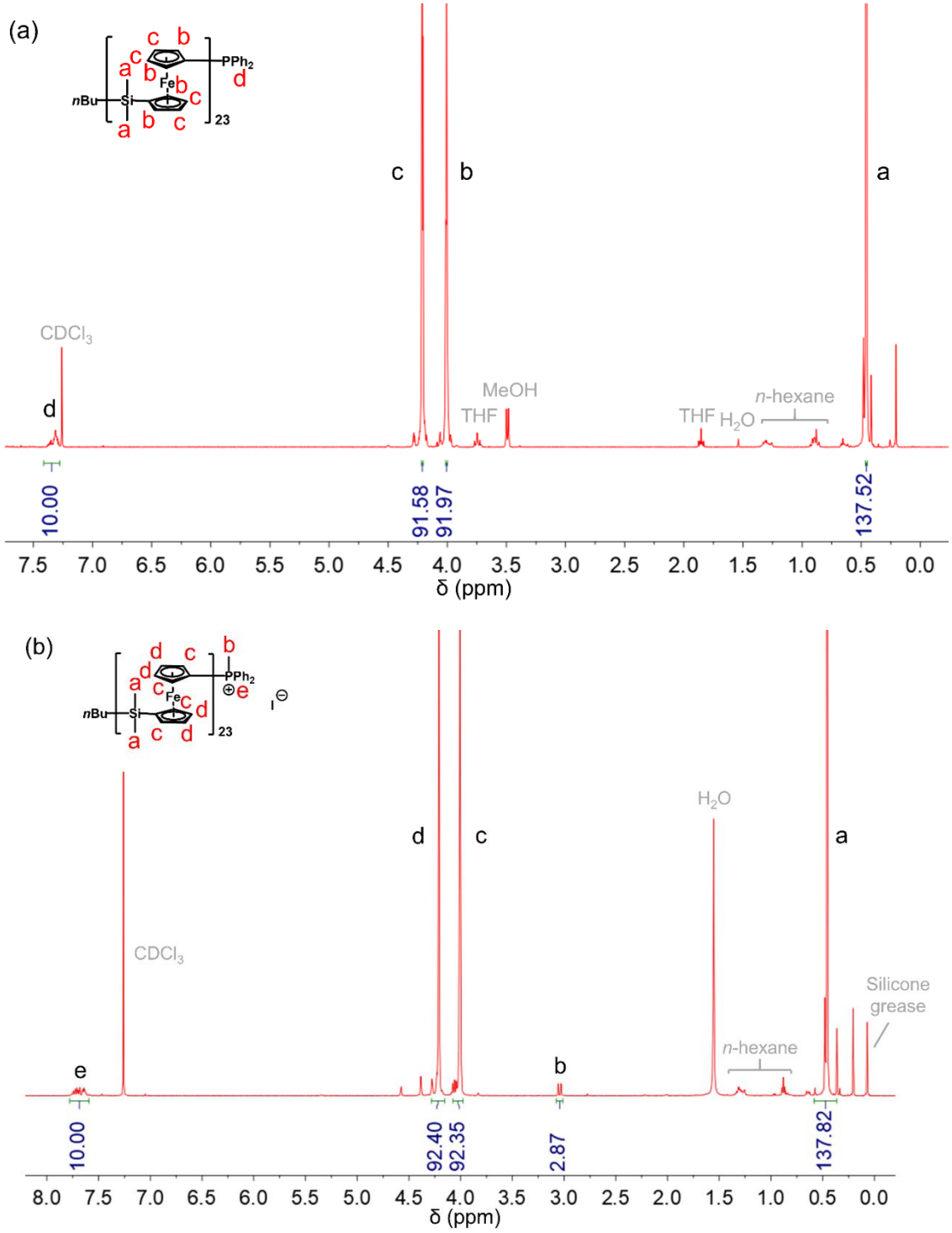

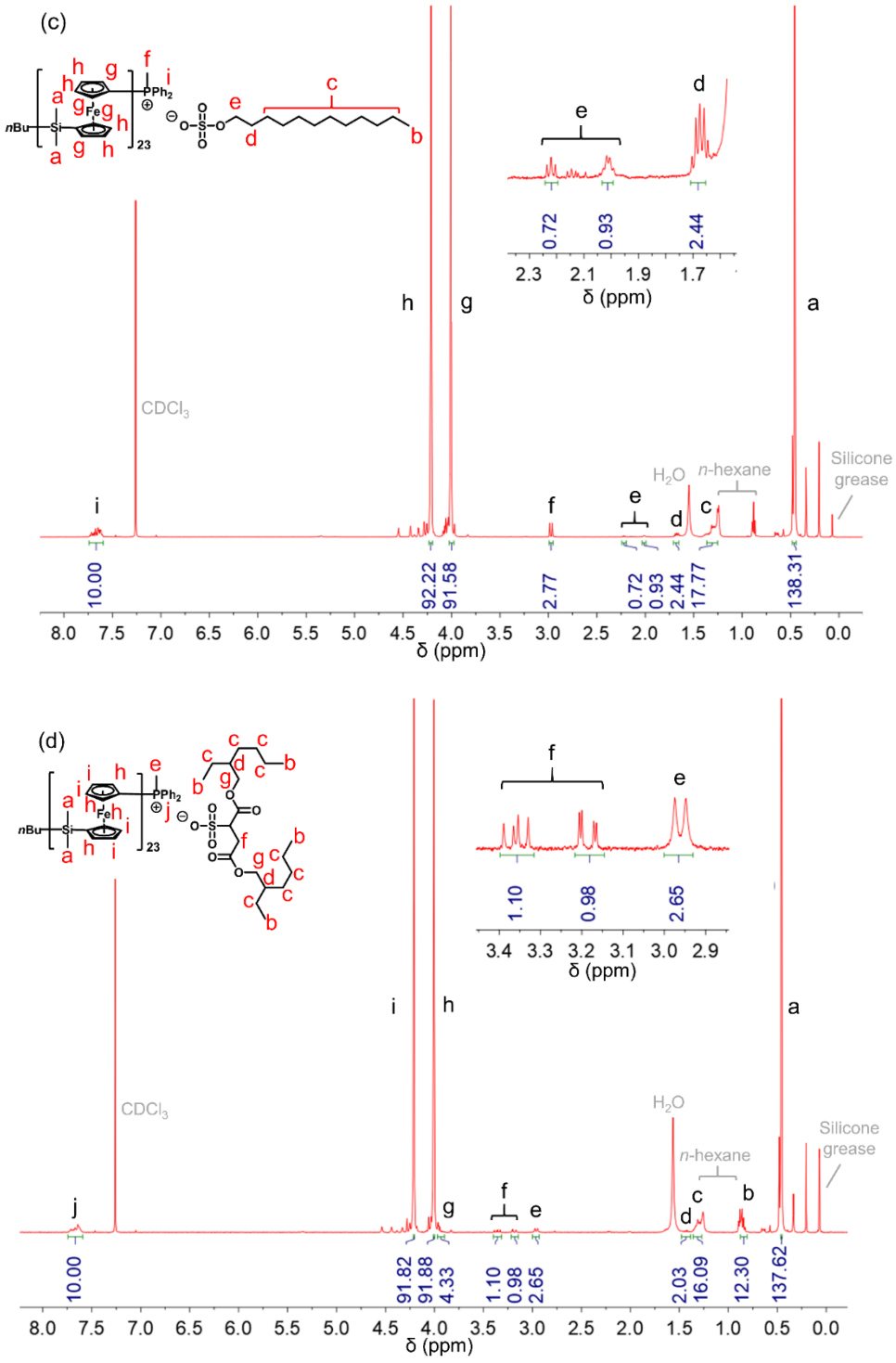

Figure S2.1 ^{1}H NMR spectra (in $CDCl_3$) of (a) $PFS_{23}PPh_2$, compared with quaternized (b) $PFS_{23}[PPh_2Me]I$, (c) $PFS_{23}[PPh_2Me]SDS$ and (d) $PFS_{23}[PPh_2Me]AOT$. Small peaks at 4.56–

4.36 ppm and 0.34–0.19 ppm correspond to locations near the polymer chain termini and are assigned on pages 83–86.

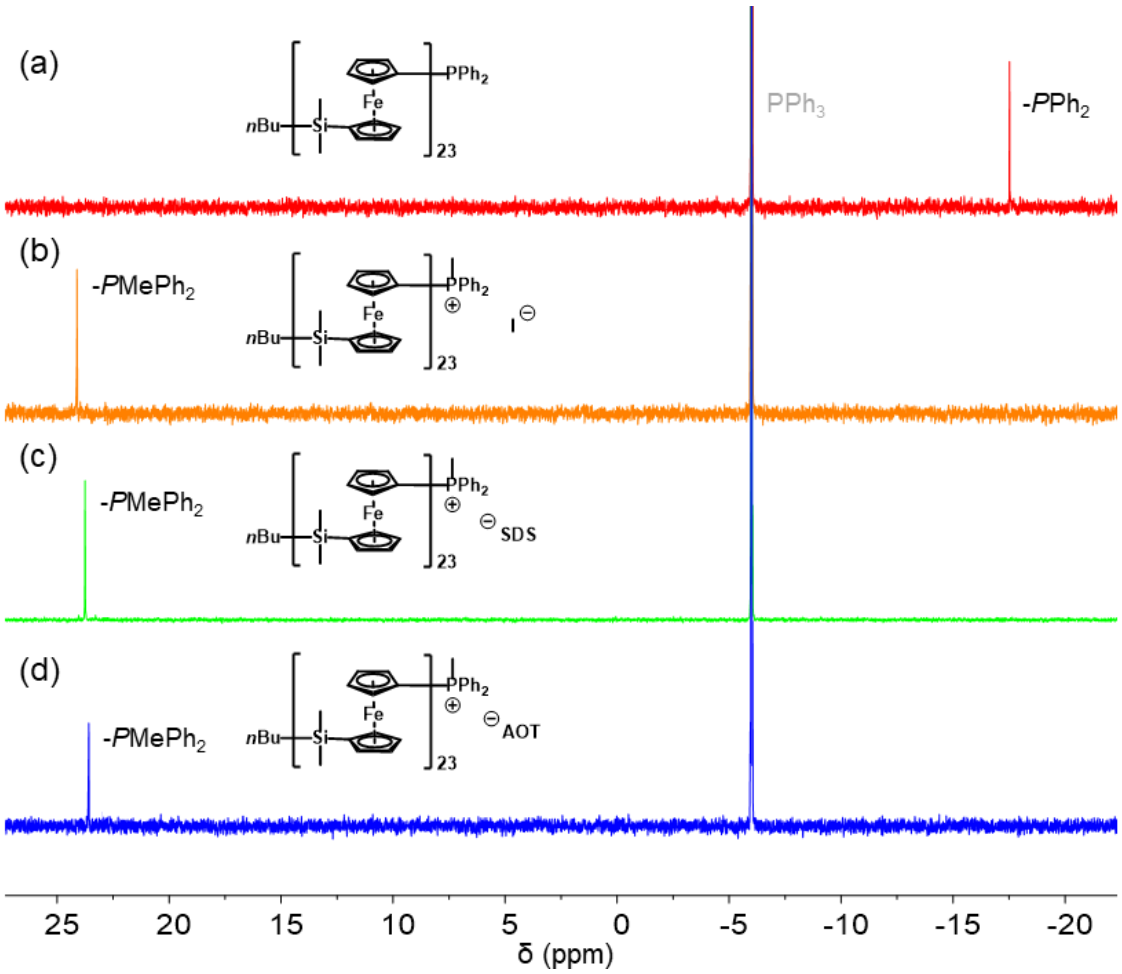

Figure S2.2 ^{31}P NMR spectra of (a) $PFS_{23}PPh_2$ compared with quaternized (b) $PFS_{23}[PPh_2Me]I$, (c) $PFS_{23}[PPh_2Me]SDS$ and (d) $PFS_{23}[PPh_2Me]AOT$. Triphenylphosphine (100 mg/mL in THF) was used as an internal reference.

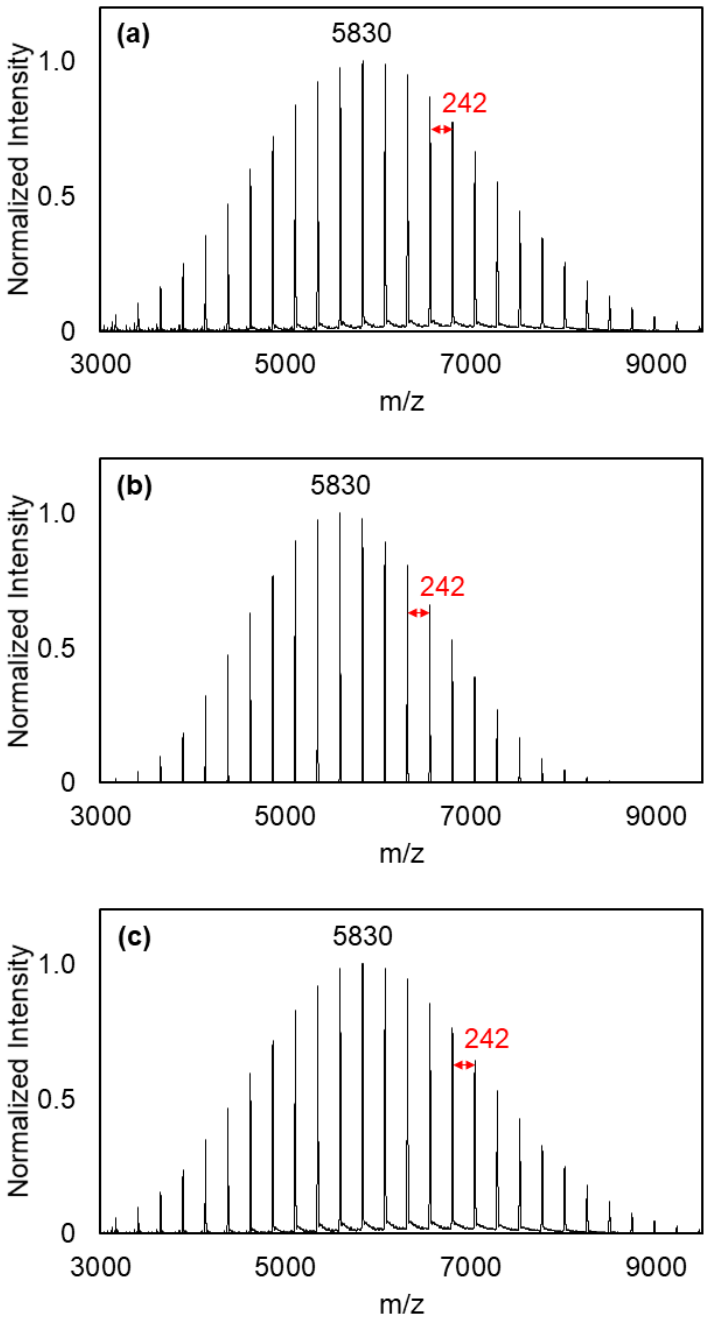

Figure S2.3 MALDI-TOF spectra of (a) $PFS_{23}[PPh_2Me]I$; $[M^+]$ = 5,830 Da, (b) $PFS_{23}[PPh_2Me]SDS$; $[M^+]$ = 5,830 Da and (c) $PFS_{23}[PPh_2Me]AOT$; $[M^+]$ = 5,830 Da. The mass difference between each peak is equal to the molecular weight of a PFS monomer unit (242 Da). The spectra were obtained in positive mode, thus the counteranions cannot be observed.

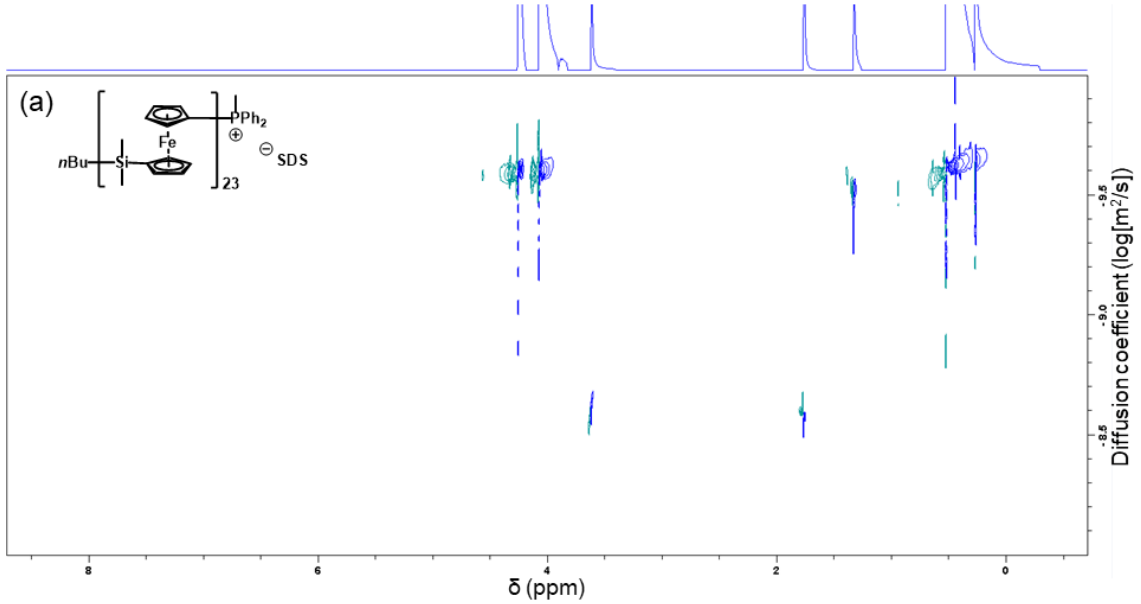
(a)
PPh2
Fe
nBu
Si
SDS
23
δ (ppm)
Diffusion coefficient (log[m2/s])

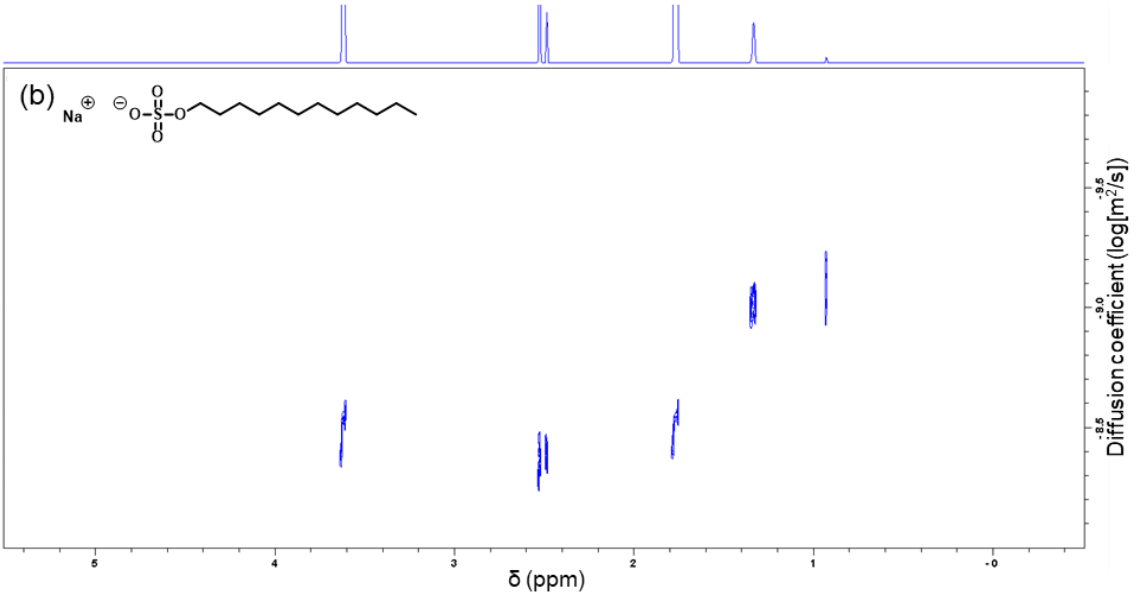
(b)
Na
O
S
δ (ppm)
Diffusion coefficient (log[m2/s])

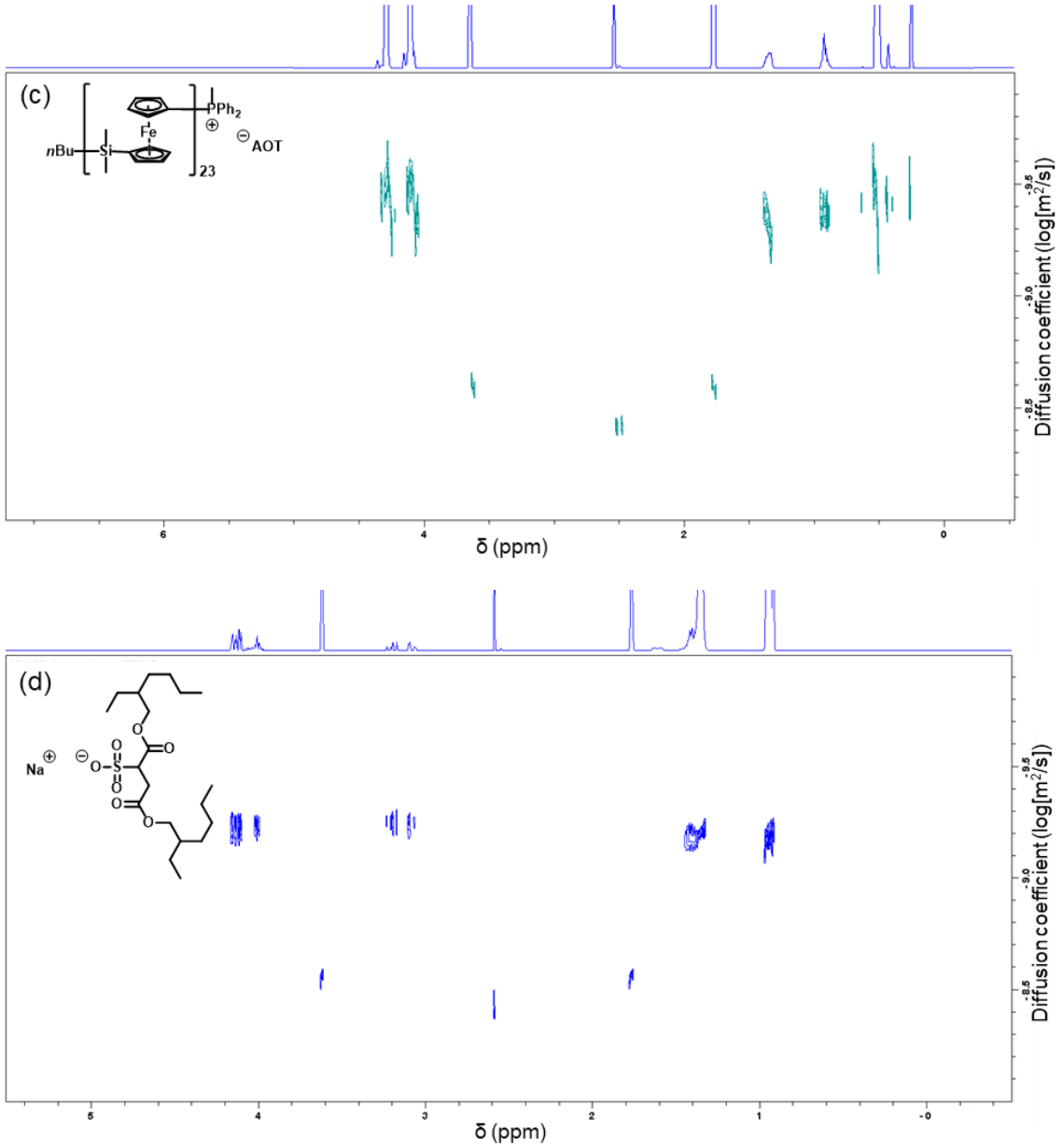

Figure S2.4 ^{1}H DOSY NMR spectra of (a) $PFS_{23}[PPh_2Me]SDS$ and (c) $PFS_{23}[PPh_2Me]AOT$, compared with that of the sodium salts of the counteranions, (b) Na[SDS] and (d) Na[AOT]. All DOSY experiments were carried out in THF-d_8 at a concentration of ca. 5 mg/mL.

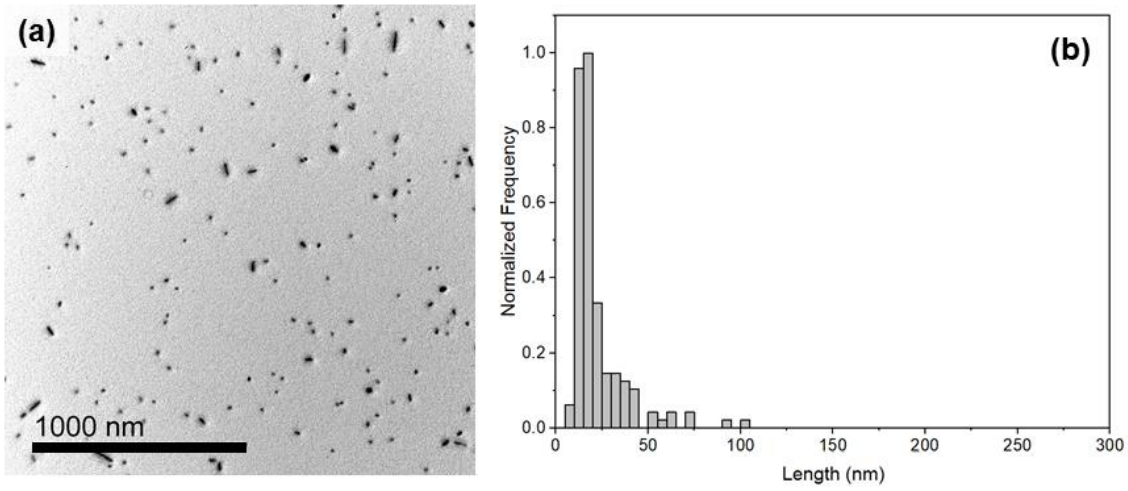

Figure S2.5 (a) Representative TEM image of PFS_{24}-*b*-$P2VP_{384}$ 1D micelles prepared by sonication of polydisperse cylindrical micelles at 0 °C for 4 h. (b) Histogram of contour length distribution, L_n = 22 nm; L_w/L_n = 1.46; 5 mg/mL (0.6 wt%). Solution samples of 0.5 mg/mL were drop-cast and imaged after solvent evaporation. Scale bar: 1000 nm.

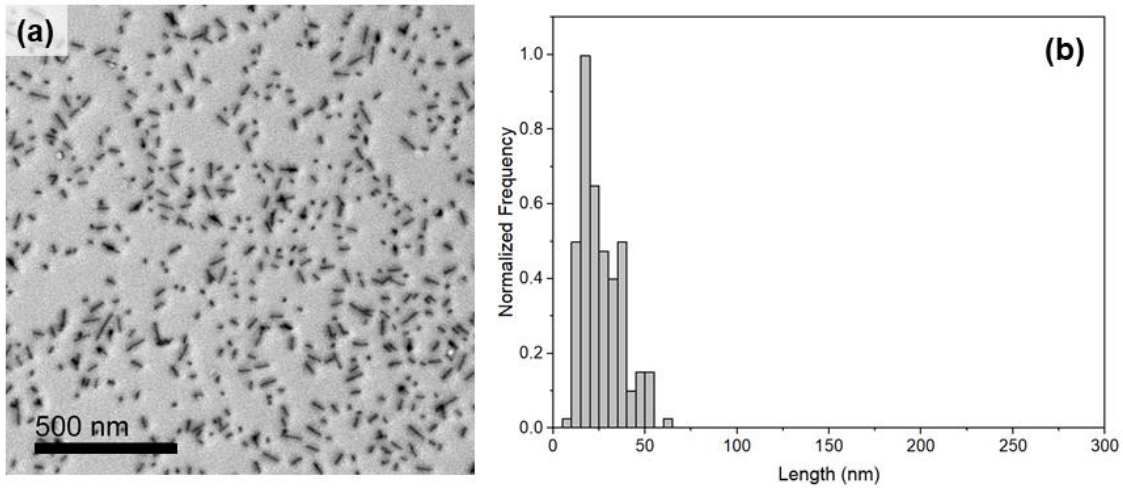

Figure S2.6 (a) Representative TEM image of PFS_{24}-*b*-$P2VP_{384}$ 1D seed micelles used in this study. (b) Histogram of contour length distribution, L_n = 26 nm; L_w/L_n = 1.19; 5 mg/mL (0.6 wt%) in *i*PrOH. Solution samples of 1 mg/mL were drop-cast and imaged after solvent evaporation. Scale bar: 500 nm.

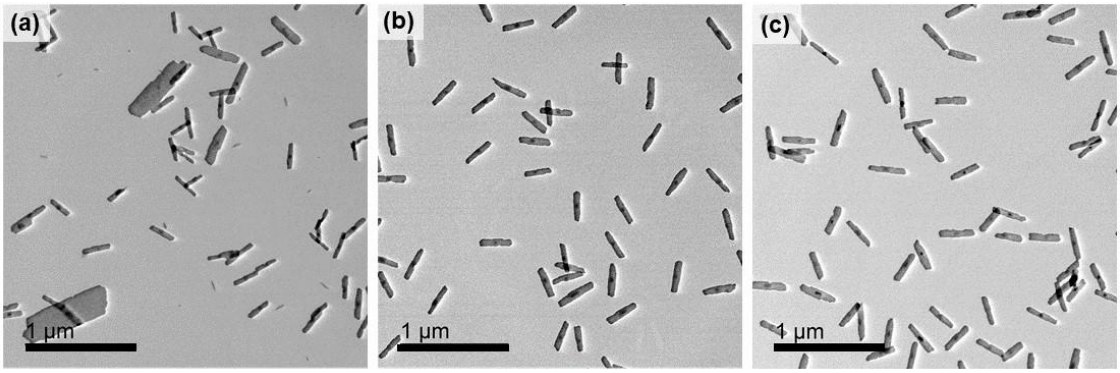

Figure S2.7 Representative TEM images of PFS_{23}[PPh_2Me]SDS platelet micelles formed through seeded growth from PFS_{24}-*b*-$P2VP_{384}$ 1D micelles (L_n = 26 nm, L_w/L_n = 1.19) in *i*PrOH at 0.01 wt% and a m_{unimer}/m_{seed} of 10 prepared (a) in the absence of vigorous mixing (A_w/A_n = 3.44), (b) with vigorous mixing for 3 s (as in this work) (A_w/A_n = 1.03), and (c) with a further 3 s of vigorous mixing (A_w/A_n = 1.03). Scale bar: 1 µm.

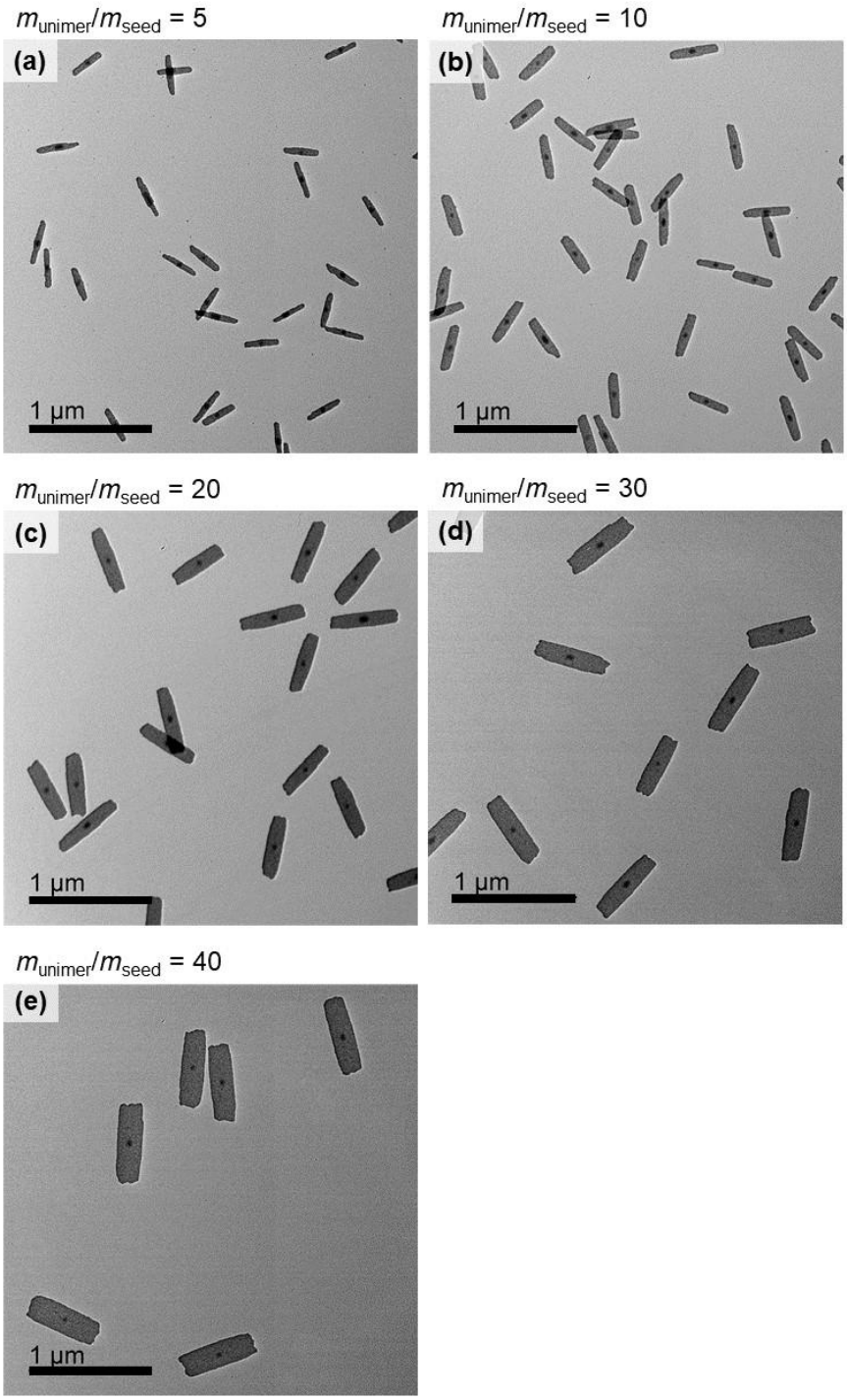

Figure S2.8 Representative TEM images of $PFS_{23}[PPh_2Me]I$ platelet micelles formed through seeded growth from PFS_{24}-*b*-$P2VP_{384}$ 1D micelles (L_n = 26 nm, L_w/L_n = 1.19) in *i*PrOH at 0.1 mg/mL (0.01 wt%) and various m_{unimer}/m_{seed}. Scale bars: 1 µm.

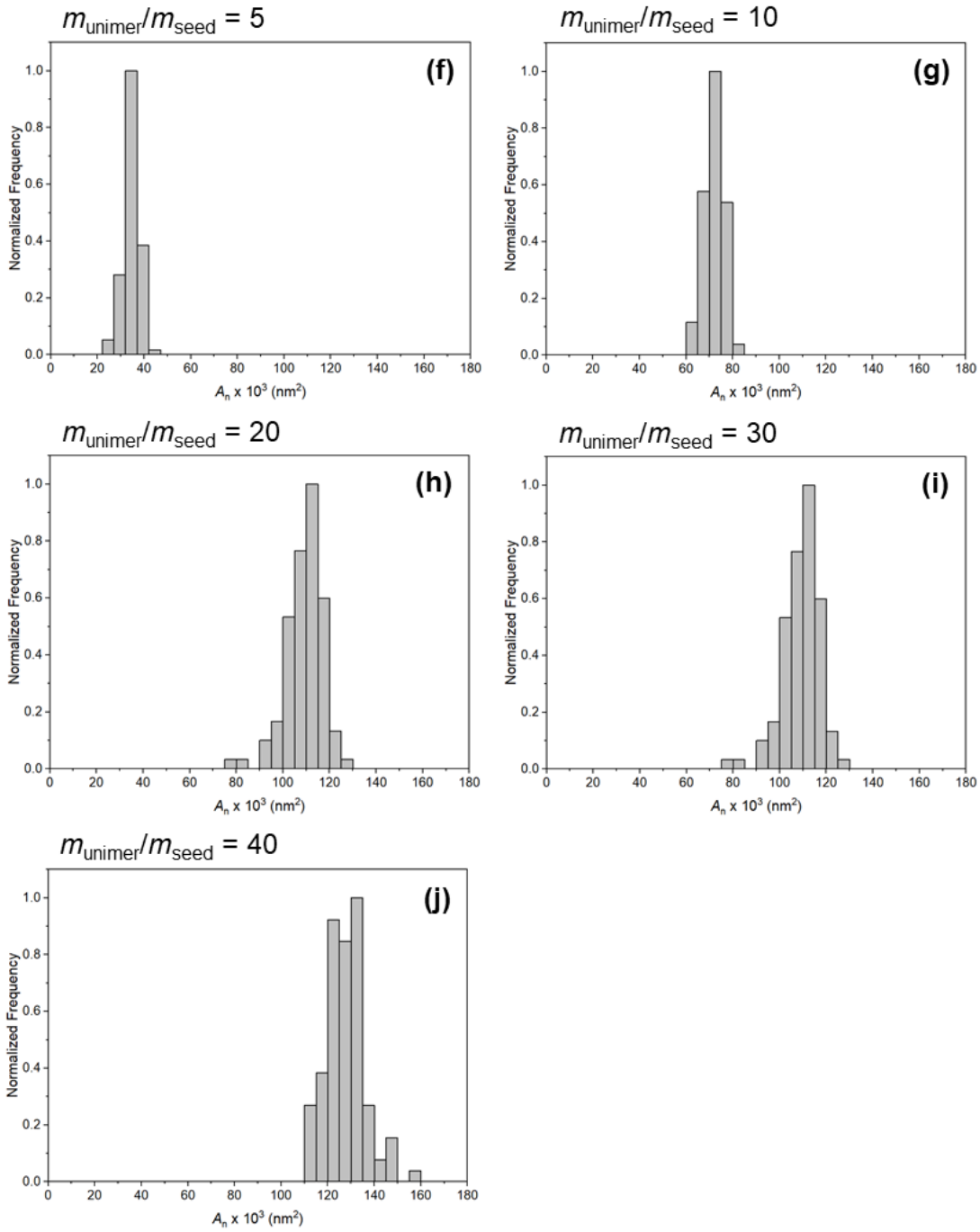

Figure S2.9 Contour area distributions of PFS_{23}[PPh_2Me]I platelet micelles formed through seeded growth from PFS_{24}-*b*-$P2VP_{384}$ 1D micelles (L_n = 26 nm, L_w/L_n = 1.19) in *i*PrOH at 0.1 mg/mL (0.01 wt%) and various m_{unimer}/m_{seed}.

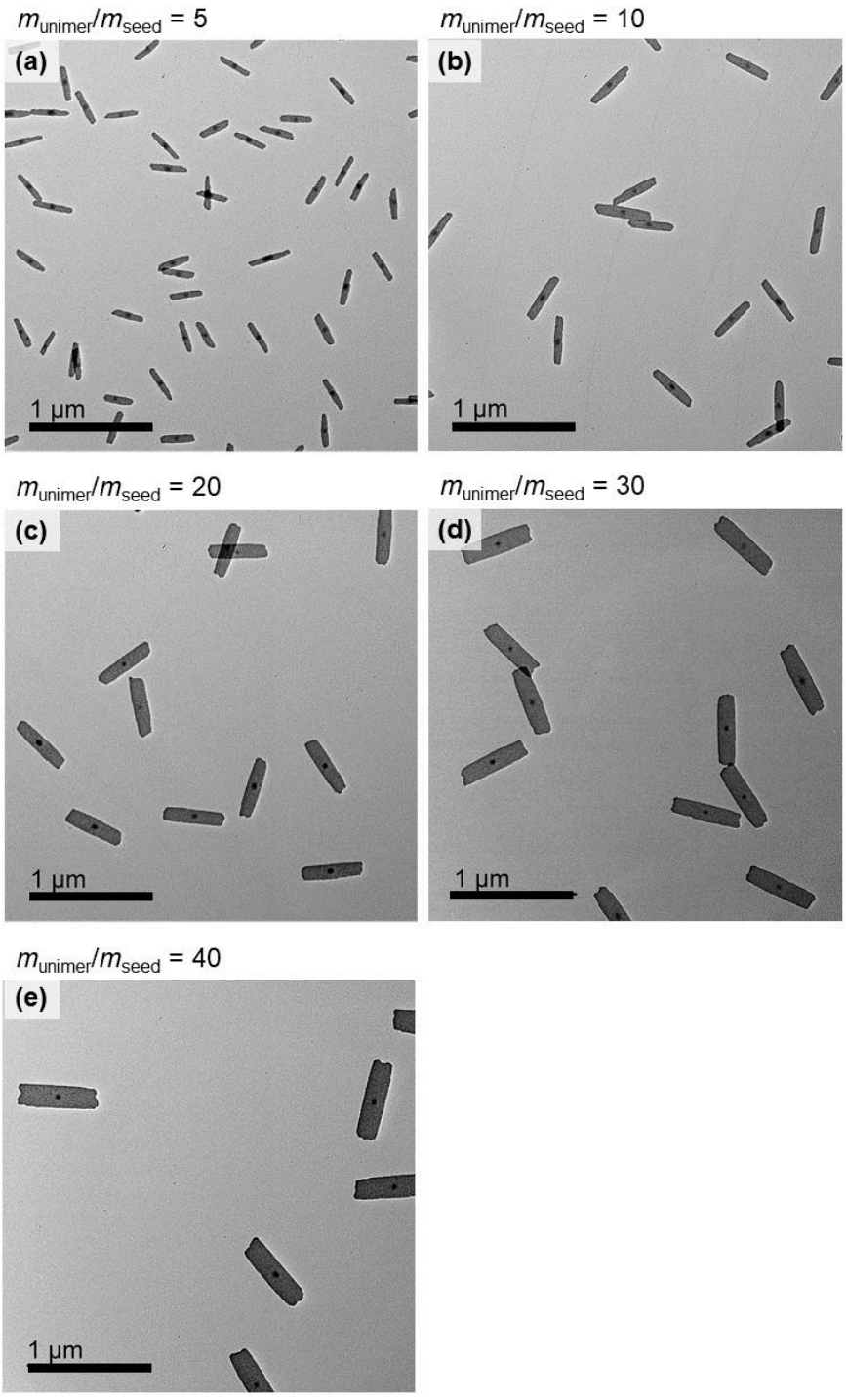

Figure S2.10 Representative TEM images of PFS_{23}[PPh_2Me]SDS platelet micelles formed through seeded growth from PFS_{24}-*b*-$P2VP_{384}$ 1D micelles (L_n = 26 nm, L_w/L_n = 1.19) in *i*PrOH at 0.1 mg/mL (0.01 wt%) and various m_{unimer}/m_{seed}. Scale bars: 1 µm.

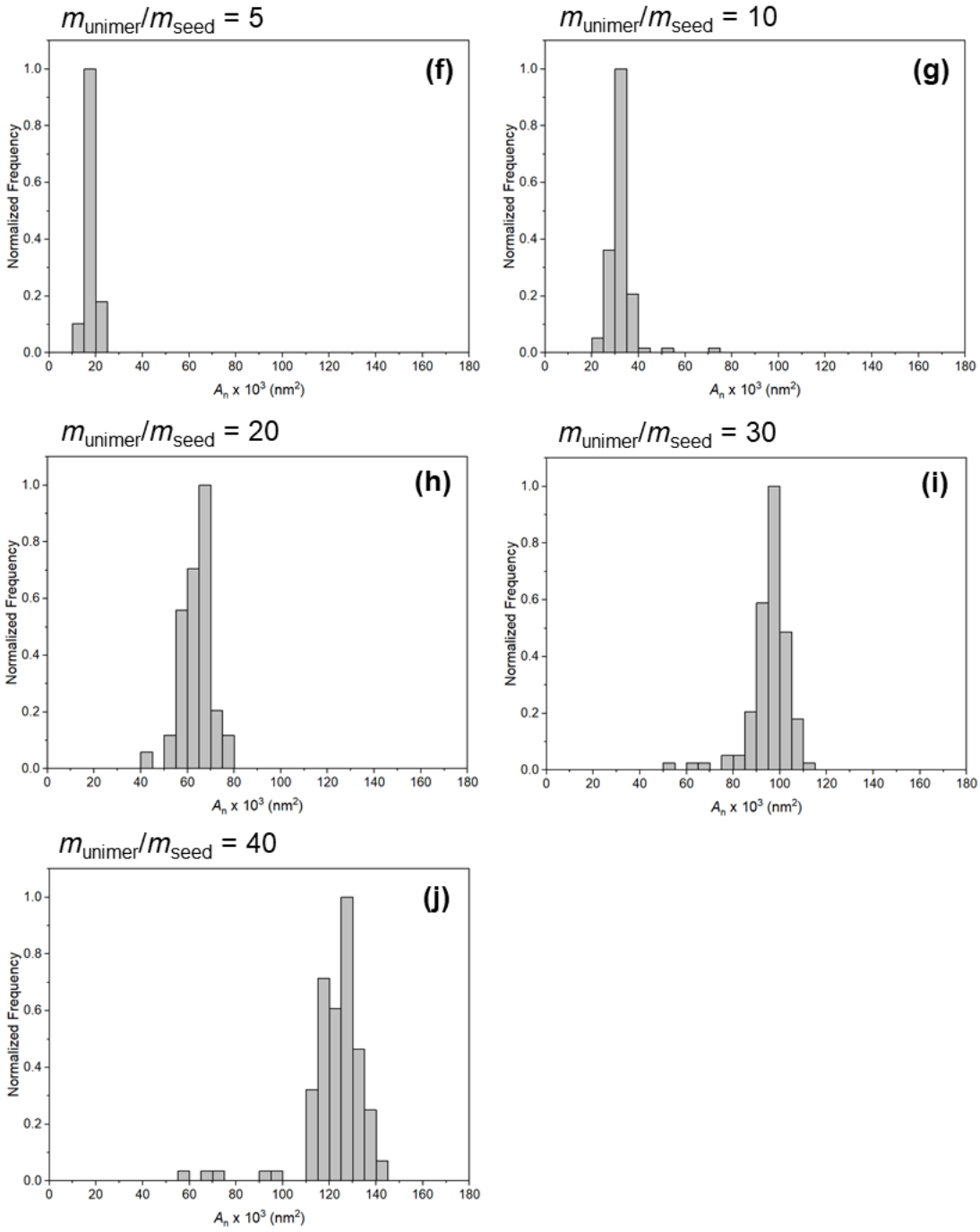

Figure S2.11 Contour area distributions of PFS_{23}[PPh_2Me]SDS platelet micelles formed through seeded growth from PFS_{24}-*b*-$P2VP_{384}$ 1D micelles (L_n = 26 nm, L_w/L_n = 1.19) in *i*PrOH at 0.1 mg/mL (0.01 wt%) and various m_{unimer}/m_{seed}.

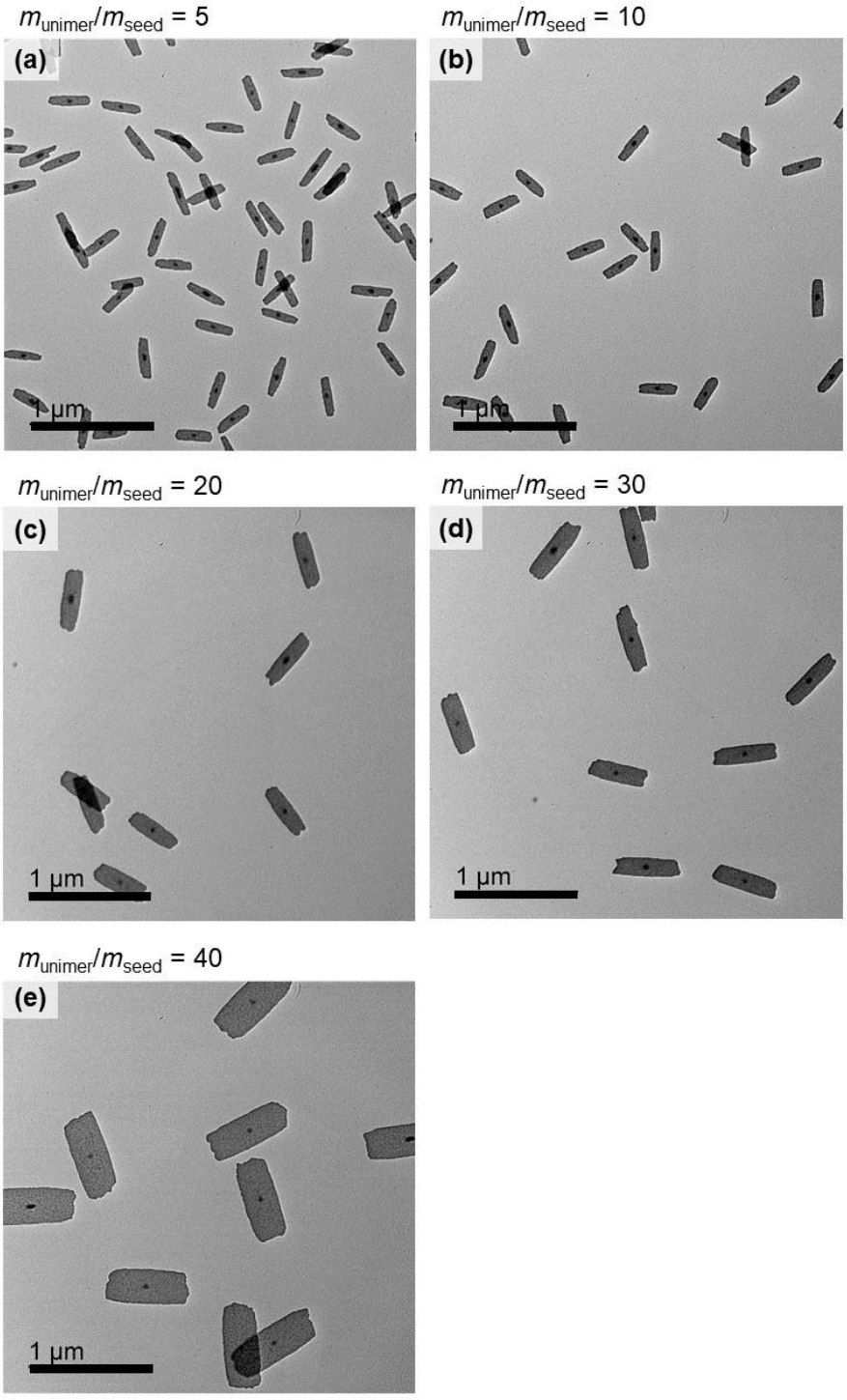

Figure S2.12 Representative TEM images of $PFS_{23}[PPh_2Me]AOT$ platelet micelles formed through seeded growth from PFS_{24}-*b*-$P2VP_{384}$ 1D micelles (L_n = 26 nm, L_w/L_n = 1.19) in *i*PrOH at 0.1 mg/mL (0.01 wt%) and various m_{unimer}/m_{seed}. Scale bars: 1 µm.

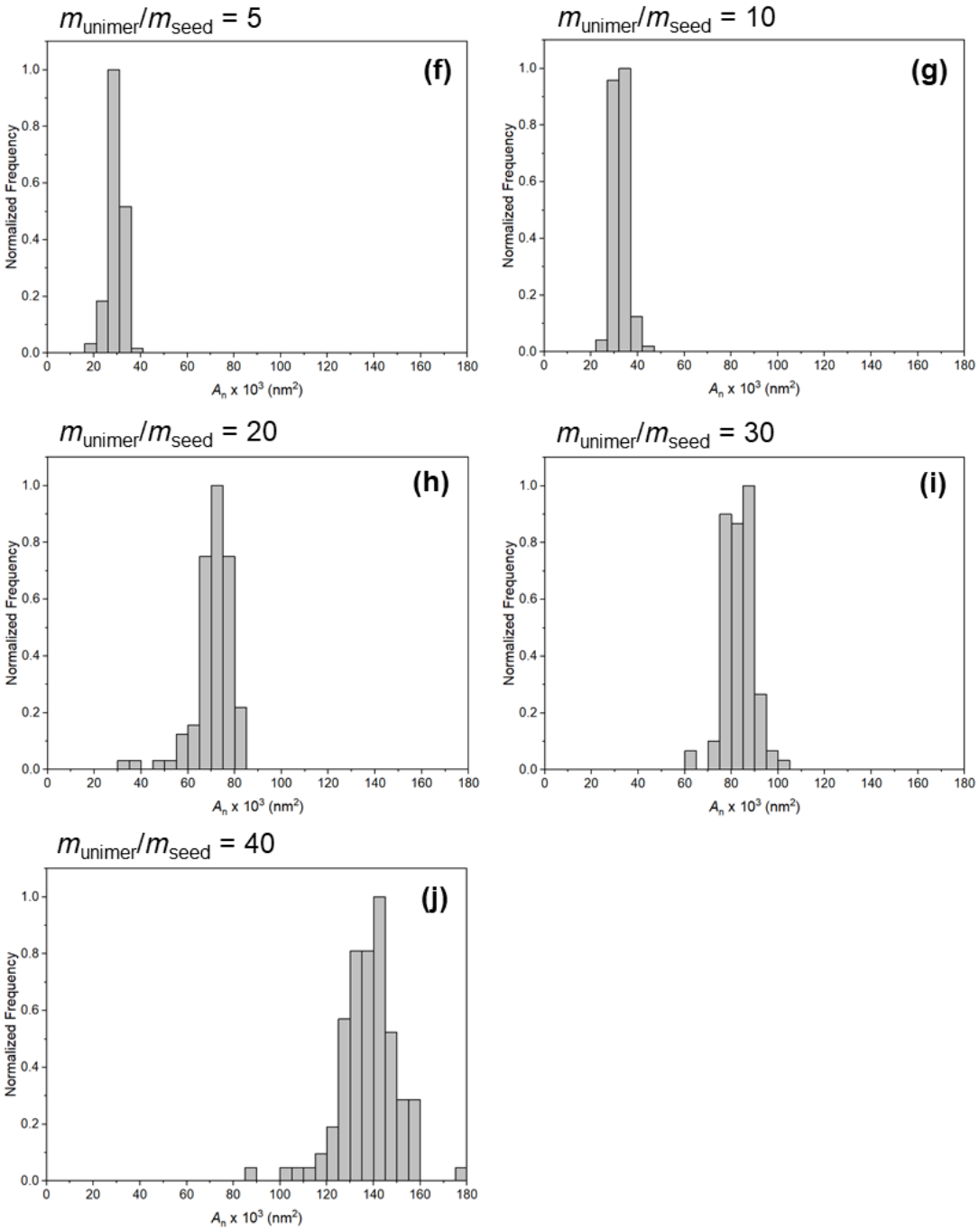

Figure S2.13 Contour area distributions of PFS_{23}[PPh_2Me]AOT platelet micelles formed through seeded growth from PFS_{24}-*b*-$P2VP_{384}$ 1D micelles (L_n = 26 nm, L_w/L_n = 1.19) in *i*PrOH at 0.1 mg/mL (0.01 wt%) and various m_{unimer}/m_{seed}.

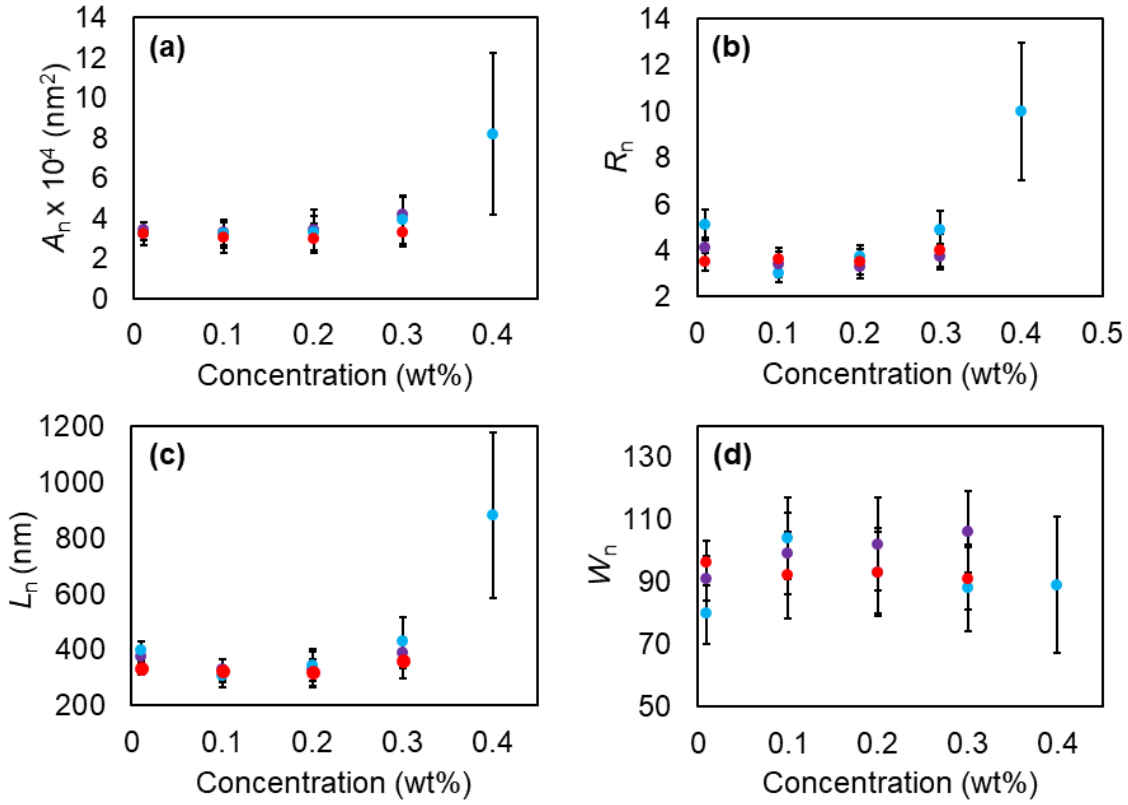

Figure S2.14 Dependence of $PFS_{23}[PPh_2Me]X$ platelet (a) number-average area (A_n), (b) number-average aspect ratio (R_n), (c) number-average length (L_n), and (d) number-average width (W_n) on 2D living CDSA concentration in *i*PrOH. X = I (purple), SDS (blue), AOT (red). Error bars represent the standard deviation of measured areas, lengths and widths, or calculated aspect ratios.

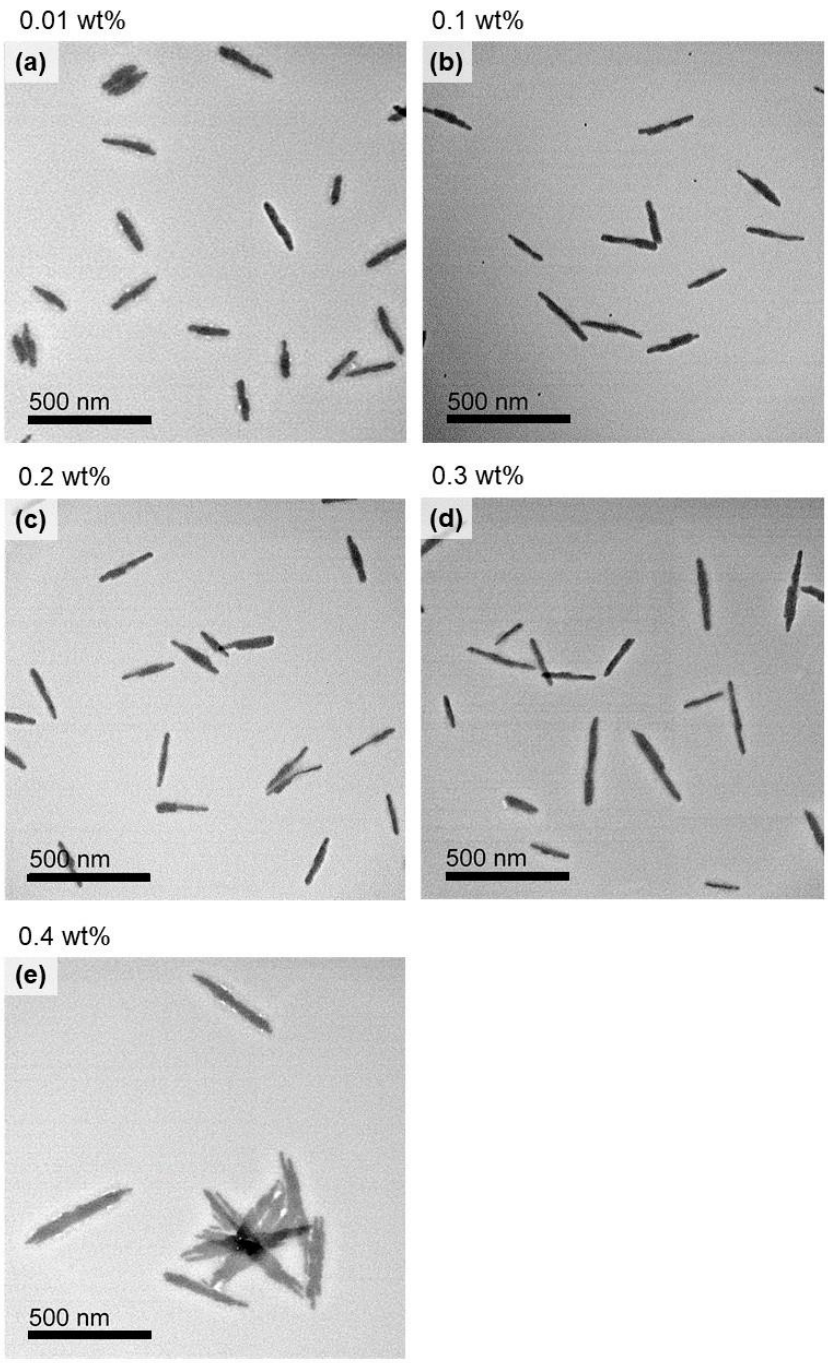

Figure S2.15 Representative TEM image of lenticular-like platelets from seeded growth of PFS_{20}-*b*-$P2VP_{19}$ from PFS_{24}-*b*-$P2VP_{384}$ 1D micelles (L_n = 26 nm, L_w/L_n = 1.19) in *i*PrOH at (a) 0.01 wt%, (b) 0.1 wt%, (c) 0.2 wt%, (d) 0.3 wt%, and (e) 0.4 wt%. Scale bars: 500 nm.

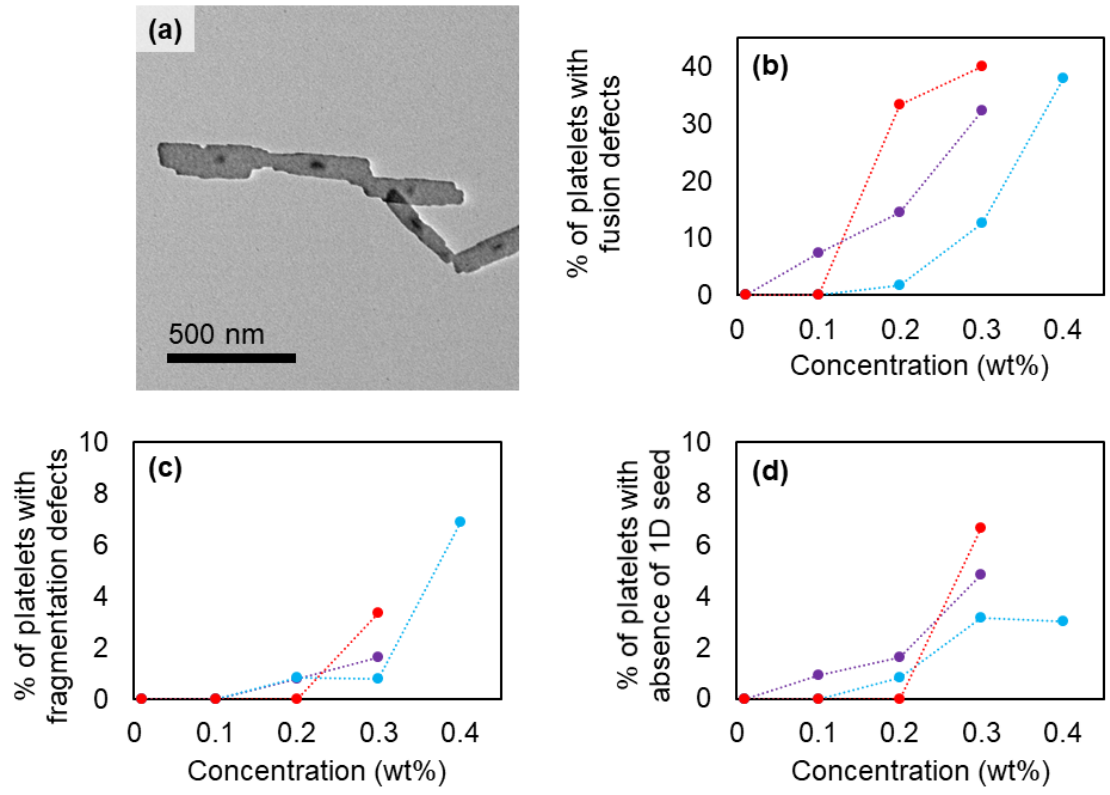

Figure S2.16 (a) Representative TEM image of platelet fusion defects observed in 2D living CDSA at higher concentrations (0.1–0.4 wt%). This example is taken from the living CDSA of $PFS_{23}[PPh_2Me]I$ at a m_{unimer}/m_{seed} of 10, carried out at 0.3 wt% *i*PrOH. It shows a "trimer" and "dimer", both formed through fusion defects. This is contrary to nanostructure overlap, which can be observed as the area of higher electron contrast where the "trimer" and "dimer" have physically aggregated, presumably on solvent evaporation during TEM sample preparation. Dependence of the percentage of $PFS_{23}[PPh_2Me]X$ platelets with (b) fusion defects, (c) fragmentation defects, or (d) in the absence of a 1D seed on the 2D living CDSA concentration. X = I (purple), SDS (blue), AOT (red). Trend lines for guidance only.

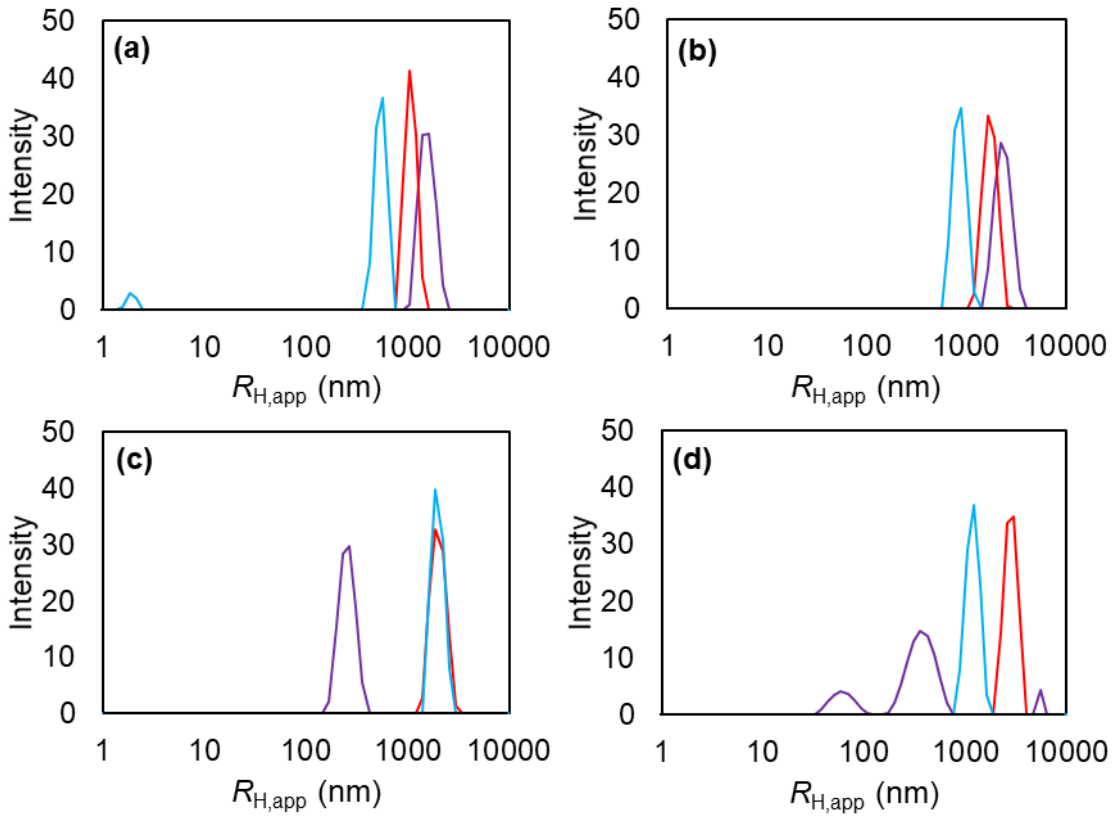

Figure S2.17 Representative intensity distribution DLS plots of $PFS_{23}[PPh_2Me]X$ platelet micelles formed through seeded growth from PFS_{24}-*b*-$P2VP_{384}$ 1D micelles (L_n = 26 nm, L_w/L_n = 1.19) in *i*PrOH at a m_{unimer}/m_{seed} of 10 and at (a) 0.1 wt%, (b) 0.2 wt%, (c) 0.3 wt%, and (d) 0.4 wt%. X = I (purple), SDS (blue), AOT (red).

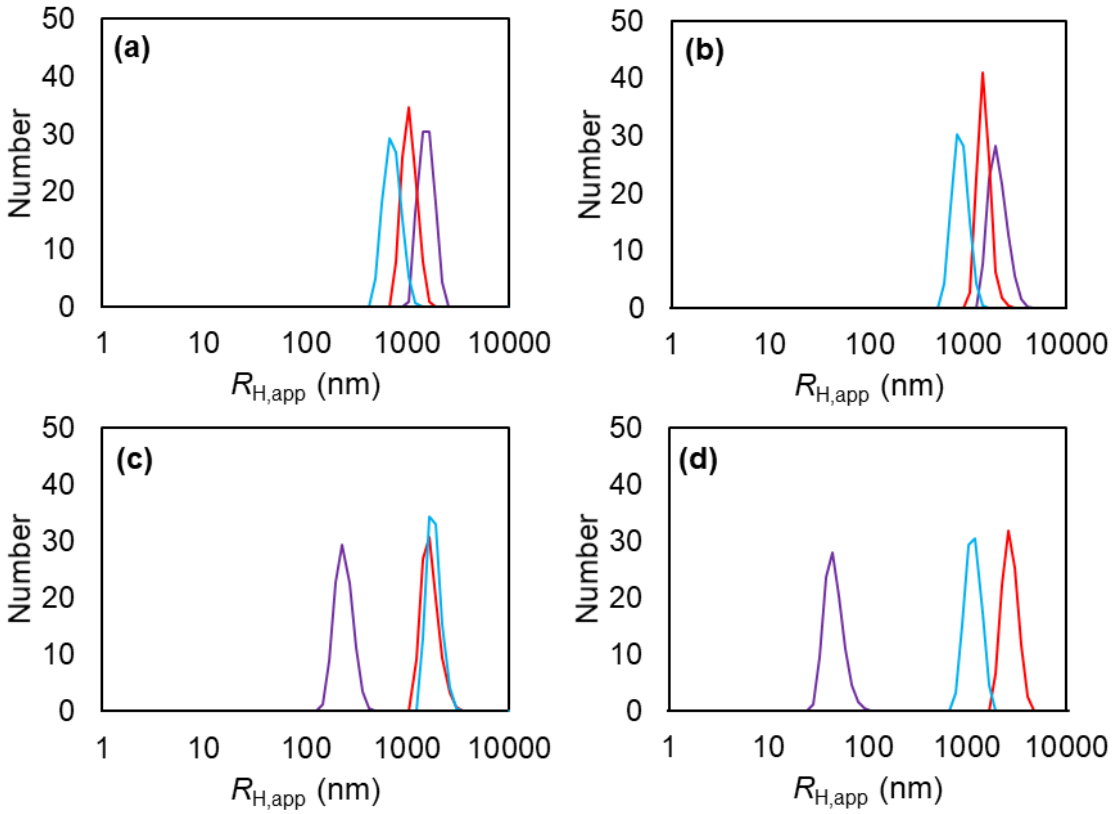

Figure S2.18 Representative number distribution DLS plots of $PFS_{23}[PPh_2Me]X$ platelet micelles formed through seeded growth from PFS_{24}-*b*-$P2VP_{384}$ 1D micelles (L_n = 26 nm, L_w/L_n = 1.19) in *i*PrOH at a m_{unimer}/m_{seed} of 10 and at (a) 0.1 wt%, (b) 0.2 wt%, (c) 0.3 wt%, and (d) 0.4 wt%. X = I (purple), SDS (blue), AOT (red).

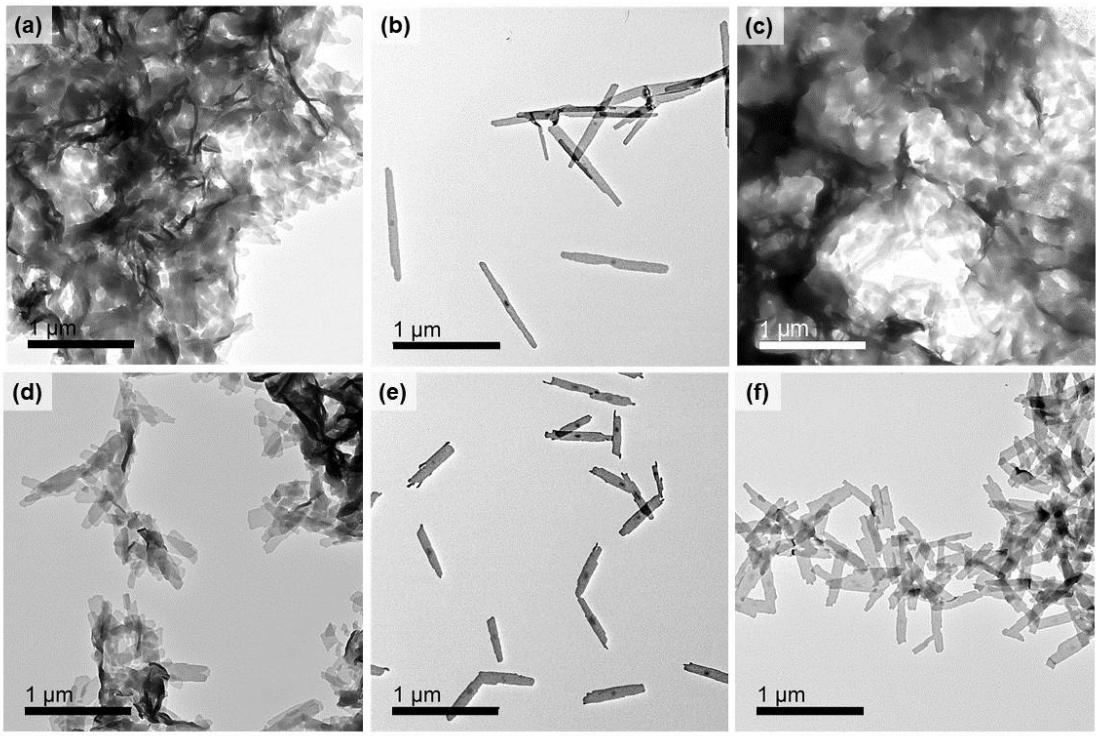

Figure S2.19 Representative TEM images of (a), (d) $PFS_{23}[PPh_2Me]I$, (b), (e) $PFS_{23}[PPh_2Me]SDS$ and (c), (f) $PFS_{23}[PPh_2Me]AOT$ platelet micelles formed through high concentration (0.4 wt%) seeded growth at (a)–(c) 22 ºC or (d)–(f) 40 ºC from PFS_{24}-*b*-$P2VP_{384}$ 1D micelles (L_n = 26 nm, L_w/L_n = 1.19) in *i*PrOH at m_{unimer}/m_{seed} = 10. Scale bars: 1 µm.

2.6.6 Supplementary Tables

Table S2.1 Diffusion coefficients of resonances arising from the surfactant counteranion obtained from ^{1}H DOSY NMR analysis of $PFS_{23}[PPh_2Me]X$ compared with that of the sodium salts of the counteranions, Na[SDS] and Na[AOT].

	δ (ppm)	**Proton**	**Diffusion coefficient (m^2/s)**
Na[SDS]	1.35–1.32	-C*H*$_2$-	4.94 x 10^{-5}
$PFS_{23}[PPh_2Me]$SDS	1.34–1.33		2.44 x 10^{-6}
Na[AOT]	0.96–0.91	-CH_2CH_3	4.47 x 10^{-9}
$PFS_{23}[PPh_2Me]$AOT	0.95–0.88		2.03 x 10^{-6}

Table S2.2 Parameters obtained from statistical analysis of contour area measurements for $PFS_{23}[PPh_2Me]$I platelet micelles formed through seeded growth from PFS_{24}-*b*-$P2VP_{384}$ 1D micelles (L_n = 26 nm, L_w/L_n = 1.19) in *i*PrOH at 0.01 wt% and various m_{unimer}/m_{seed}.

m_{unimer}/m_{seed}	A_n (x 10^2 nm^2)	σ (x 10^2 nm^2)	A_w/A_n	R_n	R_w/R_n
5	189	23	1.02	5.1	1.02
10	342	34	1.01	4.1	1.01
20	716	42	1.00	4.0	1.01
30	1086	85	1.01	3.9	1.00
40	1272	83	1.00	3.7	1.00

Table S2.3 Parameters obtained from statistical analysis of contour area measurements for PFS_{23}[PPh_2Me]SDS platelet micelles formed through seeded growth from PFS_{24}-*b*-$P2VP_{384}$ 1D micelles (L_n = 26 nm, L_w/L_n = 1.19) in *i*PrOH at 0.01 wt% and various m_{unimer}/m_{seed}.

m_{unimer}/m_{seed}	A_n (x 10^2 nm^2)	σ (x 10^2 nm^2)	A_w/A_n	R_n	R_w/R_n
5	173	21	1.01	4.7	1.02
10	320	56	1.03	5.1	1.02
20	633	63	1.01	4.0	1.01
30	952	88	1.01	3.5	1.01
40	1219	130	1.01	3.5	1.02

Table S2.4 Parameters obtained from statistical analysis of contour area measurements for PFS_{23}[PPh_2Me]AOT platelet micelles formed through seeded growth from PFS_{24}-*b*-$P2VP_{384}$ 1D micelles (L_n = 26 nm, L_w/L_n = 1.19) in *i*PrOH at 0.01 wt% and various m_{unimer}/m_{seed}.

m_{unimer}/m_{seed}	A_n (x 10^2 nm^2)	σ (x 10^2 nm^2)	A_w/A_n	R_n	R_w/R_n
5	289	32	1.01	3.8	1.01
10	319	29	1.01	3.5	1.01
20	702	82	1.01	3.0	1.01
30	829	65	1.01	3.3	1.01
40	1373	123	1.01	2.7	1.00

Table S2.5 Parameters obtained from statistical analysis of contour area measurements for PFS_{23}[PPh_2Me]I platelet micelles formed through seeded growth from PFS_{24}-*b*-$P2VP_{384}$ 1D micelles (L_n = 26 nm, L_w/L_n = 1.19) in *i*PrOH. All experiments were carried out at room temperature (22 ºC) and a m_{unimer}/m_{seed} of 10.

wt%	A_n (x 10^2 nm^2)	σ (x 10^2 nm^2)	A_w/A_n	R_n	R_w/R_n
0.01	342	34	1.01	4.1	1.01
0.1	327	63	1.04	3.4	1.02
0.2	342	102	1.09	3.3	1.02
0.3	415	98	1.06	3.7	1.02
0.4	-	-	-	-	-

Table S2.6 Parameters obtained from statistical analysis of contour area measurements for PFS_{23}[PPh_2Me]SDS platelet micelles formed through seeded growth from PFS_{24}-*b*-$P2VP_{384}$ 1D micelles (L_n = 26 nm, L_w/L_n = 1.19) in *i*PrOH. All experiments were carried out at room temperature (22 ºC) and a m_{unimer}/m_{seed} of 10.

wt%	A_n (x 10^2 nm^2)	σ (x 10^2 nm^2)	A_w/A_n	R_n	R_w/R_n
0.01	320	56	1.03	5.1	1.02
0.1	321	69	1.05	3.0	1.02
0.2	325	87	1.07	3.7	1.02
0.3	389	115	1.09	4.9	1.03
0.4	821	400	1.24	10.0	1.09

Table S2.7 Parameters obtained from statistical analysis of contour area measurements for PFS_{23}[PPh_2Me]AOT platelet micelles formed through seeded growth from PFS_{24}-*b*-$P2VP_{384}$ 1D micelles (L_n = 26 nm, L_w/L_n = 1.19) in *i*PrOH. All experiments were carried out at room temperature (22 ºC) and a m_{unimer}/m_{seed} of 10.

wt%	A_n (x 10^2 nm^2)	σ (x 10^2 nm^2)	A_w/A_n	R_n	R_w/R_n
0.01	319	32	1.01	3.5	1.01
0.1	303	73	1.06	3.6	1.02
0.2	300	75	1.06	3.5	1.02
0.3	330	74	1.05	4.0	1.03
0.4	-	-	-	-	-

Table S2.8 Parameters obtained from statistical analysis of contour area measurements for PFS_{20}-*b*-$P2VP_{19}$ platelet micelles formed through seeded growth from PFS_{24}-*b*-$P2VP_{384}$ 1D micelles (L_n = 26 nm, L_w/L_n = 1.19) in *i*PrOH. All experiments were carried out at room temperature (22 ºC) and a m_{unimer}/m_{seed} of 10.

wt%	A_n (x 10^2 nm^2)	σ (x 10^2 nm^2)	A_w/A_n	R_n	R_w/R_n
0.01	84	19	1.05	4.6	1.04
0.1	94	24	1.07	5.8	1.05
0.2	81	27	1.11	6.2	1.07
0.3	84	38	1.20	6.4	1.08
0.4	197	70	1.13	6.8	1.05

Table S2.9 Average apparent hydrodynamic radii ($R_{H,app}$) for $PFS_{23}[PPh_2Me]X$ platelet micelles formed through seeded growth from PFS_{24}-*b*-$P2VP_{384}$ 1D micelles (L_n = 26 nm, L_w/L_n = 1.19) in *i*PrOH. All self-assembly experiments were carried out at room temperature (22 ºC) and a m_{unimer}/m_{seed} of 10. Values are calculated from five repeat scattering experiments.

	$PFS_{23}[PPh_2Me]I$		$PFS_{23}[PPh_2Me]SDS$		$PFS_{23}[PPh_2Me]AOT$	
wt%	$R_{H,app}$ **(nm)**	**σ (nm)**	$R_{H,app}$ **(nm)**	**σ (nm)**	$R_{H,app}$ **(nm)**	**σ (nm)**
0.1	2127	743	2312	600	3274	432
0.2	2233	340	2390	634	2229	396
0.3	1162	417	3991	939	2618	158
0.4	270	160	1081	57	2314	273

Table S2.10 Number-average length (L_n) (obtained from statistical analysis of contour length) for $PFS_{23}[PPh_2Me]X$ platelet micelles formed through seeded growth from PFS_{24}-*b*-$P2VP_{384}$ 1D micelles (L_n = 26 nm, L_w/L_n = 1.19) in *i*PrOH. All self-assembly experiments were carried out at room temperature (22 ºC) and a m_{unimer}/m_{seed} of 10.

	$PFS_{23}[PPh_2Me]I$		$PFS_{23}[PPh_2Me]SDS$		$PFS_{23}[PPh_2Me]AOT$	
wt%	L_n **(nm)**	**σ (nm)**	L_n **(nm)**	**σ (nm)**	L_n **(nm)**	**σ (nm)**
0.1	330	38	306	39	326	41
0.2	330	63	345	56	319	48
0.3	387	55	432	85	360	60
0.4	-	-	881	297	-	-

Table S2.11 Parameters obtained from statistical analysis of contour area measurements for $PFS_{23}[PPh_2Me]X$ platelet micelles formed through seeded growth from PFS_{24}-*b*-$P2VP_{384}$ 1D micelles (L_n = 26 nm, L_w/L_n = 1.19) in *i*PrOH. Experiments were carried out at 40 °C and a m_{unimer}/m_{seed} of 10.

Homopolymer	A_n **(x 10^2 nm^2)**	**σ (x 10^2 nm^2)**	A_w/A_n	R_n	R_w/R_n
$PFS_{23}[PPh_2Me]I$	-	-	-	-	-
$PFS_{23}[PPh_2Me]SDS$	554	188	1.12	4.6	1.02
$PFS_{23}[PPh_2Me]AOT$	543	168	1.10	4.5	1.03

2.6.7 Supplementary References

(1) Rider, D. A.; Cavicchi, K. A.; Power-Billard, K. N.; Russell, T. P.; Manners, I. Diblock Copolymers with Amorphous Atactic Polyferrocenylsilane Blocks: Synthesis, Characterization, and Self-Assembly of Polystyrene-Block-Poly(Ferrocenylethylmethylsilane) in the Bulk State. *Macromolecules* **2005**, *38* (16), 6931–6938.

(2) He, X.; Hsiao, M.-S.; Boott, C. E.; Harniman, R. L.; Nazemi, A.; Li, X.; Winnik, M. A.; Manners, I. Two-Dimensional Assemblies from Crystallizable Homopolymers with Charged Termini. *Nat. Mater.* **2017**, *16*, 481–488.

(3) Wang, H.; Winnik, M. A.; Manners, I. Synthesis and Self-Assembly of Poly(Ferrocenyldimethylsilane-b-2-Vinylpyridine) Diblock Copolymers. *Macromolecules* **2007**, *40* (10), 3784–3789.

Chapter 3 Scalable, Low Dispersity, and Length-Tunable Block Copolymer Nanofibers with a Biodegradable Polycarbonate Core via Living Polymerization-Induced Crystallization-Driven Self-Assembly

3.1 Abstract

Uniform 1D block copolymer (BCP) nanofibers prepared by the seeded growth approach termed living crystallization-driven self-assembly (CDSA) offer significant potential advantages for various applications due to their anisotropy, length tunability, and spatially-defined functionalization. However, this procedure consists of a multi-step process involving independent BCP synthesis and self-assembly steps, the latter of which is performed at low solution concentrations (< 1 wt%) hindering scale-up. Here, we demonstrate the use of a one-pot BCP synthesis–self-assembly process, polymerization-induced CDSA (PI-CDSA), to access length-disperse nanofibers with a biodegradable, crystalline poly(fluorenetrimethylenecarbonate) (PFTMC) core and a hydrophilic poly(ethylene glycol) (PEG) corona derived from PEG-*b*-PFTMC at concentrations up to 20 wt%, 400 times higher than previously reported. Furthermore, living PI-CDSA could be used to access scalable, low dispersity, and length-tunable 1D PEG-*b*-PFTMC nanofibers at concentrations of up to 10 wt%. This provides the first example of living PI-CDSA involving an all-organic and biodegradable BCP and utilizing a readily implemented BCP synthesis protocol that does not involve living anionic polymerization. Significantly, samples of low dispersity nanofibers of controlled lengths from 100–660 nm (L_w/L_n = 1.08–1.20) were prepared,

allowing for upscaled access to well-defined biodegradable nanofibers at useful length-scales for applications in nanomedicine.

3.2 Introduction

One-dimensional (1D) nanostructures formed from self-assembled block copolymers (BCPs) are of interest for a wide range of applications, involving uses as additives for composite reinforcement[1,2] to cancer therapeutics[3–8] and hydrogels[9] for biomedical applications.[10,11] In the field of nanomedicine, 1D micelles have been found to exhibit advantageous characteristics as nanocarriers including enhanced circulation times,[7,8,12] retention,[13,14] cellular uptake and binding,[5,15–18] and tumor penetration,[3,4,19] as well as exhibiting low immune cell association.[6] However, the scale-up of 1D micelles remains a challenge due to two main issues associated with their preparation. First, the formation of 1D micelles via the self-assembly of the most well-studied BCPs which possess an amorphous core-forming block is challenging as spherical micelles and vesicles generally dominate the phase diagram.[20,21] As a result, morphologically pure 1D micelles typically only exist in a narrow region of phase space, making them difficult to access.[21,22] Second, BCP self-assembly is generally a multi-step process consisting of separate BCP synthesis, purification, and self-assembly steps. The post-polymerization self-assembly step is usually performed at low solution concentrations (< 1 weight percent solids (wt%)), which further hinders scale-up. A further problem is that for most applications, control of 1D micelle length and the use of low dispersity samples is highly desirable. Existing BCP self-assembly procedures with amorphous core-forming blocks generally do not permit effective length control and yield highly length-disperse samples.[20,21] Notable recent developments, however, include a promising approach using sonication.[22]

To manufacture BCP micelles on an industrial scale, a one-pot process carried out at high solution concentration is highly desirable. Polymerization-induced self-assembly (PISA), in which polymerization and self-assembly occur *in situ* at concentrations of 10–50 wt%, allows for the

scaled-up preparation of BCP micelles.[23–27] PISA initially involves the synthesis of a macroinitiator that will act as the corona in the resulting micelles. The second monomer is subsequently macroinitiated in the presence of a selective solvent for the corona-forming block. As the degree of polymerization (DP_n) of the core-forming block increases, it progressively becomes more insoluble in the selective solvent, resulting in self-assembly being induced.[25] Therefore, PISA is characterized by synchronous polymerization and self-assembly. Throughout the PISA process, the micelle morphology typically evolves through a sphere–cylinder–vesicle transition, which usually corresponds to changes in the corona-to-core block ratio during the polymerization.[28,29] Generally, PISA employs controlled radical polymerizations such as reversible addition-fragmentation chain transfer (RAFT) polymerization[23–25,30–33] and nitroxide-mediated polymerization (NMP).[26,34] These techniques allow BCPs with controlled molecular weight and low dispersity to be accessed.[28,35,36] Although PISA allows access to BCP micelles at high solution concentrations, the challenges of exclusively targeting the 1D morphology and obtaining length-control and uniform samples still remain.[37]

The presence of a crystallizable core-forming segment in the BCP provides an additional driving force for the formation of nanostructures with low curvature of the core–corona interface, such as fiber-like micelles,[21] thereby overcoming the challenge of accessing 1D micelles. Crystallization-driven self-assembly (CDSA) of BCPs with a crystallizable core-forming block therefore allows for the facile preparation of morphologically pure 1D micelles or nanofibers.[10,21,38–41] Furthermore, uniform nanofibers of targeted length can be accessed by the seeded growth method terming "living" CDSA.[42] First, small "seed" micelles which possess low length-dispersities are prepared by ultrasonication and fragmentation of polydisperse nanofibers accessed via CDSA.[43] The crystalline core termini of the seeds remain active to epitaxial growth, thereby enabling elongation of the nanofibers on addition of molecularly dissolved BCP or "unimer".[42,44] The resulting uniform

1D micelles possess narrow length-dispersities and specific fiber lengths can be targeted by simply varying the unimer-to-seed mass ratio (m_{unimer}/m_{seed}).[42]

Living CDSA[37,45–48] has been employed for a variety of amphiphilic BCPs with crystallizable core-forming segments such as poly(ferrocenyldimethylsilane) (PFS),[21,42] polyethylene,[49,50] poly(*L*-lactide) (PLLA),[40,51,52] and poly(3-hexylthiophene).[48,53,54] More recent work has focused on examples of interest for biomedical applications such as polycaprolactone,[11,55] poly(isopropyloxazoline),[6] poly(fluorenetrimethylenecarbonate) (PFTMC),[56,57] in addition to biopolymer-based building blocks that include polypeptides,[58] DNA-polymer hybrids[59] and collagen triple helices.[60] 1D micelles containing a PFTMC core segment are of significant interest for biomedical applications due to their non-toxicity, biocompatibility, and biodegradability.[56,57,61–63] Recently, we illustrated the potential use of uniform 1D PFTMC-based nanofibers as drug delivery vehicles by demonstrating their loading with hydrophobic cargo.[57] Despite the promise of PFTMC-based nanofibers for biomedical applications, these micelles have only been accessible by living CDSA at low solution concentrations (< 1 wt%), in turn hindering their investigation and development of applications.

We have previously reported a method termed polymerization-induced crystallization-driven self-assembly (PI-CDSA) whereby polymerization and self-assembly of a BCP with a crystallizable core-forming block occurs *in situ*.[64,65] PI-CDSA therefore combines the advantages of CDSA (i.e. targeting low-curvature micelle morphology) with that of PISA (i.e. scale-up capability).[64,65] The first examples of PI-CDSA employed the metallopolymer PFS as the crystalline core-forming segment in BCPs prepared via living anionic polymerization,[64,65] since PFS is an extensively studied model system for CDSA protocols. Several similar one-pot approaches have since been developed by employing various polymerization techniques, including the ring-opening metathesis PI-CDSA (ROMPI-CDSA) of a ruthenocene-containing polymer,[66] ring-opening PI-CDSA (ROPI-CDSA) of BCPs with a PLLA core-forming segment,[67] and polymerization-induced hierarchical

self-assembly (PIHSA) of liquid crystal-containing polymers.[68,69] Although these methods target exclusively morphologies with low curvature of the core–corona interface such as 1D fibers, they lack size-control and therefore uniform samples with specific fiber lengths cannot be accessed.

Uniform 1D micelles of controlled length can be accessed at scalable concentrations via the seeded growth process living PI-CDSA.[64,65] This one-pot technique combines the advantages of PISA with living CDSA to access uniform length-controlled 1D nanostructures at 10 wt% through synchronous polymerization, self-assembly, and seeded growth.[64,65] The only examples of living PI-CDSA to date, however, utilize PFS-based BCPs prepared via the challenging to implement living anionic polymerization approach and the resulting nanofibers are primarily of interest for proof-of-concept self-assembly studies.[64,65] Recent approaches in which seeds are thermally generated *in situ* have been developed to allow the scaled formation of nanofibers with a PFS core.[70]

Herein, we demonstrate the scope of living PI-CDSA can be extended to functional, all-organic BCPs. Specifically, we describe the use of living PI-CDSA to access scalable low dispersity nanofibers with a crystalline biodegradable PFTMC core and a hydrophilic "stealth" poly(ethylene glycol) (PEG) corona. Significantly, the corresponding PEG-*b*-PFTMC BCP building block can be prepared *in situ* via a convenient ring-opening polymerization (ROP) method from readily accessible precursors. We also demonstrate that the resulting upscaled biodegradable PFTMC-based nanofibers can be formed over a range of lengths useful for applications in nanomedicine.

3.3 Results and Discussion

3.3.1 Preparation of polydisperse PEG_{205}-*b*-$PFTMC_n$ fibers via PI-CDSA at various concentrations (5–20 wt%)

PI-CDSA experiments were performed using poly(ethylene glycol) methyl ether (PEG_{205}) to macroinitiate the ROP of the cyclic fluorenetrimethylenecarbonate (FTMC) monomer, using 1,8-diazabicyclo[5.4.0]undec-7-ene (DBU) as the ROP catalyst.[56] As per the criteria of the PI-CDSA

process,[64–66] using a solvent system in which the PEG_{205} corona-forming block remains soluble was essential. The same solvent system must also be a poor solvent for the PFTMC core-forming block as the DP_n increases, in order to induce self-assembly and crystallization.[64,66] The CDSA of PEG-*b*-PFTMC has previously been reported using dimethyl sulfoxide (DMSO) and methanol (MeOH) as the common and selective solvents, respectively.[56] However, since the polymerization and self-assembly occur *in situ* during the PI-CDSA process, experiments must proceed in the absence of water to avoid premature quenching. Furthermore, nucleophilic alcohol species, such as methanol, can initiate the ROP of FTMC thereby compromising the controlled polymerization process. It was therefore required that aprotic solvents were selected for the PI-CDSA experiments. A solvent screen was therefore performed using PEG_{205} and a representative $PFTMC_{18}$ homopolymer to determine an appropriate solvent system. Dichloromethane (DCM) was found to dissolve both homopolymers and was therefore selected as the common solvent. $PFTMC_{18}$ was found to be insoluble in acetonitrile (MeCN), whereas PEG_{205} dissolved. MeCN was therefore chosen to be the selective solvent. PI-CDSA experiments were carried out at solution concentrations of 5, 10, 15, and 20 wt% solids (corresponding to 47, 99, 158, and 224 mg/mL). These self-assembly concentrations are significantly higher than those used in previous studies of the CDSA of PFTMC-based BCPs which were typically performed at ca. 0.06 wt% (0.5 mg/mL).[56] Due to the *in situ* nature of the PI-CDSA process, there were no isolation or purification steps performed on the BCPs before self-assembly. First, the commercially available PEG_{205} macroinitiator was characterized by gel permeation chromatography (GPC) (**Figure S3.1** and **Table S3.1**) and was found to possess a number-average molecular weight (M_n) of 9,030 Da and a molecular weight dispersity (M_w/M_n) of 1.10. The DP_n of PEG was calculated as 205 from the M_n value obtained by GPC analysis.

The PEG_{205} macroinitiator and DBU ROP catalyst were dissolved in MeCN and to this was added FTMC monomer dissolved in DCM/MeCN (**Scheme 3.1** and **Figure S3.2**) at room temperature (22 °C), making up a final solvent composition of 20 vol% DCM/MeCN and a solution

concentration of 5, 10, 15, or 20 wt%. PFTMC core-forming blocks with a DP_n of either 40 or 18 were targeted, to give a corona-to-core block ratio of 5:1 or 11:1, respectively (**Figure S3.1** and **Table S3.1**). To monitor the PI-CDSA process and determine if synchronous polymerization and self-assembly occur, we characterized the BCP structure (via ^{1}H NMR) and micelle morphology (via TEM) throughout the process; the results are discussed below.

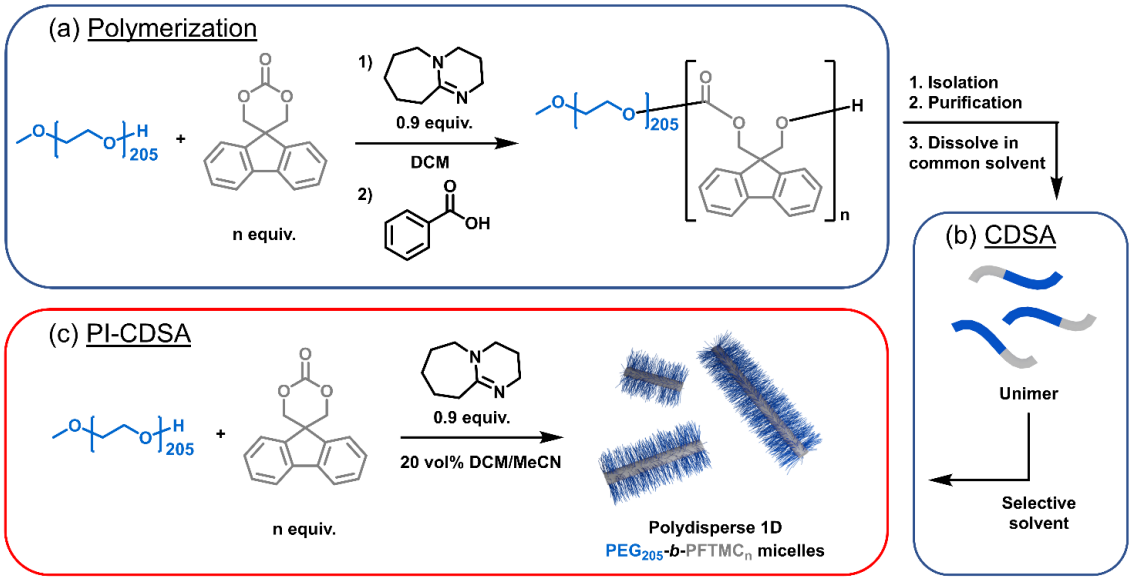

Scheme 3.1 Schematic representation of the preparation of polydisperse PEG_{205}-*b*-$PFTMC_n$ fibers (target DP_n = 40 or 18, target block ratio = 5:1 or 11:1) (a) by sequential polymerization followed by multi-step post-polymerization processing and (b) CDSA at low concentrations (ca. 0.06 wt% or 0.5 mg/mL) versus (c) by the one-pot PI-CDSA process in 20 vol% DCM/MeCN at high percentage solids of up to 20 wt% (224 mg/mL). DBU was used as the ROP catalyst. In the polymerization (a), benzoic acid was used as the quenching agent.

3.3.1.1 Effect of concentration on FTMC polymerization kinetics

PEG_{205}-*b*-$PFTMC_n$ with targeted corona-to-core block ratios of 5:1 and 11:1 (target DP_n = 40 or 18, respectively) were prepared by PI-CDSA (**Scheme 3.1**, **Figure S3.1**, and **Table S3.1**) at 5–20 wt% and 22 °C in 20 vol% DCM/MeCN. In both instances, FTMC monomer conversion at 1,

2, and 48 h after macroinitiation was calculated via ^{1}H NMR by comparing the integrals of the singlet (4.57 ppm) with that of the multiplet (4.52–4.15 ppm) which correspond to the monomeric and polymeric C*H*$_2$O protons, respectively (**Figures 3.1** and **S3.3**, and **Table S3.2**).[56,61] The final DP$_n$ of the PFTMC core-forming block of each BCP was then calculated based on the monomer conversions at each time interval (**Table S3.2**). The calculated PFTMC DP$_n$ and block ratios of each BCP corresponding to 1, 2, and 48 h after macroinitiation are shown in **Tables S3.3** and **S3.4**.

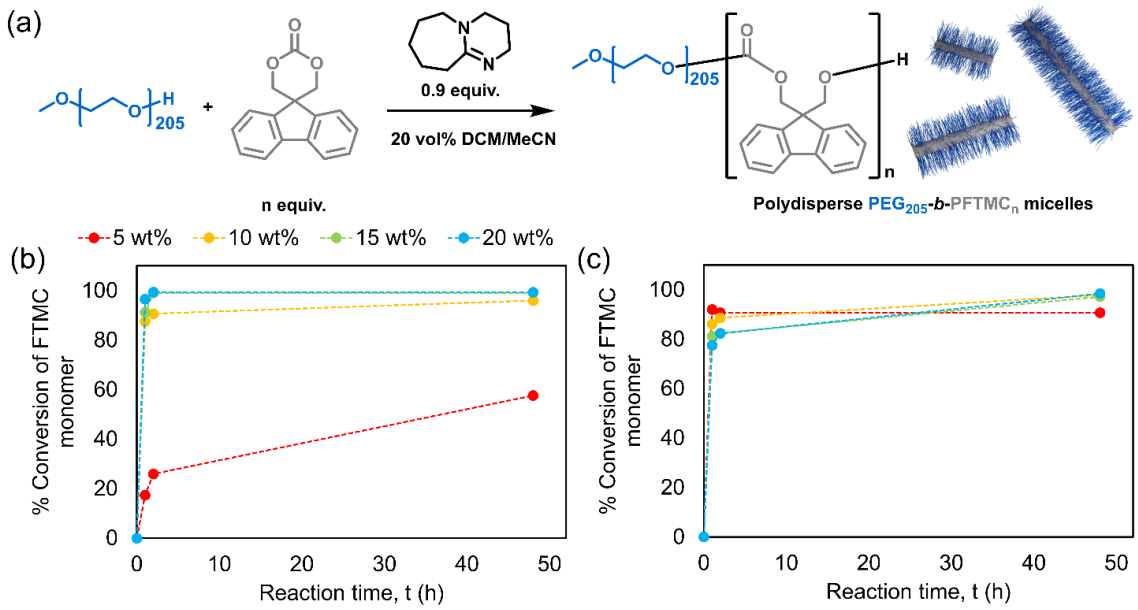

Figure 3.1 The effect of concentration on FTMC monomer conversion during the (a) PEG$_{205}$-macroinitiated ROP in the PI-CDSA of PEG$_{205}$-*b*-PFTMC$_n$ in 20 vol% DCM/MeCN at 5–20 wt%, targeting a final block ratio of (b) 5:1 or (c) 11:1. Data was obtained from ^{1}H NMR integration.

In all cases the PFTMC polymerization appeared to be complete within 1 h, as there was no significant change in PFTMC DP$_n$ or corona-to-core block ratio beyond this time interval (**Figure 3.1** and **Tables S3.3** and **S3.4**). The only exception to this was observed at a target DP$_n$ of 40 (target block ratio = 5:1) at 5 wt% (**Figure 3.1b**). As expected, higher solution concentration was found to favour increased monomer conversion (**Table S3.2**). For the targeted block ratio of 5:1, FTMC

conversion at 5 wt% was also monitored after a total of 9 days and was determined to be only 69% (DP_n = 15, block ratio = 14:1). This value was significantly lower than any monomer conversion observed at the other concentrations studied (**Figure 3.1**b, c) and may be attributed to ring–chain equilibrium effects that are well-known for other low-ring-strain monomers employed in ROPs.[61,71–73]

3.3.1.2 Effect of concentration on PEG_{205}-*b*-$PFTMC_n$ micelle morphology

The micelle morphology for the PEG_{205}-*b*-$PFTMC_n$ BCPs formed *in situ* was monitored at 1, 2, and 48 h after macroinitiation of the ROP of the FTMC monomer by taking small aliquots of the solution and immediately spotting onto carbon-coated copper grids for analysis by TEM. The samples were then stained by drop-casting uranyl acetate (3 wt% in ethanol) immediately after sample spotting. The samples were imaged by TEM after solvent evaporation. Uranyl acetate stain was used to increase the contrast of the low electron density PEG_{205}-*b*-$PFTMC_n$ micelles relative to the carbon film substrate, allowing for facile visualization of the nanostructures. The micelle cores appear bright against a dark background when stained and imaged by TEM, since uranyl acetate does not penetrate the core.[56]

The morphologies for the PEG_{205}-*b*-$PFTMC_n$ BCPs (target block ratio = 5:1, target DP_n = 40) observed throughout the PI-CDSA process are shown in **Figure 3.2**. At a lower concentration of 5 wt%, self-assembly was not complete until 48 h (**Figure 3.2**c). This is likely due to the decreased polymerization rate at this concentration (see above) resulting in low DP_n values for the PFTMC core-forming block (**Table S3.3**) and high block ratios (**Table S3.4**). At 1 and 2 h after macroinitiation, these DP_n values (4 and 7, respectively) are likely below the critical DP_n at which we would expect self-assembly to be induced at this concentration. At higher concentrations of 10–20 wt%, self-assembly was complete within 1 h of macroinitiation (**Figure 3.2**d, g, j) yielding a mixture of spherical and fiber-like micelles. The formation of spheres has been previously detected with PFTMC-containing BCPs and has been attributed to self-assembly that takes place too fast to

allow for core crystallization.[56] Higher solution concentrations would also be expected to increase the rate of self-assembly since aggregation of the amphiphilic PEG_{205}-*b*-$PFTMC_n$ BCP should be favoured to a greater extent,[74] which is also consistent with our results.

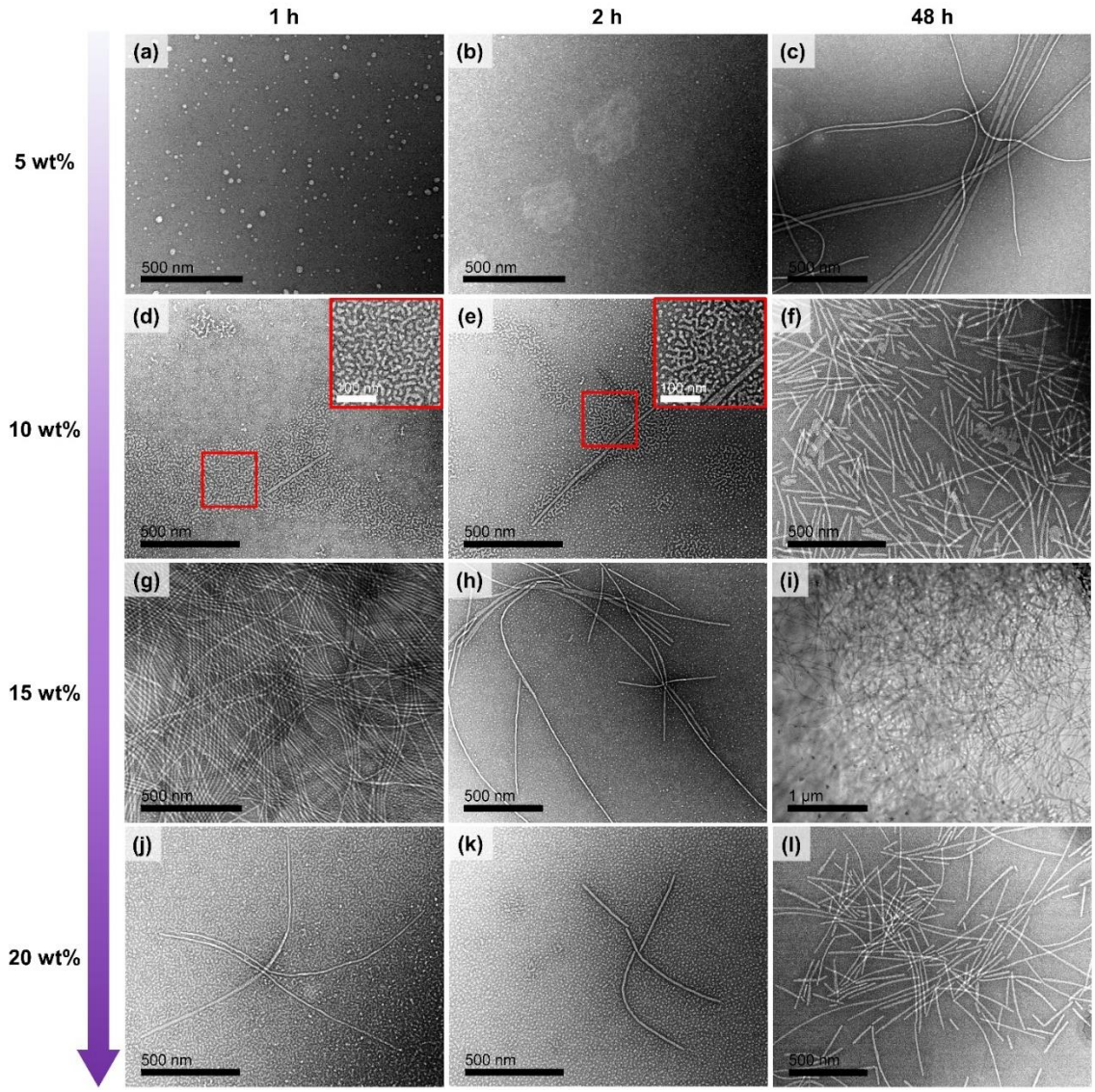

Figure 3.2 Representative TEM images of PEG_{205}-*b*-$PFTMC_n$ micelles (target DP_n = 40, target block ratio = 5:1) prepared via PI-CDSA in 20 vol% DCM/MeCN at (a)–(c) 5 wt%, (d)–(f) 10 wt%, (g)–(i) 15 wt%, or (j)–(l) 20 wt%, observed at 1, 2, or 48 h after macroinitiation. Higher magnification insets of (d) and (e) show intermediate morphology, with red box indicating location of inset. Solution samples of 0.5 mg/mL were drop-cast, stained with uranyl acetate

solution (3 wt% in ethanol), and imaged after solvent evaporation. Scale bars: (a)–(h), (j)–(l) 500 nm, (d, e) inset: 100 nm, (i) 1000 nm.

At 10–20 wt%, morphologically pure fibers were obtained after 48 h through a sphere-to-fiber transition (**Figure 3.2**f, i, l). At 5 wt%, the rate of core crystallization appears to be slower, with morphologically pure fibers obtained only after 9 days (**Figure S3.4**). Again, this is likely due to the significantly lower PFTMC DP_n exhibited at 5 wt% (DP_n = 14, block ratio = 15:1) compared with that at higher concentrations (DP_n = 34–38, block ratio = ca. 5:1) (**Tables S3.3** and **S3.4**). Interestingly, the DP_n of PFTMC after 9 days was found to be 15, an increase of only one monomer unit (and no significant change in block ratio) compared to that after 48 h, yet morphologically pure 1D fibers were observed rather than a mixture with spheres (**Figure S3.4**). This result suggests that the polymerization and self-assembly are not coupled during the PI-CDSA process (i.e. the micelle morphology is not necessarily determined by the block ratio) as is usually found to be the case in BCP self-assembly.[64]

Interestingly, potential intermediate morphologies arising during the sphere-to-fiber transition were observed in several instances. For example, in the cases of 1 and 2 h after macroinitiation at 10 wt% the presence of several elongated structures that appear to consist of fused spheres can be detected (**Figure 3.2**d and e). Size analysis was performed on these assemblies to determine their number-average width (W_n) in comparison with the number-average diameter (D_n) of the spherical micelles and the W_n of the final fiber-like micelles. After 1 and 2 h, the spherical micelles exhibited diameters of D_n = 6.0 ± 1.2 nm (D_w/D_n = 1.04) (**Figure 3.2**d) and D_n = 6.5 ± 1.1 nm (D_w/D_n = 1.03) (**Figure 3.2**e), respectively. The corresponding intermediate morphologies exhibit slightly larger widths (W_n = 7.7 ± 0.2 nm , W_w/W_n = 1.04, **Figure 3.2**d; W_n = 7.2 ± 0.2 nm, W_w/W_n = 1.05, **Figure 3.2**e), which were in turn smaller than the that for the nanofibers after 48 h (12 ± 2 nm, W_w/W_n = 1.03, **Figure 3.2**f) by TEM. The possible intermediate morphologies were also observed after 1 and 2 h of macroinitiation at 15 and 20 wt% (**Figure 3.2**g, h, j, and k). These observations may

provide insight into the mechanism of the detected morphological sphere-to-nanofiber transition. This process is presumably driven by the reorganization of amorphous PFTMC core chains into thermodynamically preferred 1D fiber-like morphology with a crystalline core. The mechanism may involve the fused sphere assemblies as intermediates and unimer release into solution may also take place.[56,75–78]

The morphologies of PEG_{205}-*b*-$PFTMC_n$ (target block ratio of 11:1, target DP_n = 18) observed throughout the PI-CDSA process are shown in **Figure 3.3**. For example, at 5 wt%, self-assembly appears to be absent (**Figure 3.3**a–c), likely resulting from the increased solubility of PEG_{205}-*b*-$PFTMC_n$ in these experiments (observed block ratios ca. 20:1, **Table S3.4**) combined with the lower solution concentration. To investigate whether unimer remained under these conditions and led to the observed TEM images (**Figure 3.3**a–c), we prepared a unimer solution (in DCM) of an independently prepared BCP, PEG_{205}-*b*-$PFTMC_{37}$, and compared images of the resulting films after solvent evaporation (**Figure S3.5**). Through visual comparison, it appears that unimer film and spherical micelles form on solvent evaporation of the samples from the PI-CDSA experiments (**Figure 3.3**a–c) thereby confirming that self-assembly is absent under these conditions. At 10 wt%, self-assembly is complete after 2 h (**Figure 3.3**e) whereas at a decreased target block ratio of 5:1, self-assembly was complete within 1 h (**Figure 3.2**d). The decreased rate of self-assembly exhibited at the larger corona-to-core block ratio of 11:1 can be explained by the resulting improved solubility of the PEG_{205}-*b*-$PFTMC_n$ BCP (observed block ratio ca. 19:1, **Table S3.4**).

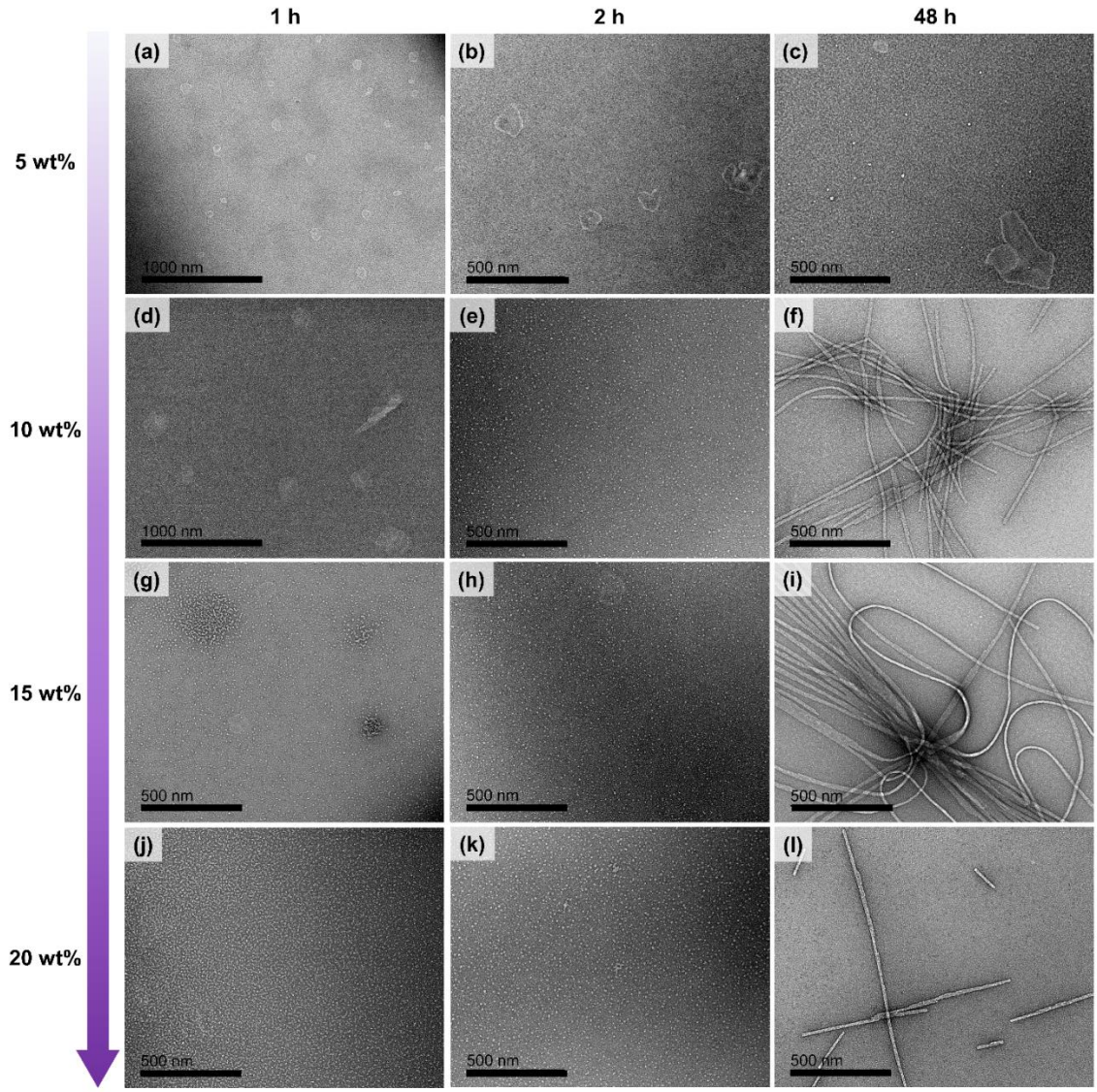

Figure 3.3 Representative TEM images of PEG_{205}-*b*-$PFTMC_n$ micelles (target DP_n = 18, target block ratio = 11:1) prepared via PI-CDSA in 20 vol% DCM/MeCN at (a)–(c) 5 wt%, (d)–(f) 10 wt%, (g)–(i) 15 wt%, or (j)–(l) 20 wt%, observed at 1, 2, or 48 h after macroinitiation. Solution samples of 0.5 mg/mL were drop-cast, stained with uranyl acetate solution (3 wt% in ethanol), and imaged after solvent evaporation. Scale bars: (a, d) 1000 nm, (b, c) and (e)–(l) 500 nm.

At a target corona-to-core block ratio of 11:1, we again observed a general increase in the rate of self-assembly with increased concentration. For instance, self-assembly was complete within 2 h

at 10 wt% (**Figure 3.3**e) and within 1 h at 15 and 20 wt% (**Figure 3.3**g and j). After 48 h following macroinitiation, morphologically pure fibers were formed at concentrations of 10–20 wt% (**Figure 3.3**f, i, and l) whereas at 5 wt%, no self-assembly was detected, as discussed above. These observations provide further support for the conclusion that the self-assembly of PEG_{205}-*b*-$PFTMC_n$ was not coupled to the polymerization, since similar block ratios within the range of 17:1–21:1 were found at 5–20 wt% after 48 h (**Table S3.4**). This range of block ratios has been shown to correspond to the formation of fibers in previous CDSA experiments,[56] yet, in this work, we observed the presence of spheres and/or fibers, or a complete lack of self-assembly, depending on the time following the macroinitiation step. Concentration therefore appears to play a crucial role, affecting the polymerization rate, which in turn affects the rate of self-assembly.

The sphere-to-fiber morphological evolution was also observed at this target block ratio of 11:1. However, morphologically pure spheres were initially observed rather than a mixture of morphologies as detected at a target block ratio of 5:1. These results suggest that, under these conditions of a larger target and observed block ratio (11:1), the sphere-to-fiber evolution occurs more slowly. A "break out" mechanism has previously been proposed whereby spherical aggregates occasionally form a single localized crystalline domain which is subsequently elongated via epitaxial growth.[77,79] The amorphous core of the spherical micelles may be penetrated by the solvent to assist the onset of crystallization and therefore the formation of nucleation sites.[77] The remaining spherical micelles could then act as a unimer reservoir to allow for 1D fiber elongation. Since the 1D fibers are generally long (> 2 μm), we conclude that nucleation events are rare with a very slow associated rate. The apparent intermediate fused sphere morphology between that of spheres and fibers was also observed in the case of the targeted 11:1 block ratio, after 2 h at 10 wt% (**Figure 3.3**e) and after both 1 and 2 h at 15 and 20 wt% (**Figure 3.3**g, h, j, and k).

Under all conditions studied, the PI-CDSA solutions were initially transparent since the PEG_{205} macroinitiator and FTMC monomer were fully dissolved. As the PI-CDSA proceeded, the solutions

generally became more turbid, with increasing concentrations yielding viscous solutions (**Figures S3.6** and **S3.7**). One exception was observed when a block ratio of 11:1 was targeted at 5 wt%, since the solution viscosity or opacity did not notably increase after 48 h (**Figure S3.7**a). This is likely due to the lack of self-assembly, as shown in **Figure 3.3**c. The increased viscosity of the PI-CDSA solutions generally correlated to the presence of fibers, which is likely due to their high aspect ratio and anisotropic shape.[80] Formation of polydisperse fiber-like micelles at a target block ratio of 11:1 and a concentration of 10 wt% was deemed to be optimal since the viscous solution was easy to process further, for example to prepare seed micelles via sonication (see below). At higher concentrations, the solutions became significantly more turbid, likely due to precipitated nanofibers resulting from the presence of only small volumes of solvent, which prevented facile processing and efficient sonication.

3.3.2 Preparation of PEG_{205}-*b*-$PFTMC_{17}$ seed micelles (L_n = 39 nm) at 10 wt% via PI-CDSA and subsequent sonication

To explore the formation of scalable uniform 1D nanofibers via living PI-CDSA, our attention first turned to preparing low dispersity seed micelles for use in the seeded growth process. Typically, seed micelles are prepared at low concentrations of ca. 0.06 wt% (0.5 mg/mL) via sonication. In previous attempts to scale-up seeded growth processes, a BCP was first synthesized and then purified before self-assembly and sonication were performed (at ca. 0.6 wt% or 5 mg/mL).[64,65,81] As the scaled-up preparation of seed micelles by PI-CDSA followed by sonication was unexplored, we performed experiments to develop this potentially highly advantageous approach.

Polydisperse 1D fibers were prepared by PI-CDSA at 10 wt% (**Figure 3.4**a) as previously described, with the final BCP structure determined to be PEG_{205}-*b*-$PFTMC_{17}$ by ^{1}H NMR (**Figure S3.8**). The fibers were sonicated at 10 °C and the fiber length (L_n) and width (W_n) were monitored as a function of sonication time from 15 min to 6 h (**Figures 3.4**, **S3.9** and **S3.10**, and **Table S3.5**). Fragmentation of PEG_{205}-*b*-$PFTMC_{17}$ 1D micelles was found to depend strongly on the micelle

length, with scission of longer fiber-like micelles occurring more easily than that of short micelles (**Figure S3.9**), as has been previously been observed for PFS-containing 1D micelles.[43] After a total sonication time of 6 h at 10 °C, uniform PEG_{205}-*b*-$PFTMC_{17}$ seed micelles (L_n = 39 nm, L_w/L_n = 1.18) at 10 wt% were accessed (**Figures 3.4**b and **S3.9**f). Fragmentation of the long polydisperse fibers resulted in a reduction of solution viscosity, likely due to the reduced fiber length and therefore aspect ratio. The 1D fiber number-average width (W_n) was found to remain constant within standard deviation at ca. 16–18 nm (determined by TEM analysis) throughout the sonication process (**Figure S3.10**). However, closer inspection shows two populations of seed micelle as a result of the micelles, which exhibit a rectangular cross-section,[56] lying on the TEM grid either on their largest face or on their narrower edge. The two widths are centered around ca. 18 and 26 nm (**Figure S3.11**), with the majority of seeds lying on their narrower edge.

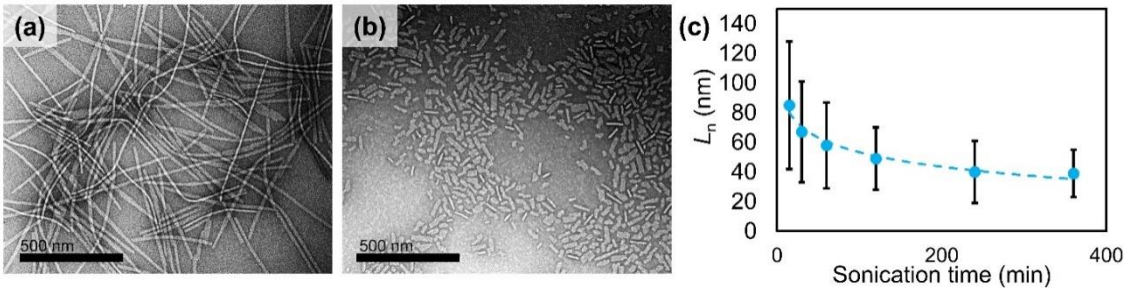

Figure 3.4 Representative TEM images of (a) polydisperse PEG_{205}-*b*-$PFTMC_{17}$ fibers prepared via PI-CDSA in 20 vol% DCM/MeCN at 10 wt% and (b) seed micelles prepared by sonication of polydisperse PEG_{205}-*b*-$PFTMC_{17}$ fibers for 6 h at 10 °C and 10 wt% (L_n = 39 nm, L_w/L_n = 1.18). (c) Plot illustrating dependence of PEG_{205}-*b*-$PFTMC_{17}$ fiber L_n on sonication time. Error bars represent standard deviation of measured L_n. Solution samples of 0.5 mg/mL were drop-cast, stained with uranyl acetate solution (3 wt% in ethanol), and imaged after solvent evaporation. Scale bars: 500 nm.

The PEG_{205}-*b*-$PFTMC_{17}$ seeds (L_n = 39 nm, L_w/L_n = 1.18) were stored in solution (20 vol% DCM/MeCN) at 10 wt% under an inert atmosphere, as prepared. To investigate whether the seeds

could be stored as a solid, an aliquot was taken, and the solvent was removed to dryness (**Figure S3.12**a). After one week in the dry state, the seeds were re-dispersed in 20 vol% DCM/MeCN to a final concentration of 10 wt% (**Figure S3.12**b). The length after drying and re-dispersing was found to be L_n = 37 nm (L_w/L_n = 1.21), which is identical to that of the original seed (L_n = 39 nm) within experimental error. This result indicates that the PEG_{205}-*b*-$PFTMC_{17}$ seed micelles of this length do not exhibit any irreversible aggregation on solvent removal.

On ageing of the seed solution for ca. 16 weeks, side-by-side fusion of micelles was observed by TEM (**Figure S3.13**a). We attribute this to the absence of a purification step in the PI-CDSA process, resulting in the presence of small quantities of PFTMC homopolymer which can fuse micelles over time. A similar phenomenon has previously been observed whereby addition of a PFS homopolymer was found to fuse together 1D micelles with a PFS core end-to-end.[82] The process is likely driven by the presence of common solvent (DCM) which acts to increase the mobility of PFTMC segments, allowing for core chain rearrangement over time,[75] as well as the high solution concentration making fusion events more probable.[81] On sonication of the fused seeds for 30 min at 10 °C (20 vol% DCM/MeCN), the structures could be fragmented to access individual seeds (L_n = 40 nm, L_w/L_n = 1.23) (**Figure S3.13**b) which are statistically comparable to the original seed length (L_n = 39 nm, L_w/L_n = 1.18).

3.3.3 Preparation of scalable, low dispersity, and length-controlled PEG_{205}-*b*-$PFTMC_n$ nanofibers via living PI-CDSA

We explored the formation of uniform 1D nanofibers via living PI-CDSA from PEG_{205}-*b*-$PFTMC_{17}$ seeds (L_n = 39 nm, L_w/L_n = 1.18) performed at 10 wt% (99 mg/mL) (**Figure 3.5**a). This concentration is ca. 200-fold greater than that of the living CDSA of PFTMC-based BCPs which is typically performed at ca. 0.06 wt% (0.5 mg/mL).[56] A corona-to-core block ratio of 11:1 (PFTMC DP_n = 18) was targeted, and various unimer-to-seed mass ratios (m_{unimer}/m_{seed} = 2, 5, 10, 15, 20, 30, and 40) were explored. First, PEG_{205} and DBU were dissolved in 20 vol% DCM/MeCN

and to this was added a solution of FTMC monomer and PEG_{205}-*b*-$PFTMC_{17}$ seeds (L_n = 39 nm) in 20 vol% DCM/MeCN at 22 °C (**Figure S3.14**). The living PI-CDSA proceeded for 48 h before the nanostructures were characterized by TEM (**Figures 3.5**b–g and **S3.15**). In the case of m_{unimer}/m_{seed} = 20 and 30, further ageing of the solution up to a total of 7 days was required due to the presence of spherical micelles after 48 h (**Figures 3.5**f, g and **S3.15**a, b). The corresponding fiber contour lengths (L_n) and histograms are shown in **Table 3.1** and **Figure S3.16**.

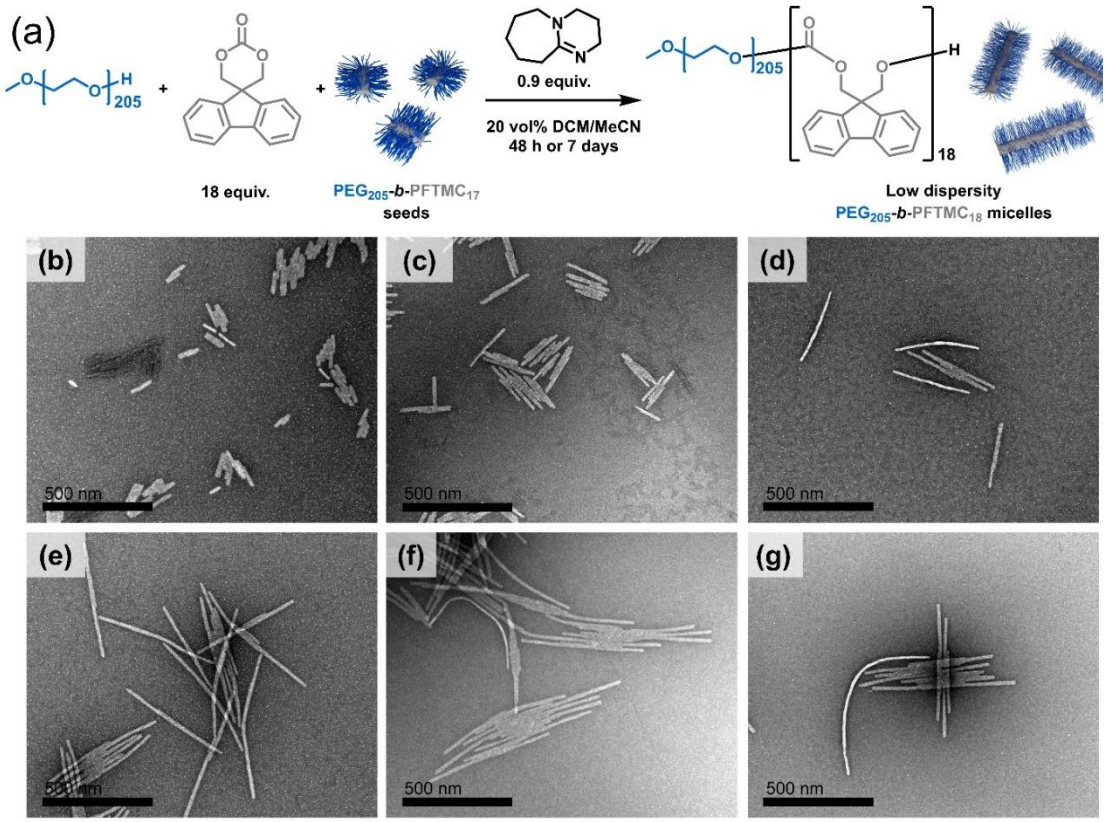

Figure 3.5 (a) Schematic representation of the preparation of low dispersity length-controlled PEG_{205}-*b*-$PFTMC_n$ nanofibers (target DP_n = 18, target block ratio = 11:1) via living PI-CDSA from PEG_{205}-*b*-$PFTMC_{17}$ seed micelles (L_n = 39 nm) in 20 vol% DCM/MeCN at 10 wt% and various m_{unimer}/m_{seed}. DBU, 1,8-diazabicyclo[5.4.0]undec-7-ene, was used as the ROP catalyst. (b–g) Representative TEM images of low dispersity length-controlled PEG_{205}-*b*-$PFTMC_n$ nanofibers (target DP_n = 18, target block ratio = 11:1) prepared via living PI-CDSA from

PEG_{205}-*b*-$PFTMC_{17}$ seed micelles (L_n = 39 nm) in 20 vol% DCM/MeCN at 10 wt% and m_{unimer}/m_{seed} values of (b) 2, (c) 5, (d) 10, (e) 15, (f) 20, and (g) 30. TEM images were obtained after (b–e) 48 h or (f, g) 7 days. Solution samples of 0.5 mg/mL were drop-cast, stained with uranyl acetate solution (3 wt% in ethanol), and imaged after solvent evaporation. Scale bars = 500 nm.

Table 3.1 Contour length (L_n), standard deviation (σ), and length-dispersity (L_w/L_n) data determined by TEM size analysis for the PEG_{205}-*b*-$PFTMC_n$ nanofibers (target DP_n = 18, target block ratio = 11:1) prepared via living PI-CDSA from PEG_{205}-*b*-$PFTMC_{17}$ seed micelles (L_n = 39 nm, L_w/L_n = 1.18) after 48 h (*or 7 days) in 20 vol% DCM/MeCN at 10 wt% and various m_{unimer}/m_{seed}.

		m_{unimer}/m_{seed}						
	Seeds	**2**	**5**	**10**	**15**	**20***	**30***	**40**
Theoretical L_n (nm)	-	117	234	429	624	819	1209	1599
L_n (nm)	39	101	163	338	465	569	658	583
σ (nm)	16	44	45	100	156	166	205	500
L_w/L_n	1.18	1.20	1.08	1.09	1.11	1.09	1.10	1.74

A linear relationship between nanofiber length (L_n) and m_{unimer}/m_{seed} was established for $m_{unimer}/m_{seed} \leq 30$, allowing for the preparation of uniform PEG-*b*-PFTMC micelles of targeted lengths (L_n = 101–658 nm) (**Figures 3.6**a and **3.5**b–g). The theoretically predicted lengths based on the seed micelles were within the 3σ confidence level in the measured lengths (**Table 3.1**). L_n values at $m_{unimer}/m_{seed} \leq 30$ were found to be accurate within error of the seed L_n measurements, (L_n + σ) and (L_n – σ), as shown in **Figure 3.6**b. Notably, micelles of length L_n = 101 nm (L_w/L_n = 1.20) and L_n = 163 nm (L_w/L_n = 1.08) could be prepared at m_{unimer}/m_{seed} = 2 or 5 (**Figure 3.5**b and c), respectively.

Particles that are < 200 nm in size are considered optimal for drug delivery applications, since nanoparticles in this size regime are large enough to avoid renal and lymphatic clearance yet are small enough to reduce toxicity and opsonization.[5,7,12,56,57,83] Therefore, the living PI-CDSA protocol reported here allows significantly upscaled access to well-defined biodegradable nanofibers at length-scales useful for applications in nanomedicine.

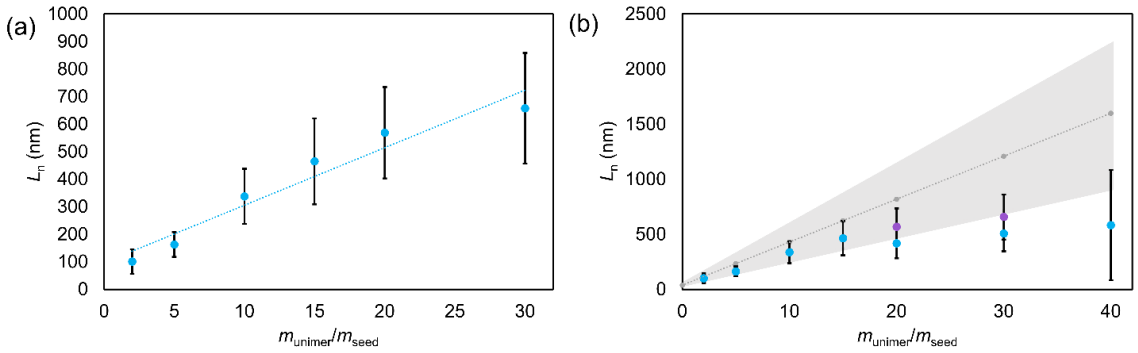

Figure 3.6 (a) Plot illustrating the dependence of fiber length (L_n) on the m_{unimer}/m_{seed} after 48 h ($m_{unimer}/m_{seed} \leq 15$) or 7 days ($m_{unimer}/m_{seed} = 20$ or 30). (b) Plot illustrating the dependence of fiber length (L_n) on the m_{unimer}/m_{seed} at $2 \leq m_{unimer}/m_{seed} \leq 40$ after 48 h (blue) or 7 days (purple) overlaid with theoretical L_n values (grey). Grey area represents theoretical error in L_n based on the upper and lower standard deviation of the L_n of the seed micelles, ($L_n + \sigma$) and ($L_n - \sigma$). Error bars represent standard deviation of measured L_n.

At $m_{unimer}/m_{seed} \leq 15$, there was no significant change in L_n after ageing beyond 48 h, which is consistent with the formation of morphologically pure fibers of similar length to the theoretical value, indicating that all unimer had been consumed. At $m_{unimer}/m_{seed} = 20$ and 30, however, a mixture of fibers and spheres was observed after 48 h (**Figure S3.15**). The resultant nanofiber L_n value was found to be significantly lower than that of the predicted value (**Figure 3.6**b) in line with unimer being consumed for spherical micelle formation. For example, at $m_{unimer}/m_{seed} = 30$, the predicted L_n value was 1209 nm, yet fibers only of length $L_n = 507$ nm ($L_w/L_n = 1.10$) were obtained after 48 h. The presence of spherical micelles indicated that the morphological evolution may be

incomplete, since our investigation into the PI-CDSA of PEG_{205}-*b*-$PFMTC_n$ demonstrated that kinetically-trapped spheres form rapidly but then transition on ageing to form morphologically pure fibers. The formation of spheres as a unimer reservoir would also decrease the unimer concentration in solution, leading to a decreased overall rate of self-assembly.[84] The samples were therefore aged for a total of 7 days. On ageing the solutions at m_{unimer}/m_{seed} = 20 and 30, morphologically pure fibers with significantly increased L_n values were obtained. Fibers of length L_n = 569 nm (L_w/L_n = 1.09) and L_n = 658 nm (L_w/L_n = 1.10) were formed at m_{unimer}/m_{seed} values of 20 and 30, respectively (**Figure 3.5**f and g). The theoretical L_n at these m_{unimer}/m_{seed} values lies within 3σ confidence of that of the measured L_n after 7 days.

At m_{unimer}/m_{seed} = 40, as well as sphere formation, we observed significantly shorter fiber-like micelles present among the long fibers (**Figures S3.15**c, **S3.16**h, and **S3.17**). This is consistent with competitive self-nucleation of unimer under these conditions. This is expected at high m_{unimer}/m_{seed}, since an increased unimer concentration will increase the rate of self-nucleation.[84] This means that the rates of elongation (seeded growth) and self-nucleation become more comparable under these conditions, resulting in compromised size-control which is reflected by the high length-dispersity of L_w/L_n = 1.74 exhibited by the fibers at m_{unimer}/m_{seed} = 40 (**Figure S3.16**h). The low length-dispersities and narrow distribution of contour lengths of fibers prepared at m_{unimer}/m_{seed} = 20 and 30 suggest that self-nucleation events are negligible under these conditions (**Figure S3.16**f and g).

The living PI-CDSA of PEG_{205}-*b*-$PFTMC_n$ at m_{unimer}/m_{seed} = 20 was then performed at an increased temperature of 35 °C (rather than at 22 °C) with the aim of targeting morphologically pure nanofibers after 48 h rather than a mixture with spheres. Increasing the temperature at which self-assembly is performed would be expected to aid plasticization of the amorphous core of spherical micelles and the crystallization-induced transition to nanofibers.[75] However, living PI-CDSA at m_{unimer}/m_{seed} = 20 at 35 °C still led to the formation of a mixture of spheres and nanofibers after 48 h (**Figure S3.18**a), similar to the results at room temperature (**Figure S3.15**a). Interestingly, size

analysis of the contour length L_n demonstrated that the nanofibers prepared at 35 °C exhibited L_n = 560 nm (L_w/L_n = 1.10), which is longer than that obtained at 22 °C (L_n = 419 nm, L_w/L_n = 1.11) after 48 h (**Table S3.6**). This could be a result of an increase in the rate of unimer exchange from the amorphous spherical micelles into the solution at higher temperature, leading to an increased value of m_{unimer}/m_{seed}. This would lead to an increased unimer concentration at 35 °C compared with that at 22 °C, which would in turn increase fiber growth.[84] After a total of 7 days, morphologically pure fibers of L_n = 545 nm (L_w/L_n = 1.14) were obtained at 35 °C (**Figure S3.18**b), which were similar to those obtained at 22 °C over the same time period (L_n = 569 nm, L_w/L_n = 1.09, **Figure 3.5**f). This result is consistent with the assertion that spherical micelles act as a unimer reservoir for the formation of fibers.[77] The lengths of fibers prepared at 35 °C after ageing for a total of 7 days were the same as those prepared at room temperature within experimental error, with the latter exhibiting a slightly lower dispersity in the length.

3.3.4 Comparison of the living PI-CDSA process with that of living CDSA

In the typical living CDSA protocol for PEG-*b*-PFTMC BCPs at 0.06 wt% in DMSO/MeOH, fibers of lengths up to L_n = 1600 nm can be obtained.[56] In this work, the upper limit of nanofiber length obtained via living PI-CDSA at 10 wt% was found to be L_n = ca. 660 nm. To determine whether the fiber L_n in this work is limited by the solvent system (20 vol% DCM/MeCN), the solution concentration (10 wt%), or by the *in situ* nature of living PI-CDSA itself, the self-assembly of a comparable BCP, PEG_{205}-*b*-$PFTMC_{19}$, was probed. PEG_{205}-*b*-$PFTMC_{19}$ was prepared via the DBU-catalyzed ROP of FTMC macroinitiated by PEG_{205}, as previously reported and described in the supporting information (**Figures S3.19** and **S3.20**).[56]

The living CDSA of PEG_{205}-*b*-$PFTMC_{19}$ in 20 vol% DCM/MeCN was performed at 10 wt%, 22 °C, and high m_{unimer}/m_{seed} (20–40) to probe the upper limit of fiber L_n achievable in this solvent system. In all cases, a mixture of nanofibers and spheres were obtained by living CDSA after 48 h (**Figure S3.21**). Ageing of the samples for a total of 7 days, which allowed for a sphere-to-fiber

morphological evolution in PI-CDSA experiments, led to no significant changes in the nanofiber-to-sphere ratio. This suggests that the spherical micelles formed via living CDSA are significantly more kinetically-trapped than those that formed via living PI-CDSA. Moreover, the nanofiber L_n value was significantly reduced compared with that obtained via living PI-CDSA (**Table S3.7**), consistent with spherical micelle formation consuming unimer. For example, after ageing the living CDSA sample at m_{unimer}/m_{seed} = 20 for 7 days, nanofibers of length L_n = 242 nm (L_w/L_n = 1.23) as well as spherical micelles were obtained (**Figure S3.22**a, b). The corresponding living PI-CDSA experiment under the same conditions yielded morphologically pure, lower dispersity fibers of length L_n = 569 nm (L_w/L_n = 1.09) (**Figure S3.22**c). These results indicate that although spherical micelles formed in the living PI-CDSA experiments act as a unimer reservoir (allowing for sphere-to-fiber transition), those formed during the analogous living CDSA experiments remain kinetically-trapped over the timescale studied (no observed sphere-to-fiber transition).

We next investigated the living CDSA of PEG_{205}-*b*-$PFTMC_{19}$ under dilute conditions to determine the effect of concentration. Living CDSA of PEG_{205}-*b*-$PFTMC_{19}$ was performed at 0.06 wt% and 22 °C in 20 vol% DCM/MeCN and m_{unimer}/m_{seed} = 10. The same PEG_{205}-*b*-$PFTMC_{17}$ seeds (L_n = 39 nm) in 20 vol% DCM/MeCN that were used in the living PI-CDSA were employed. Interestingly, even under dilute conditions, a mixture of spheres and fibers were obtained via living CDSA in 20 vol% DCM/MeCN (**Figure S3.23**). Morphologically pure PEG-*b*-PFTMC fibers are known to form in 20 vol% DMSO/MeOH at the same concentration (0.06 wt%).[56] This suggests that DCM/MeCN is a poorer solvent combination for the living CDSA of PEG-*b*-PFTMC than DMSO/MeOH. A poorer solvent combination will promote and favour the formation of kinetically-trapped spheres over the crystallization-induced elongation of the PFTMC fiber core. Remarkably, however, it should be noted that the analogous living PI-CDSA process in 20 vol% DCM/MeCN at 10 wt% (ca. 170-fold more concentrated) yields morphologically pure fibers (**Figure 3.5**d).

To confirm our postulate that 20 vol% DCM/MeCN is a poorer solvent system than 20 vol% DMSO/MeOH for PEG-*b*-PFTMC, we investigated the CDSA of PEG_{205}-*b*-$PFTMC_{19}$ in the absence of preformed seeds under the typical dilute conditions (0.06 wt%). The CDSA was performed by heating the solution of PEG_{205}-*b*-$PFTMC_{19}$ at 70 °C for 8 h, then ageing for 48 h to allow the solution to cool to 22 °C before imaging via TEM. It was found that morphologically pure polydisperse fibers could be obtained via the CDSA of PEG_{205}-*b*-$PFTMC_{19}$ at 0.06 wt% in 20 vol% DMSO/MeOH (**Figure S3.24**a). Using the same procedure in 20 vol% DCM/MeCN, however, a mixture of fibers and spheres was formed (**Figure S3.24**b), further supporting the conclusion that DCM/MeCN is a poorer quality solvent system for the BCP than DMSO/MeOH.

Although our results demonstrate that DCM/MeCN represents a relatively a poor solvent system for PEG-*b*-PFTMC BCPs which does not promote morphologically pure fiber formation via CDSA processes, remarkably PI-CDSA overcomes this limitation. A key difference between living CDSA and PI-CDSA/living PI-CDSA is the molecular weight dispersity (M_w/M_n) of the BCP which acts as unimer, as well as the evolution of the unimer "concentration" throughout the process. In living CDSA, the unimer is of low dispersity (lower M_w/M_n, in this case M_w/M_n = 1.09) and is rapidly injected into the solution of seed micelles, causing the initial unimer concentration to be very high. This high unimer concentration in a poorer quality solvent medium for the BCP is likely to favour rapid formation of spherical micelles with an amorphous core.[84] In PI-CDSA/living PI-CDSA, on the other hand, the preparation of the BCP occurs *in situ* and the chains would be expected to grow at slightly different rates resulting in significantly higher dispersities than for living polymerizations, as was observed (**Table S3.1**, M_w/M_n = 1.16–1.37). Moreover, in PI-CDSA/living PI-CDSA the core chain length must reach a critical DP_n before self-assembly is induced.[23,85] It would therefore be expected that in PI-CDSA/living PI-CDSA experiments only a small fraction of the BCP formed at any instant would possess the substantial DP_n value needed for the PFTMC block for self-assembly to take place. As this would be rapidly consumed by seeded growth

(involving seeds either formed in situ or preformed and added externally), the instantaneous concentration of unimer primed for self-assembly would effectively be kept low. We postulate that this favours fiber-like micelle formation by seeded growth rather than the formation of spheres with an amorphous PFTMC core which would be expected in a poor solvent medium when the unimer concentration is very high.

3.4 Summary

We report the preparation of 1D PEG_{205}-*b*-$PFTMC_n$ fibers by PI-CDSA at scalable concentrations of 5–20 wt% as an extension of this technique to a biocompatible and biodegradable crystalline core-forming block. Generally, the polymerization of FTMC was found to be complete within 1 h, with increased concentrations favouring higher monomer conversion and increased rate of fiber formation. Interestingly, all nanostructures prepared via PI-CDSA exhibited a sphere–intermediate–fiber morphological evolution, providing evidence that PFTMC-based spherical micelles act as unimer reservoir for the formation of 1D fibers. We also demonstrated that performing PI-CDSA and subsequent sonication can be utilized as a facile upscaled preparation of low dispersity seed micelles.

Furthermore, we report the seeded growth process, living PI-CDSA, to access low dispersity 1D PEG_{205}-*b*-$PFTMC_n$ with contour lengths of ca. 100–660 nm at 10 wt% solids. Anisotropic biocompatible nanostructures within this length range are of particular interest for application in nanomedicine. At higher m_{unimer}/m_{seed} values, competitive spherical micelle formation as well as self-nucleation events yielded mixed morphologies of spheres and fibers exhibiting high length-dispersity. Living PI-CDSA was also compared with living CDSA, demonstrating key advantages of the scalable one-pot *in situ* method described in this work over typical techniques.

3.5 References

(1) Liu, J.; Thompson, Z. J.; Sue, H. J.; Bates, F. S.; Hillmyer, M. A.; Dettloff, M.; Jacob, G.;

Verghese, N.; Pham, H. Toughening of Epoxies with Block Copolymer Micelles of Wormlike Morphology. *Macromolecules* **2010**, *43* (17), 7238–7243.

(2) Thio, Y. S.; Wu, J.; Bates, F. S. Epoxy Toughening Using Low Molecular Weight Poly(Hexylene Oxide)-Poly(Ethylene Oxide) Diblock Copolymers. *Macromolecules* **2006**, *39*, 7187–7189.

(3) Cutler, C. S.; Wang, L. V.; Liu, Y.; Xia, Y. Radioactive 198Au-Doped Nanostructures with Different Shapes for In Vivo Analyses of Their Biodistribution, Tumor Uptake, and Intratumoral Distribution. *ACS Nano* **2014**, *8* (5), 4385–4394.

(4) Yu, Q.; Roberts, M. G.; Houdaihed, L.; Liu, Y.; Ho, K.; Walker, G. C.; Allen, C.; Reilly, R. M.; Manners, I.; Winnik, M. A. Investigating the Influence of Block Copolymer Micelle Length on Cellular Uptake and Penetration in a Multicellular Tumor Spheroid Model. *Nanoscale* **2021**, *13* (1), 280–291.

(5) Street, S. T. G.; He, Y.; Jin, X.-H.; Hodgson, L.; Verkade, P.; Manners, I. Cellular Uptake and Targeting of Low Dispersity, Dual Emissive, Segmented Block Copolymer Nanofibers. *Chem. Sci.* **2020**, *11* (32), 8394–8408.

(6) Finnegan, J. R.; Pilkington, E.; Alt, K.; Rahim, M. A.; Kent, S. J.; Davis, T. P.; Kempe, K. Stealth Nanorods via the Aqueous Living Crystallisation-Driven Self-Assembly of Poly(2-Oxazoline)s. *Chem. Sci.* **2021**, *12*, 7350–7360.

(7) Mandal, S.; Eksteen-Akeroyd, Z. H.; Jacobs, M. J.; Hammink, R.; Koepf, M.; Lambeck, A. J. A.; van Hest, J. C. M.; Wilson, C. J.; Blank, K.; Figdor, C. G.; Rowan, A. E. Therapeutic Nanoworms: Towards Novel Synthetic Dendritic Cells for Immunotherapy. *Chem. Sci.* **2013**, *4* (11), 4168–4174.

(8) Geng, Y. A. N.; Dalhaimer, P.; Cai, S.; Tsai, R.; Minko, T.; Discher, D. E. Shape Effects of Filaments versus Spherical Particles in Flow and Drug Delivery. *Nat. Nanotechnol.* **2007**, *2* (4), 249–255.

(9) Canton, I.; Warren, N. J.; Chahal, A.; Amps, K.; Wood, A.; Weightman, R.; Wang, E.; Moore, H.; Armes, S. P. Mucin-Inspired Thermoresponsive Synthetic Hydrogels Induce Stasis in Human Pluripotent Stem Cells and Human Embryos. *ACS Cent. Sci.* **2016**, *2* (2), 65–74.

(10) Truong, N. P.; Quinn, J. F.; Whittaker, M. R.; Davis, T. P. Polymeric Filomicelles and

Nanoworms: Two Decades of Synthesis and Application. *Polym. Chem.* **2016**, *7* (26), 4295–4312.

(11) Arno, M. C.; Inam, M.; Coe, Z.; Cambridge, G.; Macdougall, L. J.; Keogh, R.; Dove, A. P.; O'Reilly, R. K. Precision Epitaxy for Aqueous 1D and 2D Poly(ϵ-Caprolactone) Assemblies. *J. Am. Chem. Soc.* **2017**, *139* (46), 16980–16985.

(12) Elsabahy, M.; Wooley, K. L. Design of Polymeric Nanoparticles for Biomedical Delivery Applications. *Chem. Soc. Rev.* **2012**, *41*, 2545–2561.

(13) Bruckman, M. A.; Randolph, L. N.; Vanmeter, A.; Hern, S.; Shoffstall, A. J.; Taurog, R. E.; Steinmetz, N. F. Biodistribution, Pharmacokinetics, and Blood Compatibility of Native and PEGylated Tobacco Mosaic Virus Nano-Rods and -Spheres in Mice. *Virology* **2014**, *449*, 163–173.

(14) Zhao, Y.; Wang, Y.; Ran, F.; Cui, Y.; Liu, C.; Zhao, Q.; Gao, Y.; Wang, D. A Comparison between Sphere and Rod Nanoparticles Regarding Their in Vivo Biological Behavior and Pharmacokinetics. *Sci. Rep.* **2017**, *7*, 4131.

(15) Dasgupta, S.; Auth, T.; Gompper, G. Shape and Orientation Matter for the Cellular Uptake of Nonspherical Particles. *Nano Lett.* **2014**, *14* (2), 687–693.

(16) Song, Y.; Elsabahy, M.; Collins, C. A.; Khan, S.; Li, R.; Hreha, T. N.; Shen, Y.; Lin, Y.-N.; Letteri, R. A.; Su, L.; Dong, M.; Zhang, F.; Hunstad, D. A.; Wooley, K. L. Morphologic Design of Silver-Bearing Sugar-Based Polymer Nanoparticles for Uroepithelial Cell Binding and Antimicrobial Delivery. *Nano Lett.* **2021**, *21* (12), 4990–4998.

(17) Huang, X.; Teng, X.; Chen, D.; Tang, F.; He, J. The Effect of the Shape of Mesoporous Silica Nanoparticles on Cellular Uptake and Cell Function. *Biomaterials* **2010**, *31* (3), 438–448.

(18) Barua, S.; Yoo, J.; Kolhar, P.; Wakankar, A.; Gokarn, Y. R.; Mitragotri, S. Particle Shape Enhances Specificity of Antibody-Displaying Nanoparticles. *Proc. Natl. Acad. Sci.* **2013**, *110* (9), 3270–3275.

(19) Kinnear, C.; Moore, T. L.; Rodriguez-Lorenzo, L.; Rothen-Rutishauser, B.; Petri-Fink, A. Form Follows Function: Nanoparticle Shape and Its Implications for Nanomedicine. *Chem. Rev.* **2017**, *117* (17), 11476–11521.

(20) Warren, N. J.; Mykhaylyk, O. O.; Mahmood, D.; Ryan, A. J.; Armes, S. P. RAFT Aqueous

Dispersion Polymerization Yields Poly(Ethylene Glycol)-Based Diblock Copolymer Nano-Objects with Predictable Single Phase Morphologies. *J. Am. Chem. Soc.* **2014**, *136*, 1023–1033.

(21) Tritschler, U.; Pearce, S.; Gwyther, J.; Whittell, G. R.; Manners, I. 50th Anniversary Perspective: Functional Nanoparticles from the Solution Self-Assembly of Block Copolymers. *Macromolecules* **2017**, *50* (9), 3439–3463.

(22) Nahi, O.; Cayre, O. J.; Kim, Y. Y.; Smith, A. J.; Warren, N. J.; Meldrum, F. C. A Facile Method for Generating Worm-like Micelles with Controlled Lengths and Narrow Polydispersity. *Chem. Commun.* **2020**, *56* (54), 7463–7466.

(23) Canning, S. L.; Smith, G. N.; Armes, S. P. A Critical Appraisal of RAFT-Mediated Polymerization-Induced Self-Assembly. *Macromolecules* **2016**, *49* (6), 1985–2001.

(24) Warren, N. J.; Armes, S. P. Polymerization-Induced Self-Assembly of Block Copolymer Nano-Objects via RAFT Aqueous Dispersion Polymerization. *J. Am. Chem. Soc.* **2014**, *136* (29), 10174–10185.

(25) Hunter, S. J.; Armes, S. P. Pickering Emulsifiers Based on Block Copolymer Nanoparticles Prepared by Polymerization-Induced Self-Assembly. *Langmuir* **2020**, *36* (51), 15463–15484.

(26) Charleux, B.; Delaittre, G.; Rieger, J.; D'Agosto, F. Polymerization-Induced Self-Assembly: From Soluble Macromolecules to Block Copolymer Nano-Objects in One Step. *Macromolecules* **2012**, *45* (17), 6753–6765.

(27) Sun, J.-T.; Hong, C.-Y.; Pan, C.-Y. Recent Advances in RAFT Dispersion Polymerization for Preparation of Block Copolymer Aggregates. *Polym. Chem.* **2013**, *4* (4), 873–881.

(28) Pearce, S.; Perez-Mercader, J. PISA: Construction of Self-Organized and Self-Assembled Functional Vesicular Structures. *Polym. Chem.* **2021**, *12* (1), 29–49.

(29) Gavrilov, A. A.; Shupanov, R. M.; Chertovich, A. V. Phase Diagram for Ideal Diblock-Copolymer Micelles Compared to Polymerization-Induced Self Assembly. *Polymers (Basel).* **2020**, *12* (11), 2599.

(30) Masuko, K.; Kumano, C.; Sugawara, R.; Nakabayashi, K.; Mori, H. Polymerization-induced Self-assembly of Amino-acid-based Nano-objects by Reversible Addition–Fragmentation Chain-transfer Dispersion Polymerization. *J. Polym. Sci.* **2021**, *59*, 1664–

1677.

(31) Guimarães, T. R.; Bong, Y. L.; Thompson, S. W.; Moad, G.; Perrier, S.; Zetterlund, P. B. Polymerization-Induced Self-Assembly via RAFT in Emulsion: Effect of Z-Group on the Nucleation Step. *Polym. Chem.* **2021**, *12* (1), 122–133.

(32) Dao, T. P. T.; Vezenkov, L.; Subra, G.; Amblard, M.; In, M.; Le Meins, J.-F.; Aubrit, F.; Moradi, M.-A.; Ladmiral, V.; Semsarilar, M. Self-Assembling Peptide-Polymer Nano-Objects via Polymerization-Induced Self-Assembly. *Macromolecules* **2020**, *53* (16), 7034–7043.

(33) Czajka, A.; Armes, S. P. In Situ SAXS Studies of a Prototypical RAFT Aqueous Dispersion Polymerization Formulation: Monitoring the Evolution in Copolymer Morphology during Polymerization-Induced Self-Assembly. *Chem. Sci.* **2020**, *11* (42), 11443–11454.

(34) Qiao, X. G.; Dugas, P.-Y.; Charleux, B.; Lansalot, M.; Bourgeat-Lami, E. Nitroxide-Mediated Polymerization-Induced Self-Assembly of Amphiphilic Block Copolymers with a pH/Temperature Dual Sensitive Stabilizer Block. *Polym. Chem.* **2017**, *8* (27), 4014–4029.

(35) Liu, C.; Hong, C.-Y.; Pan, C.-Y. Polymerization Techniques in Polymerization-Induced Self-Assembly (PISA). *Polym. Chem.* **2020**, *11* (22), 3673–3689.

(36) Perrier, S. 50th Anniversary Perspective: RAFT Polymerization - A User Guide. *Macromolecules* **2017**, *50* (19), 7433–7447.

(37) Foster, J. C.; Varlas, S.; Couturaud, B.; Coe, Z.; O'Reilly, R. K. Getting into Shape: Reflections on a New Generation of Cylindrical Nanostructures' Self-Assembly Using Polymer Building Blocks. *J. Am. Chem. Soc.* **2019**, *141* (7), 2742–2753.

(38) Massey, J. A.; Temple, K.; Cao, L.; Rharbi, Y.; Raez, J.; Winnik, M. A.; Manners, I. Self-Assembly of Organometallic Block Copolymers: The Role of Crystallinity of the Core-Forming Polyferrocene Block in the Micellar Morphologies Formed by Poly(Ferrocenylsilane-b-Dimethylsiloxane) in n-Alkane Solvents. *J. Am. Chem. Soc.* **2000**, *122* (47), 11577–11584.

(39) Cao, L.; Manners, I.; Winnik, M. A. Influence of the Interplay of Crystallization and Chain Stretching on Micellar Morphologies: Solution Self-Assembly of Coil-Crystalline Poly(Isoprene-Block-Ferrocenylsilane). *Macromolecules* **2002**, *35* (22), 8258–8260.

(40) Inam, M.; Cambridge, G.; Pitto-Barry, A.; Laker, Z. P. L.; Wilson, N. R.; Mathers, R. T.;

Dove, A. P.; O'Reilly, R. K. 1D vs. 2D Shape Selectivity in the Crystallization-Driven Self-Assembly of Polylactide Block Copolymers. *Chem. Sci.* **2017**, *8* (6), 4223–4230.

(41) Karayianni, M.; Pispas, S. Block Copolymer Solution Self-Assembly: Recent Advances, Emerging Trends, and Applications. *J. Polym. Sci.* **2021**, *59*, 1874–1898.

(42) Gilroy, J. B.; Gädt, T.; Whittell, G. R.; Chabanne, L.; Mitchels, J. M.; Richardson, R. M.; Winnik, M. A.; Manners, I. Monodisperse Cylindrical Micelles by Crystallization-Driven Living Self-Assembly. *Nat. Chem.* **2010**, *2*, 566–570.

(43) Guerin, G.; Wang, H.; Manners, I.; Winnik, M. A. Fragmentation of Fiberlike Structures: Sonication Studies of Cylindrical Block Copolymer Micelles and Behavioral Comparisons to Biological Fibrils. *J. Am. Chem. Soc.* **2008**, *130* (44), 14763–14771.

(44) Wang, X.; Manners, I.; Winnik, M. A. Cylindrical Block Copolymer Micelles and Co-Micelles of Controlled Length and Architecture. *Science* **2007**, *317* (5838), 644–648.

(45) MacFarlane, L. R.; Zhao, C.; Cai, J.; Qiu, H.; Manners, I. Emerging Applications for Living Crystallization-Driven Self-Assembly. *Chem. Sci.* **2021**, *12* (13), 4661–4682.

(46) Ganda, S.; Stenzel, M. H. Concepts, Fabrication Methods and Applications of Living Crystallization-Driven Self-Assembly of Block Copolymers. *Prog. Polym. Sci.* **2020**, *101*, 101195.

(47) He, W.-N.; Xu, J.-T. Crystallization Assisted Self-Assembly of Semicrystalline Block Copolymers. *Prog. Polym. Sci.* **2012**, *37*, 1350–1400.

(48) Ma, J.; Lu, G.; Huang, X.; Feng, C. π-Conjugated-Polymer-Based Nanofibers through Living Crystallization-Driven Self-Assembly: Preparation, Properties and Applications. *Chem. Commun.* **2021**, *57*, 13259–13274.

(49) Hils, C.; Schmelz, J.; Drechsler, M.; Schmalz, H. Janus Micelles by Crystallization-Driven Self-Assembly of an Amphiphilic, Double-Crystalline Triblock Terpolymer. *J. Am. Chem. Soc.* **2021**, *143* (38), 15582–15586.

(50) Frank, A.; Hils, C.; Weber, M.; Kreger, K.; Schmalz, H.; Schmidt, H.-W. Hierarchical Superstructures by Combining Crystallization-driven and Molecular Self-assembly. *Angew. Chem. Int. Ed.* **2021**, *60*, 21767–21771.

(51) Inam, M.; Jones, J. R.; Pérez-Madrigal, M. M.; Arno, M. C.; Dove, A. P.; O'Reilly, R. K.

Controlling the Size of Two-Dimensional Polymer Platelets for Water-in-Water Emulsifiers. *ACS Cent. Sci.* **2018**, *4* (1), 63–70.

(52) He, Y.; Eloi, J.-C.; Harniman, R. L.; Richardson, R. M.; Whittell, G. R.; Mathers, R. T.; Dove, A. P.; O'Reilly, R. K.; Manners, I. Uniform Biodegradable Fiber-Like Micelles and Block Comicelles via "Living" Crystallization-Driven Self-Assembly of Poly(L-Lactide) Block Copolymers: The Importance of Reducing Unimer Self-Nucleation via Hydrogen Bond Disruption. *J. Am. Chem. Soc.* **2019**, *141* (48), 19088–19098.

(53) Fukui, T.; Garcia-Hernandez, J. D.; MacFarlane, L. R.; Lei, S.; Whittell, G. R.; Manners, I. Seeded Self-Assembly of Charge-Terminated Poly(3-Hexylthiophene) Amphiphiles Based on the Energy Landscape. *J. Am. Chem. Soc.* **2020**, *142* (35), 15038–15048.

(54) Sneyd, A. J.; Fukui, T.; Paleček, D.; Prodhan, S.; Wagner, I.; Zhang, Y.; Sung, J.; Collins, S. M.; Slater, T. J. A.; Andaji-Garmaroudi, Z.; Macfarlane, L. R.; Garcia-Hernandez, J. D.; Wang, L.; Whittell, G. R.; Hodgkiss, J. M.; Chen, K.; Beljonne, D.; Manners, I.; Friend, R. H.; Rao, A. Efficient Energy Transport in an Organic Semiconductor Mediated by Transient Exciton Delocalization. *Sci. Adv.* **2021**, *7* (32), eabh4232.

(55) Ganda, S.; Wong, C. K.; Stenzel, M. H. Corona-Loading Strategies for Crystalline Particles Made by Living Crystallization-Driven Self-Assembly. *Macromolecules* **2021**, *54* (14), 6662–6669.

(56) Finnegan, J. R.; He, X.; Street, S. T. G.; Garcia-Hernandez, J. D.; Hayward, D. W.; Harniman, R. L.; Richardson, R. M.; Whittell, G. R.; Manners, I. Extending the Scope of "Living" Crystallization-Driven Self Assembly: Well-Defined 1D Micelles and Block Comicelles from Crystallizable Polycarbonate Block Copolymers. *J. Am. Chem. Soc.* **2018**, *140* (49), 17127–17140.

(57) Garcia-Hernandez, J. D.; Street, S. T. G.; Kang, Y.; Zhang, Y.; Manners, I. Cargo Encapsulation in Uniform, Length-Tunable Aqueous Nanofibers with a Coaxial Crystalline and Amorphous Core. *Macromolecules* **2021**, *54* (12), 5784–5796.

(58) Tang, Z.; Gao, L.; Lin, J.; Cai, C.; Yao, Y.; Guerin, G.; Tian, X.; Lin, S. Anchorage-Dependent Living Supramolecular Self-Assembly of Polymeric Micelles. *J. Am. Chem. Soc.* **2021**, *143* (36), 14684–14693.

(59) Bousmail, D.; Chidchob, P.; Sleiman, H. F. Cyanine-Mediated DNA Nanofiber Growth with Controlled Dimensionality. *J. Am. Chem. Soc.* **2018**, *140* (30), 9518–9530.

(60) Merg, A. D.; Van Genderen, E.; Bazrafshan, A.; Su, H.; Zuo, X.; Touponse, G.; Blum, T. B.; Salaita, K.; Abrahams, J. P.; Conticello, V. P. Seeded Heteroepitaxial Growth of Crystallizable Collagen Triple Helices: Engineering Multifunctional Two-Dimensional Core-Shell Nanostructures. *J. Am. Chem. Soc.* **2019**, *141* (51), 20107–20117.

(61) Venkataraman, S.; Hedrick, J. L.; Yang, Y. Y. Fluorene-Functionalized Aliphatic Polycarbonates: Design, Synthesis and Aqueous Self-Assembly of Amphiphilic Block Copolymers. *Polym. Chem.* **2014**, *5* (6), 2035–2040.

(62) Fukushima, K. Poly(Trimethylene Carbonate)-Based Polymers Engineered for Biodegradable Functional Biomaterials. *Biomater. Sci.* **2016**, *4*, 9–24.

(63) Street, S. T. G.; He, Y.; Harniman, R. L.; Garcia-Hernandez, J. D.; Manners, I. Precision Polymer Nanofibers as a Modular, Functionalizable Platform Designed for Nuclei Acid Delivery Applications. *To be submitted for publication*.

(64) Boott, C. E.; Gwyther, J.; Harniman, R. L.; Hayward, D. W.; Manners, I. Scalable and Uniform 1D Nanoparticles by Synchronous Polymerization, Crystallization and Self-Assembly. *Nat. Chem.* **2017**, *9*, 785–792.

(65) Oliver, A. M.; Gwyther, J.; Boott, C. E.; Davis, S. A.; Pearce, S.; Manners, I. Scalable Fiber-like Micelles and Block Co-Micelles by Polymerization-Induced Crystallization-Driven Self-Assembly. *J. Am. Chem. Soc.* **2018**, *140* (51), 18104–18114.

(66) Sha, Y.; Rahman, M. A.; Zhu, T.; Cha, Y.; McAlister, C. W.; Tang, C. ROMPI-CDSA: Ring-Opening Metathesis Polymerization-Induced Crystallization-Driven Self-Assembly of Metallo-Block Copolymers. *Chem. Sci.* **2019**, *10* (42), 9782–9787.

(67) Hurst, P. J.; Rakowski, A. M.; Patterson, J. P. Ring-Opening Polymerization-Induced Crystallization-Driven Self-Assembly of Poly-L-Lactide-Block-Polyethylene Glycol Block Copolymers (ROPI-CDSA). *Nat. Commun.* **2020**, *11*, 4690.

(68) Guan, S.; Chen, A. One-Pot Synthesis of Cross-Linked Block Copolymer Nanowires via Polymerization-Induced Hierarchical Self-Assembly and Photodimerization. *ACS Macro Lett.* **2020**, *9* (1), 14–19.

(69) Guan, S.; Wen, W.; Yang, Z.; Chen, A. Liquid Crystalline Nanowires by Polymerization Induced Hierarchical Self-Assembly. *Macromolecules* **2020**, *53* (1), 465–472.

(70) Song, S.; Liu, X.; Nikbin, E.; Howe, J. Y.; Yu, Q.; Manners, I.; Winnik, M. A. Uniform 1D

Micelles and Patchy & Block Comicelles via Scalable, One-Step Crystallization-Driven Block Copolymer Self-Assembly. *J. Am. Chem. Soc.* **2021**, *143* (16), 6266–6280.

(71) Save, M.; Schappacher, M.; Soum, A. Controlled Ring-Opening Polymerization of Lactones and Lactide Initiated by Lanthanum Isopropoxide, 2a: Mechanistic Studies. *Macromol. Chem. Phys.* **2002**, *203*, 889–899.

(72) Guo, A.; Yang, F.; Yu, R.; Wu, Y. Real-Time Monitoring of Living Cationic Ring-Opening Polymerization of THF and Direct Prediction of Equilibrium Molecular Weight of PolyTHF. *Chinese J. Polym. Sci. (English Ed.* **2015**, *33* (1), 23–35.

(73) Deng, H.; Shen, Z.; Li, L.; Yin, H.; Chen, J. Real-Time Monitoring of Ring-Opening Polymerization of Tetrahydrofuran via in Situ Fourier Transform Infrared Spectroscopy. *J. Appl. Polym. Sci.* **2014**, *131* (15), 1–7.

(74) Sobotta, F. H.; Kuchenbrod, M.; Hoeppener, S.; Brendel, J. C. One Polymer Composition, Various Morphologies: The Decisive Influence of Conditions on the Polymerization-Induced Self-Assembly (PISA) of: N-Acryloyl Thiomorpholine. *Nanoscale* **2020**, *12* (39), 20171–20176.

(75) Hsiao, M.-S.; Yusoff, S. F. M.; Winnik, M. A.; Manners, I. Crystallization-Driven Self-Assembly of Block Copolymers with a Short Crystallizable Core-Forming Segment: Controlling Micelle Morphology through the Influence of Molar Mass and Solvent Selectivity. *Macromolecules* **2014**, *47* (7), 2361–2372.

(76) Vilgis, T.; Halperin, A. Aggregation of Coil-Crystalline Block Copolymers: Equilibrium Crystallization. *Macromolecules* **1991**, *24* (8), 2090–2095.

(77) Shen, L.; Wang, H.; Guerin, G.; Wu, C.; Manners, I.; Winnik, M. A. A Micellar Sphere-to-Cylinder Transition of Poly(Ferrocenyldimethylsilane-b-2-Vinylpyridine) in a Selective Solvent Driven by Crystallization. *Macromolecules* **2008**, *41*, 4380–4389.

(78) Petzetakis, N.; Walker, D.; Dove, A. P.; O'Reilly, R. K. Crystallization-Driven Sphere-to-Rod Transition of Poly(Lactide)-b-Poly(Acrylic Acid) Diblock Copolymers: Mechanism and Kinetics. *Soft Matter* **2012**, *8* (28), 7408–7414.

(79) Loo, Y. L.; Register, R. A.; Ryan, A. J. Modes of Crystallization in Block Copolymer Microdomains: Breakout, Templated, and Confined. *Macromolecules* **2002**, *35* (6), 2365–2374.

(80) Verber, R.; Blanazs, A.; Armes, S. P. Rheological Studies of Thermo-Responsive Diblock Copolymer Worm Gels. *Soft Matter* **2012**, *8*, 9915–9922.

(81) Ellis, C. E.; Fukui, T.; Cordoba, C.; Blackburn, A.; Manners, I. Towards Scalable, Low Dispersity, and Dimensionally Tunable 2D Platelets Using Living Crystallization-Driven Self-Assembly. *Polym. Chem.* **2021**, *12* (25), 3650–3660.

(82) Mohd Yusoff, S. F.; Gilroy, J. B.; Cambridge, G.; Winnik, M. A.; Manners, I. End-to-End Coupling and Network Formation Behavior of Cylindrical Block Copolymer Micelles with a Crystalline Polyferrocenylsilane Core. *J. Am. Chem. Soc.* **2011**, *133* (29), 11220–11230.

(83) Blanco, E.; Shen, H.; Ferrari, M. Principles of Nanoparticle Design for Overcoming Biological Barriers to Drug Delivery. *Nat. Biotechnol.* **2015**, *33* (9), 941–951.

(84) Boott, C. E.; Leitao, E. M.; Hayward, D. W.; Laine, R. F.; Mahou, P.; Guerin, G.; Winnik, M. A.; Richardson, R. M.; Kaminski, C. F.; Whittell, G. R.; Manners, I. Probing the Growth Kinetics for the Formation of Uniform 1D Block Copolymer Nanoparticles by Living Crystallization-Driven Self-Assembly. *ACS Nano* **2018**, *12* (9), 8920–8933.

(85) Rho, J. Y.; Scheutz, G. M.; Häkkinen, S.; Garrison, J. B.; Song, Q.; Yang, J.; Richardson, R.; Perrier, S.; Sumerlin, B. S. In Situ Monitoring of PISA Morphologies. *Polym. Chem.* **2021**, No. 27, 3947–3952.

3.6 Supplementary Material

3.6.1 Materials and Methods

All reactions were performed in an MBraun 200B glovebox under a nitrogen atmosphere or using standard Schlenk line techniques. Dichloromethane (DCM) was dried and de-oxygenated using an MBraun Grubbs/Dow solvent purification system. Acetonitrile (MeCN) was dried over CaH_2, purified by distillation under reduced pressure, and stored over molecular sieves (3 Å). All reagents were purchased from Sigma-Aldrich, VWR, or Fisher Scientific and were used as received unless otherwise noted. Methoxy PEG, 5 kDa, (PEG_{205}) was purchased from Polymer Source. 1,8-Diazabicyclo[5.4.0]undec-7-ene (DBU) was dried over CaH_2 and purified by distillation under reduced pressure. Spiro[fluorene-9,5'-[1,3]dioxin]-2-one (fluorenetrimethylenecarbonate, FTMC) was synthesized according to the previously reported literature procedure.[1] PEG_{205} was dried via vacuum desiccation over phosphorus pentoxide prior to use.

3.6.2 Instrumentation

Nuclear magnetic resonance (NMR) spectroscopy. ^1H NMR spectra were obtained using a Varian 500 MHz spectrometer.

Gel permeation chromatography (GPC). GPC was conducted using a Malvern Omnisec Resolve/Reveal equipped with a triple detector array, automatic sampler, pump, injector, inline degasser column oven (set at 35 °C), elution columns consisting of styrene/divinylbenzene gels (of pore size 500 Å–5,000 Å), refractometer, four-capillary differential viscometer, UV/Vis detector (λ = 440 nm) and dual angle laser light scattering detector (7° and 90°). GPC grade THF with 1 wt% triethylamine was used as the eluent, with a set flow rate of 1 mL/min. Samples were dissolved in THF at 1 mg/mL and filtered through a 0.2 µm polytetrafluoroethylene membrane prior to analysis.

Transmission electron microscopy (TEM). Copper grids (500 mesh) were purchased from Ted Pella, Inc. and carbon films were prepared by using a Leica EM ACE600 instrument. Carbon films were deposited onto the copper grids by floatation on water and allowed to dry over 24 hours. Prior to drop-casting PEG-*b*-PFTMC micelle samples, the copper grids were increased in hydrophilicity by use of the glow discharge function on the Leica EM ACE600 instrument. Samples for electron microscopy were prepared by drop-casting 8 μL of micelle colloidal solution onto a carbon-coated copper grid followed by solvent evaporation. Samples were then stained by drop-casting 8 μL of a 20 wt% solution of uranyl acetate in ethanol. TEM images were obtained using a JEOL JEM 1011 operating at 80 kV, equipped with a Gatan Orius SC1000 CCD camera.

Measurements were undertaken by hand using ImageJ software, developed by the US National Institute for Health.

The number-average length (L_n) and weight-average length (L_w) were calculated according to the following equations:

$$L_n = \frac{\sum_i^n N_i L_i}{\sum_i^n N_i} \qquad\qquad L_w = \frac{\sum_i^n N_i L_i^2}{\sum_i^n N_i L_i}$$

The number-average width (W_n) and weight-average width (W_w) were calculated according to the following equations:

$$W_n = \frac{\sum_i^n N_i W_i}{\sum_i^n N_i} \qquad\qquad W_w = \frac{\sum_i^n N_i W_i^2}{\sum_i^n N_i W_i}$$

A minimum of 100 micelles were measured for each data point. Errors displayed are standard deviations of each data set.

Ultrasonication. Micelle sonication was carried out using a Fisherbrand FB11203 sonication bath. The instrument was operated in sweep mode at 80% power and 37 kHz at 10 °C.

3.6.3 Synthetic Procedures

3.6.3.1 Synthesis of PEG_{205}-*b*-$PFTMC_{19}$ by ROP

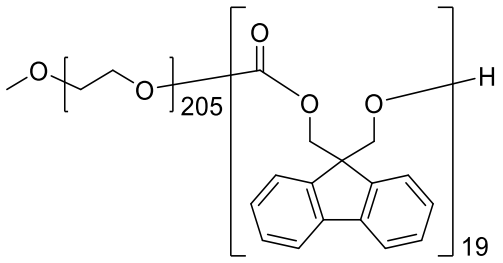

In a glovebox under a nitrogen atmosphere, PEG_{205} (102 mg, 0.011 mmol, 1 equiv.) and DBU (1.3 M in DCM, 7.6 µL, 0.0102 mmol, 0.9 equiv.) were dissolved in anhydrous DCM (750 µL) and stirred for 15 min. To this was added FTMC (51 mg, 0.203 mmol, 18 equiv.) dissolved in anhydrous DCM (750 µL) with rapid stirring. The reaction proceeded for 2 h before being quenched with an excess of benzoic acid (4.3 µL, 0.045, 4 equiv.). The polymer was precipitated three times in ice-cold diethyl ether and dried under vacuum to yield PEG_{205}-*b*-$PFTMC_{19}$ as a white solid. ^{1}H NMR (Figure S20) was used to determine the DP_n of the PFTMC segment as 19, by comparing the integrals of the multiplet at 4.52–4.15 ppm, corresponding to the PFTMC C*H*$_2$O protons, with that of the multiplet at 3.80–3.32 ppm, corresponding to the PEG_{205} backbone.

Yield: 111 mg (72%). ^{1}H NMR (500 MHz, CD_2Cl_2): δ (ppm) = 7.89–7.18 (m, 151H, fluorene), 4.52–4.15 (m, 76H, C*H*$_2$OCOO), 3.80–3.32 (m, 820H, C*H*$_2$C*H*$_2$O); M_n (GPC) = 10,340 Da; M_w/M_n = 1.09.

3.6.4 Self-Assembly Procedures

3.6.4.1 Preparation of polydisperse PEG_{205}-*b*-$PFTMC_n$ micelles (target DP_n = 40, target block ratio = 5:1) via PI-CDSA at various concentrations (5–20 wt%)

In a glovebox under a nitrogen atmosphere, PEG_{205} (51 mg, 0.0056 mmol, 1 equiv.) and DBU (1.3 M in DCM, 3.8 µL, 0.005 mmol, 0.9 equiv.) were dissolved in the minimum amount of anhydrous MeCN and stirred for 15 min. To this was added FTMC (57 mg, 0.224 mmol, 40 equiv.) dissolved in anhydrous DCM and the remaining volume of MeCN required to make the appropriate concentration. The monomer was added with rapid stirring. Immediately after monomer addition, the stirring rate was reduced to 100 rpm to minimize breakage of self-assembled structures.

At time intervals of 1, 2, and 48 h after macroinitiation, aliquots of 5 µL and 75 µL were removed.

The aliquots of 5 µL were diluted to 0.5 mg/mL in 20 v/v DCM/MeCN and immediately drop-cast for analysis by TEM. The samples were then immediately stained with uranyl acetate (3 wt% in ethanol).

The solvent was immediately removed from the aliquots of 75 µL using a flow of air. The samples were redispersed in CD_2Cl_2 for characterization by ^{1}H NMR spectroscopy.

3.6.4.2 Preparation of polydisperse PEG_{205}-*b*-$PFTMC_n$ micelles (target DP_n = 18, target block ratio = 11:1) via PI-CDSA at various concentrations (5–20 wt%)

In a glovebox under a nitrogen atmosphere, PEG_{205} (51 mg, 0.0056 mmol, 1 equiv.) and DBU (1.3 M in DCM, 3.8 µL, 0.005 mmol, 0.9 equiv.) were dissolved in the minimum amount of anhydrous MeCN and stirred for 15 min. To this was added FTMC (25 mg, 0.101 mmol, 18 equiv.) dissolved in anhydrous DCM and the remaining volume of MeCN required to make the appropriate

concentration. The monomer was added with rapid stirring. Immediately after monomer addition, the stirring rate was reduced to 100 rpm to minimize breakage of self-assembled structures.

At time intervals of 1, 2, and 48 h after macroinitiation, aliquots of 5 µL and 75 µL were removed.

The aliquots of 5 µL were diluted to 0.5 mg/mL in 20 v/v DCM/MeCN and immediately drop-cast for analysis by TEM. The samples were then immediately stained with uranyl acetate (3 wt% in ethanol).

The solvent was immediately removed from the aliquots of 75 µL using a flow of air. The samples were redispersed in CD_2Cl_2 for characterization by ^{1}H NMR spectroscopy.

3.6.4.3 Preparation of PEG_{205}-*b*-$PFTMC_{17}$ seed micelles (L_n = 39 nm, L_w/L_n = 1.18) for the living PI-CDSA of PEG_{205}-*b*-$PFTMC_n$

Polydisperse fibers were first prepared at 10 wt%, according to the experimental described above (target DP_n = 18, target block ratio = 11:1).

In a glovebox under a nitrogen atmosphere, PEG_{205} (99 mg, 0.011 mmol, 1 equiv.) and DBU (1.3 M in DCM, 7.4 µL, 0.0099 mmol, 0.9 equiv.) were dissolved in anhydrous MeCN (901 µL) and stirred for 15 min. To this was added FTMC (50 mg, 0.198 mmol, 18 equiv.) dissolved in anhydrous DCM (300 µL) and MeCN (300 µL). The monomer was added with rapid stirring. Immediately after monomer addition, the stirring rate was reduced to 100 rpm to minimize breakage of self-assembled structures.

After 48 h, fiber formation was confirmed by TEM analysis. The BCP structure was determined to be PEG_{205}-*b*-$PFTMC_{17}$ by ^{1}H NMR analysis in CD_2Cl_2. The polydisperse fibers were sonicated for a total of 6 h at 10 °C to prepare small seed micelles (L_n = 39 nm, L_w/L_n = 1.18).

3.6.4.4 Preparation of low dispersity PEG_{205}-*b*-$PFTMC_n$ micelles via living PI-CDSA at 10 wt%

In a glovebox under a nitrogen atmosphere, PEG_{205} (27 mg, 0.003 mmol, 1 equiv.) and DBU (1.3 M in DCM, 2.0 µL, 0.0027 mmol, 0.9 equiv.) were dissolved in 20 vol% DCM/MeCN and stirred for 15 min. FTMC (14 mg, 0.054 mmol, 18 equiv.) was dissolved in the remaining volume of 20 vol% DCM/MeCN. To the FTMC in 20 vol% DCM/MeCN solution was added a volume of PEG_{205}-*b*-$PFTMC_{17}$ seed micelle solutions (L_n = 39 nm, L_w/L_n = 1.18) in 20 vol% DCM/MeCN, to make the appropriate m_{unimer}/m_{seed}. The monomer/seed solution was added to the PEG/DBU solution with rapid stirring. Immediately after addition, the stirring rate was reduced to 100 rpm to minimize breakage of self-assembled structures.

3.6.5 Supplementary Figures

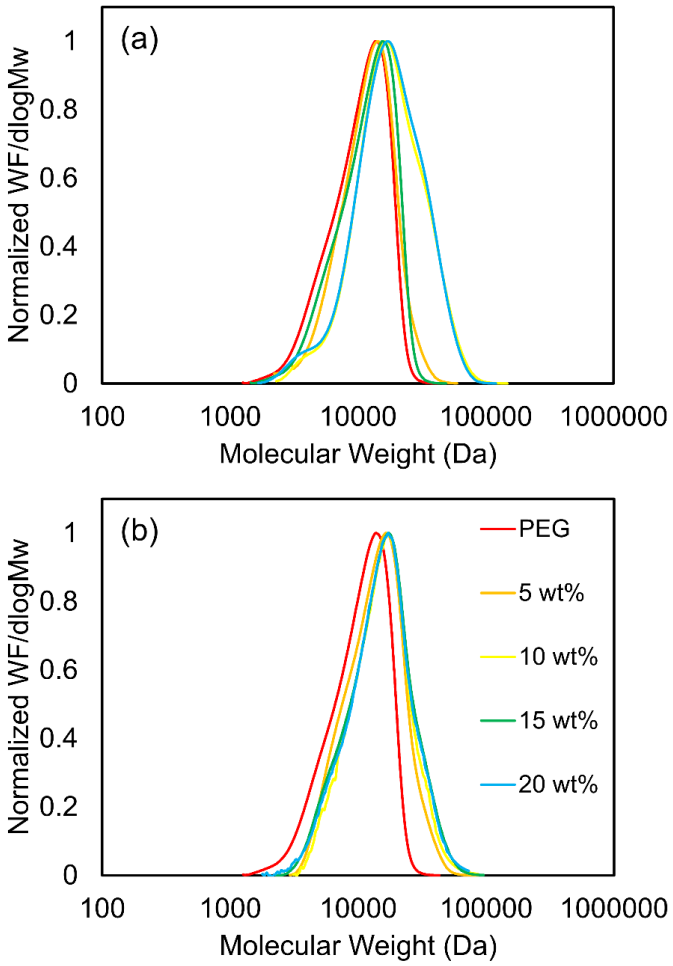

Figure S3.1 GPC traces (refractive index) eluted in triethylamine/THF (1 vol%) at 1 mL/min and 35 °C of PEG_{205} (red trace) and PEG_{205}-*b*-$PFTMC_n$ BCPs prepared via PI-CDSA at 5–20 wt% and 48 h after macroinitiation, with (a) a target PFTMC DP_n = 40 (target block ratio = 5:1) and (b) a target PFTMC DP_n = 18 (target block ratio = 11:1). The y-axis reflects the distribution of weight fractions of the polymer by molecular weight.

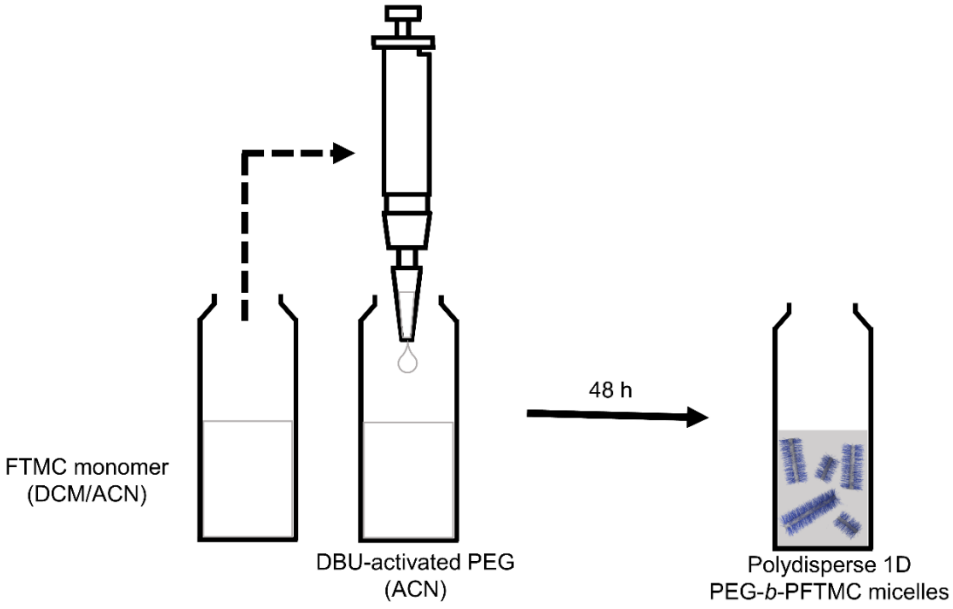

Figure S3.2 Representation of the experimental procedure of the preparation of polydisperse PEG_{205}-*b*-$PFTMC_n$ fiber-like micelles via PI-CDSA at high percentage solids of up to 20 wt% in 20 vol% DCM/MeCN. DBU, 1,8-diazabicyclo[5.4.0]undec-7-ene, was used as the ROP catalyst.

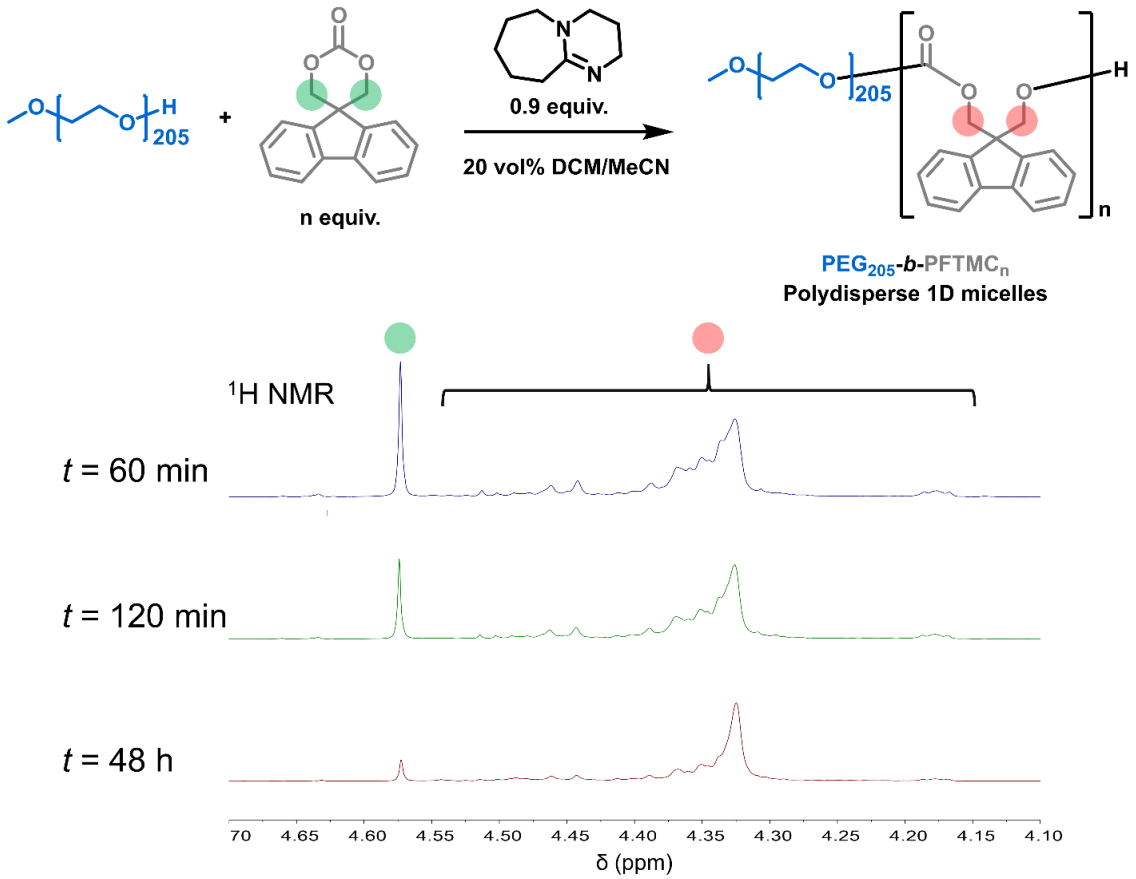

Figure S3.3 Representative example of the use of ^{1}H NMR (500 MHz, CD_2Cl_2) to determine FTMC monomer conversion throughout the PI-CDSA of PEG_{205}-*b*-$PFTMC_n$ in 20 vol% DCM/MeCN at 5–20 wt%. FTMC monomer conversion at 1, 2, and 48 h after macroinitiation was calculated via ^{1}H NMR by comparing the integrals of the singlet at 4.57 ppm (green) with that of the multiplet at 4.52–4.15 ppm (red) which correspond to the monomeric and polymeric C*H*$_2$O protons, respectively.

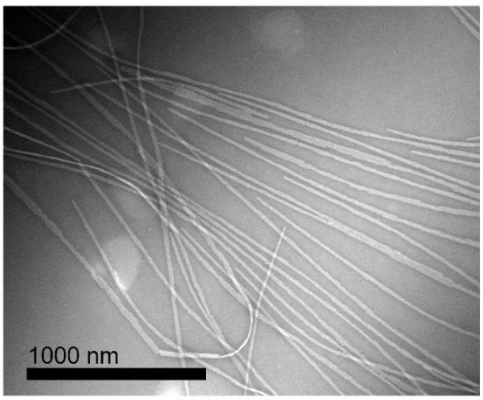

Figure S3.4 Representative TEM image of PEG_{205}-*b*-$PFTMC_n$ fibers (FTMC monomer conversion = 69% PFTMC DP_n = 15, block ratio = 13:1) prepared via PI-CDSA in 20 vol% DCM/MeCN at 5 wt% after 9 days. A solution sample of 0.5 mg/mL was drop-cast, stained with uranyl acetate solution (3 wt% in ethanol), and imaged after solvent evaporation. Scale bar: 1000 nm.

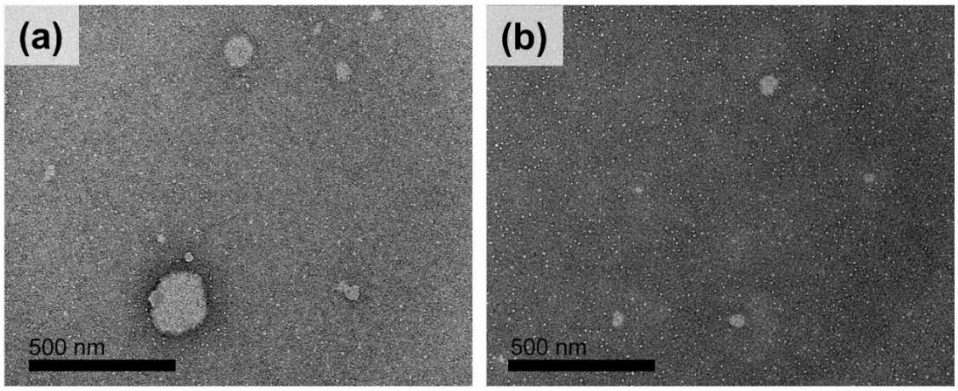

Figure S3.5 Representative TEM images of PEG_{205}-*b*-$PFTMC_{37}$ unimer solution (2.5 mg/mL in DCM) demonstrating the formation of unimer film and spherical micelles on sample preparation and solvent evaporation. Solution samples were drop-cast, stained with uranyl acetate solution (3 wt% in ethanol), and imaged after solvent evaporation. Scale bars: 500 nm.

Figure S3.6 Photos showing visual comparison of PEG_{205}-*b*-$PFTMC_n$ micelle solutions (target DP_n = 40, target block ratio = 5:1) prepared via PI-CDSA in 20 vol% DCM/MeCN at 5–20 wt%.

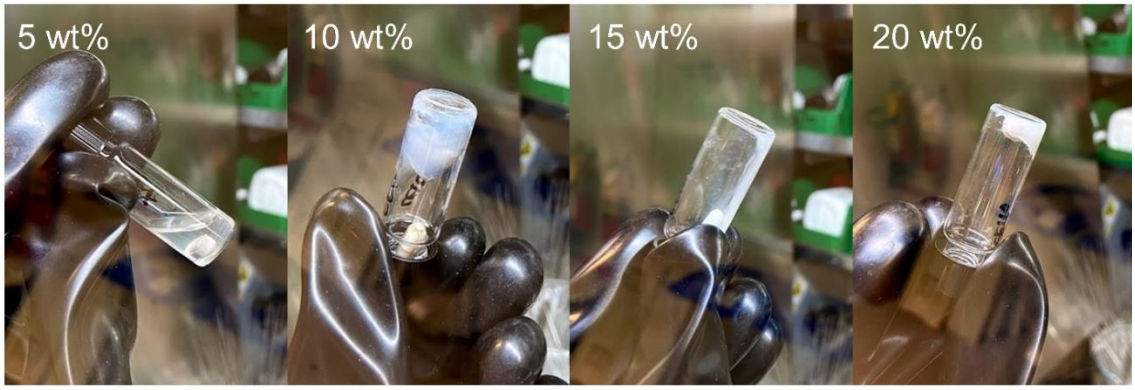

Figure S3.7 Photos showing visual comparison of PEG_{205}-*b*-$PFTMC_n$ micelle solutions (target DP_n = 18, target block ratio = 11:1) prepared via PI-CDSA in 20 vol% DCM/MeCN at 5–20 wt%.

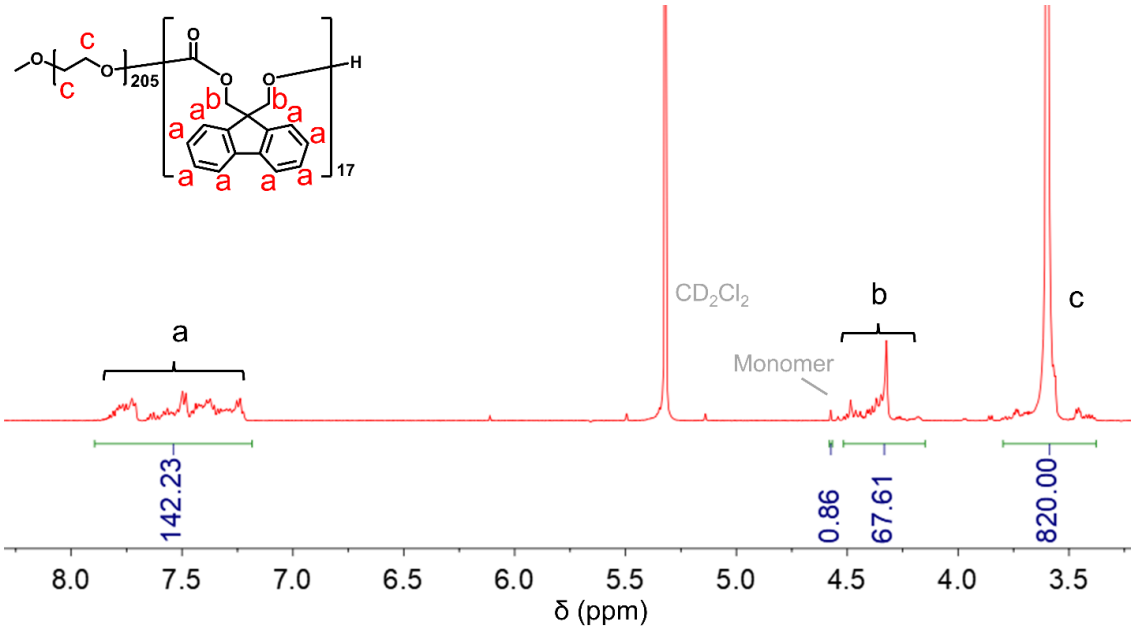

Figure S3.8 ^{1}H NMR (500 MHz, CD_2Cl_2) of PEG_{205}-*b*-$PFTMC_{17}$ prepared via PI-CDSA in 20 vol% DCM/MeCN at 10 wt% for use as seed micelles in living PI-CDSA.

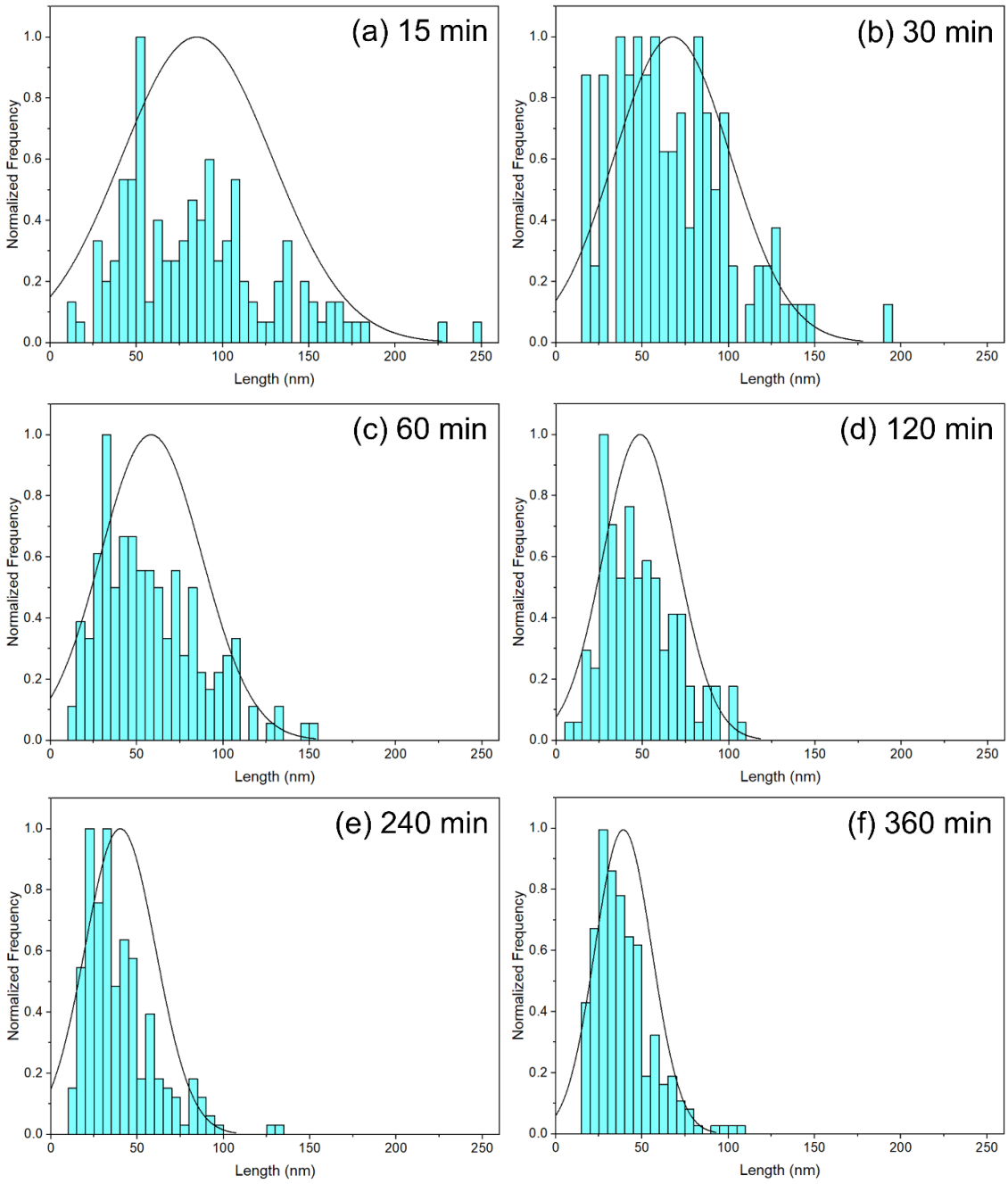

Figure S3.9 Histograms of contour length distributions of PEG_{205}-*b*-$PFTMC_{17}$ fiber-like micelles. Polydisperse PEG_{205}-*b*-$PFTMC_{17}$ micelles were sonicated at 10 °C and analyzed by TEM at (a) 15, (b) 30, (c) 60, (d) 120, (e) 240, and (f) 360 min.

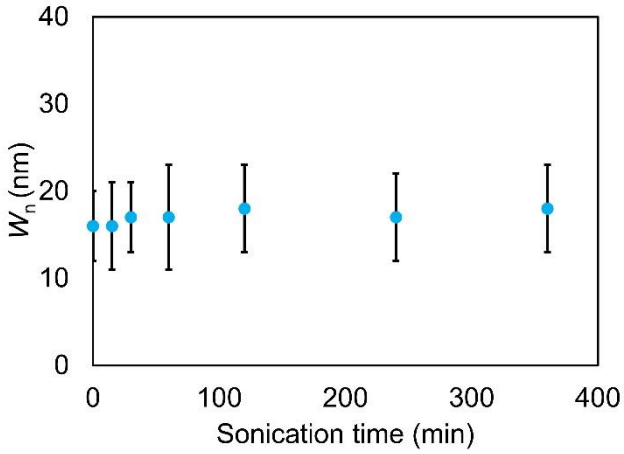

Figure S3.10 Plot illustrating the independence of PEG_{205}-*b*-$PFTMC_{17}$ fiber width (W_n) on sonication time. Polydisperse PEG_{205}-*b*-$PFTMC_{17}$ fibers were prepared via PI-CDSA in 20 vol% DCM/MeCN at 10 wt%. Sonication of fibers was performed at 10 °C. Error bars represent standard deviation of measured W_n.

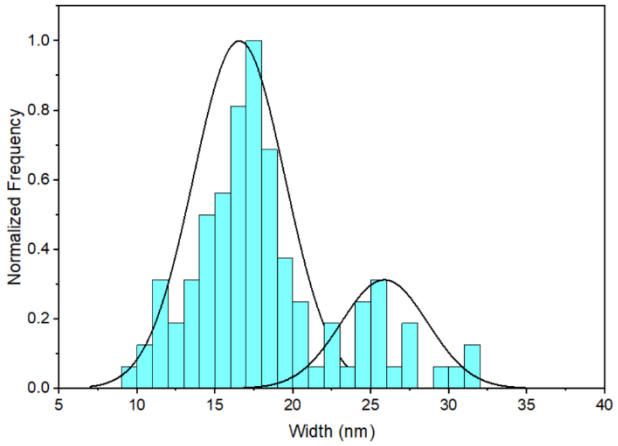

Figure S3.11 Histogram of contour width distribution of PEG_{205}-*b*-$PFTMC_{17}$ fiber-like micelles after sonication at 10 °C for 360 min.

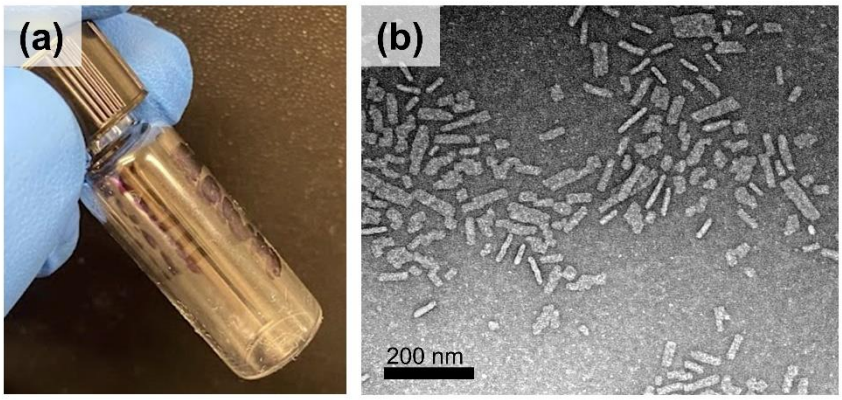

Figure S3.12 (a) Photo showing PEG_{205}-*b*-$PFTMC_{17}$ seeds (L_n = 39 nm) after solvent evaporation. (b) TEM image of PEG_{205}-*b*-$PFTMC_{17}$ seed micelles (L_n = 39 nm) after drying to the solid state. A solution sample of 0.5 mg/mL (20 vol% DCM/MeCN) was drop-cast, stained with uranyl acetate solution (3 wt% in ethanol), and imaged after solvent evaporation. Scale bar: (a) 200 nm.

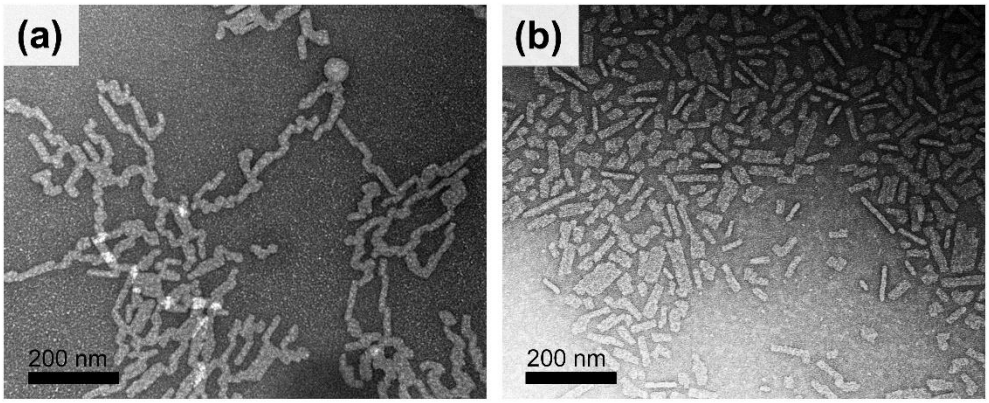

Figure S3.13 TEM image of PEG_{205}-*b*-$PFTMC_{17}$ seed micelles (L_n = 39 nm) prepared at 10 wt% in 20 vol% DCM/MeCN having (a) fused after ageing in solution for ca. 16 weeks and then (b) re-fragmented after re-dispersion in 20 vol% DCM/MeCN and subsequent sonication for 30 min at 10 °C (L_n = 40 ± 19 nm). A solution sample of 0.5 mg/mL (20 vol% DCM/MeCN) was drop-cast, stained with uranyl acetate solution (3 wt% in ethanol), and imaged after solvent evaporation. Scale bars: 200 nm.

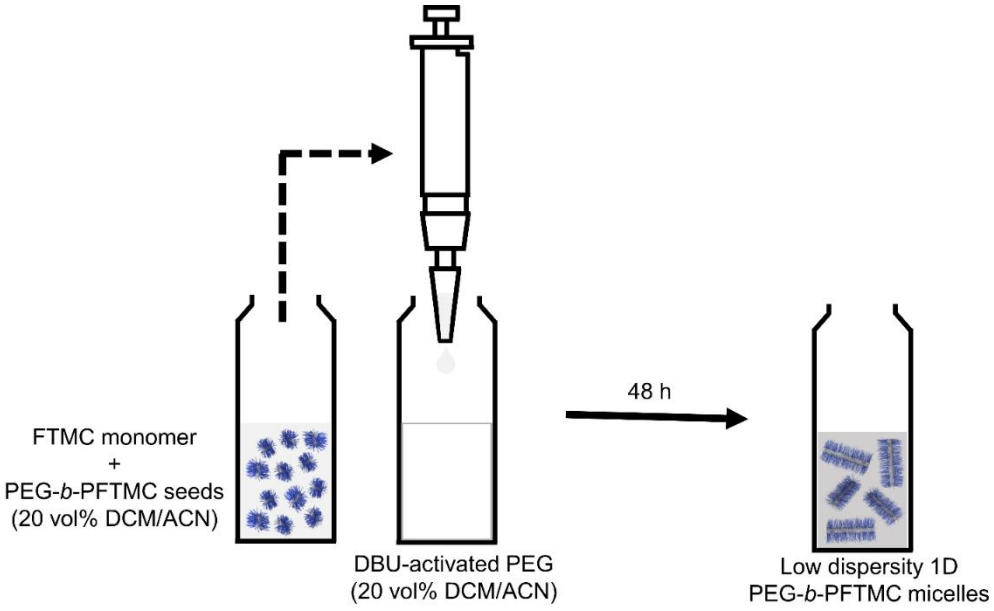

Figure S3.14 Representation of the experimental procedure of the preparation of low dispersity PEG_{205}-*b*-$PFTMC_n$ fiber-like micelles via living PI-CDSA at 10 wt% in 20 vol% DCM/MeCN and various m_{unimer}/m_{seed}. DBU, 1,8-diazabicyclo[5.4.0]undec-7-ene, was used as the ROP catalyst.

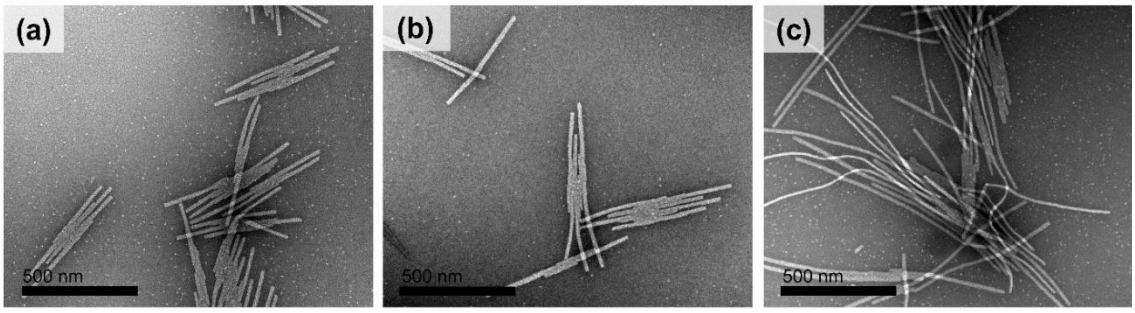

Figure S3.15 Representative TEM images of PEG_{205}-*b*-$PFTMC_n$ nanofibers (target DP_n = 18, target block ratio = 11:1) prepared via living PI-CDSA from PEG_{205}-*b*-$PFTMC_{17}$ seed micelles (L_n = 39 nm) in 20 vol% DCM/MeCN at 10 wt% and m_{unimer}/m_{seed} values of (a) 20, (b) 30, and (c) 40 after 48 h. Spherical micelle formation can be observed in each instance. Solution samples of 0.5 mg/mL were drop-cast, stained with uranyl acetate solution (3 wt% in ethanol), and imaged after solvent evaporation. Scale bars: 500 nm.

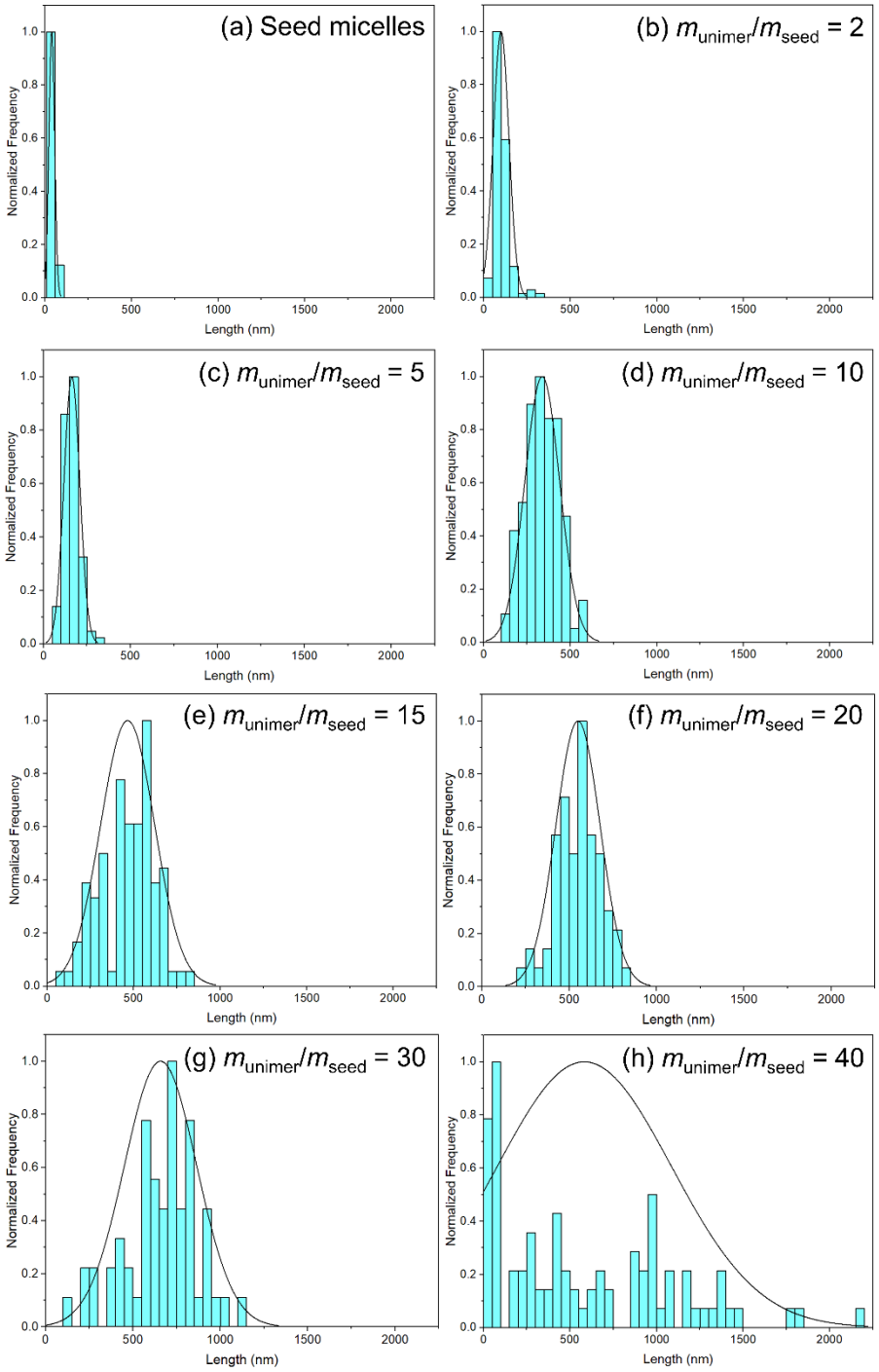

Figure S3.16 Histograms of contour length distributions of PEG_{205}-*b*-$PFTMC_n$ nanofibers (target DP_n = 18, target block ratio = 11:1) prepared via living PI-CDSA from (a) PEG_{205}-*b*-$PFTMC_{17}$

seed micelles (L_n = 39 nm) in 20 vol% DCM/MeCN at 10 wt% and m_{unimer}/m_{seed} values of (b) 2, (c) 5, (d) 10, (e) 15, (f) 20, (g) 30, and (h) 40 after 48 h.

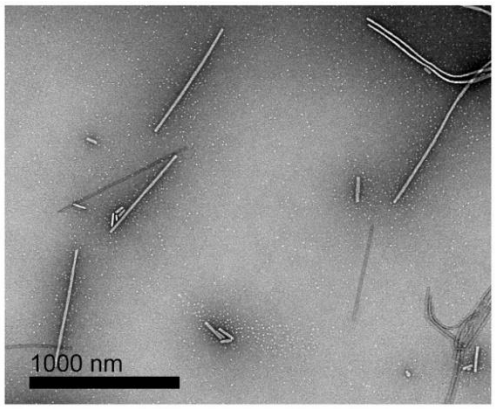

Figure S3.17 TEM image of PEG_{205}-*b*-$PFTMC_n$ fibers (target DP_n = 18, target block ratio = 11:1) prepared via living PI-CDSA from PEG_{205}-*b*-$PFTMC_{17}$ seeds (L_n = 39 nm) in 20 vol% DCM/MeCN at 10 wt% and m_{unimer}/m_{seed} = 40 demonstrating the presence of short fibers which provide evidence for competitive self-nucleation. A solution sample of 0.5 mg/mL was drop-cast, stained with uranyl acetate solution (3 wt% in ethanol), and imaged after solvent evaporation. Scale bar: 1000 nm.

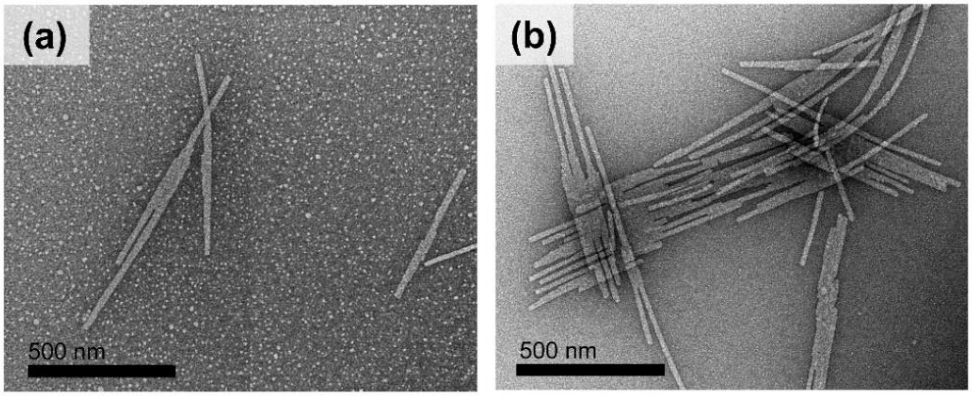

Figure S3.18 Representative TEM images of PEG_{205}-*b*-$PFTMC_n$ nanofibers (target DP_n = 18, target block ratio = 11:1) prepared via living PI-CDSA from PEG_{205}-*b*-$PFTMC_{17}$ seed micelles (L_n = 39 nm) in 20 vol% DCM/MeCN at 10 wt% and m_{unimer}/m_{seed} = 20 at 35 °C after (a) 48 h or

(b) 7 days. Solution samples of 0.5 mg/mL were drop-cast, stained with uranyl acetate solution (3 wt% in ethanol), and imaged after solvent evaporation. Scale bars: 500 nm.

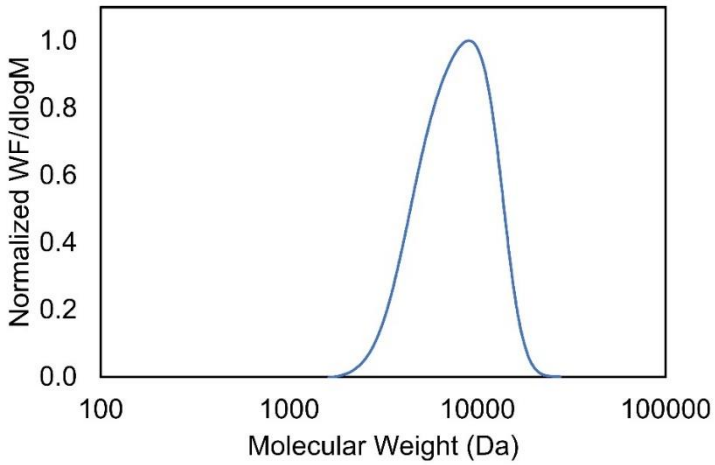

Figure S3.19 GPC trace (refractive index) eluted in triethylamine/THF (1 vol%) at 1 mL/min and 35 °C of PEG_{205}-*b*-$PFTMC_{19}$ prepared via ROP.

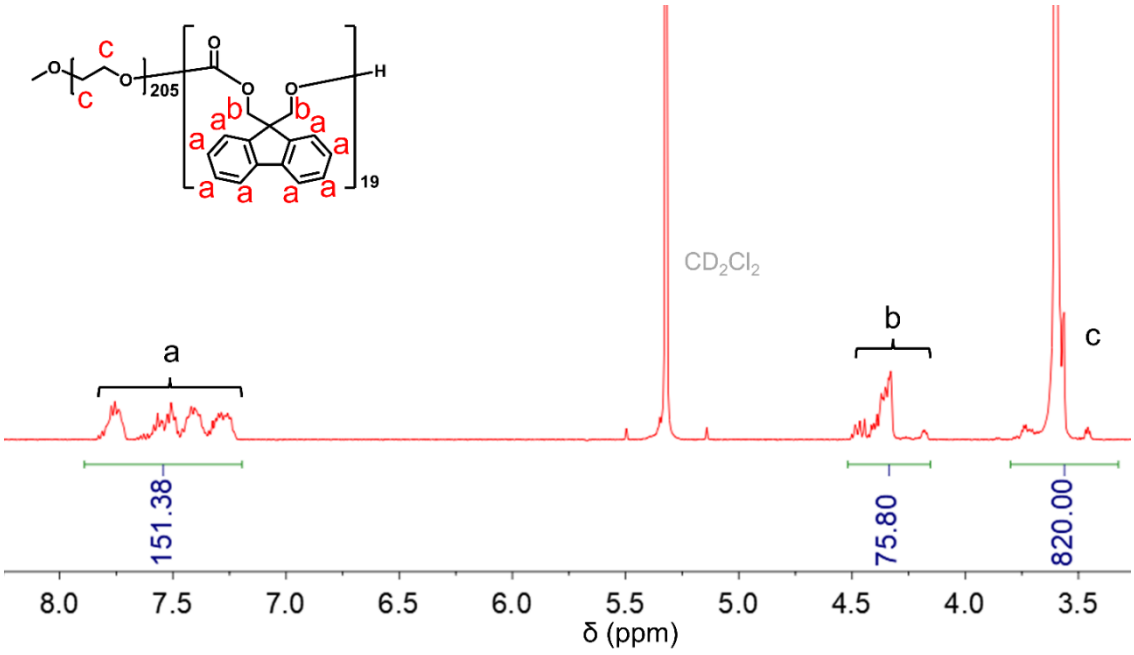

Figure S3.20 ^{1}H NMR (500 MHz, CD_2Cl_2) of PEG_{205}-*b*-$PFTMC_{19}$ prepared via ROP in DCM.

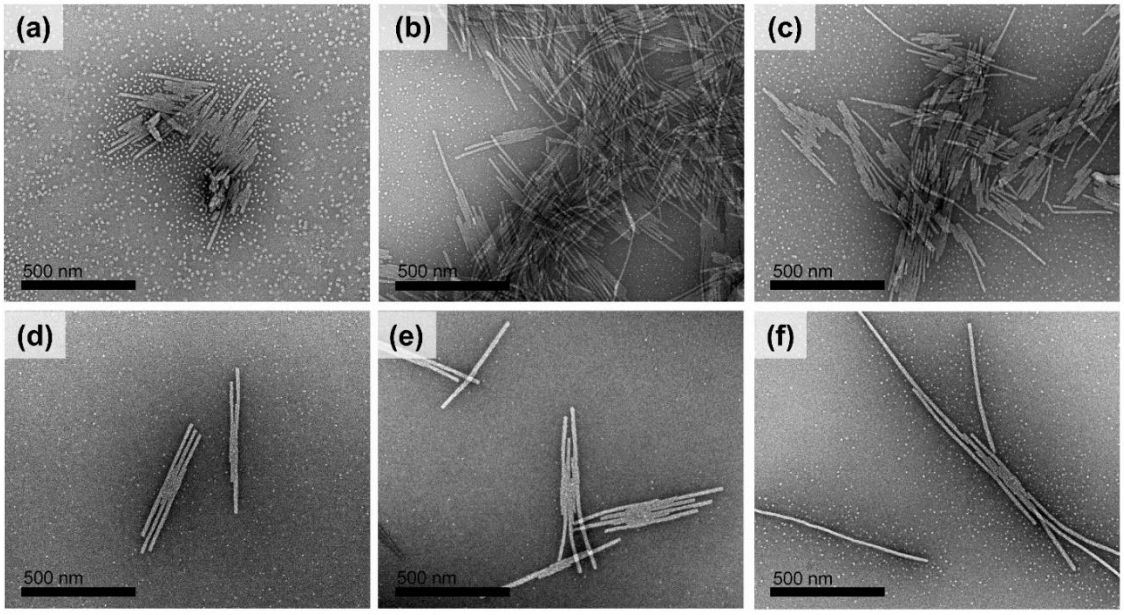

Figure S3.21 Representative TEM images of PEG_{205}-*b*-$PFTMC_{19}$ fibers prepared via (a–c) living CDSA or (d–f) living PI-CDSA from PEG_{205}-*b*-$PFTMC_{17}$ seeds (L_n = 39 nm) in 20 vol% DCM/MeCN at 10 wt% and m_{unimer}/m_{seed} values of (a, d) 20, (b, e) 30, and (c, f) 40 after 48 h. Solution samples of 0.5 mg/mL were drop-cast, stained with uranyl acetate solution (3 wt% in ethanol), and imaged after solvent evaporation. Scale bars: 500 nm.

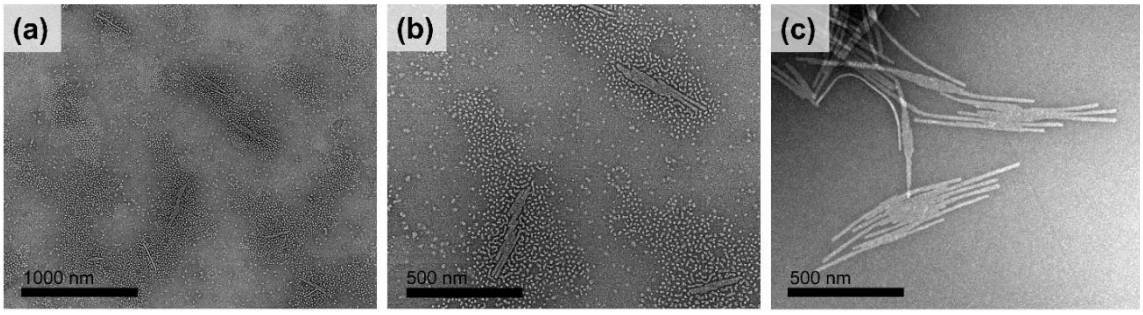

Figure S3.22 Representative TEM images of PEG_{205}-*b*-$PFTMC_{19}$ fibers prepared via (a, b) living CDSA or (c) living PI-CDSA from PEG_{205}-*b*-$PFTMC_{17}$ seeds (L_n = 39 nm) in 20 vol% DCM/MeCN at 10 wt% and m_{unimer}/m_{seed} = 20 after 7 days. Solution samples of 0.5 mg/mL were drop-cast, stained with uranyl acetate solution (3 wt% in ethanol), and imaged after solvent evaporation. Scale bars: (a) 1000 nm. (b, c) 500 nm.

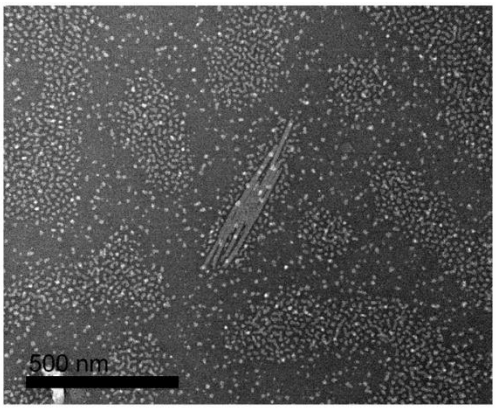

Figure S3.23 TEM image of PEG_{205}-*b*-$PFTMC_{19}$ fibers (L_n = 294 ± 90 nm, L_w/L_n = 1.09) prepared via living CDSA from PEG_{205}-*b*-$PFTMC_{17}$ seeds (L_n = 39 nm) in 20 vol% DCM/MeCN at 0.06 wt% and m_{unimer}/m_{seed} = 10 after 48 h. A solution sample was drop-cast, stained with uranyl acetate solution (3 wt% in ethanol), and imaged after solvent evaporation. Scale bar: 500 nm.

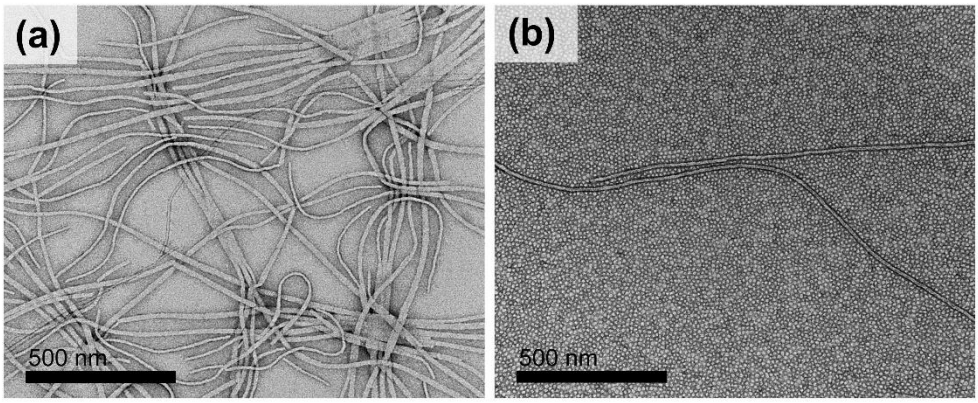

Figure S3.24 Representative TEM images of PEG_{205}-*b*-$PFTMC_{19}$ nanostructures prepared via CDSA at 0.06 wt% in (a) 20 vol% DMSO/MeOH or (b) 20 vol% DCM/MeCN. Scale bars: 500 nm.

3.6.6 Supplementary Tables

Table S3.1 Molecular weight characterization data of PEG_{205}-*b*-$PFTMC_n$ BCPs prepared via PI-CDSA in 20 vol% DCM/MeCN at 5–20 wt% determined by GPC.

Target block ratio	Concentration (wt%)	M_n (g/mol)	M_w/M_n
PEG_{205}	-	9,030	1.10
5:1	5	25,860	1.16
	10	20,580	1.26
	15	21,510	1.25
	20	20,340	1.25
11:1	5	15,830	1.23
	10	13,050	1.31
	15	16,180	1.31
	20	12,540	1.37

Table S3.2 Summary of FTMC monomer conversion in the PI-CDSA of PEG_{205}-*b*-$PFTMC_n$ in 20 vol% DCM/MeCN at 5–20 wt% at 1, 2, and 48 h after macroinitiation determined by ^1H NMR. (*Experiment repeated three times, yielding same result.)

		FTMC monomer conversion		
Target block ratio (Target PFTMC DP_n)	**Concentration (wt%)**	***t* = 1 h**	***t* = 2 h**	***t* = 48 h**
5:1 (40)	5*	18%	27%	58%
	10	87%	91%	96%
	15	91%	99%	99%
	20	97%	99%	99%
11:1 (18)	5	92%	91%	91%
	10	86%	89%	98%
	15	81%	82%	97%
	20	78%	82%	98%

Table S3.3 Summary of PFTMC DP_n in the PI-CDSA of PEG_{205}-*b*-$PFTMC_n$ in 20 vol% DCM/MeCN at 5–20 wt% at 1, 2, and 48 h after macroinitiation calculated using the corresponding FTMC monomer conversions determined by ^1H NMR. (*Experiment repeated three times, yielding same result.)

		Calculated PFTMC DP_n		
Target block ratio (Target PFTMC DP_n)	**Concentration (wt%)**	***t* = 1 h**	***t* = 2 h**	***t* = 48 h**
5:1 (40)	5*	4	7	14
	10	35	36	38
	15	35	38	38
	20	33	34	34
11:1 (18)	5	11	10	10
	10	10	11	12
	15	8	9	10
	20	8	8	10

Table S3.4 Summary of the PEG_{205}:$PFTMC_n$ block ratio in the PI-CDSA of PEG_{205}-*b*-$PFTMC_n$ in 20 vol% DCM/MeCN at 5–20 wt% at 1, 2, and 48 h after macroinitiation calculated using the corresponding PFTMC DP_n. (*Experiment repeated three times, yielding same result.)

		PEG_{205}:$PFTMC_n$ block ratio		
Target block ratio (Target PFTMC DP_n)	**Concentration (wt%)**	***t* = 1 h**	***t* = 2 h**	***t* = 48 h**
5:1 (40)	5*	51:1	29:1	15:1
	10	6:1	6:1	5:1
	15	6:1	5:1	5:1
	20	6:1	6:1	6:1
11:1 (18)	5	19:1	21:1	21:1
	10	21:1	19:1	17:1
	15	26:1	23:1	21:1
	20	26:1	26:1	21:1

Table S3.5 Contour length (L_n) and width (W_n) data determined by TEM size analysis of PEG_{205}-*b*-$PFTMC_{17}$ fibers at various sonication times. PEG_{205}-*b*-$PFTMC_n$ fibers were prepared via PI-CDSA in 20 vol% DCM/MeCN at 10 wt%. Sonication of fibers was performed at 10 °C.

Sonication time (min)	L_n **(nm)**	**σ (nm)**	W_n **(nm)**	**σ (nm)**
15	85	43	16	5
30	67	34	17	4
60	58	29	17	6
120	49	21	18	5
240	40	21	17	5
360	39	16	18	5

Table S3.6 Contour length (L_n), standard deviation (σ), and length-dispersity (L_w/L_n) data determined by TEM size analysis for the PEG_{205}-*b*-$PFTMC_{19}$ nanofibers prepared via living CDSA from PEG_{205}-*b*-$PFTMC_{17}$ seed micelles (L_n = 39 nm) in 20 vol% DCM/MeCN at 10 wt%, m_{unimer}/m_{seed} = 20, and either 22 or 35 °C after 48 h.

Temperature (°C)	22	35
Theoretical L_n **(nm)**	819	
L_n **(nm)**	419	560
σ (nm)	137	179
L_w/L_n	1.11	1.10

Table S3.7 Contour length (L_n), standard deviation (σ), and length-dispersity (L_w/L_n) data determined by TEM size analysis for the PEG_{205}-*b*-$PFTMC_{19}$ nanofibers prepared via living CDSA from PEG_{205}-*b*-$PFTMC_{17}$ seed micelles (L_n = 39 nm) in 20 vol% DCM/MeCN at 10 wt% and various m_{unimer}/m_{seed} after 7 days (*or 48 h).

m_{unimer}/m_{seed}	20		30		40	
Seeded growth technique	Living CDSA	Living PI-CDSA	Living CDSA	Living PI-CDSA	Living CDSA	Living PI-CDSA
Theoretical L_n (nm)	819		1209		1599	
L_n (nm)	242	569	372	658	323	583*
σ (nm)	116	166	191	205	150	500*
L_w/L_n	1.23	1.09	1.26	1.10	1.22	1.74*

3.6.7 Supplementary References

(1) Venkataraman, S.; Hedrick, J. L.; Yang, Y. Y. Fluorene-Functionalized Aliphatic Polycarbonates: Design, Synthesis and Aqueous Self-Assembly of Amphiphilic Block Copolymers. *Polym. Chem.* **2014**, *5* (6), 2035–2040.

Chapter 4 Scalable Preparation of 1D Micelles via Living Crystallization-Driven Self-Assembly in Continuous Flow

4.1 Abstract

Living crystallization-driven self-assembly (CDSA) represents a robust route to access anisotropic block copolymer-based nanostructures of controlled morphology and size, which exhibit low size-dispersity. Consequently, one-dimensional (1D) cylindrical micelles prepared by living CDSA are of interest for a diverse range of applications. Typically performed under dilute conditions, recent efforts have focused on upscaling living CDSA by increasing the solution concentration at which the process is performed. Here, we report the development of simple and cost-effective continuous flow setups to prepare 1D polydisperse micelles, seeds, and low dispersity 1D micelles. This approach allows for remarkably higher throughput of 1D micelles compared with that which is feasibly achievable in batch.

4.2 Introduction

One-dimensional (1D) nanostructures formed from the self-assembly of block copolymers (BCPs) are of great interest for potential applications in the areas of nanomedicine,[1–6] catalysis,[7–9] rheological modifiers,[10] and optoelectronics.[11–13] Crystallization-driven self-assembly (CDSA) of BCPs containing a crystallizable core-forming block is a robust method of targeting the formation of 1D cylindrical or two-dimensional (2D) platelet micelles. Compared with their amorphous analogues, BCPs with a crystalline core-forming block favour the formation of nanostructures with low curvature of the core–corona interface, due to the additional enthalpic contribution of crystallization. The resulting morphology minimizes the core–non-solvent interfacial energy whilst

also decreasing the entropic penalty of coronal chain stretching.[14–16] The rate of self-nucleation in CDSA processes is typically much slower than that of the elongation step involving growth of unimer to form the crystalline 1D micelle core. As a consequence, the micelles obtained are generally polydisperse and lack size-control. Polydisperse micelles prepared by CDSA can be sonicated, thereby fragmenting the nanostructures to access low aspect ratio seed micelles. Crucially, the exposed crystalline core of the seed micelles remains active to epitaxial crystal growth.[17]

Size-control of 1D and 2D BCP-based micelles can be achieved through the seeded growth process termed "living" CDSA. In this case, molecular dissolved BCP (unimer) is added to pre-formed seed micelles, which act as efficient initiators for elongation via epitaxial growth. Specific nanofiber lengths or platelet areas can also be targeted by simply altering the mass ratio of unimer-to-seeds (m_{unimer}/m_{seed}). Through circumventing self-nucleation, low dispersity micelles with controlled dimensions can therefore be accessed by living CDSA. Living CDSA has been demonstrated using polymeric amphiphiles containing a variety of crystallizable segments, including poly(ferrocenyldimethylsilane) (PFS),[18,19] polyethylene,[20] poly(3-hexylthiophene), poly and oligo(*p*-phenylenevinylene),[21–23] poly(*L*-lactide),[24,25] poly(ε-caprolactone),[26,27] polycarbonate,[28] and poly(isopropyloxazoline).[6] Living CDSA is typically performed under dilute conditions to minimize competitive self-nucleation events which would other compromise size-dispersity. Limited examples of upscaled preparation of size-controlled 1D or 2D micelle have previously been reported.[19,29–31] This, in turn, limits the investigation and implementation of low dispersity size-controlled micelles for their potential applications.

The living CDSA process can be considered analogous with living covalent polymerizations of molecular monomers, where the rate of initiation is faster than that of propagation, and chain-termination processes are absent.[32] In recent years, the ability to obtain polymers which exhibit low molecular weight dispersities by performing living anionic polymerization in continuous flow

systems has been demonstrated.[33–36] This is of great significance for facilitating the industrial application of living anionic polymerizations, as continuous flow processes exhibit many benefits over their batch counterparts. For example, a variety of polymer molecular weights can be accessed by living anionic polymerization in flow by simply adjusting the stream flow ratios of monomer and initiator after the process has begun. Heat transfer is also vastly improved compared with that in batch, due to the reactor's high surface area to volume ratio, meaning polymerizations can typically be performed without the need for addition cooling.[34]

In this work, we demonstrate CDSA, seed micelle preparation, and living CDSA processes in continuous flow. We employ a simple home-built continuous flow setup with a cost-effective T-joint mixer to access polydisperse or seed micelles. We also describe our efforts towards the preparation of length-controlled 1D micelles by living CDSA in continuous flow through using a packed-bed column mixer which provides the improved mixing required to access nanostructures with low length-dispersities.

4.3 Results and Discussion

4.3.1 Synthesis and Characterization of PFS_{32}-*b*-$P2VP_{480}$

PFS_{32}-*b*-$P2VP_{480}$ (chemical structure shown in **Figure 4.1**) was prepared by living anionic polymerization.[18] A small aliquot of PFS was removed for characterization by matrix-assisted laser desorption/ionization time-of-flight (MALDI-TOF) mass spectrometry. The number-average molecular weight (M_n) of the PFS block was found to be 7,740 Da, corresponding to a degree of polymerization (DP_n) of 32 (target DP_n = 30). ^{1}H NMR was used to determine the corona-to-core block ratio as 15, through a comparison of the integration of peaks corresponding to Cp*H* of PFS (multiplet at 4.02 ppm) and the aromatic protons of P2VP (multiplet at 7.40–6.08 ppm) (**Figure S4.1**). The molecular weight dispersity (M_w/M_n) of the BCP was determined to be M_w/M_n = 1.05 by gel permeation chromatography. A large corona-to-core block ratio of 15 was targeted since this is

expected to reduce the micelle growth rate.[37] In principle, we expected that a reduction in micelle growth rate should minimize the requirement for rapid mixing in the following investigations, allowing for low dispersity micelles to be obtained more easily.

With the aim of accessing uniform 1D micelles via continuous flow, we identified three key stages to investigate: (1) the formation of polydisperse fibers via CDSA in flow, (2) the preparation of seed micelles via synchronous CDSA and sonication in flow, and (3) the formation of low dispersity fibers via living CDSA in flow. Herein, we describe the optimization of these processes utilizing PFS_{32}-*b*-$P2VP_{480}$ as proof-of-concept experiments. We discuss the results in terms of flow rate (µL/min), which is calculated by addition of the feed stream flow rates, and residence time (min), which is defined by the time it takes to entirely exchange the volume of the reactor.

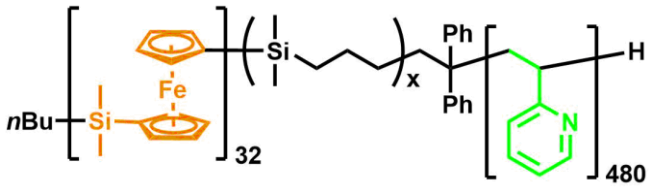

Figure 4.1 Chemical structure of PFS_{32}-*b*-$P2VP_{480}$ utilized in this study.

4.3.2 Preparation of Polydisperse PFS_{32}-*b*-$P2VP_{480}$ fibers via CDSA in Continuous Flow

We began our investigation by examining the preparation of polydisperse PFS_{32}-*b*-$P2VP_{480}$ fibers by CDSA in continuous flow. A simple and cost-effective two-feed coil reactor comprised of fluorinated ethylene propylene (FEP) tubing and a T-joint mixer was built (**Scheme 4.1**), with a reactor volume of 4712 µL. To access polydisperse fibers via CDSA in flow, it is required that a unimer solution (whereby the BCP is molecularly dissolved) is mixed with a selective solvent which will induce self-assembly and crystallization of the core-forming block. Therefore, the two feeds contained a PFS_{32}-*b*-$P2VP_{480}$ unimer solution in THF (25 mg/mL) and isopropanol (*i*PrOH), a selective solvent for the P2VP corona, respectively. The feeds were pumped through the

continuous flow setup by syringe pumps with a flow rate ratio of 4, to give a final solvent composition of 20 vol% THF/*i*PrOH, a final concentration of 5 mg/mL, and an overall flow rate of 26 µL/min. The resulting micelle solution was collected into a vial after a residence time of 180 min. On performing the continuous CDSA process under these conditions, polydisperse PFS_{32}-*b*-$P2VP_{480}$ 1D micelles were formed (**Scheme 4.1**).

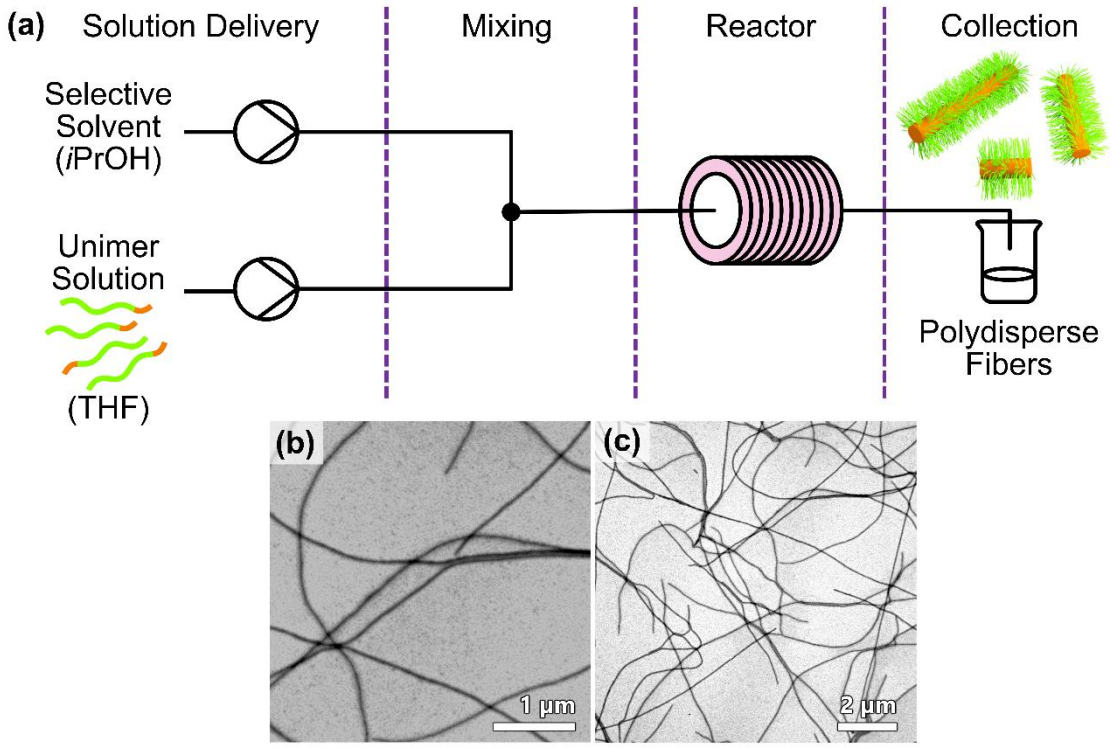

Scheme 4.1 (a) Preparation of polydisperse PFS_{32}-*b*-$P2VP_{480}$ fibers by CDSA in continuous flow. Coil reactor (reactor volume = 4712 µL) with T-joint mixer and two reagent streams comprising of selective solvent (*i*PrOH) and unimer solution (PFS_{32}-*b*-$P2VP_{480}$ in THF, 25 mg/mL) were used. (b, c) TEM images of polydisperse PFS_{32}-*b*-$P2VP_{480}$ fibers (5 mg/mL, 20 vol% THF/*i*PrOH) prepared using the flow set-up depicted at (b) low and (c) high magnification. A solution sample was drop-cast immediately from collection vial, with no ageing, and imaged after solvent evaporation. Scale bars: (b) 1 µm, (c) 2 µm.

4.3.3 Preparation of PFS_{32}-*b*-$P2VP_{480}$ Seed Micelles via Synchronous CDSA and Sonication in Continuous Flow

On demonstrating the successful use of CDSA in continuous flow to access polydisperse PFS_{32}-*b*-$P2VP_{480}$ micelles, we looked to perform synchronous CDSA and sonication to access seed micelles in a simple one-step continuous process. We utilized the simple coil reactor with FEP tubing and a T-joint mixer that we built previously (reactor volume = 4712 µL) with the same two feeds of unimer solution (PFS_{32}-*b*-$P2VP_{480}$ in THF, 25 mg/mL) and selective solvent (*i*PrOH). The coil reactor was then placed into a sonication bath and maintained at ca. 10 °C (**Scheme 4.2**) throughout the experiment. The resulting seed solution was collected into a vial.

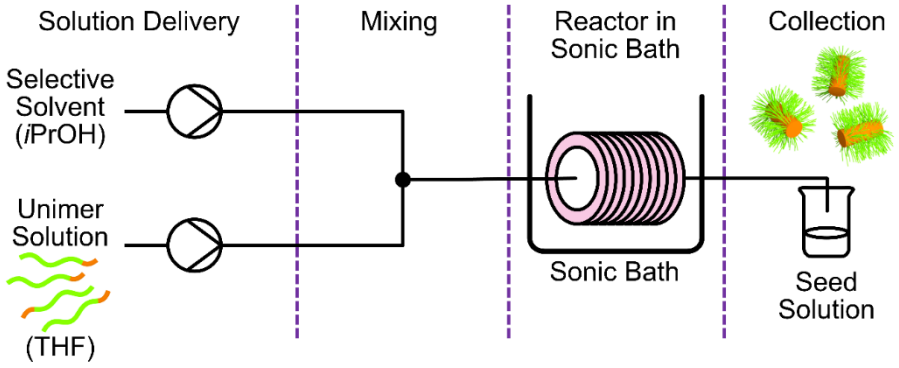

Scheme 4.2 Preparation of PFS_{32}-*b*-$P2VP_{480}$ seed micelle preparation by synchronous CDSA and sonication in continuous flow. Coil reactor (reactor volume = 4712 µL) with T-joint mixer and two reagent streams comprising of selective solvent (*i*PrOH) and unimer solution (PFS_{32}-*b*-$P2VP_{480}$ in THF, 25 mg/mL) were used. The reactor was placed in a sonication bath maintained at 10 °C throughout the experiment.

During optimization studies, we varied the residence time (11–120 min) by altering the flow rate (**Table S4.1**). The ratio of feed flow rates was kept constant at 4 (selective solvent/unimer solution). Aliquots were taken from the collection vial after the appropriate residence time and were spotted immediately onto carbon-coated copper grids for analysis by TEM. The aliquots were also aged for 24 h before being spotted and reimaged to determine whether the CDSA/sonication process went

to completion inside the flow reactor itself, or whether the process continued in batch in the collection vial. Size analysis was performed to determine the number-average length (L_n) and length-dispersity (L_w/L_n) of the micelles prior to and after ageing (**Figures 4.2**a, **S4.2** and **S4.3**, and **Table S4.1**).

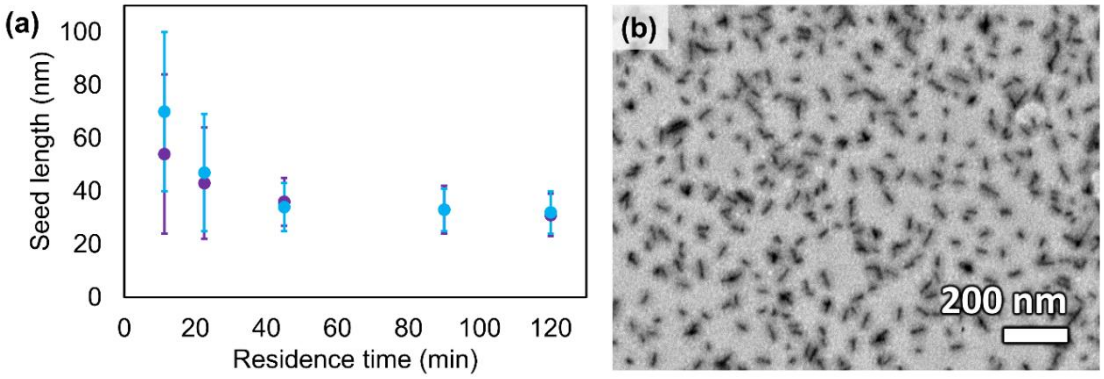

Figure 4.2 (a) Effect of residence time on the micelle length obtained from synchronous CDSA/sonication in continuous flow. Error bars represent standard deviation of the measured length. Samples were either spotted immediately from the flow process (no ageing, blue) or were aged in batch for 24 h before being spotted (purple). (b) TEM image of PFS_{32}-*b*-$P2VP_{480}$ seed micelles (L_n = 36 nm, L_w/L_n = 1.06) prepared by synchronous CDSA/sonication in continuous flow (20 vol% THF/*i*PrOH, 5 mg/mL, residence time = 45 min). A solution sample was drop-cast immediately from collection vial, with no ageing, and imaged after solvent evaporation. Scale bar: 200 nm.

For residence times below 45 min, it is evident that the CDSA/sonication process is incomplete within the flow reactor. For example, using a residence time of 11 min, the micelles formed during the flow process exhibited a length of L_n = 54 nm and had a relatively high length-dispersity of L_w/L_n = 1.28 (**Figures 4.2**a, **S4.2**a and **S4.3**a, and **Table S4.1**). This indicated that the fragmentation of fibers is incomplete, likely due to the short residence (and therefore sonication) time. It is known that the scission of PFS-based micelles depends strongly on fiber length, with longer micelles being fragmented easily and short micelles being more stable.[38] We would therefore expect to see a

significant decrease in fiber length at the start of the sonication process. Then with increasing sonication time, we would expect to observe a slower rate of fragmentation since scission of shorter micelles would be more challenging.[38] Furthermore, on ageing of these micelles for 24 h, the fibers increased in length to L_n = 70 nm (L_w/L_n = 1.20), demonstrating that the elongation process (CDSA) was also incomplete after the 11 min residence time.

On increasing the residence time to 45 min, low dispersity nanofibers (L_n = 36 nm, L_w/L_n = 1.06) were obtained from the continuous flow process (**Figures 4.2**b and **S4.2**c). The lack of any significant change in the micelle length or length-dispersity after ageing (L_n = 34 nm, L_w/L_n = 1.06, **Figure S4.2**h) indicated that both the CDSA and sonication processes went to completion in the reactor. Experiments with longer residences times (90 and 120 min) also resulted in the formation of PFS_{32}-*b*-$P2VP_{480}$ seed micelles with statistically identical lengths and dispersities to that when using a residence time of 45 min (**Figures 4.2**a, **S4.2**d, e and **S4.3**d, e, and **Table S4.1**). On ageing of these samples for 24 h, no significant change in these values was observed (**Figures 4.2**a, **S4.2**i, j, and **S4.3**i, j, and **Table S4.1**). These results corroborate that the synchronous CDSA and sonication processes are complete within a 45 min residence time.

The seed preparation optimization process was repeated using an alternative, more specialized T-joint micromixer which we anticipated to improve our results further due to exhibiting more rapid mixing.[39–41] However, this setup yielded similar results as those achieved using a basic T-joint mixer (**Tables S4.1** and **S4.2**). Therefore, seed micelles can be prepared using a simple cost-effective continuous flow setup without the requirement of specialized micromixing units. The optimized seed preparation via synchronous CDSA and sonication in continuous flow was repeated a total of five times to yield seed micelles with statistically identical lengths within error (**Table S4.3**), demonstrating the robustness of our method. Using this continuous flow setup under these optimized conditions, we can access 20 mL (100 mg) of PFS_{32}-*b*-$P2VP_{480}$ seed micelles (5 mg/mL)

in 210 min. The theoretical yield of this process is therefore ca. 137 mL/day, which equates to the preparation 685 mg of seed micelles per day.

4.3.4 Preparation of Low Dispersity PFS_{32}-*b*-$P2VP_{480}$ Cylindrical Micelles via Living CDSA in Continuous Flow

We began our investigation by considering the key factors which should affect living CDSA in continuous flow: flow rate, residence time, and mixer volume. We anticipated the biggest challenge in performing living CDSA in a continuous flow process would be achieving fast and efficient mixing of the unimer and seed solution streams. We expected that the relatively large corona-to-core block ratio of 15 for PFS_{32}-*b*-$P2VP_{480}$ could minimize this issue by reducing the rate of micelle growth.[37] Drawing from the analogy of living CDSA and living anionic polymerization,[32] it is postulated that fast mixing is essential with highly reactive reagents. In living anionic polymerizations in continuous flow, it is crucial to reach solution equilibrium quickly to ensure control over the resulting polymer.[33–36] In batch, the importance of efficient mixing of the seed and unimer solutions has also been demonstrated to access controlled micelles which exhibit low size-dispersity.[31]

Preliminary investigations demonstrated that the simple T-joint mixer, described and employed previously to prepare seed micelles, did not allow for sufficient mixing to occur during the living CDSA process. This resulted in polydisperse fibers being formed, presumably because some seeds were not exposed to unimer at all, resulting in negligible growth, whereas those that were exposed to unimer would elongate rapidly (**Figure S4.4**). We calculated the Reynolds number, a dimensionless mass transfer coefficient which can be used to predict the type of flow exhibited for a fluid,[39] to be ca. 0.2 for the final solvent composition of 20 vol% THF/*i*PrOH within the T-joint mixer. This value of Reynolds number, along with our observations, suggests that laminar flow is occurring under these conditions. Laminar flow is characterized by ordered layers of liquid sliding past each other parallel to the reactor tubing, with radial mixing of the layers being limited to

molecular diffusion.[42,43] We would expect this to lead to the formation of 1D micelles which are length-disperse, as was observed. With this in mind, we investigated the use of the specialized T-joint micromixer, as previously described in Section 4.3.3, which consists of many microchannels in an effort to improve mixing. However, significant fouling occurred after repeated use due to accumulation of solids,[44] limiting the application of this micromixer for living CDSA in continuous flow. Therefore, we investigated the use of a packed-bed column mixer housing sand herein, which is reported to provide efficient mixing via distributive mixing.[40,45]

The packed-bed column mixer is a relatively cheap mixing unit comprised of stainless-steel tubing containing a frit and filled with sand. It is easy to customize the mixer volume by simply changing out the main tubular section of the mixer for a different length of stainless-steel tube.[45] Moreover, if clogging were to occur, the frit and sand bed are extremely easy to replace, with pieces costing a fraction of the price of alternative micromixing technologies. For our optimization studies, we tested mixer column lengths of 5 and 10 cm, corresponding to mixer volumes of 717 and 1302 µL, respectively. The living CDSA was carried out using two feed streams comprising of seed solution (1 mg/mL, 10 vol% THF/*i*PrOH) and unimer solution (21 mg/mL in THF) (**Scheme 4.3**) with a flow rate ratio of 4 (unimer/seeds), to make a final unimer-to-seed ratio m_{unimer}/m_{seed} of 5. Residence times of 20, 90, and 180 min (corresponding to flow rates of 1018–1047, 226–233, and 113–116 µL/min, respectively) were investigated. The resulting fibers were obtained at 1 mg/mL in 28 vol% THF/*i*PrOH. The TEM images and corresponding size-analysis of the micelles are shown in **Figures 4.3**, **S4.5**–**S4.7**, and **Tables S4.4** and **S4.5**, respectively. Size analysis was performed prior to and after ageing for 24 h to determine whether living CDSA goes to completion within the flow reactor.

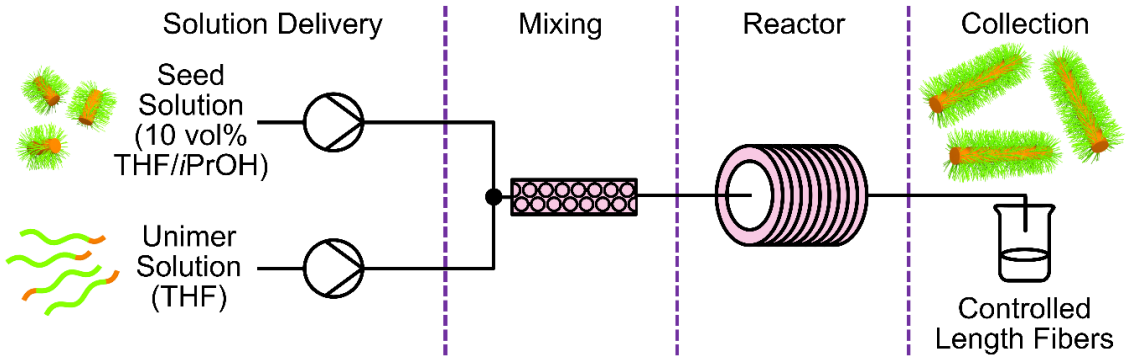

Scheme 4.3 Preparation of low dispersity PFS_{32}-*b*-$P2VP_{480}$ cylindrical micelles by living CDSA in continuous flow using m_{unimer}/m_{seed} = 5. Coil reactor with packed-bed column mixer and two feed streams comprising of seed solution (1 mg/mL, 10 vol% THF/*i*PrOH) and unimer solution (PFS_{32}-*b*-$P2VP_{480}$ in THF, 25 mg/mL) were used.

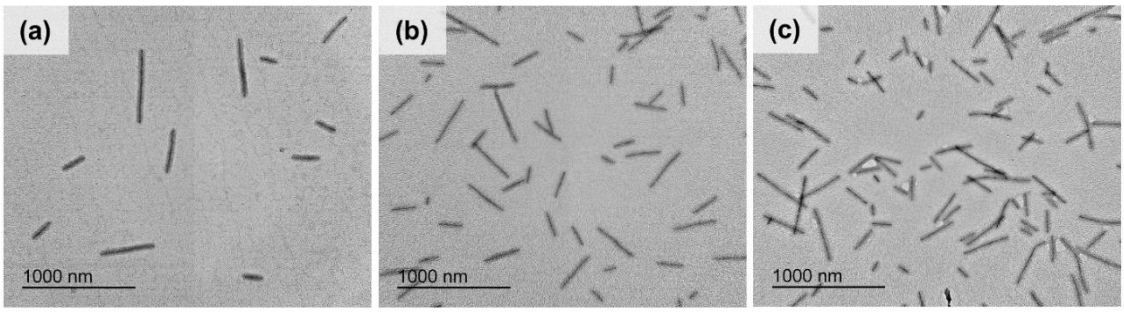

Figure 4.3 TEM images of PFS_{32}-*b*-$P2VP_{480}$ cylindrical micelles prepared by living CDSA from PFS_{32}-*b*-$P2VP_{480}$ seed micelles (L_n = 39 nm, L_w/L_n = 1.09) in continuous flow using a packed-bed column mixer of length 10 cm and a residence time of (a) 20 min (L_n = 268 nm, L_w/L_n = 1.44), (b) 90 min (L_n = 275 nm, L_w/L_n = 1.20), or (c) 180 min (L_n = 216 nm, L_w/L_n = 1.38). Micelles were prepared in 28 vol% THF/*i*PrOH at 1 mg/mL, using m_{unimer}/m_{seed} = 5. Solution samples were drop-cast immediately from collection vial, with no ageing, and imaged after solvent evaporation. Scale bars: 1000 nm.

For the living CDSA from seeds of length L_n = 39 nm and using m_{unimer}/m_{seed} = 5, the theoretical fiber length is 234 nm. When a residence time of 180 min and mixer length of 10 cm are employed in the living CDSA in continuous flow, PFS_{32}-*b*-$P2VP_{480}$ fibers of length 216 nm (L_w/L_n = 1.38)

were obtained (**Figure 4.3**c). After ageing of this sample for 24 h, a negligible change in the fiber lengths was observed, but the length-dispersity decreased (L_n = 231 nm, L_w/L_n = 1.14, **Figure S4.5**c). This indicates that a residence time of 180 min allows for fiber elongation to almost go to completion within the flow reactor, but some unimer must still be present in the collection vial to affect the length-dispersity on ageing. Using a mixer length of 5 cm with the same residence time (180 min) also resulted in negligible fiber growth after ageing (L_n = 204 and 207 nm) but a decrease in length-dispersity from L_w/L_n = 1.34 to 1.20 (**Figures S4.6**c and **S4.7**c), suggesting that the mixer volume has no significant effect on living CDSA at this residence time or flow rate. At lower residence times of 20 and 90 min, however, a more significant increase in fiber length was observed upon ageing for 24 h (**Figures S4.5**a, b, **S4.6**a, b, **S4.7**a, b, and **Tables S4.4** and **S4.5**). Moreover, larger values of σ/L_n, which indicate a large variation of fiber length, were generally obtained on decreasing the residence time (**Tables S4.4** and **S4.5**). This is likely due to the elongation process being incomplete within this time (≤ 90 min), with shorter residence times allowing for less elongation to occur in the flow reactor. On ageing, this would lead to a more significant increase in fiber length.

The 1D PFS_{32}-*b*-$P2VP_{480}$ micelles obtained immediately after the residence time (with no ageing) possessed the highest length-dispersities observed in this work (L_w/L_n = 1.20–1.61) (**Figures 4.3** and **S4.6**). On ageing of these samples for 24 h, however, the length-dispersity decreased in every case (L_w/L_n = 1.12–1.33) (**Figures S4.5** and **S4.7**). Notably, an increased mixer length of 10 cm yielded lower dispersity fibers (L_w/L_n = 1.20–1.44 prior to ageing, L_w/L_n = 1.12–1.14 after ageing) than that obtained with a mixer length of 5 cm (L_w/L_n = 1.34–1.61 prior to ageing, L_w/L_n = 1.20–1.33 after ageing) (**Tables S4.4** and **S4.5**). Decreased values of σ/L_n were also obtained when using a mixer length of 10 cm. These findings indicate that an increased mixer volume allows for improved mixing efficiency during living CDSA in continuous flow to access lower dispersity fibers.

Given the results discussed in this section, work is ongoing and will focus on further optimizing living CDSA in continuous flow to access low dispersity length-controlled fibers. We anticipate that an increased mixer length should allow for fibers of even lower length-dispersity to be prepared, likely due to the improved mixing of the unimer and seed solution feed streams. It is evident that longer residence times are required to allow for living CDSA to go to completion. We therefore aim to probe residence times longer than 180 min. However, as the residence time is increased, the flow rate will inherently decrease since the reactor volume is kept constant. It is likely that a trade-off between these variables will exist, such that although increased residence time should allow for living CDSA to go to completion, the resulting decreased flow rate may compromise mixing efficiency and therefore length-dispersity. We aim to investigate these effects to optimize the preparation of low dispersity 1D micelles in continuous flow.

4.4 Summary

We have demonstrated the successful transfer of CDSA and seed micelle preparation to continuous flow. Polydisperse PFS_{32}-*b*-$P2VP_{480}$ 1D micelles were accessed using a residence time of 180 min. It was demonstrated that synchronous CDSA and sonication performed in continuous flow allowed access to low aspect ratio 1D seed micelles using a residence time of 45 min and a ratio of flow rates of 4 (selective solvent/unimer solution). No significant change in the micelle length or length-dispersity was observed after ageing the resulting seed solution for 24 h, indicating that the CDSA and sonication processes went to completion in the flow reactor. This method, which employs a simple cost-effective T-joint mixer, could facilitate the preparation of 685 mg of seed micelles per day.

Living CDSA was performed in continuous flow, employing a packed-bed column mixer housing sand, to access 1D micelles which exhibit low length-dispersity. It was found that longer residence times are essential to allow for living CDSA to go to completion within the flow reactor.

Furthermore, increasing the mixer length was found to improve mixing of the streams, leading to cylindrical micelles with lower length-dispersities being formed.

4.5 References

(1) Geng, Y. A. N.; Dalhaimer, P.; Cai, S.; Tsai, R.; Minko, T.; Discher, D. E. Shape Effects of Filaments versus Spherical Particles in Flow and Drug Delivery. *Nat. Nanotechnol.* **2007**, *2* (4), 249–255.

(2) Oltra, N. S.; Nair, P.; Discher, D. E. From Stealthy Polymersomes and Filomicelles to "Self" Peptide-Nanoparticles for Cancer Therapy. *Annu. Rev. Chem. Biomol. Eng.* **2014**, *5*, 281–299.

(3) Ganda, S.; Dulle, M.; Drechsler, M.; Förster, B.; Förster, S.; Stenzel, M. H. Two-Dimensional Self-Assembled Structures of Highly Ordered Bioactive Crystalline-Based Block Copolymers. *Macromolecules* **2017**, *50* (21), 8544–8553.

(4) Garcia-Hernandez, J. D.; Street, S. T. G.; Kang, Y.; Zhang, Y.; Manners, I. Cargo Encapsulation in Uniform, Length-Tunable Aqueous Nanofibers with a Coaxial Crystalline and Amorphous Core. *Macromolecules* **2021**, *54* (12), 5784–5796.

(5) Street, S. T. G.; He, Y.; Jin, X.-H.; Hodgson, L.; Verkade, P.; Manners, I. Cellular Uptake and Targeting of Low Dispersity, Dual Emissive, Segmented Block Copolymer Nanofibers. *Chem. Sci.* **2020**, *11* (32), 8394–8408.

(6) Finnegan, J. R.; Pilkington, E.; Alt, K.; Rahim, M. A.; Kent, S. J.; Davis, T. P.; Kempe, K. Stealth Nanorods via the Aqueous Living Crystallisation-Driven Self-Assembly of Poly(2-Oxazoline)S. *Chem. Sci.* **2021**, *12*, 7350–7360.

(7) Schöbel, J.; Burgard, M.; Hils, C.; Dersch, R.; Dulle, M.; Volk, K.; Karg, M.; Greiner, A.; Schmalz, H. Bottom-Up Meets Top-Down: Patchy Hybrid Nonwovens as an Efficient Catalysis Platform. *Angew. Chem. Int. Ed.* **2017**, *56* (1), 405–408.

(8) Frank, A.; Hils, C.; Weber, M.; Kreger, K.; Schmalz, H.; Schmidt, H.-W. Hierarchical Superstructures by Combining Crystallization-driven and Molecular Self-assembly. *Angew. Chem. Int. Ed.* **2021**, *60*, 21767–21771.

(9) Tian, J.; Zhang, Y.; Du, L.; He, Y.; Jin, X.-H.; Pearce, S.; Eloi, J.-C.; Harniman, R. L.; Alibhai, D.; Ye, R.; Phillips, D. L.; Manners, I. Tailored Self-Assembled Photocatalytic

Nanofibres for Visible-Light-Driven Hydrogen Production. *Nat. Chem.* **2020**, *12*, 1150–1156.

(10) Liu, J.; Thompson, Z. J.; Sue, H. J.; Bates, F. S.; Hillmyer, M. A.; Dettloff, M.; Jacob, G.; Verghese, N.; Pham, H. Toughening of Epoxies with Block Copolymer Micelles of Wormlike Morphology. *Macromolecules* **2010**, *43* (17), 7238–7243.

(11) Sneyd, A. J.; Fukui, T.; Paleček, D.; Prodhan, S.; Wagner, I.; Zhang, Y.; Sung, J.; Collins, S. M.; Slater, T. J. A.; Andaji-Garmaroudi, Z.; Macfarlane, L. R.; Garcia-Hernandez, J. D.; Wang, L.; Whittell, G. R.; Hodgkiss, J. M.; Chen, K.; Beljonne, D.; Manners, I.; Friend, R. H.; Rao, A. Efficient Energy Transport in an Organic Semiconductor Mediated by Transient Exciton Delocalization. *Sci. Adv.* **2021**, *7* (32), eabh4232.

(12) MacFarlane, L. R.; Shaikh, H.; Garcia-Hernandez, J. D.; Vespa, M.; Fukui, T.; Manners, I. Functional Nanoparticles through π-Conjugated Polymer Self-Assembly. *Nat. Rev. Mater.* **2021**, *6*, 7–26.

(13) Guan, S.; Wen, W.; Yang, Z.; Chen, A. Liquid Crystalline Nanowires by Polymerization Induced Hierarchical Self-Assembly. *Macromolecules* **2020**, *53* (1), 465–472.

(14) Vilgis, T.; Halperin, A. Aggregation of Coil-Crystalline Block Copolymers: Equilibrium Crystallization. *Macromolecules* **1991**, *24* (8), 2090–2095.

(15) Tang, X.; Chen, W.; Li, L. The Tough Journey of Polymer Crystallization: Battling with Chain Flexibility and Connectivity. *Macromolecules* **2019**, *52* (10), 3575–3591.

(16) Cao, L.; Manners, I.; Winnik, M. A. Influence of the Interplay of Crystallization and Chain Stretching on Micellar Morphologies: Solution Self-Assembly of Coil-Crystalline Poly(Isoprene-Block-Ferrocenylsilane). *Macromolecules* **2002**, *35* (22), 8258–8260.

(17) Guerin, G.; Rupar, P. A.; Winnik, M. A. In-Depth Analysis of the Effect of Fragmentation on the Crystallization-Driven Self-Assembly Growth Kinetics of 1D Micelles Studied by Seed Trapping. *Polymers (Basel).* **2021**, *13*, 3122.

(18) Hsiao, M.-S.; Yusoff, S. F. M.; Winnik, M. A.; Manners, I. Crystallization-Driven Self-Assembly of Block Copolymers with a Short Crystallizable Core-Forming Segment: Controlling Micelle Morphology through the Influence of Molar Mass and Solvent Selectivity. *Macromolecules* **2014**, *47* (7), 2361–2372.

(19) Song, S.; Liu, X.; Nikbin, E.; Howe, J. Y.; Yu, Q.; Manners, I.; Winnik, M. A. Uniform 1D

Micelles and Patchy & Block Comicelles via Scalable, One-Step Crystallization-Driven Block Copolymer Self-Assembly. *J. Am. Chem. Soc.* **2021**, *143* (16), 6266–6280.

(20) Schmelz, J.; Schedl, A. E.; Steinlein, C.; Manners, I.; Schmalz, H. Length Control and Block-Type Architectures in Worm-like Micelles with Polyethylene Cores. *J. Am. Chem. Soc.* **2012**, *134* (34), 14217–14225.

(21) Han, L.; Wang, M.; Jia, X.; Chen, W.; Qian, H.; He, F. Uniform Two-Dimensional Square Assemblies from Conjugated Block Copolymers Driven by π-π Interactions with Controllable Sizes. *Nat. Commun.* **2018**, *9*, 865.

(22) Shin, S.; Menk, F.; Kim, Y.; Lim, J.; Char, K.; Zentel, R.; Choi, T.-L. Living Light-Induced Crystallization-Driven Self-Assembly for Rapid Preparation of Semiconducting Nanofibers. *J. Am. Chem. Soc.* **2018**, *140* (19), 6088–6094.

(23) Tao, D.; Feng, C.; Cui, Y.; Yang, X.; Manners, I.; Winnik, M. A.; Huang, X. Monodisperse Fiber-like Micelles of Controlled Length and Composition with an Oligo(p-Phenylenevinylene) Core via "Living" Crystallization-Driven Self-Assembly. *J. Am. Chem. Soc.* **2017**, *139* (21), 7136–7139.

(24) Inam, M.; Jones, J. R.; Pérez-Madrigal, M. M.; Arno, M. C.; Dove, A. P.; O'Reilly, R. K. Controlling the Size of Two-Dimensional Polymer Platelets for Water-in-Water Emulsifiers. *ACS Cent. Sci.* **2018**, *4* (1), 63–70.

(25) He, Y.; Eloi, J.-C.; Harniman, R. L.; Richardson, R. M.; Whittell, G. R.; Mathers, R. T.; Dove, A. P.; O'Reilly, R. K.; Manners, I. Uniform Biodegradable Fiber-Like Micelles and Block Comicelles via "Living" Crystallization-Driven Self-Assembly of Poly(L-Lactide) Block Copolymers: The Importance of Reducing Unimer Self-Nucleation via Hydrogen Bond Disruption. *J. Am. Chem. Soc.* **2019**, *141* (48), 19088–19098.

(26) Arno, M. C.; Inam, M.; Coe, Z.; Cambridge, G.; Macdougall, L. J.; Keogh, R.; Dove, A. P.; O'Reilly, R. K. Precision Epitaxy for Aqueous 1D and 2D Poly(ϵ-Caprolactone) Assemblies. *J. Am. Chem. Soc.* **2017**, *139* (46), 16980–16985.

(27) Yu, W.; Foster, J. C.; Dove, A. P.; O'Reilly, R. K. Length Control of Biodegradable Fiber-Like Micelles via Tuning Solubility: A Self-Seeding Crystallization-Driven Self-Assembly of Poly(ε-Caprolactone)-Containing Triblock Copolymers. *Macromolecules* **2020**, *53* (4), 1514–1521.

(28) Finnegan, J. R.; He, X.; Street, S. T. G.; Garcia-Hernandez, J. D.; Hayward, D. W.; Harniman, R. L.; Richardson, R. M.; Whittell, G. R.; Manners, I. Extending the Scope of "Living" Crystallization-Driven Self Assembly: Well-Defined 1D Micelles and Block Comicelles from Crystallizable Polycarbonate Block Copolymers. *J. Am. Chem. Soc.* **2018**, *140* (49), 17127–17140.

(29) Boott, C. E.; Gwyther, J.; Harniman, R. L.; Hayward, D. W.; Manners, I. Scalable and Uniform 1D Nanoparticles by Synchronous Polymerization, Crystallization and Self-Assembly. *Nat. Chem.* **2017**, *9*, 785–792.

(30) Oliver, A. M.; Gwyther, J.; Boott, C. E.; Davis, S. A.; Pearce, S.; Manners, I. Scalable Fiber-like Micelles and Block Co-Micelles by Polymerization-Induced Crystallization-Driven Self-Assembly. *J. Am. Chem. Soc.* **2018**, *140* (51), 18104–18114.

(31) Ellis, C. E.; Fukui, T.; Cordoba, C.; Blackburn, A.; Manners, I. Towards Scalable, Low Dispersity, and Dimensionally Tunable 2D Platelets Using Living Crystallization-Driven Self-Assembly. *Polym. Chem.* **2021**, *12* (25), 3650–3660.

(32) Lei, S.; Tian, J.; Fukui, T.; Winnik, M. A.; Manners, I. Probing the Analogy between Living Crystallization-Driven Self-Assembly and Living Covalent Polymerizations: Length-Independent Growth Behavior for 1D Block Copolymer Nanofibers. *Macromolecules* **2021**, *55* (1), 359–369.

(33) Nagaki, A.; Takahashi, Y.; Akahori, K.; Yoshida, J.-I. Living Anionic Polymerization of Tert-Butyl Acrylate in a Flow Microreactor System and Its Applications to the Synthesis of Block Copolymers. *Macromol. React. Eng.* **2012**, *6* (11), 467–472.

(34) Natalello, A.; Morsbach, J.; Friedel, A.; Alkan, A.; Tonhauser, C.; Müller, A. H. E.; Frey, H. Living Anionic Polymerization in Continuous Flow: Facilitated Synthesis of High-Molecular Weight Poly(2-Vinylpyridine) and Polystyrene. *Org. Process Res. Dev.* **2014**, *18* (11), 1408–1412.

(35) Nakahara, Y.; Furusawa, M.; Endo, Y.; Shimazaki, T.; Ohtsuka, K.; Takahashi, Y.; Jiang, Y.; Nagaki, A. Practical Continuous-Flow Controlled/Living Anionic Polymerization. *Chem. Eng. Technol.* **2019**, *42* (10), 2154–2163.

(36) Takahashi, Y.; Nagaki, A. Anionic Polymerization Using Flow Microreactors. *Molecules* **2019**, *24* (8), 1532.

(37) Boott, C. E.; Leitao, E. M.; Hayward, D. W.; Laine, R. F.; Mahou, P.; Guerin, G.; Winnik, M. A.; Richardson, R. M.; Kaminski, C. F.; Whittell, G. R.; Manners, I. Probing the Growth Kinetics for the Formation of Uniform 1D Block Copolymer Nanoparticles by Living Crystallization-Driven Self-Assembly. *ACS Nano* **2018**, *12* (9), 8920–8933.

(38) Guerin, G.; Wang, H.; Manners, I.; Winnik, M. A. Fragmentation of Fiberlike Structures: Sonication Studies of Cylindrical Block Copolymer Micelles and Behavioral Comparisons to Biological Fibrils. *J. Am. Chem. Soc.* **2008**, *130* (44), 14763–14771.

(39) Plutschack, M. B.; Pieber, B.; Gilmore, K.; Seeberger, P. H. The Hitchhiker's Guide to Flow Chemistry. *Chem. Rev.* **2017**, *117* (18), 11796–11893.

(40) Hessel, V.; Löwe, H.; Schönfeld, F. Micromixers - A Review on Passive and Active Mixing Principles. *Chem. Eng. Sci.* **2005**, *60*, 2479–2501.

(41) Falk, L.; Commenge, J. M. Performance Comparison of Micromixers. *Chem. Eng. Sci.* **2010**, *65*, 405–411.

(42) Soleymani, A.; Yousefi, H.; Turunen, I. Dimensionless Number for Identification of Flow Patterns inside a T-Micromixer. *Chem. Eng. Sci.* **2008**, *63*, 5291–5297.

(43) Reis, M. H.; Varner, T. P.; Leibfarth, F. A. The Influence of Residence Time Distribution on Continuous-Flow Polymerization. *Macromolecules* **2019**, *52* (9), 3551–3557.

(44) Schoenitz, M.; Grundemann, L.; Augustin, W.; Scholl, S. Fouling in Microstructured Devices: A Review. *Chem. Commun.* **2015**, *51* (39), 8213–8228.

(45) Britton, J.; Jamison, T. F. The Assembly and Use of Continuous Flow Systems for Chemical Synthesis. *Nat. Protoc.* **2017**, *12* (11), 2423–2446.

(46) Rider, D. A.; Cavicchi, K. A.; Power-Billard, K. N.; Russell, T. P.; Manners, I. Diblock Copolymers with Amorphous Atactic Polyferrocenylsilane Blocks: Synthesis, Characterization, and Self-Assembly of Polystyrene-Block-Poly(Ferrocenylethylmethylsilane) in the Bulk State. *Macromolecules* **2005**, *38* (16), 6931–6938.

4.6 Supplementary Materials

4.6.1 Materials and Methods

Solvents were dried and de-oxygenated using a Solvent Purification System (SPS). Tetrahydrofuran (THF) used for anionic polymerization was distilled from Na/benzophenone. Self-assembly experiments were performed in HPLC grade solvents, filtered through a 0.2 μm membrane. All materials were purchased from Sigma-Aldrich and used as received unless otherwise stated. Monomer, dimethylsila[1]ferrocenophane, was prepared by literature procedure.[1] PFS_{32}-*b*-$P2VP_{480}$ (M_n = 48,880 Da, M_w/M_n = 1.05), was prepared by literature procedure.[2]

4.6.2 Continuous Flow Instrumentation

Fluorinated ethylene propylene (FEP) tubing of coil reactors has an inner diameter of 1 mm and were purchased from Analytics-Shop USA. T-joint mixer was manufactured by Supelco Analytical and purchased from MilliporeSigma. T-joint micromixer was manufactured by and purchased from Microflow CVO.

Packed-bed column mixer housing sand, used for the preparation of low dispersity micelles, was assembled according to the literature protocol.[3] Union, ferrule, and nuts for assembly of the packed-bed column mixer were manufactured by Supelco Analytical and purchased from Analytics-Shop USA. To calculate the volume of the sand bed column mixer, it was filled with THF, and the mass of the solvent was obtained. Using the density of THF as 0.882 g/mL (at ca. 24 °C), the volume was calculated to be 0.717 mL.

KD Scientific Legato 270P and 180P programmable syringe pumps were purchased from Analytical West. Syringes (10 and 25 mL) were manufactured by Scientific Glass Engineering and purchased from Fisher Scientific.

4.6.3 Instrumentation

Nuclear magnetic resonance (NMR) spectroscopy. ^{1}H NMR was obtained using a Varian 500 MHz spectrometer. NMR data was processed using MestReNova.

Gel permeation chromatography (GPC). GPC was conducted using a Malvern Omnisec Resolve/Reveal equipped with a triple detector array, automatic sampler, pump, injector, inline degasser column oven (set at 35 °C), elution columns consisting of styene/divinylbenzene gels (of pore size 500 Å – 5,000 Å), refractometer, four-capillary differential viscometer, UV/Vis detector (λ = 440 nm) and dual angle laser light scattering detector (7° and 90°). GPC grade THF with 1 wt% triethylamine was used as the eluent, with a set flow rate of 1 mL/min. Samples were dissolved in THF at 2 mg/mL and filtered through a 0.2 µm polytetrafluoroethylene membrane prior to analysis.

Transmission electron microscopy (TEM). Copper grids (500 mesh) were purchased from Ted Pella, Inc. and carbon films were prepared by using a Leica EM ACE600 instrument. Carbon films were deposited onto the copper grids by floatation on water and allowed to dry over 24 hours. Samples for electron microscopy were prepared by drop-casting 8 µL of micelle colloidal solution onto a carbon-coated copper grid followed by solvent evaporation. TEM images were obtained using a JEOL JEM 1011 operating at 80 kV, equipped with a Gatan Orius SC1000 CCD camera.

Measurements were undertaken by hand using ImageJ software, developed by the US National Institute for Health. The micelle number-average length (L_n) and weight-average length (L_w) were calculated according to the following equations:

$$L_n = \frac{\sum_i^n N_i L_i}{\sum_i^n N_i} \qquad\qquad L_w = \frac{\sum_i^n N_i L_i^2}{\sum_i^n N_i L_i}$$

A minimum of 100 micelles were measured for each data point. Errors displayed are standard deviations of each data set.

Ultrasonication. Micelle sonication was carried out using a Fisherbrand FB11203 sonication bath (37 W sonication power).

4.6.4 Synthetic Procedures

4.6.4.1 Synthesis of PFS_{32}-*b*-$P2VP_{480}$

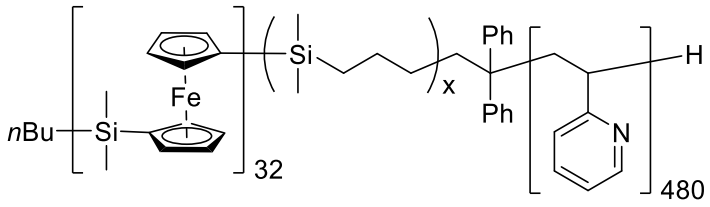

Dimethylsila[1]ferrocenophane (100 mg, 0.4 mmol) in THF (1 mL) was initiated with *n*-butyl lithium (1.6 M in hexanes, 8 µL, 0.013 mmol) at room temperature with vigorous stirring. After 30 min, the colour of the solution changed from red to amber, indicating complete conversion of the monomer. Sequential addition of 1,1-dimethylsilacyclobutane (DMSB) (5 µL, 0.039 mmol) followed by 1,1-diphenylethylene (DPE) (13.8 µL, 0.078 mmol) into the living PFS polymer solution caused a change in colour from amber to dark red within a minute, indicating the formation of radical species. After a total of 40 min, an aliquot (200 µL) for molecular weight analysis was removed and quenched with 4-*t*-butylphenol. Dry LiCl (ca. 405 mg) and 2-vinylpyridine (492 µL, 4.8 mmol) were dissolved in THF (1 mL). The living PFS and 2-vinylpyridine/LiCl solutions were both cooled to -78 °C for 15 min before they were combined. The reaction proceeded for 60 min at -78 °C before termination with 4-*t*-butylphenol. The polymer was precipitated into hexanes from THF 3 times and was then dried under vacuum overnight to afford a light orange solid. GPC and ^{1}H NMR analysis were used to determine the final block copolymer composition of PFS_{32}-*b*-$P2VP_{480}$.

Yield: 396 mg (68%). ^{1}H NMR (500 MHz, $CDCl_3$): δ (ppm) = 8.27 (m, 15H, NC*H*C), 7.40–6.08 (m, 45H, aromatic *H*), 4.23 (m, 4H, Cp*H*), 4.02 (m, 4H, Cp*H*), 2.45–1.39 (br, alkyl *H*), 0.48 (s, 6H, Si(CH_3)$_2$); M_n (GPC) = 48,880 Da; M_w/M_n (GPC) = 1.05.

4.6.5 Self-Assembly Procedures

4.6.5.1 Formation of polydisperse 1D PFS$_{32}$-*b*-P2VP cylindrical micelles in continuous flow

Feed streams of unimer solution (PFS$_{32}$-*b*-P2VP$_{480}$ in THF, 25 mg/mL) (flow rate = 5 μL/min) and selective solvent (*i*PrOH) (flow rate = 21 μL/min) were mixed using a T-joint mixer, with a total additive flow rate of 26 μL/min and a residence time of 3 h.

4.6.5.2 Formation of 1D PFS$_{32}$-*b*-P2VP$_{480}$ seed micelles in continuous flow

The following procedure corresponds to that of the optimized preparation of 1D PFS$_{32}$-*b*-P2VP$_{480}$ seed micelles. Feed streams of unimer solution (PFS$_{32}$-*b*-P2VP$_{480}$ in THF, 25 mg/mL) (flow rate = 21 μL) and selective solvent (*i*PrOH) (flow rate = 84 μL/min) were mixed using a T-joint mixer, with a total additive flow rate of 105 μL and a residence time of 45 min. The tubing reactor was placed in a sonication bath maintained at 10 °C throughout the experiment.

4.6.5.3 Formation of low dispersity 1D PFS$_{32}$-*b*-P2VP$_{480}$ cylindrical micelles in continuous flow

The following procedure corresponds to that of the optimized preparation of low dispersity 1D PFS$_{32}$-*b*-P2VP$_{480}$ micelles in this work. Feed streams of unimer solution (PFS$_{32}$-*b*-P2VP$_{480}$ in THF, 21 mg/mL) (flow rate = 93 μL) and seed micelle solution (PFS$_{32}$-*b*-P2VP$_{480}$ seeds in 10 vol% THF/*i*PrOH, 1 mg/mL, L_n = 39 nm, L_w/L_n = 1.09) (flow rate = 23 μL/min) were mixed using a packed-bed column mixer housing sand, with a total additive flow rate of 116 μL and a residence time of 180 min.

4.6.6 Supplementary Figures

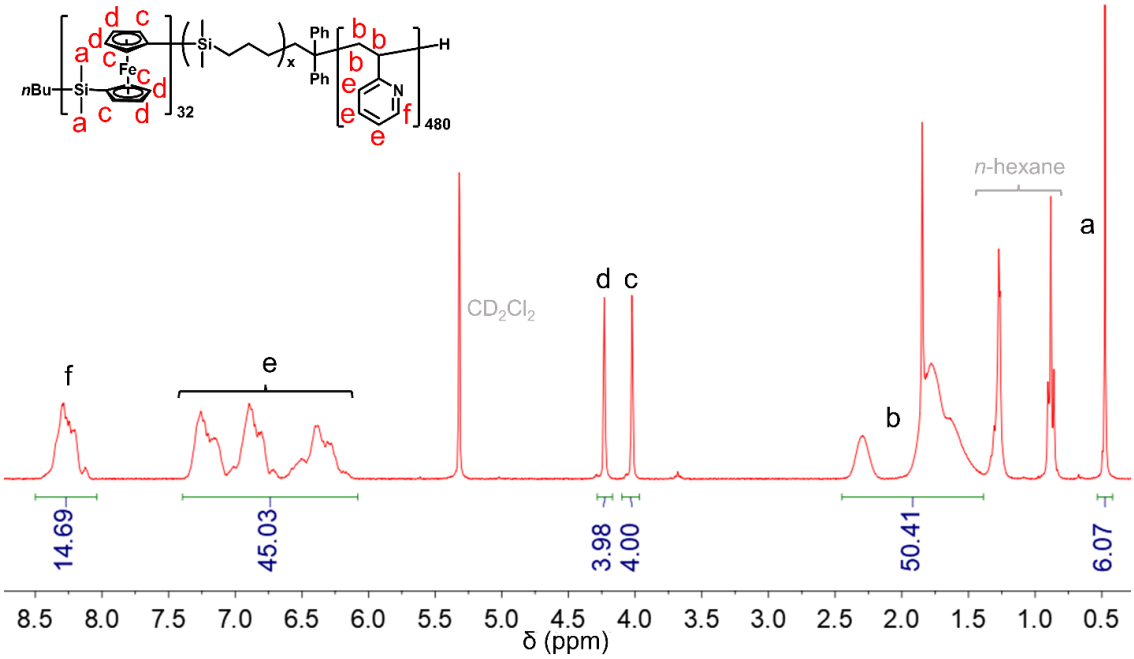

Figure S4.1 ^{1}H NMR spectra (in CD_2Cl_2) of PFS_{32}-*b*-$P2VP_{480}$.

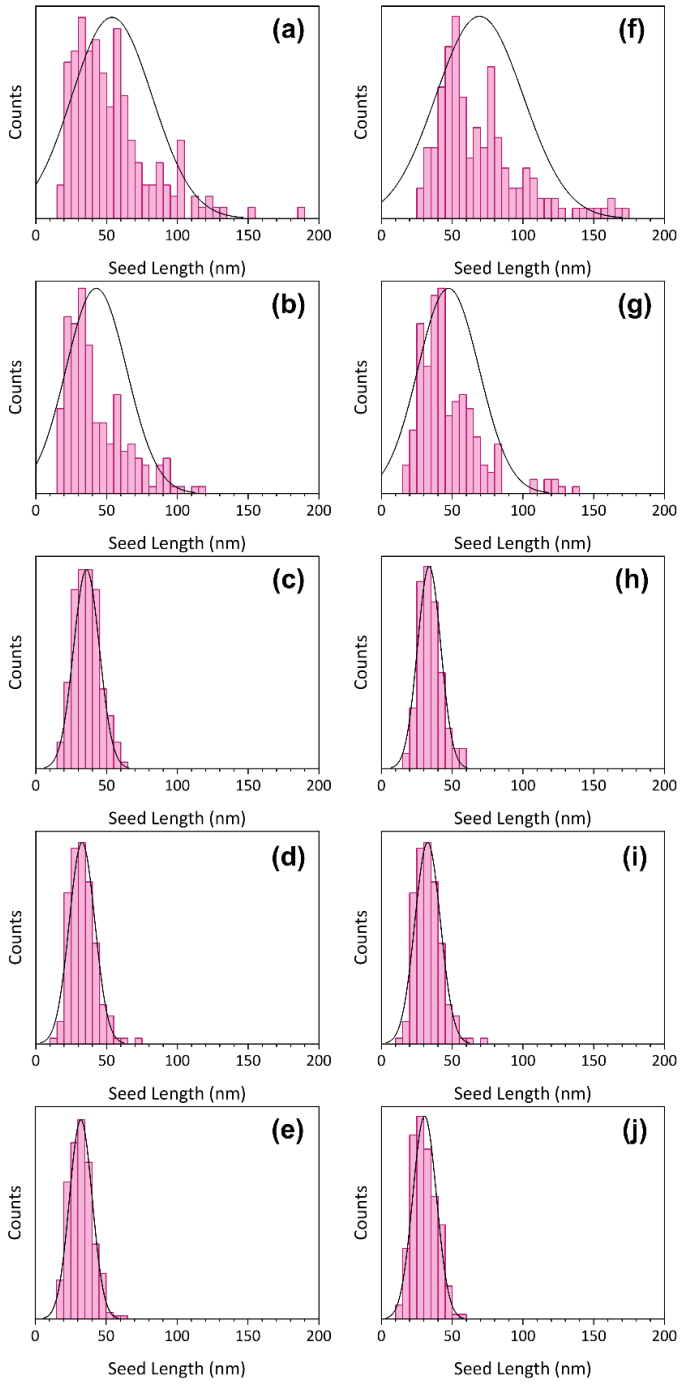

Figure S4.2 Contour area distributions of PFS_{32}-*b*-$P2VP_{480}$ seed micelles formed by synchronous CDSA and sonication in continuous flow (20 vol% THF/*i*PrOH, 5 mg/mL) (a)–(e) with no ageing, or (f)–(j) after 24 h ageing. Residence times = (a, f) 11, (b, g) 22, (c, h) 45, (d, i) 90, and (e, j) 120 min.

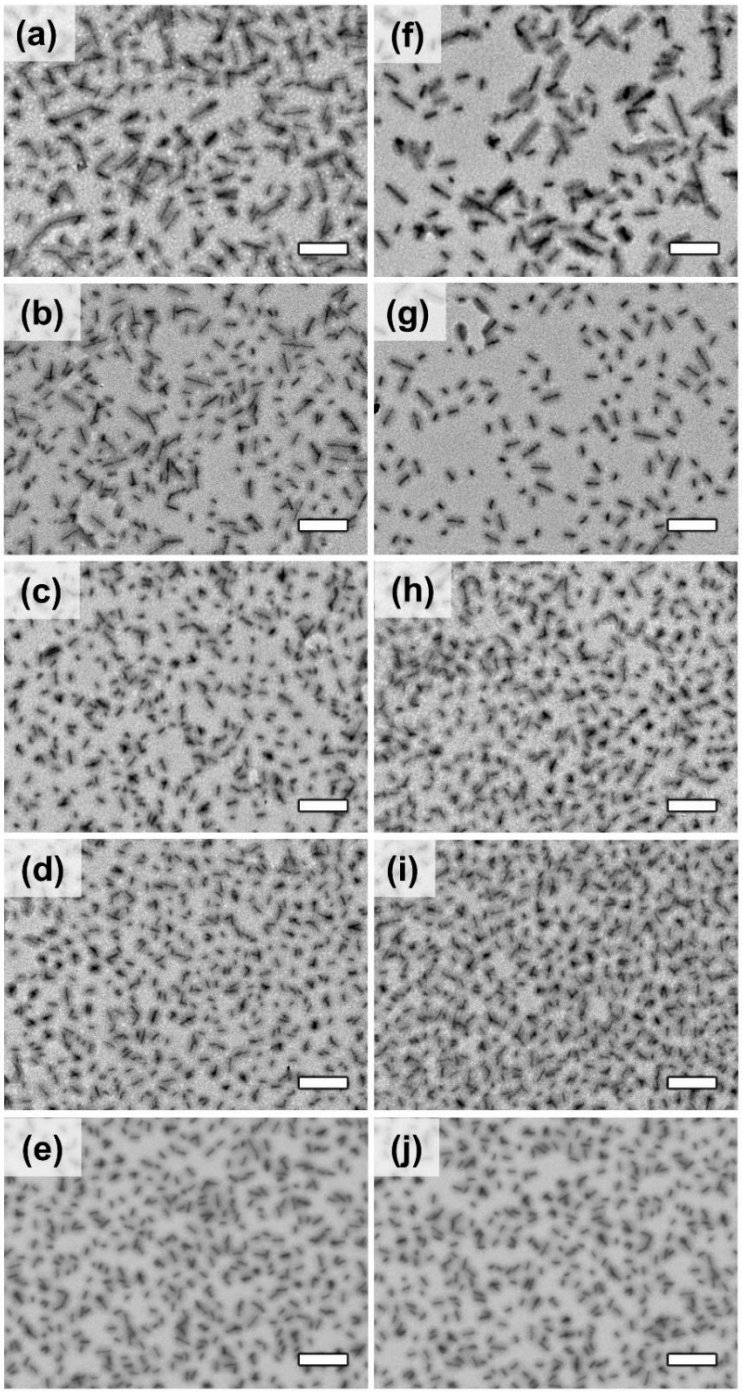

Figure S4.3 TEM images of PFS_{32}-*b*-$P2VP_{480}$ seed micelles prepared by synchronous CDSA/sonication in continuous flow (20 vol% THF/*i*PrOH, 5 mg/mL) (a)–(e) with no ageing, or (f)–(i) after 24 h ageing. Residence times = (a, f) 11, (b, g) 22, (c, h) 45, (d, i) 90, and (e, j) 120 min. Scale bars: 200 nm.

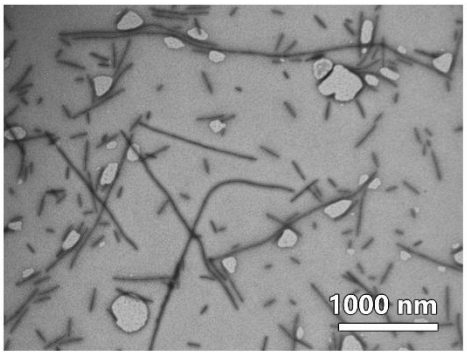

Figure S4.4 Representative TEM image of preliminary experiments for the living CDSA of PFS_{32}-*b*-$P2VP_{480}$ in continuous flow using T-joint mixer.

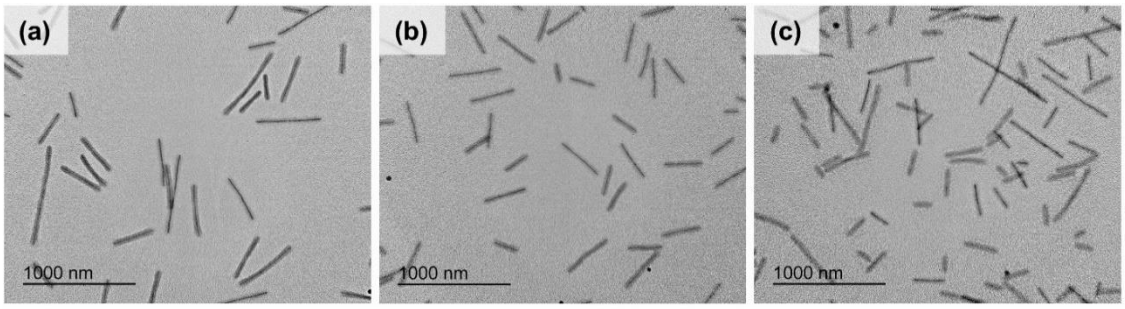

Figure S4.5 TEM images of PFS_{32}-*b*-$P2VP_{480}$ cylindrical micelles prepared by living CDSA from PFS_{32}-*b*-$P2VP_{480}$ seed micelles (L_n = 39 nm, L_w/L_n = 1.09) in continuous flow using a packed-bed column mixer of length 10 cm and a residence time of (a) 20, (b) 90, or (c) 180 min. Micelles were prepared in 28 vol% THF/*i*PrOH at 1 mg/mL, using m_{unimer}/m_{seed} = 5. Solution samples were aged for 24 h before being drop-cast and imaged after solvent evaporation. Scale bars: 1000 nm.

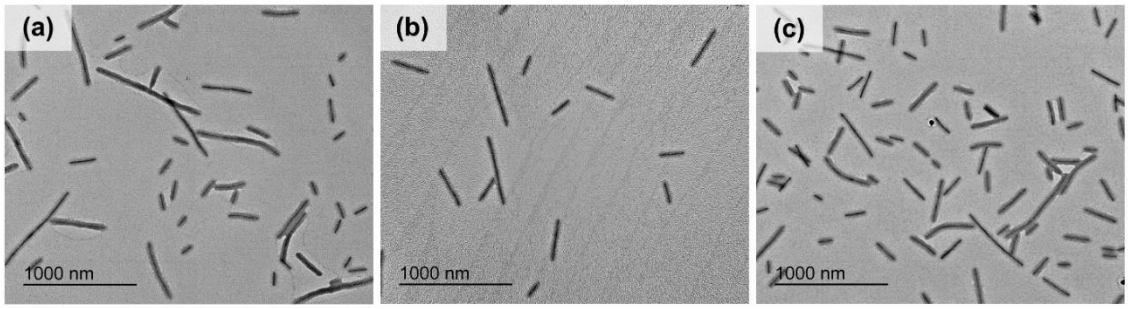

Figure S4.6 TEM images of PFS_{32}-*b*-$P2VP_{480}$ cylindrical micelles prepared by living CDSA from PFS_{32}-*b*-$P2VP_{480}$ seed micelles (L_n = 39 nm, L_w/L_n = 1.09) in continuous flow using a packed-bed column mixer of length 5 cm and a residence time of (a) 20, (b) 90, or (c) 180 min. Micelles were prepared in 28 vol% THF/*i*PrOH at 1 mg/mL, using m_{unimer}/m_{seed} = 5. Solution samples were drop-cast immediately from collection vial, with no ageing, and imaged after solvent evaporation. Scale bars: 1000 nm.

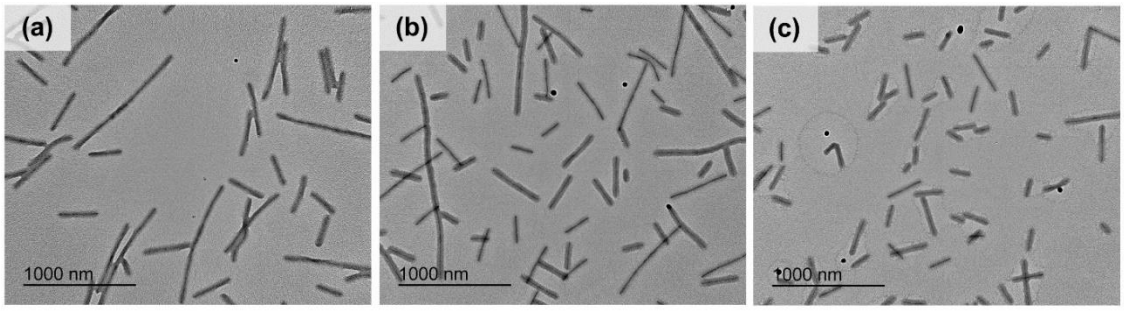

Figure S4.7 TEM images of PFS_{32}-*b*-$P2VP_{480}$ cylindrical micelles prepared by living CDSA from PFS_{32}-*b*-$P2VP_{480}$ seed micelles (L_n = 39 nm, L_w/L_n = 1.09) in continuous flow using a packed-bed column mixer of length 5 cm and a residence time of (a) 20, (b) 90, or (c) 180 min. Micelles were prepared in 28 vol% THF/*i*PrOH at 1 mg/mL, using m_{unimer}/m_{seed} = 5. Solution samples were aged for 24 h before being drop-cast and imaged after solvent evaporation. Scale bars: 1000 nm.

4.6.7 Supplementary Tables

Table S4.1 Flow parameters and size analysis data collected during the optimization of PFS_{32}-*b*-$P2VP_{480}$ seed micelle preparation via synchronous CDSA and sonication in continuous flow. Coil reactor with T-joint mixer and two reagent streams comprising of selective solvent (*i*PrOH) and unimer solution (PFS_{32}-*b*-$P2VP_{480}$ in THF, 25 mg/mL) were used. The reactor was placed in a sonication bath maintained at 10 °C throughout the experiment.

		No ageing			**Aged for 24 h**		
Residence time (min)	**Flow rate (µL/min)**	L_n **(nm)**	σ **(nm)**	L_w/L_n	L_n **(nm)**	σ **(nm)**	L_w/L_n
11	419	54	30	1.28	70	30	1.20
23	209	43	21	1.25	47	22	1.21
45	105	36	9	1.06	34	9	1.06
90	52	33	9	1.08	33	8	1.06
120	26	31	8	1.07	32	8	1.06

Table S4.2 Flow parameters and size analysis data collected during the optimization of PFS_{32}-*b*-$P2VP_{480}$ seed micelle preparation via synchronous CDSA and sonication in continuous flow. Coil reactor with T-joint micromixer and two reagent streams comprising of selective solvent (*i*PrOH) and unimer solution (PFS_{32}-*b*-$P2VP_{480}$ in THF, 25 mg/mL) were used. The reactor was placed in a sonication bath maintained at 10 °C throughout the experiment.

		No ageing			**Aged for 24 h**		
Residence time (min)	**Flow rate (μL/min)**	L_n **(nm)**	σ **(nm)**	L_w/L_n	L_n **(nm)**	σ **(nm)**	L_w/L_n
11	419	51	28	1.30	66	35	1.28
23	209	39	16	1.17	48	33	1.22
45	105	33	9	1.08	34	10	1.09
90	52	35	9	1.07	38	13	1.12
120	26	32	9	1.09	32	8	1.07

Table S4.3 Repeat experiments of PFS_{32}-*b*-$P2VP_{480}$ seed micelle preparation via synchronous CDSA and sonication in continuous flow. Coil reactor with T-joint micromixer and two reagent streams comprising of selective solvent (*i*PrOH) and unimer solution (PFS_{32}-*b*-$P2VP_{480}$ in THF, 25 mg/mL) were used. Residence time = 45 min, flow rate = 21 µL/min. The reactor was placed in a sonication bath maintained at 10 °C throughout the experiment.

Experiment replicate	L_n **(nm)**	σ **(nm)**	L_w/L_n
1	33	9	1.08
2	36	9	1.09
3	32	8	1.06
4	39	12	1.09
5	42	10	1.05

Table S4.4 Flow parameters and size analysis data collected during the optimization of living CDSA of PFS_{32}-*b*-$P2VP_{480}$ seeded from PFS_{32}-*b*-$P2VP_{480}$ seed micelles (L_n = 39 nm, L_w/L_n = 1.09) (m_{unimer}/m_{seed} = 5) in continuous flow using a packed-bed column mixer (length = 5 cm).

		No ageing				**Aged for 24 h**			
Residence time (min)	**Flow rate (μL/min)**	L_n **(nm)**	σ **(nm)**	σ/L_n	L_w/L_n	L_n **(nm)**	σ **(nm)**	σ/L_n	L_w/L_n
20	1018	255	199	0.8	1.61	372	162	0.4	1.20
90	226	234	139	0.6	1.35	317	182	0.6	1.33
180	113	204	120	0.6	1.34	207	93	0.4	1.20

Table S4.5 Flow parameters and size analysis data collected during the optimization of living CDSA of PFS_{32}-*b*-$P2VP_{480}$ seeded from PFS_{32}-*b*-$P2VP_{480}$ seed micelles (L_n = 39 nm, L_w/L_n = 1.09) (m_{unimer}/m_{seed} = 5) in continuous flow using a packed-bed column mixer (length = 10 cm).

		No ageing				**Aged for 24 h**			
Residence time (min)	**Flow rate (μL/min)**	L_n **(nm)**	σ **(nm)**	σ/L_n	L_w/L_n	L_n **(nm)**	σ **(nm)**	σ/L_n	L_w/L_n
20	1047	268	178	0.7	1.44	367	127	0.3	1.12
90	233	275	123	0.4	1.20	312	106	0.3	1.12
180	116	216	133	0.6	1.38	231	85	0.4	1.14

4.6.8 Supplementary References

(1) Rider, D. A.; Cavicchi, K. A.; Power-Billard, K. N.; Russell, T. P.; Manners, I. Diblock Copolymers with Amorphous Atactic Polyferrocenylsilane Blocks: Synthesis, Characterization, and Self-Assembly of Polystyrene-Block-Poly(Ferrocenylethylmethylsilane) in the Bulk State. *Macromolecules* **2005**, *38* (16), 6931–6938.

(2) Hsiao, M.-S.; Yusoff, S. F. M.; Winnik, M. A.; Manners, I. Crystallization-Driven Self-Assembly of Block Copolymers with a Short Crystallizable Core-Forming Segment: Controlling Micelle Morphology through the Influence of Molar Mass and Solvent Selectivity. *Macromolecules* **2014**, *47* (7), 2361–2372.

(3) Britton, J.; Jamison, T. F. The Assembly and Use of Continuous Flow Systems for Chemical Synthesis. *Nat. Protoc.* **2017**, *12* (11), 2423–2446.

Chapter 5 Electrospinning and Coaxial Electrospinning of 1D Fiber-Like Micelles

5.1 Abstract

Electrospinning is a simple, low cost, and high throughput technique that allows for processing of polymers into fibers. The process can be controlled to allow access for well-defined continuous fibers that are of interest for a wide range of applications including as tissue scaffolds, as nanowires in optoelectronic devices, and in catalysis. Conventional electrospinning processes use polymer solutions with high molecular weights. Here, we report the electrospinning of one-dimensional (1D) fiber-like block copolymer micelles containing a crystalline core. We successfully accessed core-shell microfibers in which 1D micelles containing a crystalline poly(ferrocenyldimethylsilane) (PFS) core are immobilized on a polystyrene microfiber via coaxial electrospinning. Furthermore, we describe efforts to extend this approach to the use of 1D micelles comprising of a crystalline, π-conjugated poly(di-*n*-hexylfluorene) (PDHF) core. Electrospinning was also successfully used to prepare microfibers consisting solely of 1D micelles with a PFS crystalline core, the first examples where a template material is not required.

5.2 Introduction

The solution self-assembly of amphiphilic block copolymers (BCPs) has been recognised as a valuable bottom-up approach to yield a vast range of micelle morphologies including spheres, worms, lamellae, and vesicles.[1,2] In particular, one-dimensional (1D) micelles are of considerable interest in fields such as catalysis,[3,4] optoelectronics,[5,6] and nanomedicine.[7–13] Non-spherical nanostructures, such as 1D fiber-like micelles, are often challenging to access via the self-assembly of BCPs with amorphous cores as these morphologies with low interfacial curvature typically only exist in restricted regions of the phase space.[2] In the self-assembly of BCPs with a crystallizable

core-forming block, however, crystallization provides an additional driving force for the formation of 1D micelles.[14] This phenomenon is termed crystallization-driven self-assembly (CDSA). CDSA yields polydisperse micelles with a lack of length-control resulting from the slow and random nature of self-nucleation events which overlap with the growth/elongation step.[1] Low dispersity micelles can be accessed by circumventing the spontaneous (homogeneous) nucleation step of CDSA and performing the self-assembly in the presence of preformed seeds, which act as efficient initiators for the growth/elongation step.[15] Seed micelles are prepared through sonication and fragmentation of polydisperse 1D micelles.[16,17] This seeded growth process is termed "living" CDSA[18,19] and has been achieved using a variety of crystalline core chemistries such as poly(ferrocenyldimethylsilane) (PFS),[1,15,20] poly(di-*n*-hexylfluorene) (PDHF),[21–23] poly(*ε*-caprolactone),[24,25] polyethylene,[26,27] and poly(*p*-phenylenevinylene) and related materials.[28–30]

Recent advances have led to further developments of CDSA protocols which have allowed for the upscaled production of 1D micelles with crystalline cores, to help realize their potential applications.[31–35] For example, a process termed polymerization-induced CDSA (PI-CDSA) whereby the BCP synthesis and self-assembly occur *in situ* allows access to 1D micelles at up to 25 wt%.[31,32] As a result of the diverse range of crystalline core and coronal chemistries compatible with CDSA protocols, 1D micelles prepared using these methods are of interest for a wide range of applications.

Electrospinning is a simple, low cost, and high throughput method for fabricating continuous fibers with inherently high surface-to-volume ratios.[36–39] The electrohydrodynamic phenomenon depends on a complex interplay of factors such as surface tension, viscosity, and electrical charge.[36] These factors interact in various ways to affect the electrified jet of polymer solution which is ejected from the electrospinning needle.[36] Examples of electrospinning high molecular weight polymer solutions are ubiquitous, however the concept has recently been extended to supramolecular assemblies and crystallizable block copolymers.[40,41]

Coaxial electrospinning is a process which employs a specialized core-shell capillary needle containing distinct core and shell solutions for electrospinning.[3,42–46] High molecular weight polystyrene (PS) is often employed as the core since fibers can be easily accessed and optimized, allowing for facile templating of the shell material. When a voltage difference is applied between the collector plate and the needle, the solutions are drawn out to form fibers with a core-shell structure. This technique is a cost effective and high throughput method of processing and preparing fibers for use in devices.[3,47,48] Electrospun and coaxially electrospun fibers have various applications such as in biomedical engineering as tissue scaffolds,[49–51] or in optoelectronics as nanowires.[41,52]

One of our groups and also others have previously demonstrated that coaxial electrospinning can be used to prepare polystyrene microfibers with a sheath of 1D polyethylene-core micelles,[3,45] yet the scope has not been extended beyond this crystalline core chemistry. Herein, we explore the electrospinning of a variety of different 1D fiber-like micelles by both coaxial and conventional electrospinning methods to access microfibers either exhibiting a core-shell structure or consisting solely of 1D micelles, respectively.

5.3 Results and Discussion

5.3.1 Coaxial Electrospinning of PFS-Based 1D Micelles with Polystyrene

Coaxial electrospinning allows for the preparation of core-shell microfibers and assists the electrospinning of materials by using a carrier, most commonly high molecular weight PS (**Scheme 5.1**). The use of a carrier or template is of significant importance for the electrospinning of materials which would typically form particles by "electrospraying".[3,45] BCP micelles generally form electrosprayed particles in electrospinning processes,[53] leading to several challenges in the preparation of fibers containing these nanostructures. Therefore, high molecular weight PS (M_n = 1.4 x 10^6 Da) was employed as the carrier in this work, since this polymer forms well-defined fibers

without “beading” (**Figure S5.1**).[3,45] The chemical structures of all BCPs utilized in this study are shown in **Figure S5.2**.

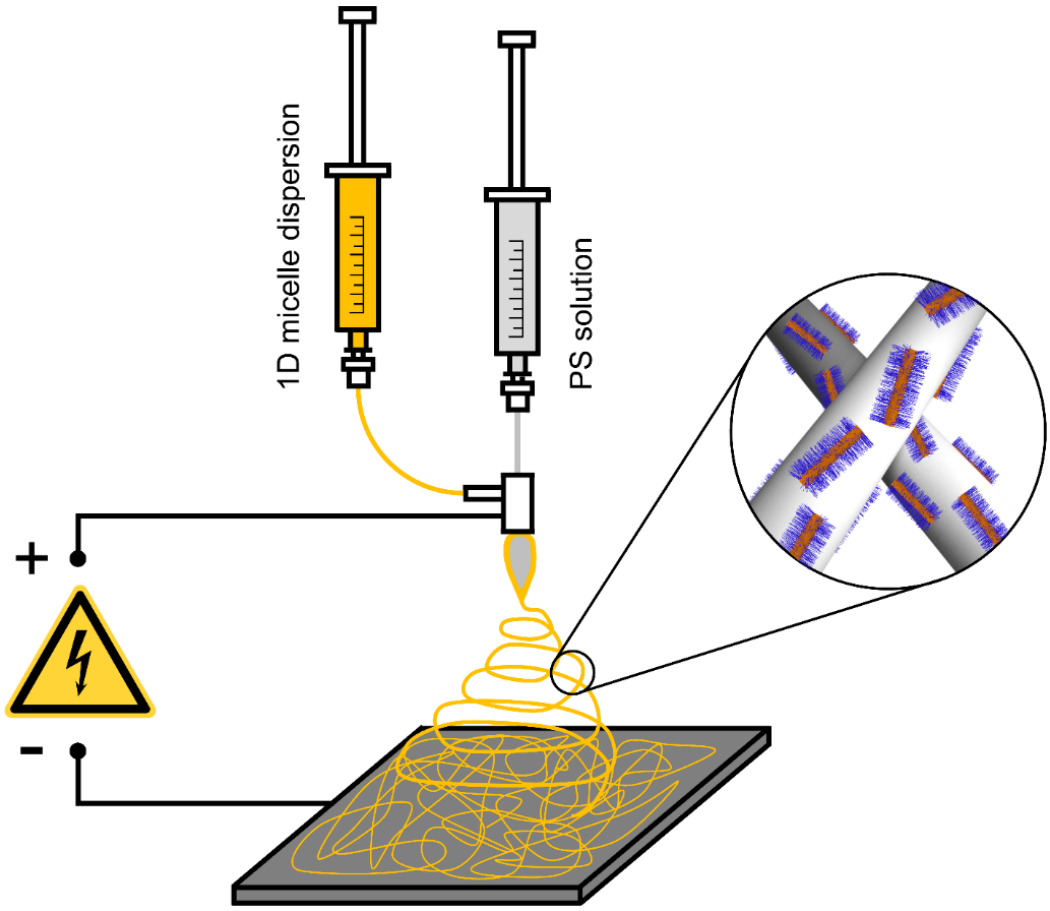

Scheme 5.1 Preparation of core-shell microfibers by coaxial electrospinning of PS (core, grey) and a dispersion of 1D micelles (shell, orange).

We first investigated the coaxial electrospinning of polydisperse PI_{192}-*b*-PFS_{27} 1D micelles which were prepared via PI-CDSA (L_n = 500–3000 nm, W_n = 9 ± 1 nm, **Figure S5.3**a).[31,32] For use as the shell, a dispersion of PI_{192}-*b*-PFS_{27} micelles (2.8 wt% in 20 vol% THF/hexanes) (THF = tetrahydrofuran) was prepared. The electrospinning droplet was extremely stable under the conditions studied (**Table S5.1**) resulting in the production of well-defined microfibers with relatively monodisperse widths (**Figure 5.1**). Adhesion of 1D polydisperse micelles to the PS fiber surface was detected by SEM (**Figure 5.1**c). Generally, long micelles that are oriented along the

long axis of the core PS fiber were observed. However, some short (ca. 100 nm) micelles were also discerned, indicating that some fragmentation may have occurred during the coaxial electrospinning process. The preferred orientation along the long axis of the fiber is presumably a result of shear forces during the electrospinning process.[3,45]

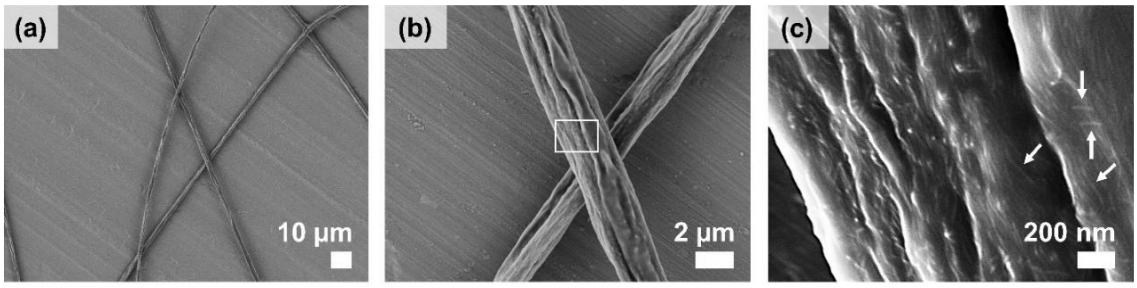

Figure 5.1 (a) Low magnification and (b), (c) high magnification SEM images of microfibers prepared via coaxial electrospinning of 1D PI_{192}-*b*-PFS_{27} micelles (2.8 wt% in 20 vol% THF/hexanes, shell) with PS (7 wt% in dimethylformamide (DMF), core). Inset box on (b) shows location of high magnification image (c). Arrows depict adhesion of 1D PI_{192}-*b*-PFS_{27} micelles to the PS core fiber. Scale bars: (a) 10 µm, (b) 2 µm, (c) 200 nm.

To further characterize the microfibers prepared via coaxial electrospinning, and to determine the coverage of PI_{192}-*b*-PFS_{27} micelles on the PS fiber surface, Raman spectroscopy was performed (**Figure 5.2**). The PI_{192}-*b*-PFS_{27} micelles were found to be dispersed evenly over the PS fiber surface by Raman imaging (**Figure 5.2**b). The presence of sharp peaks in the Raman spectra corresponding to PI_{192}-*b*-PFS_{27} also confirmed the presence of a crystalline PFS core (**Figure 5.2**e),[54] indicating that the core crystallinity is not compromised during the electrospinning process. The peaks corresponding to the PFS crystalline core also appeared sharper than those assigned to the PI corona.[55,56]

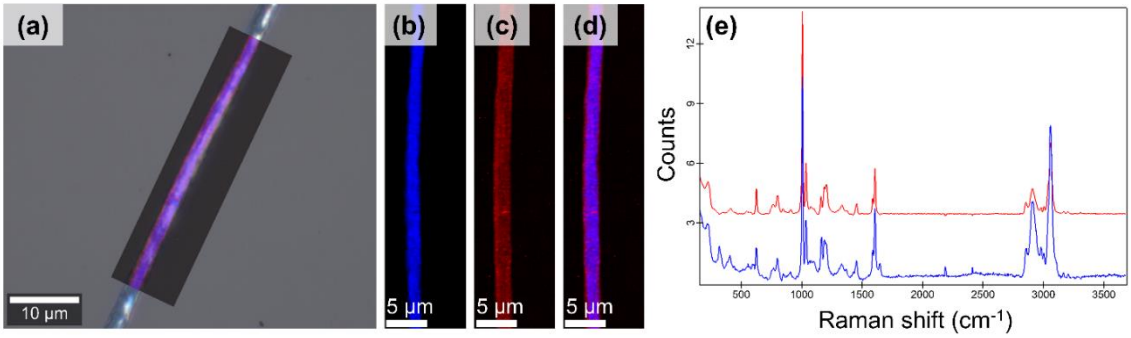

Figure 5.2 (a) Overlay of optical microscopy image with component distribution from Raman imaging for a microfiber prepared via coaxial electrospinning of PI_{192}-*b*-PFS_{27} micelles (2.8 wt% in 20 vol% THF/hexanes, shell) with PS (7 wt% in DMF, core). Areas rich in PI_{192}-*b*-PFS_{27} and PS are coloured in blue (b) and red (c), respectively. Consequently, mixed phases in the combined distribution (d) appear purple. (e) Raman spectra of the mixed PS/PI_{192}-*b*-PFS_{27} micelle phase (blue) and PS (red) derived from True Component Analysis. In the Raman spectrum of the mixed PS/PI_{192}-*b*-PFS_{27} micelle phase the characteristic peaks at $\tilde{\upsilon}$ = 316 cm^{-1} and 1645 cm^{-1} prove the presence of the PI_{192}-*b*-PFS_{27} micelles. Due to the smaller diameter of the micelles compared to that of the excited confocal volume the micelle spectrum is always superimposed with the PS spectrum. Scale bars: (a) 10 µm, (b)–(d) 5 µm.

To further investigate the behaviour of PFS-based micelles in coaxial electrospinning, we repeated the procedure using micelle dispersions containing BCPs with different corona-forming blocks, *ran*-PI_{124}/$PtBS_{125}$-*b*-PFS_{37} (**Figure S5.3**b) and $PtBS_{257}$-*b*-PFS_{38} (**Figure S5.3**c), while keeping the corona-to-core block ratio constant (ca. 7:1). Under the conditions studied (**Table S5.1**), microfibers akin to those when using PI_{192}-*b*-PFS_{27} micelles were afforded (**Figure S5.4**). However, the 1D micelles were not clearly discernible by SEM analysis (**Figure S5.4**b and d). The microfibers obtained when using *ran*-PI_{124}/$PtBS_{125}$-*b*-PFS_{37} micelles or $PtBS_{257}$-*b*-PFS_{38} micelles as the shell solution also exhibited a texture and morphology more similar to that of PS microfibers prepared via conventional electrospinning processes (**Figure S5.1**c).[3] This indicates that coaxial electrospinning was ineffective under these conditions. This could be due to the corona-forming

segments, *ran*-PI_{124}/$PtBS_{125}$ and $PtBS_{257}$, exhibiting more PS-character than that of PI_{192}, causing the core and shell solutions to mix prior to ejection of the microfiber. This could lead to the fiber-like micelles being buried in the PS fiber due to greater coronal compatibility, preventing the formation of a core-shell fiber.

5.3.2 Extension of Coaxial Electrospinning Approach to $PDHF_{17}$-*b*-$P2VP_{150}$ 1D Micelles with Polystyrene

The emergence of 1D nanoparticles based on BCPs with a π-conjugated crystalline core has led to considerable interest in their application as nanowires in devices.[6,57–59] In this work, our attention turns to the use of 1D micelles containing a PDHF crystalline core prepared via CDSA.[21] Long-range exciton transport (> 200 nm) that is far superior to that of thin-films of conjugated polymers has been achieved for PDHF-containing nanofibers, owing to the highly ordered crystalline core.[21] Recent studies have further demonstrated the promise of π-conjugated polymer nanofibers containing the donor PDHF crystalline core for optoelectronic applications,[22] such as energy-funneling which enabled a 4-fold enhancement of quantum rod emission.[23]

It has been demonstrated that alignment of 1D micelles with a π-conjugated poly(3-hexylthiophene) crystalline core can greatly enhance charge-carrier mobility.[59] In electrospinning processes, shear forces are exerted on the solution as it passes through the needle, causing BCP micelles to align along the long axis of the resulting fiber.[3] This phenomenon was demonstrated in the coaxial electrospinning of PI_{192}-*b*-PFS_{27} micelles (**Figure 5.1**c) as well as in previous work.[3,45] We were therefore interested in exploring the potential alignment of PDHF-containing micelles with the ultimate future aim of preparing electroactive fibers.

We studied the coaxial electrospinning of $PDHF_{17}$-*b*-$P2VP_{250}$ 1D micelles (**Figure S5.5**) (1.0 wt% in 25/25/50 vol% THF/MeOH/DMSO) (MeOH = methanol, DMSO = dimethyl sulfoxide) with PS (M_n = 1.1 x 10^6 Da, 7 wt% in DMF) as a carrier material. The $PDHF_{17}$-*b*-$P2VP_{250}$ 1D micelles were

employed as either the core (**Figure 5.3**a) or shell (**Figures 5.3**b and **5.4**b) of the coaxially electrospun fiber. The conditions of the coaxial electrospinning experiments were optimized to stabilize the droplet formation and yield fibers with minimal beading (**Table S5.2**). Fluorescence images indicated relatively even distribution of $PDHF_{17}$-*b*-$P2VP_{250}$ micelles throughout the core (**Figure 5.3**a) and shell (**Figure 5.3**b) of the coaxially electrospun fibers, compared with drop-cast micelle dispersion (**Figure S5.6**). On closer inspection, SEM analysis indicated that large populations of micelles exist at beads rather than being evenly distributed over the fiber surface (**Figure 5.4**b). Beading of fibers results from various factors including low solution viscosity, high net charge density of the jet, and high surface tension.[60] There was not sufficient evidence from SEM analysis to determine whether the $PDHF_{17}$-*b*-$P2VP_{250}$ micelles aligned during the coaxial electrospinning process, as individual 1D micelles could not be identified. Further optimization of the processing parameters is required to obtain a homogeneous coverage of $PDHF_{17}$-*b*-$P2VP_{250}$ micelles on the core PS fiber, as well as accessing electrospun fibers without beading.

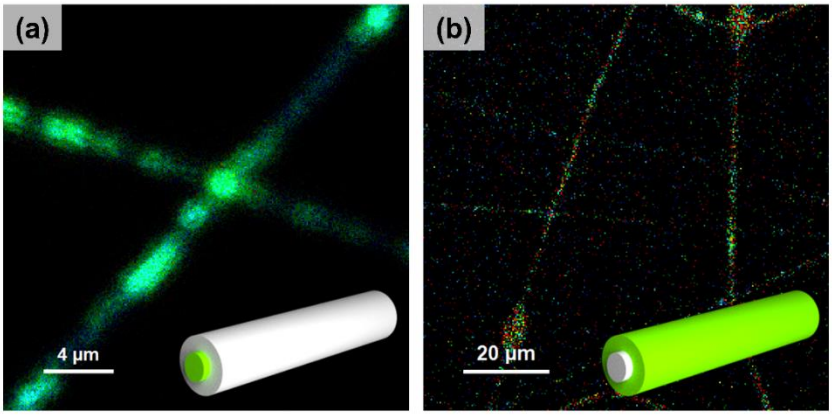

Figure 5.3 Confocal fluorescence microscope images of microfibers prepared via coaxial electrospinning of $PDHF_{17}$-*b*-$P2VP_{250}$ 1D micelles (1.0 wt% in 25/25/50 vol% THF/MeOH/DMSO) with PS (7 wt% in DMF) in which the micelles form (a) the core or (b) the shell of the fiber. Inset are representations of the core-shell microfiber structure composed of PS (white) and $PDHF_{17}$-*b*-$P2VP_{250}$ micelles (green). Scale bars: (a) 4 µm, (b) 20 µm.

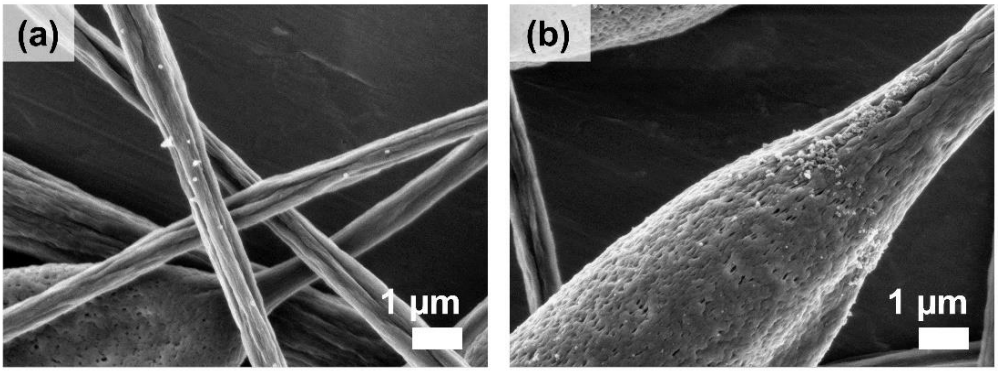

Figure 5.4 High magnification SEM images of microfibers formed via coaxial electrospinning of $PDHF_{17}$-*b*-$P2VP_{250}$ 1D micelles (1.0 wt% in 25/25/50 vol% THF/MeOH/DMSO, shell) with PS (7 wt% in DMF, core). A collector distance of 20 cm and pump speeds of 1.2 mL/h (core) and 0.4 mL/h (shell) were used. Scale bars: 1 µm.

5.3.3 Electrospinning of PI_{192}-*b*-PFS_{27} 1D Micelles

With the aim of developing microfibers formed exclusively of fiber-like BCP micelles, without the use of a template polymer, electrospinning of PI_{192}-*b*-PFS_{27} 1D micelle dispersions was investigated. As previously mentioned, BCP micelle dispersions typically form particles by electrospray in conventional electrospinning procedures,[53] as a result of the many parameters and conditions which require optimization to produce well-defined fibers. We began by exploring the electrospinning of polydisperse PI_{192}-b-PFS_{27} micelles (L_n = 500–3000 nm) prepared by PI-CDSA at various concentrations (5–20 wt%) in 20 vol% THF/hexanes (**Figure S5.3**a).[31,32] Electrospinning experimental parameters are detailed in **Table S5.3**.

At lower concentrations (≤ 10 wt%), electrospraying of the 1D micelle dispersions was observed (**Figure 5.5**a,b), resulting in almost exclusively particle formation. This is likely a result of the low viscosity of the micelle dispersions at these concentrations preventing electrospinning.[53] At 5 wt%, large particles of diameter 76 ± 26 µm were obtained. On increasing the dispersion concentration to 20 wt%, however, a mixture of fibers and particles was detected (**Figure 5.5**c,d). Interestingly, on the edge of the electrospinning substrate, the formation of short fibers dominated over that of

particles (**Figure 5.5**d). Although these results were promising, further optimization was required to access longer continuous electrospun fibers as well as to minimize beading.

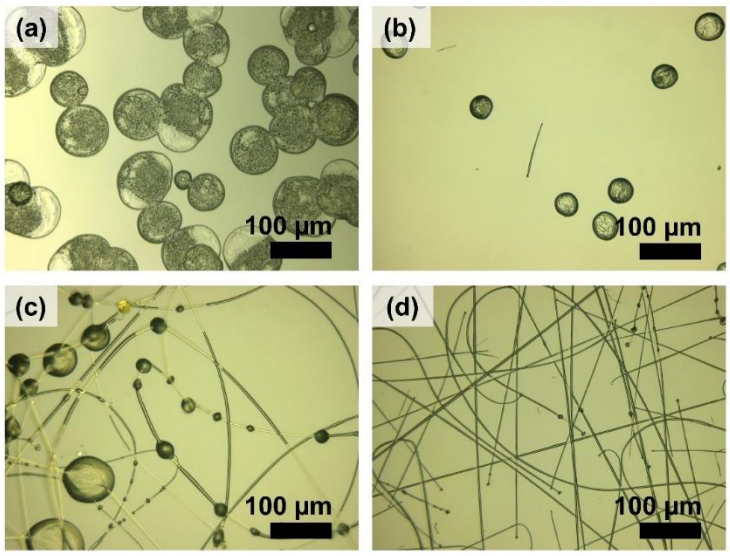

Figure 5.5 Optical microscope images of structures formed via electrospinning of PI_{192}-b-PFS_{27} 1D polydisperse micelle dispersions in 20 vol% THF/hexanes at (a) 5 wt%, (b) 10 wt%, and (c,d) 20 wt% formed at the (c) centre and (d) edge of the substrate. Scale bars: 100 µm.

Since fiber formation was favoured at increased concentration, we looked to further optimize electrospinning conditions using micelle dispersions at high concentrations of 16–20 wt%. First, electrospinning of 1D micelles (L_n = 500–3000 nm) at 20 wt% was performed at lower voltages (**Figure S5.7** and **Table S5.4**) with the aim of increasing the stabilization of the droplet and promoting improved electrospinning.[61] Fibers were successfully formed via electrospinning, however the widths varied and some beading was also observed (**Figure S5.7**).

To prevent localized evaporation and therefore minimize beading, a solvent with a higher boiling point (T_b) than the current system, 20 vol% THF/hexanes ($T_b \approx$ 66–69 °C), was explored. DMF (T_b = 153 °C) has been commonly used as a solvent for the electrospinning of polymeric materials and was therefore explored in this work. However, DMF is a poor solvent for both the PI corona-forming segment and the PFS core-forming segment, meaning only low volume fractions could be

studied to prevent precipitation of the micelles. Therefore, micelle dispersions were diluted to 16 wt% with DMF, resulting in a solvent system consisting of 9 vol% DMF and 18 vol% THF in hexanes. Under these conditions (**Table S5.4**), long continuous fibers with relatively monodisperse widths (ca. 3 μm) and the absence of beading were accessed (**Figure 5.6**). This is likely a result of an increase in stabilization of the electrospinning droplet caused by the presence of DMF, which increases the boiling point of the solvent system. Although individual fiber-like micelles could not be discerned on the microfiber surface by SEM (**Figure 5.6**d), we performed a control experiment whereby PI_{273} homopolymer was electrospun to investigate whether microfibers were formed in the absence of a PFS crystalline core. It was found that, in the absence of 1D PFS crystalline cores, PI_{273} homopolymer did not form electrospun fibers and instead produced particles by electrospraying (**Figure S5.8**). To the best of our knowledge, this work is the first example of electrospun fibers comprising solely of BCP micelles.

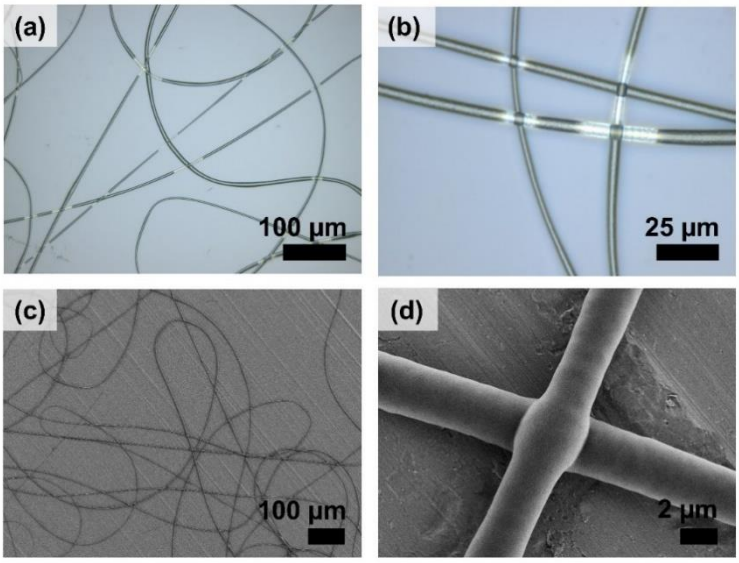

Figure 5.6 (a) low magnification and (b) high magnification optical microscope images and (c) low magnification and (b) high magnification SEM images of microfibers formed via electrospinning of PI_{192}-b-PFS_{27} 1D polydisperse micelle dispersions in 9 vol% DMF and

18 vol% THF in hexanes at 16 wt%. A collector distance of 23 cm and pump speed of 0.8 mL/h were used. Scale bars: (a, c) 100 µm, (b) 25 µm, (d) 2 µm.

It was postulated that the micelle length could also influence the structures obtained via electrospinning. The polydisperse PI_{192}-*b*-PFS_{27} 1D micelles were sonicated for 1 h at 0 °C to fragment the nanostructures and allow for the study of how micelle length affects the electrospinning process. The resulting micelles were analysed by TEM (**Figure S5.9**) and were determined to have a length (L_n) and length dispersity (L_w/L_n) of L_n = 71 nm and L_w/L_n = 1.25. On electrospinning of these shorter micelles, similar results were obtained to that of the long polydisperse micelles. Electrospraying dominated at lower concentrations (≤ 10 wt%) (**Figure S5.10**a–c) and electrospinning was achieved at 20 wt% (**Figure S5.10**d, see **Table S5.4** for experimental details). The particles formed via electrospraying exhibited diameters with low dispersity. At 5 and 7.5 wt%, the particles had comparable diameters of 5.9 ± 1.8 µm and 7.5 ± 2.0 µm, respectively, whereas at 10 wt% the diameter was significantly larger (59 ± 26 µm). These findings suggest that entanglement of micelles in solution does not play a dominant role on the structures obtained. Rather, it is likely that the dispersion concentration plays a more significant role in the electrohydrodynamical phenomenon.

Electrospinning of PFS-based micelles with different corona-forming segments was also explored. Dispersions of *ran*-PI_{124}/$PtBS_{125}$-*b*-PFS_{37} micelles and $PtBS_{257}$-*b*-PFS_{38} micelles at 10 wt% in 10/10/80 vol% cyclohexane/THF/hexanes were investigated; however, the solution viscosity was too high to obtain any electrospinning results. On dilution to 5 wt%, only electrospraying to form particles was observed, similar to the case of PI_{192}-*b*-PFS_{27} micelles.[53]

5.4 Summary

The processing of 1D micelles via electrospinning techniques (coaxial and conventional electrospinning) was investigated. Using coaxial electrospinning, core-shell fibers whereby the

shell consisted of polydisperse PFS-based 1D micelles could be obtained. Coaxial electrospinning using PI_{192}-*b*-PFS_{27} micelles as the shell yielded fibers in which the micelles were clearly discerned on the surface via SEM analysis. Under the optimized conditions, the electrospinning droplet was extremely stable which resulted in the production of well-defined microfibers without beading. Furthermore, Raman imaging also confirmed the even coverage of PI_{192}-*b*-PFS_{27} micelles on the PS fiber and indicated that the PFS core remained crystalline throughout the process.

The coaxial electrospinning of 1D $PDHF_{17}$-*b*-$P2VP_{250}$ micelles with a π-conjugated crystalline core was also explored. In this case, fibers containing 1D micelles as either the core or shell could be obtained. However, coaxially electrospun fibers were found to exhibit beading with uneven micelle distribution over the fiber surface. Future work will aim to optimize the coaxial electrospinning of $PDHF_{17}$-*b*-$P2VP_{250}$ 1D micelles to produce well-defined fibers for use in optoelectronic devices.

Conventional electrospinning to produce fibers consisting solely of 1D PI_{192}-*b*-PFS_{27} micelles was also described. Fibers consisting of either long (L_n = 500–3000 nm) or short (L_n = 71 nm) micelles were obtained at solution concentrations of 20 wt% but required further optimization to avoid beading. The addition of DMF to the micelle dispersion (to make a final concentration of 16 wt%) was found to stabilize the droplet formation to allow access to well-defined continuous fibers. To the best of our knowledge, this is the first example of fibers prepared via electrospinning of BCP micelle dispersions, without the use of a carrier or template.

5.5 References

(1) Tritschler, U.; Pearce, S.; Gwyther, J.; Whittell, G. R.; Manners, I. 50th Anniversary Perspective: Functional Nanoparticles from the Solution Self-Assembly of Block Copolymers. *Macromolecules* **2017**, *50* (9), 3439–3463.

(2) Mai, Y.; Eisenberg, A. Self-Assembly of Block Copolymers. *Chem. Soc. Rev.* **2012**, *41* (18), 5969–5985.

(3) Schöbel, J.; Burgard, M.; Hils, C.; Dersch, R.; Dulle, M.; Volk, K.; Karg, M.; Greiner, A.;

Schmalz, H. Bottom-Up Meets Top-Down: Patchy Hybrid Nonwovens as an Efficient Catalysis Platform. *Angew. Chem. Int. Ed.* **2017**, *56* (1), 405–408.

(4) Tian, J.; Zhang, Y.; Du, L.; He, Y.; Jin, X.-H.; Pearce, S.; Eloi, J.-C.; Harniman, R. L.; Alibhai, D.; Ye, R.; Phillips, D. L.; Manners, I. Tailored Self-Assembled Photocatalytic Nanofibres for Visible-Light-Driven Hydrogen Production. *Nat. Chem.* **2020**, *12*, 1150–1156.

(5) Yang, S.; Kang, S.; Choi, T. Semi-Conducting 2D Rectangles with Tunable Length via Uniaxial Living Crystallization-Driven Self-Assembly of Homopolymer. *Nat. Commun.* **2021**, *12*, 2602.

(6) MacFarlane, L. R.; Shaikh, H.; Garcia-Hernandez, J. D.; Vespa, M.; Fukui, T.; Manners, I. Functional Nanoparticles through π-Conjugated Polymer Self-Assembly. *Nat. Rev. Mater.* **2021**, *6*, 7–26.

(7) Elsabahy, M.; Wooley, K. L. Design of Polymeric Nanoparticles for Biomedical Delivery Applications. *Chem. Soc. Rev.* **2012**, *41*, 2545–2561.

(8) Ge, Z.; Liu, S. Functional Block Copolymer Assemblies Responsive to Tumor and Intracellular Microenvironments for Site-Specific Drug Delivery and Enhanced Imaging Performance. *Chem. Soc. Rev.* **2013**, *42* (17), 7289–7325.

(9) Kinnear, C.; Moore, T. L.; Rodriguez-Lorenzo, L.; Rothen-Rutishauser, B.; Petri-Fink, A. Form Follows Function: Nanoparticle Shape and Its Implications for Nanomedicine. *Chem. Rev.* **2017**, *117* (17), 11476–11521.

(10) Garcia-Hernandez, J. D.; Street, S. T. G.; Kang, Y.; Zhang, Y.; Manners, I. Cargo Encapsulation in Uniform, Length-Tunable Aqueous Nanofibers with a Coaxial Crystalline and Amorphous Core. *Macromolecules* **2021**, *54* (12), 5784–5796.

(11) Arno, M. C.; Inam, M.; Weems, A. C.; Li, Z.; Binch, A. L. A.; Platt, C. I.; Richardson, S. M.; Hoyland, J. A.; Dove, A. P.; O'Reilly, R. K. Exploiting the Role of Nanoparticle Shape in Enhancing Hydrogel Adhesive and Mechanical Properties. *Nat. Commun.* **2020**, *11*, 1420.

(12) He, Y.; Eloi, J.-C.; Harniman, R. L.; Richardson, R. M.; Whittell, G. R.; Mathers, R. T.; Dove, A. P.; O'Reilly, R. K.; Manners, I. Uniform Biodegradable Fiber-Like Micelles and Block Comicelles via "Living" Crystallization-Driven Self-Assembly of Poly(L-Lactide)

Block Copolymers: The Importance of Reducing Unimer Self-Nucleation via Hydrogen Bond Disruption. *J. Am. Chem. Soc.* **2019**, *141* (48), 19088–19098.

(13) Street, S. T. G.; He, Y.; Jin, X.-H.; Hodgson, L.; Verkade, P.; Manners, I. Cellular Uptake and Targeting of Low Dispersity, Dual Emissive, Segmented Block Copolymer Nanofibers. *Chem. Sci.* **2020**, *11* (32), 8394–8408.

(14) Massey, J. A.; Temple, K.; Cao, L.; Rharbi, Y.; Raez, J.; Winnik, M. A.; Manners, I. Self-Assembly of Organometallic Block Copolymers: The Role of Crystallinity of the Core-Forming Polyferrocene Block in the Micellar Morphologies Formed by Poly(Ferrocenylsilane-b-Dimethylsiloxane) in n-Alkane Solvents. *J. Am. Chem. Soc.* **2000**, *122* (47), 11577–11584.

(15) Gilroy, J. B.; Gädt, T.; Whittell, G. R.; Chabanne, L.; Mitchels, J. M.; Richardson, R. M.; Winnik, M. A.; Manners, I. Monodisperse Cylindrical Micelles by Crystallization-Driven Living Self-Assembly. *Nat. Chem.* **2010**, *2*, 566–570.

(16) Guerin, G.; Wang, H.; Manners, I.; Winnik, M. A. Fragmentation of Fiberlike Structures: Sonication Studies of Cylindrical Block Copolymer Micelles and Behavioral Comparisons to Biological Fibrils. *J. Am. Chem. Soc.* **2008**, *130* (44), 14763–14771.

(17) Guerin, G.; Rupar, P. A.; Winnik, M. A. In-Depth Analysis of the Effect of Fragmentation on the Crystallization-Driven Self-Assembly Growth Kinetics of 1D Micelles Studied by Seed Trapping. *Polymers (Basel).* **2021**, *13*, 3122.

(18) Ganda, S.; Stenzel, M. H. Concepts, Fabrication Methods and Applications of Living Crystallization-Driven Self-Assembly of Block Copolymers. *Prog. Polym. Sci.* **2020**, *101*, 101195.

(19) MacFarlane, L. R.; Zhao, C.; Cai, J.; Qiu, H.; Manners, I. Emerging Applications for Living Crystallization-Driven Self-Assembly. *Chem. Sci.* **2021**, *12* (13), 4661–4682.

(20) Wang, X.; Manners, I.; Winnik, M. A. Cylindrical Block Copolymer Micelles and Co-Micelles of Controlled Length and Architecture. *Science* **2007**, *317* (5838), 644–648.

(21) Jin, X.; Price, M. B.; Finnegan, J. R.; Boott, C. E.; Richter, J. M.; Rao, A.; Menke, S. M.; Friend, R. H.; Whittell, G. R.; Manners, I. Long-Range Exciton Transport in Conjugated Polymer Nanofibers Prepared by Seeded Growth. *Science* **2018**, *900* (6391), 897–900.

(22) Shaikh, H.; Jin, X.-H.; Harniman, R. L.; Richardson, R. M.; Whittell, G. R.; Manners, I.

Solid-State Donor-Acceptor Coaxial Heterojunction Nanowires via Living Crystallization-Driven Self-Assembly. *J. Am. Chem. Soc.* **2020**, *142* (31), 13469–13480.

(23) Zhang, Y.; Shaikh, H.; Sneyd, A. J.; Tian, J.; Xiao, J.; Blackburn, A.; Rao, A.; Friend, R. H.; Manners, I. Efficient Energy Funneling in Spatially Tailored Segmented Conjugated Block Copolymer Nanofiber−Quantum Dot or Rod Conjugates. *J. Am. Chem. Soc.* **2021**, *143* (18), 7032–7041.

(24) Arno, M. C.; Inam, M.; Coe, Z.; Cambridge, G.; Macdougall, L. J.; Keogh, R.; Dove, A. P.; O'Reilly, R. K. Precision Epitaxy for Aqueous 1D and 2D Poly(ϵ-Caprolactone) Assemblies. *J. Am. Chem. Soc.* **2017**, *139* (46), 16980–16985.

(25) Yu, W.; Foster, J. C.; Dove, A. P.; O'Reilly, R. K. Length Control of Biodegradable Fiber-Like Micelles via Tuning Solubility: A Self-Seeding Crystallization-Driven Self-Assembly of Poly(ε-Caprolactone)-Containing Triblock Copolymers. *Macromolecules* **2020**, *53* (4), 1514–1521.

(26) Schmelz, J.; Schedl, A. E.; Steinlein, C.; Manners, I.; Schmalz, H. Length Control and Block-Type Architectures in Worm-like Micelles with Polyethylene Cores. *J. Am. Chem. Soc.* **2012**, *134* (34), 14217–14225.

(27) Hils, C.; Schmelz, J.; Drechsler, M.; Schmalz, H. Janus Micelles by Crystallization-Driven Self-Assembly of an Amphiphilic, Double-Crystalline Triblock Terpolymer. *J. Am. Chem. Soc.* **2021**, *143* (38), 15582–15586.

(28) Shin, S.; Menk, F.; Kim, Y.; Lim, J.; Char, K.; Zentel, R.; Choi, T.-L. Living Light-Induced Crystallization-Driven Self-Assembly for Rapid Preparation of Semiconducting Nanofibers. *J. Am. Chem. Soc.* **2018**, *140* (19), 6088–6094.

(29) Han, L.; Wang, M.; Jia, X.; Chen, W.; Qian, H.; He, F. Uniform Two-Dimensional Square Assemblies from Conjugated Block Copolymers Driven by π-π Interactions with Controllable Sizes. *Nat. Commun.* **2018**, *9*, 865.

(30) Tao, D.; Feng, C.; Cui, Y.; Yang, X.; Manners, I.; Winnik, M. A.; Huang, X. Monodisperse Fiber-like Micelles of Controlled Length and Composition with an Oligo(p-Phenylenevinylene) Core via "Living" Crystallization-Driven Self-Assembly. *J. Am. Chem. Soc.* **2017**, *139* (21), 7136–7139.

(31) Boott, C. E.; Gwyther, J.; Harniman, R. L.; Hayward, D. W.; Manners, I. Scalable and

Uniform 1D Nanoparticles by Synchronous Polymerization, Crystallization and Self-Assembly. *Nat. Chem.* **2017**, *9*, 785–792.

(32) Oliver, A. M.; Gwyther, J.; Boott, C. E.; Davis, S. A.; Pearce, S.; Manners, I. Scalable Fiber-like Micelles and Block Co-Micelles by Polymerization-Induced Crystallization-Driven Self-Assembly. *J. Am. Chem. Soc.* **2018**, *140* (51), 18104–18114.

(33) Sha, Y.; Rahman, M. A.; Zhu, T.; Cha, Y.; McAlister, C. W.; Tang, C. ROMPI-CDSA: Ring-Opening Metathesis Polymerization-Induced Crystallization-Driven Self-Assembly of Metallo-Block Copolymers. *Chem. Sci.* **2019**, *10* (42), 9782–9787.

(34) Hurst, P. J.; Rakowski, A. M.; Patterson, J. P. Ring-Opening Polymerization-Induced Crystallization-Driven Self-Assembly of Poly-L-Lactide-Block-Polyethylene Glycol Block Copolymers (ROPI-CDSA). *Nat. Commun.* **2020**, *11*, 4690.

(35) Guan, S.; Wen, W.; Yang, Z.; Chen, A. Liquid Crystalline Nanowires by Polymerization Induced Hierarchical Self-Assembly. *Macromolecules* **2020**, *53* (1), 465–472.

(36) Reneker, D. H.; Yarin, A. L. Electrospinning Jets and Polymer Nanofibers. *Polymer* **2008**, *49*, 2387–2425.

(37) Agarwal, S.; Greiner, A.; Wendorff, J. H. Functional Materials by Electrospinning of Polymers. *Prog. Polym. Sci.* **2013**, *38* (6), 963–991.

(38) Greiner, A.; Wendorff, J. H. Electrospinning: A Fascinating Method for the Preparation of Ultrathin Fibers. *Angew. Chem. Int. Ed.* **2007**, *46* (30), 5670–5703.

(39) Greiner, A.; Wendorff, J. H. Elektrospinnen: Eine Faszinierende Methode Zur Präparation Ultradünner Fasern. *Angew. Chemie* **2007**, *119* (30), 5770–5805.

(40) Tayi, A. S.; Pashuck, E. T.; Newcomb, C. J.; McClendon, M. T.; Stupp, S. I. Electrospinning Bioactive Supramolecular Polymers from Water. *Biomacromolecules* **2014**, *15* (4), 1323–1327.

(41) Huang, W.; Wang, M.-J.; Liu, C.-L.; You, J.; Chen, S.-C.; Wang, Y.-Z.; Liu, Y. Phase Separation in Electrospun Nanofibers Controlled by Crystallization Induced Self-Assembly. *J. Mater. Chem. A* **2014**, *2* (22), 8416–8424.

(42) Burgard, M.; Weiss, D.; Kreger, K.; Schmalz, H.; Agarwal, S.; Schmidt, H. W.; Greiner, A. Mesostructured Nonwovens with Penguin Downy Feather-Like Morphology—Top-Down

Combined with Bottom-Up. *Adv. Funct. Mater.* **2019**, *29*, 1903166.

(43) Hils, C.; Dulle, M.; Sitaru, G.; Gekle, S.; Schöbel, J.; Frank, A.; Drechsler, M.; Greiner, A.; Schmalz, H. Influence of Patch Size and Chemistry on the Catalytic Activity of Patchy Hybrid Nonwovens. *Nanoscale Adv.* **2020**, *2* (1), 438–452.

(44) Duan, G.; Greiner, A. Air-Blowing-Assisted Coaxial Electrospinning toward High Productivity of Core/Sheath and Hollow Fibers. *Macromol. Mater. Eng.* **2019**, *304* (5), 1800669.

(45) Frank, A.; Hils, C.; Weber, M.; Kreger, K.; Schmalz, H.; Schmidt, H.-W. Hierarchical Superstructures by Combining Crystallization-driven and Molecular Self-assembly. *Angew. Chem. Int. Ed.* **2021**, *60*, 21767–21771.

(46) Han, D.; Steckl, A. J. Coaxial Electrospinning Formation of Complex Polymer Fibers and Their Applications. *Chempluschem* **2019**, *84* (10), 1453–1497.

(47) Lu, Y.; Huang, J.; Yu, G.; Cardenas, R.; Wei, S.; Wujcik, E. K.; Guo, Z. Coaxial Electrospun Fibers: Applications in Drug Delivery and Tissue Engineering. *Wiley Interdiscip. Rev. Nanomedical Nanobiotechnology* **2016**, *8* (5), 654–677.

(48) Sun, Z.; Zussman, E.; Yarin, A. L.; Wendorff, J. H.; Greiner, A. Compound Core-Shell Polymer Nanofibers by Co-Electrospinning. *Adv. Mater.* **2003**, *15* (22), 1929–1932.

(49) Jing, X.; Mi, H.-Y.; Wang, X.-C.; Peng, X.-F.; Turng, L.-S. Shish-Kebab-Structured Poly(ε-Caprolactone) Nanofibers Hierarchically Decorated with Chitosan-Poly(ε-Caprolactone) Copolymers for Bone Tissue Engineering. *ACS Appl. Mater. Interfaces* **2015**, *7* (12), 6955–6965.

(50) Yu, T.; Gleeson, S. E.; Li, C. Y.; Marcolongo, M. Electrospun Poly(ε-Caprolactone) Nanofiber Shish Kebabs Mimic Mineralized Bony Surface Features. *J. Biomed. Mater. Res. - Part B Appl. Biomater.* **2019**, *107* (4), 1141–1149.

(51) Norouzi, M.; Boroujeni, S. M.; Omidvarkordshouli, N. Advances in Skin Regeneration: Application of Electrospun Scaffolds. *Adv. Healthc. Mater.* **2015**, *4*, 1114–1133.

(52) Chen, H.; Wang, N.; Di, J.; Zhao, Y.; Song, Y.; Jiang, L. Nanowire-in-Microtube Structured Core/Shell Fibers via Multifluidic Coaxial Electrospinning. *Langmuir* **2010**, *26* (13), 11291–11296.

(53) Wang, L.; Topham, P. D.; Mykhaylyk, O. O.; Yu, H.; Ryan, A. J.; Fairclough, J. P. A.; Bras, W. Self-Assembly-Driven Electrospinning: The Transition from Fibers to Intact Beaded Morphologies. *Macromol. Rapid Commun.* **2015**, *36* (15), 1437–1443.

(54) Stuart, B. H. Polymer Crystallinity Studied Using Raman Spectroscopy. *Vib. Spectrosc.* **1996**, *10* (2), 79–87.

(55) Cornell, S. W.; Koenig, J. L. Raman Spectra of Polyisoprene Rubbers. *Macromolecules* **1969**, *2* (5), 546–549.

(56) Arjunan, V.; Puviarasan, N.; Mohan, S.; Murugesan, P. Fourier Transform Infrared and Raman Spectral Assignments and Analysis of 7-Amino-4-Trifluoromethylcoumarin. *Spectrochim. Acta - Part A Mol. Biomol. Spectrosc.* **2007**, *67* (5), 1290–1296.

(57) Persson, N. E.; Chu, P. H.; McBride, M.; Grover, M.; Reichmanis, E. Nucleation, Growth, and Alignment of Poly(3-Hexylthiophene) Nanofibers for High-Performance OFETs. *Acc. Chem. Res.* **2017**, *50* (4), 932–942.

(58) El-Zubir, O.; Kynaston, E. L.; Gwyther, J.; Nazemi, A.; Gould, O. E. C.; Whittell, G. R.; Horrocks, B. R.; Manners, I.; Houlton, A. Bottom-up Device Fabrication via the Seeded Growth of Polymer-Based Nanowires. *Chem. Sci.* **2020**, *11* (24), 6222–6228.

(59) Li, X.; Wolanin, P. J.; MacFarlane, L. R.; Harniman, R. L.; Qian, J.; Gould, O. E. C.; Dane, T. G.; Rudin, J.; Cryan, M. J.; Schmaltz, T.; Frauenrath, H.; Winnik, M. A.; Faul, C. F. J.; Manners, I. Uniform Electroactive Fibre-like Micelle Nanowires for Organic Electronics. *Nat. Commun.* **2017**, *8*, 15909.

(60) Fong, H.; Chun, I.; Reneker, D. H. Beaded Nanofibers Formed during Electrospinning. *Polymer* **1999**, *40*, 4585–4592.

(61) Han, T.; Yarin, A. L.; Reneker, D. H. Viscoelastic Electrospun Jets: Initial Stresses and Elongational Rheometry. *Polymer* **2008**, *49*, 1651–1658.

5.6 Supplementary Material

5.6.1 Materials and Methods

Hexanes, DMF, THF, and cyclohexane were all purchased from Sigma Aldrich (p.a. grade). All other reagents and chemicals were used as received unless otherwise stated. PI_{192}-*b*-PFS_{37}, *ran*-PI_{124}/$PtBS_{125}$-*b*-PFS_{37} and $PtBS_{257}$-*b*-PFS_{38} 1D micelles were prepared by PI-CDSA, as previously reported.[1,2] $PDHF_{17}$-*b*-$P2VP_{250}$ was synthesized and self-assembled via CDSA, as previously reported.[3] The high molecular weight polystyrenes used for coaxial electrospinning (M_n = 1.1 x 10^6 Da and M_n = 1.4 x 10^6 Da) were synthesized by living anionic polymerization of styrene in THF at -80°C employing sec-butyllithium as initiator.

5.6.2 Instrumentation

Nuclear magnetic resonance (NMR) spectroscopy. ^{1}H NMR spectra were obtained using a Varian 500 MHz spectrometer.

Transmission electron microscopy (TEM). Copper grids (500 mesh) were purchased from Ted Pella, Inc. and carbon films were prepared by using a Leica EM ACE600 instrument. Carbon films were deposited onto the copper grids by floatation on water and allowed to dry over 24 hours. Samples for electron microscopy were prepared by drop-casting 8 µL of micelle colloidal solution onto a carbon-coated copper grid followed by solvent evaporation. TEM micrographs were obtained using a JEOL JEM 1011 operating at 80 kV, equipped with a Gatan Orius SC1000 CCD camera.

Measurements were undertaken by hand using ImageJ software, developed by the US National Institute for Health. The number-average length (L_n) and weight-average length (L_w) were calculated according to the following equations:

$$L_n = \frac{\sum_i^n N_i L_i}{\sum_i^n N_i} \qquad L_w = \frac{\sum_i^n N_i L_i^2}{\sum_i^n N_i L_i}$$

A minimum of 100 micelles were measured for each data point. Errors displayed are standard deviations of each data set.

Ultrasonication. Micelle sonication was carried out using a Fisherbrand FB11203 sonication bath. The instrument was operated at 100% power and 37 kHz at 10 °C.

Electrospinning. For coaxial electrospinning experiments, a coaxial needle (COAX_2DISP sealed coaxial needles, LINARI NanoTech, d_{core} = 0.51 mm, d_{shell} = 1.37 mm) and a 7 wt% polystyrene (PS) (M_n = 1.1 x 10^6 Da and M_n = 1.4 x 10^6 Da) solution in DMF were used. Processing parameters for the coaxial electrospinning experiments are detailed in **Table S5.1**. For electrospinning, parameters are detailed in **Table S5.3**, **Table S5.4**, and **Table S5.5**. Fibers were spun onto a collector (12 x 14 cm) placed at a distance of ca. 20 cm from the coaxial needle.

Optical microscopy. Optical microscope images were taken with a Keyence VHX-100.

Scanning electron microscopy (SEM). SEM analysis was performed using a Zeiss 1530 with field emission cathode at an acceleration voltage of 3 kV with secondary electrons (SE2) and Inlens SE detectors. Samples were applied to a conductive adhesive carrier mounted on an aluminium plate, fixed with an aluminum adhesive strip and coated with a thin layer of platinum (d = ca. 1.3 nm) using Cressington 208HR high resolution sputter coater with MTM-20 thickness controller.

Confocal fluorescence microscopy. Fluorescence microscopy was performed using a MicroTime 200 fluorescence microscope at an excitation wavelength of λ = 425 nm.

Raman imaging. For Raman analyses a confocal WITec Alpha 300 RA+ Raman imaging system equipped with a UHTS 300 spectrometer and a back-illuminated Andor Newton 970 EMCCD camera together with the WITec Suite FIVE 5.3 software package was employed. All measurements were conducted with an excitation wavelength of λ = 532 nm and a 100x objective (Zeiss EC "Epiplan-Neofluar" DIC, NA = 0.9). For Raman imaging a step size of 100 nm pixel^{-1}, a laser intensity of 4 mW and an integration time of 0.9 sec were used. All spectra were subjected

to a cosmic ray removal routine and background subtraction. Component distributions were derived from the Raman imaging data with the help of the True Component Analysis integrated in the WITec Project Five 5.3 evaluation software.

5.6.3 Synthetic Procedures

PI_{192}-*b*-PFS_{27}, *ran*-PI_{124}/$PtBS_{125}$-*b*-PFS_{37} and $PtBS_{257}$-*b*-PFS_{38} 1D micelles were prepared by PI-CDSA, as previously reported.[1,2]

5.6.3.1 Synthesis of PI_{192}-*b*-PFS_{27}

GPC was used to characterize an aliquot of the PI segment before polymerization of the PFS block. This analysis provided an M_n value of 13,100 Da, corresponding to a DP_n of 192. ^{1}H NMR was used to determine the block ratio by comparing the integrals of the signals corresponding to the vinyl protons of PI (4.39–5.12 ppm) with that of the Cp protons of PFS (4.03 and 4.23 ppm). The corona-to-core block ratio was found to be 7.1, which could then be used to determine the DP_n of the PFS block as 27.

^{1}H NMR (400 MHz, CD_2Cl_2): δ (ppm) = 4.39–5.12 (br, 16H, vinylic PI), 4.23 (m, 4H, Cp), 4.03 (m, 4H, Cp), 2.52–1.18 (br, 41H, aliphatic PI), 0.51 (s, 6H, $Si(CH_3)_2$); M_n (GPC) = 21,800 Da; M_w/M_n = 1.12.

5.6.3.2 Synthesis of *ran*-PI_{124}/$PtBs_{125}$-*b*-PFS_{37}

GPC was used to characterize an aliquot of the *ran*-PI/PtBS segment before polymerization of the PFS block. This analysis provided an M_n value of 28,500 Da, corresponding to a total DP_n of ca. 250. ^{1}H NMR was used to determine the block ratio by comparing the integrals of the signals corresponding to the vinyl protons of PI (5.12–4.39 ppm) with that of the aromatic protons of PtBS (7.30–6.11 ppm). The PI/PtBS block ratio was found to be 1. ^{1}H NMR of the final BCP could then be used to determine the DP_n of the PFS block, by comparison of the integrals corresponding to the

Cp protons (4.23 and 4.03 ppm). The corona-to-core block ratio was found to be 6.7, therefore the DP_n of the PFS block was 37.

^{1}H NMR (400 MHz, CD_2Cl_2): δ (ppm) = 7.30–6.11 (br, 13H, $CH_2CH(Ph)C(CH_3)$), 4.39–5.12 (br, 7H, vinylic PI), 4.23 (m, 4H, Cp), 4.03 (m, 4H, Cp), 1.29 (s, br, 30H, $C(CH_3)_3$), 2.52–1.12 (br, 3H, CH_2CH(Ph); 6H, α-CCH_2; 19H, aliphatic PI), 0.51 (s, 6H, $Si(CH_3)_2$); M_n (GPC) = 38,900 Da; M_w/M_n = 1.13.

5.6.3.3 Synthesis of $PtBS_{257}$-*b*-PFS_{38}

GPC was used to characterize an aliquot of the PtBS segment before polymerization of the PFS block. This analysis provided an M_n value of 41,100 Da, corresponding to a DP_n of 257. ^{1}H NMR was used to determine the block ratio by comparing the integrals of the signals corresponding to the aromatic protons of PtBS (7.30–6.11 ppm) with that of the Cp protons of PFS (4.23 and 4.03 ppm). The corona-to-core block ratio was found to be 6.8, which could then be used to determine the DP_n of the PFS block as 38.

^{1}H NMR (400 MHz, CD_2Cl_2): δ (ppm) = 7.30–6.11 (br, 27H, $CH_2CH(Ph)C(CH_3)$), 4.23 (m, 4H, Cp), 4.03 (m, 4H, Cp), 1.29 (s, br, 61H, $C(CH_3)_3$), 2.26–1.12 (br, 7H, CH_2CH(Ph); 14H, α-CCH_2), 0.51 (s, 6H, $Si(CH_3)_2$); M_n (GPC) = 47,200 Da; M_w/M_n = 1.26.

5.6.3.4 Synthesis of $PDHF_{17}$-*b*-$P2VP_{250}$

$PDHF_{17}$-*b*-$P2VP_{250}$ was synthesized and self-assembled via CDSA, as previously reported.[3]

Azide-terminated $P2VP_{250}$ was synthesized according to a previously reported procedure and the DP_n was determined by ^{1}H NMR analysis by comparing the integrals of the signals corresponding to the aromatic protons of P2VP (7.57–6.09 ppm) with that of the RAFT CTA (3.51 ppm). ^{1}H NMR analysis was used to determine the BCP structure as $PDHF_{17}$-*b*-$P2VP_{250}$ by comparing the integrals of the aromatic protons of PDHF (8.73–7.57 ppm) with that of P2VP (7.57–6.09 ppm).

^{1}H NMR (500 MHz, $CDCl_3$): δ (ppm) = 8.73–7.57 (m, 363H, polyfluorene aromatic x 6 and poly(2-vinyl pyridine) C*H*-N aromatic), 7.57–6.09 (m, 724H, poly(2-vinyl pyridine) C*H* x 3 aromatic), 3.51 (br s, 2H, RAFT CTA CH_2-O); M_n (GPC) = 14,700 Da; M_w/M_n = 1.24.[3]

5.6.4 Self-Assembly Procedures

PI_{192}-*b*-PFS_{37}, *ran*-PI_{124}/$PtBS_{125}$-*b*-PFS_{37}, and $PtBS_{257}$-*b*-PFS_{38} 1D micelles were prepared via PI-CDSA, as previously reported.[1,2]

$PDHF_{17}$-*b*-$P2VP_{250}$ 1D micelles were prepared via CDSA, as previously reported.[3]

5.6.5 Supplementary Figures

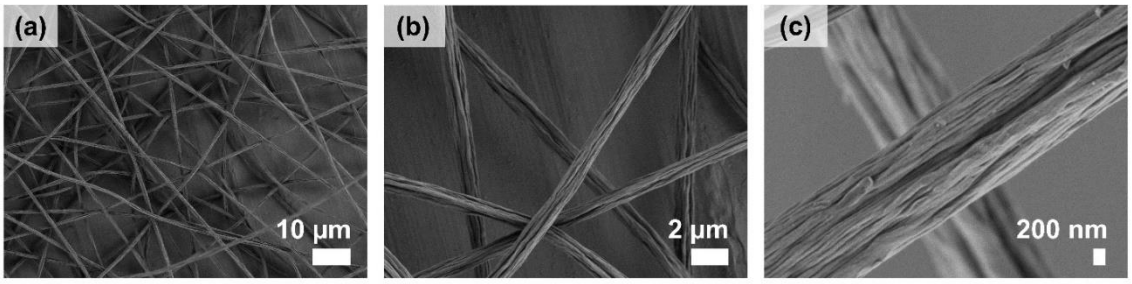

Figure S5.1 SEM image of microfibers formed via electrospinning of 7 wt% PS (M_n = 1.4 x 10^6 Da) in DMF. Scale bars: (a) 10 µm, (b) 2 µm, (c) 200 nm.

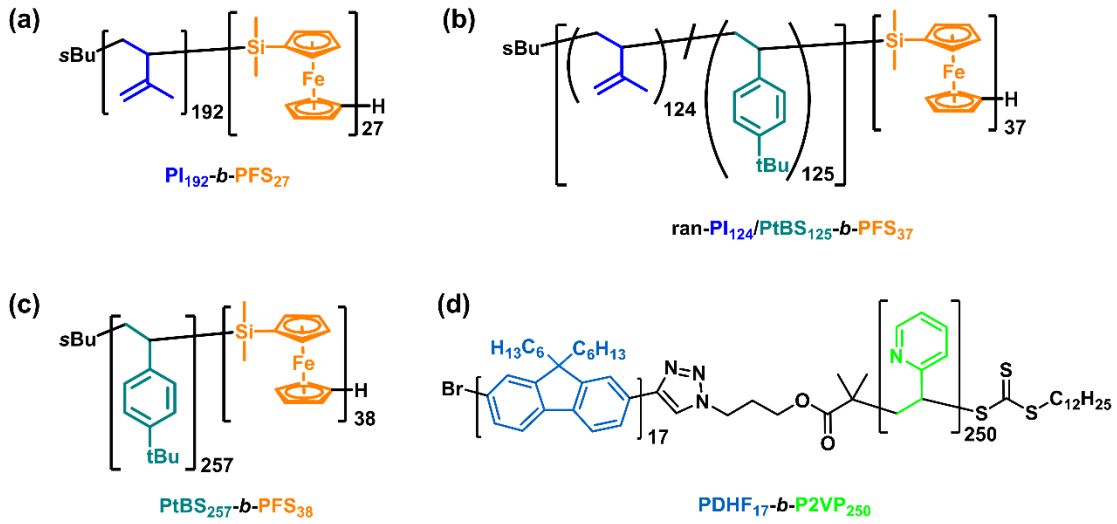

Figure S5.2 Chemical structures of (a)–(c) PFS-based and (d) PDHF-based BCPs utilized in this study.

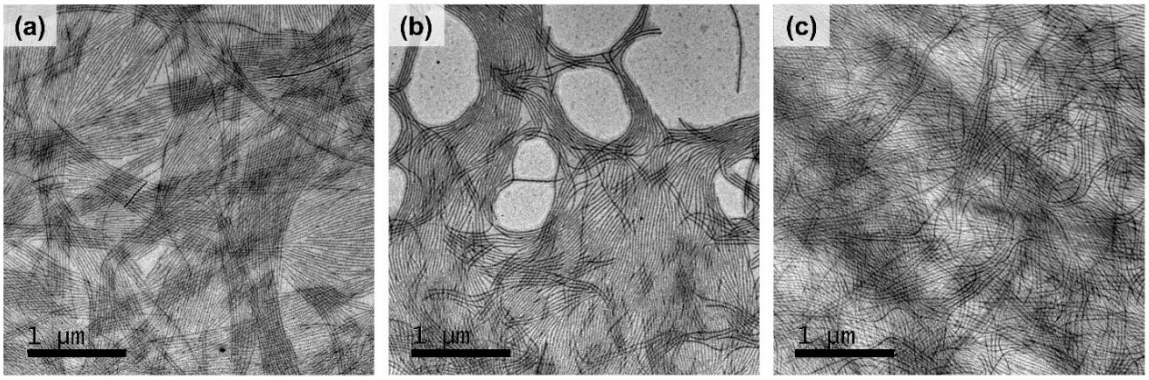

Figure S5.3 TEM images of polydisperse (a) PI_{192}-*b*-PFS_{27}, (b) *ran*-PI_{124}/$PtBS_{125}$-*b*-PFS_{37}, and (c) $PtBS_{257}$-*b*-PFS_{38} 1D micelles prepared via PI-CDSA (L_n = 500–3000 nm). Scale bars: 1000 nm.

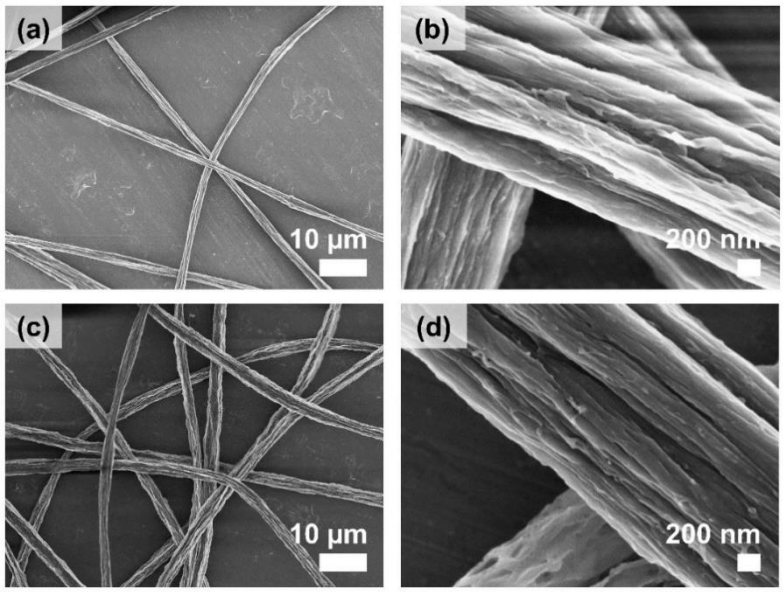

Figure S5.4 SEM images of microfibers prepared via coaxial electrospinning of (a), (b) *ran*-PI_{124}/$PtBS_{125}$-*b*-PFS_{37} micelles and (c), (d) $PtBS_{257}$-*b*-PFS_{38} micelles (2.8 wt% in 20 vol% THF/hexanes, shell) with PS (7 wt% in DMF, core). (a) and (c) are low magnification, (b) and (d) are high magnification. Scale bars: (a, c) 10 μm, (b, d) 200 nm.

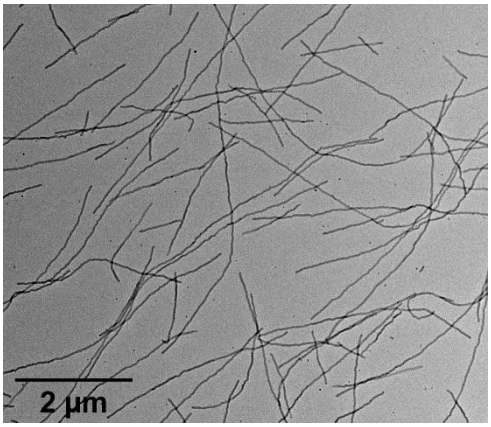

Figure S5.5 TEM image of polydisperse $PDHF_{17}$-*b*-$P2VP_{250}$ 1D micelles (L_n = 500–6000 nm) prepared by CDSA (1.0 wt% in 25/25/50 vol% THF/MeOH/DMSO). Scale bar: 2 μm.

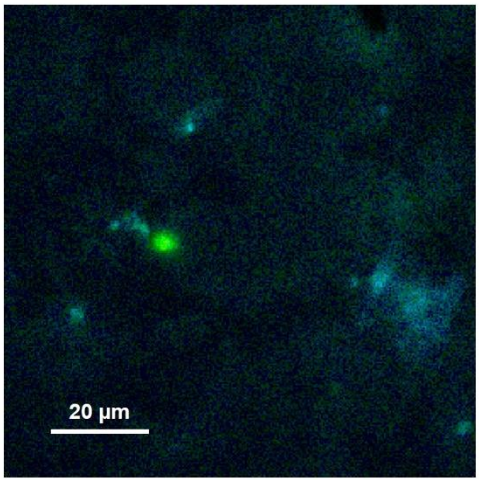

Figure S5.6 Confocal fluorescence microscope image of drop-cast neat $PDHF_{17}$-*b*-$P2VP_{250}$ 1D micelles (3.3 wt% in 25/25/50 vol% THF/MeOH/DMSO). Scale bar: 20 µm.

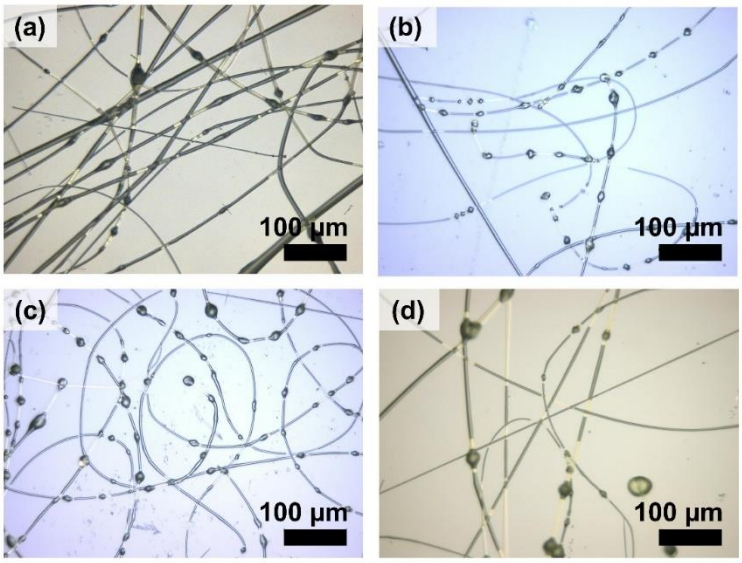

Figure S5.7 Optical microscope images of structures formed via electrospinning of PI_{192}-b-PFS_{27} 1D polydisperse micelle dispersions (L_n = 500–3000 nm) in 20 vol% THF/hexanes at 20 wt%. Collector distance and pump speeds of (a) 23 cm, 1.0 mL/h, (b) 23 cm, 0.8 mL/h, (c) 19 cm, 1.0 mL/h, and (d) 19 cm, 0.8 mL/h, were used. Scale bars: 100 µm.

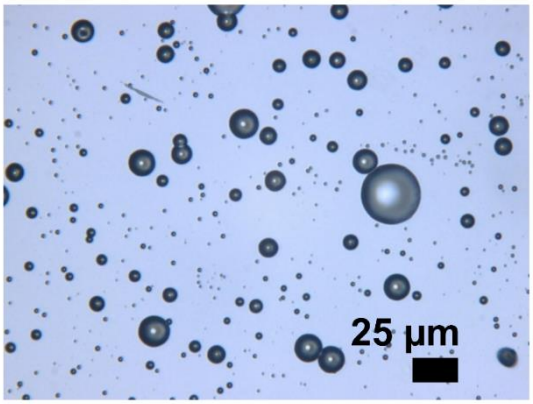

Figure S5.8 Optical microscope images of droplets formed via electrospinning of PI_{273} homopolymer. Scale bar: 25 µm.

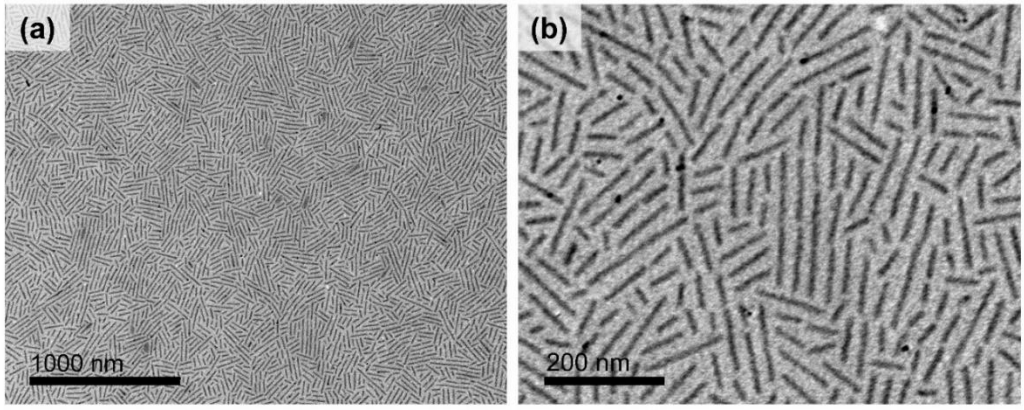

Figure S5.9 (a) Low and (b) high magnification TEM images of PI_{192}-*b*-PFS_{27} 1D micelles prepared via sonication of polydisperse micelles in 20 vol% THF/hexane at 20 wt% for 1 h at 0 °C (L_n = 71 nm, L_w/L_n = 1.25). Scale bars: (a) 1000 nm, (b) 200 nm.

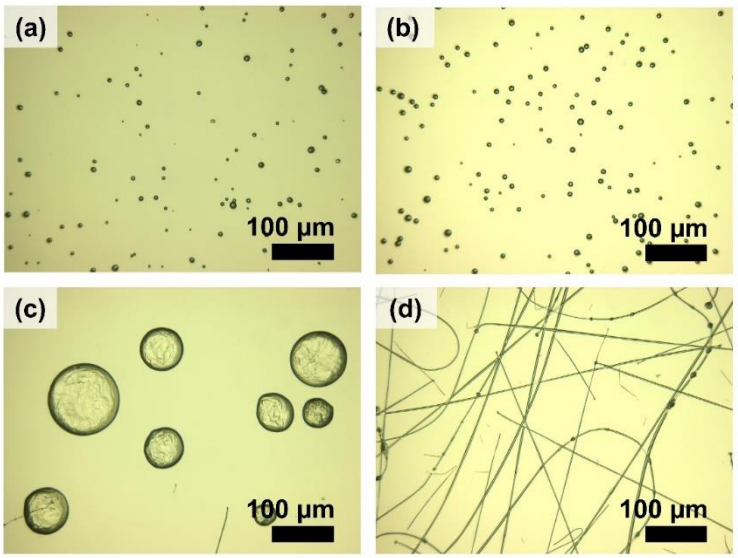

Figure S5.10 Optical microscope images of structures formed via electrospinning of PI_{192}-b-PFS_{27} 1D micelle dispersions (L_n = 71 nm, L_w/L_n = 1.25) in 20 vol% THF/hexanes at (a) 5 wt%, (b) 7.5 wt%, (c) 10 wt%, and (d) 20 wt%. Scale bars: 100 µm.

5.6.6 Supplementary Tables

Table S5.1 Experimental conditions used for coaxial electrospinning of polydisperse PFS-based micelle solutions (2.8 wt% in 20 vol% THF/hexanes, shell) with PS (7 wt% in DMF, core) where Q = pump rate, U = potential, d = distance, H = humidity, and T = temperature.

Material	$Q_{micelles}$ **(mL/h)**	Q_{PS} **(mL/h)**	U_{needle} **(kV)**	$U_{collector}$ **(kV)**	***d*** **(cm)**	***H*** **(%)**	***T*** **(°C)**
PI_{192}-*b*-PFS_{27}	1.1	1.1	11.7	-1.2	33	43	19.8
ran-PI_{124}/$PtBS_{125}$-*b*-PFS_{37}	1.1	1.1	11.7	-1.2	29	43	19.8
$PtBS_{257}$-*b*-PFS_{38}	1.1	1.1	13.5	-1.2	29	42	19.8

Table S5.2 Experimental conditions used for coaxial electrospinning of $PDHF_{17}$-*b*-$P2VP_{250}$ 1D micelles (1.0 wt% in 25/25/50 vol% THF/MeOH/DMSO) with PS (7 wt% in DMF) where Q = pump rate, U = potential, d = distance, H = humidity, and T = temperature.

Material	Q_{core} **(mL/h)**	Q_{shell} **(mL/h)**	U_{needle} **(kV)**	$U_{collector}$ **(kV)**	d **(cm)**	H **(%)**	T **(°C)**
$PDHF_{17}$-*b*-$P2VP_{250}$	1.2	0.4	13.6	-1.0	20	27	17.8

Table S5.3 Experimental conditions used for electrospinning of PI_{192}-*b*-PFS_{27} polydisperse micelle solutions (20 vol% THF/hexanes) where Q = pump rate, U = potential, d = distance, H = humidity, and T = temperature.

Concentration (wt%)	$Q_{micelles}$ **(mL/h)**	$U_{micelles}$ **(kV)**	$U_{collector}$ **(kV)**	d **(cm)**	H **(%)**	T **(°C)**
5	1.0	12.0	-1.2	33	29	20.8
10	1.0	13.1	-1.2	33	29	20.8
20	1.0	10.2	-1.2	33	29	20.8
20	1.0	8.4	-1.1	23	28	20.2
20	0.8	8.3	-1.1	23	27	20.9
20	1.0	8.5	-1.1	19	27	20.6
20	0.8	8.4	-1.1	19	27	20.6

Table S5.4 Experimental conditions used for electrospinning of PI_{192}-*b*-PFS_{27} polydisperse micelle solutions where Q = pump rate, U = potential, d = distance, H = humidity, and T = temperature.

	Solvent content (vol%)								
Conc. (wt%)	**DMF**	**THF**	**Hexanes**	$Q_{micelles}$ **(mL/h)**	$U_{micelles}$ **(kV)**	$U_{collector}$ **(kV)**	d **(cm)**	H **(%)**	T **(°C)**
20	0	20	80	0.8	8.5	-1.1	19	27	20.5
16	9	18	73	1.0	8.4	-1.1	23	30	20.6
16	9	18	73	0.8	8.4	-1.1	23	30	20.9
16	9	18	73	1.0	8.5	-1.1	19	30	20.9
16	9	18	73	0.8	8.5	-1.1	19	30	20.8

Table S5.5 Experimental conditions used for electrospinning of short PI_{192}-*b*-PFS_{27} micelle solutions (L_n = 71 nm, 20 vol% THF/hexanes) where Q = pump rate, U = potential, d = distance, H = humidity, and T = temperature.

Concentration (wt%)	$Q_{micelles}$ **(mL/h)**	$U_{micelles}$ **(kV)**	$U_{collector}$ **(kV)**	d **(cm)**	H **(%)**	T **(°C)**
5	1.0	8.8	-1.2	33	27	20.9
7.5	1.0	8.8	-1.2	33	27	20.9
10	1.0	13.4	-1.2	33	27	20.9
20	1.0	13.2	-1.2	33	27	20.9

5.6.7 Supplementary References

(1) Boott, C. E.; Gwyther, J.; Harniman, R. L.; Hayward, D. W.; Manners, I. Scalable and Uniform 1D Nanoparticles by Synchronous Polymerization, Crystallization and Self-Assembly. *Nat. Chem.* **2017**, *9*, 785–792.

(2) Oliver, A. M.; Gwyther, J.; Boott, C. E.; Davis, S. A.; Pearce, S.; Manners, I. Scalable Fiber-

like Micelles and Block Co-Micelles by Polymerization-Induced Crystallization-Driven Self-Assembly. *J. Am. Chem. Soc.* **2018**, *140* (51), 18104–18114.

(3) Zhang, Y.; Shaikh, H.; Sneyd, A. J.; Tian, J.; Xiao, J.; Blackburn, A.; Rao, A.; Friend, R. H.; Manners, I. Efficient Energy Funneling in Spatially Tailored Segmented Conjugated Block Copolymer Nanofiber−Quantum Dot or Rod Conjugates. *J. Am. Chem. Soc.* **2021**, *143* (18), 7032–7041.

Chapter 6 Summary and Outlook

The overall aim of the work presented in this thesis is to scale-up the preparation of size-tunable, low dispersity 1D and 2D micelles with a crystalline core by combining living crystallization-driven self-assembly (CDSA) and polymerization-induced crystallization-driven self-assembly (PI-CDSA) protocols. In this chapter, the key results contributing towards this objective will be discussed. Finally, potential future directions for the work in this thesis are described.

6.1 Summary and Future Work

6.1.1 Upscaled Preparation of Low Dispersity 2D Platelet Micelles

Chapter 2 demonstrates the living CDSA of phosphonium-capped poly(ferrocenyldimethylsilane) (PFS) homopolymers with surfactant counteranions as a route to access low dispersity 2D platelets at scalable concentrations. First, the CDSA and subsequent sonication of cylinder-forming PFS-*b*-P2VP (P2VP = poly(2-vinylpyridine)) were performed at 0.6 wt% to access upscaled 1D seed micelles. The living CDSA of phosphonium-capped PFS homopolymers with surfactant counteranions was then probed up to concentrations of 0.4 wt%. The effects of concentration and temperature on the platelet dimensions, core crystallinity, and structure fidelity were studied. Significantly, it was found that performing the living CDSA at increased temperature resulted in the formation of platelets which exhibit a lower aspect ratio, improved structure fidelity, and lower size-dispersity, despite the concentration being 40-fold higher than previously reported.

Future work should focus on improving the platelet colloidal stability further, as well as providing a more in-depth understanding of the relationship between platelet dimensions and self-assembly conditions. Increasing the charge density on the platelet surface could potentially improve the scalability of this protocol further by increasing the platelet colloidal stability. For example, by using a crystallizable homopolymer with charged groups at both termini, or by employing an

alternative charged end group such as trimethylammonium.[1] Alternatively, using a more solvophobic charged group as well as careful counteranion selection could have a similar stabilizing effect. To provide further understanding of the relationship between platelet structure and dimensions on the self-assembly conditions, studies into the mechanism of 2D living CDSA could be performed.

6.1.2 Upscaled Preparation of Low Dispersity 1D Nanofibers with a Biocompatible Crystalline Core

Although nanofibers prepared using living CDSA are of interest for a wide range of applications, their scale-up presents a key obstacle. Chapter 3 describes the preparation of length-disperse nanofibers with a biodegradable, crystalline poly(fluorenetrimethylenecarbonate) (PFTMC) core and a hydrophilic poly(ethylene glycol) (PEG) corona at 20 wt% by PI-CDSA, 400-times higher concentration that previously reported.

Scalable, low dispersity, and length-tunable 1D PEG-*b*-PFTMC nanofibers were also accessed via living PI-CDSA at 10 wt%. Nanofibers of controlled lengths from 100–660 nm were prepared, demonstrating a facile route to the upscaled preparation of biocompatible nanostructures at biologically relevant length-scales (< 200 nm). This work provides the first example of living PI-CDSA using a crystalline core-forming segment other than PFS, extending the scope to an all-organic block copolymer (BCP).

Expanding on this, future work could involve investigating the preparation of more complex nanofiber architectures relevant in nanomedical applications and beyond. This should include nanostructures such as segmented block comicelles, which could incorporate a functional corona to encapsulate hydrophobic cargo or targeting agents to allow for specific targeting of cancer cells, for example. A potential candidate for the coronal segment could be poly(*N*-isopropylacrylamide) (PNIPAM), which is water-soluble and biocompatible, and therefore has potential application in

the field of nanomedicine.[2] PNIPAM is also a thermoresponsive polymer, which can potentially be exploited for targeted cargo release.[3] It has been previously demonstrated that incorporating folic acid as a targeting group in the terminal coronal segment of a block comicelles led to uptake of 1D nanofibers into more than 97% of folate receptor positive HeLa cells.[4] This idea could be translated to the 1D micelles prepared by living PI-CDSA in this work, with the objective of facilitating the scalable preparation of nanofibers for use in targeted therapies and diagnostics.

Expanding the scope of living PI-CDSA to access fiber-like micelles containing other crystallizable core-forming segments is also of great interest. In particular, 1D micelles containing a π-conjugated crystalline core are of considerable interest for optoelectronic applications.[5,6] In order to further develop the field, their upscaled preparation is of crucial importance. The *in situ* nature of the living PI-CDSA process may help minimize competitive self-nucleation events to access scalable 1D fibers containing a π-conjugated crystalline core, without compromising on length-dispersity.

6.1.3 Preparation of 1D Cylindrical Micelles in Continuous Flow

An alternative route to the upscaled preparation of 1D micelles by living CDSA consists of translating the process from batch to continuous flow. The work in Chapter 4 first describes the successful implementation of a simple, cost-effective, and home-built flow setup to prepare 1D micelles by CDSA. A simple adjustment to the setup, whereby sonication was performed during the CDSA in flow, led to the preparation of low dispersity seed micelles in a residence time of 45 min. By this method, 685 mg of 1D seed micelles can be prepared per day. The preparation of low dispersity, length-controlled 1D micelles was also successfully facilitated by performing living CDSA in continuous flow. In this case, improved mixing of the unimer and seed solution streams was found to be fundamental to access micelles of low length-dispersity. This work provides the first example in which CDSA protocols are performed in continuous flow.

The results discussed in Chapter 4 provide a foundation for future studies on living CDSA in continuous flow. For example, the preparation of more complex nanofibers with segmented coronal structures should be easily facilitated using this technique. For example, by using PFS-*b*-P2VP seed micelles but employing a unimer which has a different corona-forming segment, such as PI-*b*-PFS (PI = polyisoprene) would allow access to micelles with a segmented PI/P2VP corona. Naturally, the work should also be demonstrated for the preparation of nanofibers with interesting potential applications, including those containing other crystalline cores for interest in biomedical applications, such as PFTMC,[7,8] or those with promising optoelectronic applications, such as poly(3-hexylthiophene)[9] or poly(di-*n*-hexylfluorene) (PDHF).[5] Another potential direction for this work could include investigating the living CDSA in two dimensions to access 2D platelet micelles in continuous flow. The colloidal stability of 2D platelet micelles is generally considerably lower than that of 1D micelles. This presents additional challenges, generally limiting their preparation via living CDSA to dilute conditions (ca. 0.002–0.01 wt%). Performing living CDSA in continuous flow therefore presents a promising route for the scale-up of 2D platelet micelles, since it can be performed at lower concentrations whilst maintaining a high throughput.

Future work will also focus on the preparation of low dispersity length-controlled 1D micelles via subsequent CDSA, sonication, and living CDSA in continuous flow (**Scheme 6.1**). In this case, the overall efficiency of the process would be vastly improved by simply combining the previously described optimized setups for both phases (seed preparation and living CDSA). Seed micelles would be prepared *in situ*, meaning only unimer solution would be required for use as the feed streams. Future efforts could also work towards incorporating the living anionic polymerization itself into the continuous flow setup,[10,11] potentially allowing for the preparation of the unimer solution *in situ* as well.

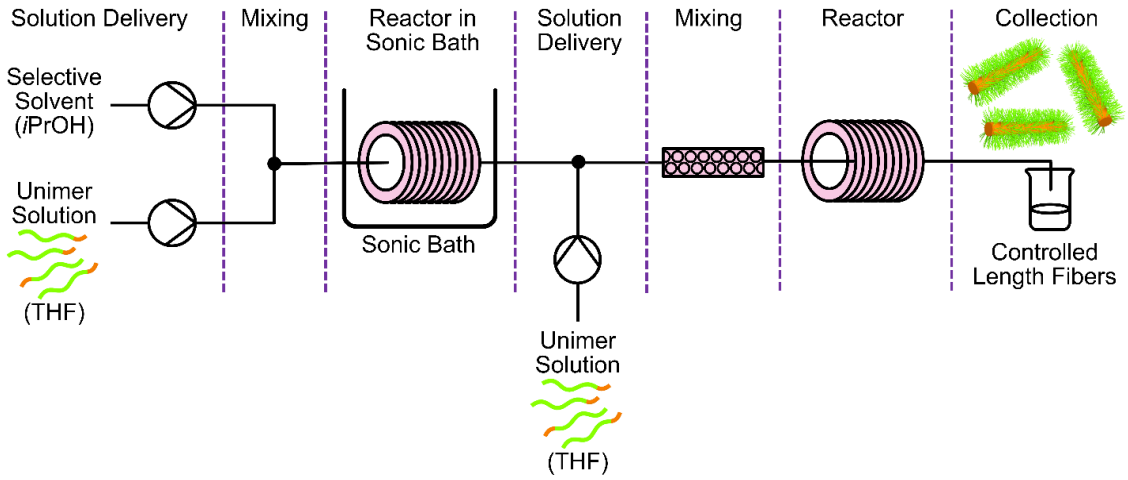

Scheme 6.1 Proposed setup for the preparation of length-controlled low dispersity PFS_{32}-*b*-$P2VP_{480}$ cylindrical micelles by CDSA, sonication, and subsequent living CDSA in continuous flow. *In situ* preparation of seed micelles is performed by synchronous CDSA and sonication in continuous flow, using a coil reactor with T-joint mixer and two reagent streams comprising of selective solvent (*i*PrOH) and unimer solution (PFS_{32}-*b*-$P2VP_{480}$ in THF, 25 mg/mL). Subsequent living CDSA is performed using a coil reactor with a packed-bed column mixer, with the addition of a third reagent stream comprising of unimer solution (PFS_{32}-*b*-$P2VP_{480}$ in THF, 25 mg/mL).

6.1.4 Electrospinning and Coaxial Electrospinning of 1D Micelles

Chapter 5 presents the use of electrospinning techniques as a simple, low cost, and high throughput method of producing microfibers comprising of 1D micelles containing a crystalline core. Coaxial electrospinning could be used to access core-shell microfibers in which 1D micelles with a PFS crystalline core are immobilized on a polystyrene (PS) microfiber. This work also describes efforts to extend this technique to use 1D micelles containing a π-conjugated PDHF crystalline core.

Future work will focus on optimizing the coaxial electrospinning of PDHF-containing micelles to produce well-defined microfibers for potential use in optoelectronic devices. One strategy should focus on preventing bead formation during the coaxial electrospinning process. Beading results

from low solution viscosity, high net charge density of the solution jet, and high surface tension.[12] Possibly, more concentrated solutions of 1D PDHF-containing micelles could be used to increase viscosity and prevent beading.

It was also demonstrated in Chapter 5 that electrospinning was successfully used to prepare microfibers consisting solely of 1D micelles containing a PFS crystalline core. This is the first example where a template material is not required to prepare microfibers of 1D micelles. In the future, efforts to expand the scope of this process to other 1D micelles should be made. In particular, microfibers comprising of biocompatible 1D micelles would be of great interest for potential applications in biomedical applications, such as tissue scaffolds and regenerative medicine.[13–15] Moreover, this process should be extended to prepare microfibers formed from 1D micelles with a π-conjugated crystalline core. It has previously been demonstrated that alignment of 1D micelles containing a poly(3-hexylthiophene) crystalline core enhanced charge-carrier mobility two-fold.[16] During electrospinning processes, 1D fibers typically align due to shear forces that are exerted on the solution as it passes through the needle.[17] Therefore, employing microfibers comprising of 1D micelles with a π-conjugated crystalline core in optoelectronic devices could result in improved device performance.

6.2 Outlook

Living CDSA has been proven as a powerful tool to access 1D and 2D nanostructures of controlled size and low size-dispersity. Depending on the nanostructure morphology and coronal and crystalline core chemistries, micelles prepared by living CDSA are of interest for various applications including those in nanomedicine, catalysis, optoelectronics, and materials engineering.[18] It is therefore of utmost importance that these 1D and 2D nanostructures can be prepared on a larger scale to facilitate their further investigation and application. Future challenges include scaling up the preparation of more complex nanostructures, such as segmented block comicelles. Moreover, gaining further insight into how factors such as temperature and

concentration affect the dimensions, size-dispersity, and structure fidelity of 1D and 2D micelles is of great importance.

6.3 References

(1) Pearce, S.; He, X.; Hsiao, M.-S.; Harniman, R. L.; MacFarlane, L. R.; Manners, I. Uniform, High-Aspect-Ratio, and Patchy 2D Platelets by Living Crystallization-Driven Self-Assembly of Crystallizable Poly(Ferrocenyldimethylsilane)-Based Homopolymers with Hydrophilic Charged Termini. *Macromolecules* **2019**, *52* (16), 6068–6079.

(2) Capella, V.; Rivero, R. E.; Liaudat, A. C.; Ibarra, L. E.; Roma, D. A.; Alustiza, F.; Mañas, F.; Barbero, C. A.; Bosch, P.; Rivarola, C. R.; Rodriguez, N. Cytotoxicity and Bioadhesive Properties of Poly-N-Isopropylacrylamide Hydrogel. *Heliyon* **2019**, *5* (4), 1–19.

(3) Akimoto, J.; Nakayama, M.; Sakai, K.; Okano, T. Temperature-Induced Intracellular Uptake of Thermoresponsive Polymeric Micelles. *Biomacromolecules* **2009**, *10* (6), 1331–1336.

(4) Street, S. T. G.; He, Y.; Jin, X.-H.; Hodgson, L.; Verkade, P.; Manners, I. Cellular Uptake and Targeting of Low Dispersity, Dual Emissive, Segmented Block Copolymer Nanofibers. *Chem. Sci.* **2020**, *11* (32), 8394–8408.

(5) Jin, X.; Price, M. B.; Finnegan, J. R.; Boott, C. E.; Richter, J. M.; Rao, A.; Menke, S. M.; Friend, R. H.; Whittell, G. R.; Manners, I. Long-Range Exciton Transport in Conjugated Polymer Nanofibers Prepared by Seeded Growth. *Science* **2018**, *900* (6391), 897–900.

(6) Sneyd, A. J.; Fukui, T.; Paleček, D.; Prodhan, S.; Wagner, I.; Zhang, Y.; Sung, J.; Collins, S. M.; Slater, T. J. A.; Andaji-Garmaroudi, Z.; Macfarlane, L. R.; Garcia-Hernandez, J. D.; Wang, L.; Whittell, G. R.; Hodgkiss, J. M.; Chen, K.; Beljonne, D.; Manners, I.; Friend, R. H.; Rao, A. Efficient Energy Transport in an Organic Semiconductor Mediated by Transient Exciton Delocalization. *Sci. Adv.* **2021**, *7* (32), eabh4232.

(7) Finnegan, J. R.; He, X.; Street, S. T. G.; Garcia-Hernandez, J. D.; Hayward, D. W.; Harniman, R. L.; Richardson, R. M.; Whittell, G. R.; Manners, I. Extending the Scope of "Living" Crystallization-Driven Self Assembly: Well-Defined 1D Micelles and Block Comicelles from Crystallizable Polycarbonate Block Copolymers. *J. Am. Chem. Soc.* **2018**, *140* (49), 17127–17140.

(8) Garcia-Hernandez, J. D.; Street, S. T. G.; Kang, Y.; Zhang, Y.; Manners, I. Cargo Encapsulation in Uniform, Length-Tunable Aqueous Nanofibers with a Coaxial Crystalline and Amorphous Core. *Macromolecules* **2021**, *54* (12), 5784–5796.

(9) Macfarlane, L. R.; Li, X.; Faul, C. F. J.; Manners, I. Efficient and Controlled Seeded Growth of Poly(3-Hexylthiophene) Block Copolymer Nanofibers through Suppression of Homogeneous Nucleation. *Macromolecules* **2021**, *54* (24), 11269–11280.

(10) Nagaki, A.; Takahashi, Y.; Akahori, K.; Yoshida, J.-I. Living Anionic Polymerization of Tert-Butyl Acrylate in a Flow Microreactor System and Its Applications to the Synthesis of Block Copolymers. *Macromol. React. Eng.* **2012**, *6* (11), 467–472.

(11) Natalello, A.; Morsbach, J.; Friedel, A.; Alkan, A.; Tonhauser, C.; Müller, A. H. E.; Frey, H. Living Anionic Polymerization in Continuous Flow: Facilitated Synthesis of High-Molecular Weight Poly(2-Vinylpyridine) and Polystyrene. *Org. Process Res. Dev.* **2014**, *18* (11), 1408–1412.

(12) Fong, H.; Chun, I.; Reneker, D. H. Beaded Nanofibers Formed during Electrospinning. *Polymer* **1999**, *40*, 4585–4592.

(13) Ogueri, K. S.; Laurencin, C. T. Nanofiber Technology for Regenerative Engineering. *ACS Nano* **2020**, *14* (8), 9347–9363.

(14) Yu, T.; Gleeson, S. E.; Li, C. Y.; Marcolongo, M. Electrospun Poly(ε-Caprolactone) Nanofiber Shish Kebabs Mimic Mineralized Bony Surface Features. *J. Biomed. Mater. Res. - Part B Appl. Biomater.* **2019**, *107* (4), 1141–1149.

(15) Lu, Y.; Huang, J.; Yu, G.; Cardenas, R.; Wei, S.; Wujcik, E. K.; Guo, Z. Coaxial Electrospun Fibers: Applications in Drug Delivery and Tissue Engineering. *Wiley Interdiscip. Rev. Nanomedical Nanobiotechnology* **2016**, *8* (5), 654–677.

(16) Li, X.; Wolanin, P. J.; MacFarlane, L. R.; Harniman, R. L.; Qian, J.; Gould, O. E. C.; Dane, T. G.; Rudin, J.; Cryan, M. J.; Schmaltz, T.; Frauenrath, H.; Winnik, M. A.; Faul, C. F. J.; Manners, I. Uniform Electroactive Fibre-like Micelle Nanowires for Organic Electronics. *Nat. Commun.* **2017**, *8*, 15909.

(17) Schöbel, J.; Burgard, M.; Hils, C.; Dersch, R.; Dulle, M.; Volk, K.; Karg, M.; Greiner, A.; Schmalz, H. Bottom-Up Meets Top-Down: Patchy Hybrid Nonwovens as an Efficient Catalysis Platform. *Angew. Chem. Int. Ed.* **2017**, *56* (1), 405–408.

(18) MacFarlane, L. R.; Zhao, C.; Cai, J.; Qiu, H.; Manners, I. Emerging Applications for Living Crystallization-Driven Self-Assembly. *Chem. Sci.* **2021**, *12* (13), 4661–4682.